Geometry-Based Channel Models for Car-to-Car Communication Systems and Applications

Nurilla Avazov

Geometry-Based Channel Models for Car-to-Car Communication Systems and Applications

Doctoral Dissertation for the Degree *Philosophiae Doctor (PhD)* in
Information and Communication Technology

University of Agder
Faculty of Engineering and Science
2015

Doctoral Dissertation by the University of Agder 113
ISBN: 978-82-7117-799-7
ISSN: 1504-9272

Printed in the Printing Office, University of Agder
Kristiansand

To my parents, Khabibulla and Nigora,
to my wife, Khosiyat and to
my sons, Mukhammadamin and Asadbek

Preface and Acknowledgements

Praise be to Almighty Allah, the most merciful and the most gracious. Without HIS endless blessings and guidance my accomplishment would never have been possible.

The research work in this dissertation is carried out at the Department of Information Communication Technology (ICT), Mobile Communication Group (MCG) of University of Agder (UiA) in Grimstad, Norway. The completion of this dissertation would not be possible without technical and emotional support of many individuals to whom I would like to express my deep gratitude.

First and foremost, I would like to express my sincerest gratitude to my supervisor Prof. Matthias Pätzold. His excellent guidance, active involvement, extensive cooperation, valuable comments, encouragement, and constant support helped me in all the time of research and during the course of my dissertation. I am also grateful to my co-supervisor Prof. Frank Yong Li for his timely supports.

I am also thankful to the Secretary of the MCG, Mrs. Katharina Pätzold for her extensive support and the help provided in administrative and personal matters. Moreover, I would like to acknowledge all the stuffs at the Department of ICT for their timely support and advices. Especially, I would like to thank the Head of the Department of ICT, UiA, Prof. Andreas Prinz and the Coordinator of the PhD program at the Department of ICT, UiA, Mrs. Emma Elizabeth Horneman. It would be unfair if I do not mention the assistance provided by the former Coordinator of the PhD program at the Department of the ICT, UiA, Mrs. Trine Tønnessen, in several formalities associated with our PhD program.

My sincere gratitude goes to my Doctoral Fellows from the Department of ICT, especially to Ali Chelli, Alireza Borhani, Akmal Fayziyev, Anis Yazidi, Batool Talha, Gulzaib Rafiq, Meisam Naderi, Parvaneh Sarshar, Yuanyuan Ma. During my stay in Grimstad, their continuous encouragement, lovely and friendly support created a very comfortable working environment around me.

Last, but certainly not least, I would like to express my endless gratitude to my parents, Khabubilla and Nigora, my brother Khayrulla and my sister Shakhnoza for their commitment, sacrifice, and continuing support. Finally, I would like to thank my wife, Khosiyat who has shown infinite love and patience during my doctoral studies.

Nurilla Avazov
April 2015
Grimstad, Norway

Summary

In last two decades, intelligent transportation systems (ITS) have received considerable attention due to new road traffic safety applications that significantly improve the efficiency of traffic flow and reduce the number of road accidents. Consequently, there has been an increased interest in studying and developing car-to-car (C2C) communication systems, which play a key role in ITS. C2C communications has also gained the attention of standardization bodies, such as the IEEE[1] and 3GPP LTE[2], which aim to provide improvements in C2C communication systems. As it follows from the title, in this dissertation, we present the state-of-the-art regarding the modeling and analysis of different C2C channels in C2C communication systems. In C2C communication systems, the underlying radio channel differs from the conventional fixed-to-mobile (F2M) and fixed-to-fixed (F2F) channels in the way that both the mobile transmitter and the mobile receiver are in motion. In this regard, reliable and robust traffic telematic systems have to be designed, developed and tested. This leads to a demand for new radio channel models for C2C communication systems. Therefore, this dissertation is devoted to design, develop and validate new geometry-based channel models for C2C communication systems. In particular, two goals are aimed, which are study and investigation of the propagation characteristics of C2C fading channels and analyzing the performance of C2C communication systems over those fading channels correlated in time and space.

For the development of future communication systems, efficient channel modeling is essential, which allows designing, evaluating and optimizing wireless communications. Designed channel models should be as accurate as possible, simple, and easy to implement. In the literature, there exist several channel modeling approaches, such as the deterministic approach, the stochastic approach, the geometry-based stochastic approach, and the measurement-based approach. In this dissertation, the geometry-based stochastic approach is considered to model the channel for C2C communications in urban street areas and tunnel environments. The usefulness of this geometry-based stochastic approach is that the proposed channel models can be easily implemented and enable us to predict the fading behavior for various propagation environments in different communication scenarios.

The significant part of this work is that we consider such geometrical models, which are close to realistic scenarios, i.e., the rectangle street scattering model, curved street model, and the tunnel model. The most important statistical properties of the proposed channel models, such as the two-dimensional (2D) space

[1] Institute of Electrical and Electronics Engineer

[2] Third-Generation Partnership Project Long-Term Evolution

cross-correlation function (CCF), the temporal autocorrelation function (ACF), and the frequency correlation function (FCF) are studied and analyzed. Using the generalized principle of deterministic channel modeling, simulation channel models, namely channel simulators, are obtained from the reference model by using a finite number of scatterers. A validation of the usefulness of the proposed channel models is demonstrated by the excellent fitting of the analytical results, such as the Doppler statistics and the delay statistics of the reference model, to those of measured channels.

Moreover, another part of this dissertation is focused on the investigation of the performance analysis of multiple-input multiple-output (MIMO) orthogonal frequency division multiplexing (OFDM) communication systems used for C2C communications. The performance of Alamouti coded OFDM systems over different types of wideband MIMO C2C channels correlated in time and space is studied and analyzed. A generalized expression of the time-variant transfer function (TVTF) for wideband MIMO C2C channels is derived, which is used to describe the rectangle model, curve model, street line model, and the tunnel model as special cases. Consequently, a generalized expression for the bit error probability (BEP) is presented. The proposed generalized channel model allows us to study the impact of the channel model parameters on the system performance.

Contents

List of Figures

List of Tables

Abbreviations

3GPP	3rd Generation Partnership Project
2D	two-dimensional
3D	three-dimensional
ACF	autocorrelation function
ADF	average duration of fades
AF	amplify-and-forward
AOA	angle-of-arrival
AOD	angle-of-departure
AWGN	additive white Gaussian noise
BS	base station
BEP	bit error probability
BER	bit error rate
BPSK	binary phase shift keying
C2C	car-to-car
C2C-CC	car-to-car communication consortium
C2I	car-to-infrastructure
CC	code combining
CCF	cross-correlation function
CDF	cumulative distribution function
CIR	channel impulse response
COOPERS	Cooperative Systems for Intelligent Road Safety
CSI	channel state information
CT	coherence time
CVIS	Cooperative Vehicle-Infrastructure Systems
DD	Doppler delay
DFT	discrete Fourier transform
DSRC	dedicated short-range communications
DWM	Driver Workload Metrics
EMEDS	extended method of exact Doppler spread

ERTICO	European Road Transport Telematics Implementation Coordinating Organization
F2F	fixed-to-fixed
F2M	fixed-to-mobile
FEC	forward error correction
FFT	fast Fourier transform
GMEA	generalized method of equal areas
HARQ	hybrid automatic repeat request
HW	highway
ICI	intercarrier interference
IDFT	inverse discrete Fourier transform
IEEE	Institute of Electrical and Electronics Engineer
IR	incremental redundancy
ITS	Intelligent Transportation Systems
LCR	level-crossing rate
LOS	line-of-sight
LPNM	L_p-norm method
LTE	Long Term Evolution
MAC	medium access control
M2M	mobile-to-mobile
M2F	mobile-to-fixed
MAC	medium access control
MIMO	multiple-input multiple-output
MS_T	mobile transmitter
MS_R	mobile receiver
NLOS	non-line-of-sight
OFDM	orthogonal frequency division multiplexing
PDF	probability density function
PDP	power delay profile
PER	packet error rate
PL	pathloss
PP	power profile
PBC	precoding-based cancellation
PRESERVE	Preparing Secure Vehicle-to-X Communication Systems
PSD	power spectral density
QAM	quadrature amplitude modulation
QoS	quality of services
QPSK	quadrature phase shift keying

RA	rural area
RMS DS	root mean squared delay spread
SA	suburban area
SDF	space-Doppler-frequency
SISO	single-input single-output
SNR	signal-to-noise ratio
SOC	sum-of-cisoids
SOS	sum-of-sinusoids
SCT	semicircular tunnel
STC	space-time code
ST-CCF	space-time cross-correlation function
STBC	space-time block code
STF-CCF	space-time-frequency cross-correlation function
STTC	space-time trellis code
TDL	tapped-delay-line
TF-CCF	time-frequency cross-correlation function
TTT	Transport and Traffic Telematics
TVTF	time-variant transfer function
UA	urban area
V2V	vehicle-to-vehicle
VPL	vertical plane launching
VSC	Vehicle Safety Communications
WAVE	wireless access in vehicular environment
WiFi	Wireless Fidelity
WiMax	Worldwide Interoperability for Microwave Access
WSSUS	wide-sense stationary uncorrelated scattering

Chapter 1

Introduction

1.1 Overview of C2C Communications

In recent years, the number of cars on traffic roads increased, which has in turn resulted in an upsurge of interest in car-to-car (C2C) communication systems. The reason is that C2C communications come along with many advantages such as new traffic telematic applications that improve the efficiency of the traffic flow, reduce the number of road accidents as well as the fuel consumption, and provide in-car Internet access, support convoy driving and automatic driving [1]. In the literature [2–5], several excellent papers appeared, which provide a comprehensive overview of the state-of-the-art of traffic telematic applications, architectures, challenges and their proposed solutions in C2C communications. For example, Karagiannis *et. al* [3] provides an overview of a highway cooperative collision avoidance safety application, in which cars send collision warning messages to avoid road accidents. Hence, reliable and fast warning message delivery is important to develop efficient safety applications. These warning messages can be disseminated by using roadside units (RSU) and on-board units (OBU) deployed on cars, which constitute car-to-infrastructure (C2I) communications and C2C communications, respectively. The reliability of traffic warning systems is ultimately dictated by the properties of the wireless propagation channel. Thus, the radio propagation channel conditions, in which C2C communications will be used, need to be evaluated before rushing to any conclusions regarding the reliability and robustness of such systems. In this context, a large number of research projects pertaining to C2C communications are being carried out throughout the world [3, 5] aiming to improve the traffic flow and road user safety [6, 7]. For example, in the USA, several research projects under the broader umbrella of the Intelligent Transportation Systems (ITS) [8] program have been carried out on the development of safety applications using C2C communica-

tions, such as Driver Workload Metrics (DWM) Project [9], the Forward Collision Warning (FCW) Requirement Project [10], and the Vehicle Safety Communications (VSC) Project [11].

The development of future C2C communication technologies is also supported in Europe by respected organizations, such as the European Road Transport Telematics Implementation Coordinating Organization (ERTICO) [12] and the C2C Communication Consortium (C2C-CC) [13]. In Europe, there are more than 60 past and on-going research projects dealing with ITS [3, 14]. Cooperative C2C communications are investigated in several projects, such as the Cooperative Vehicle-Infrastructure Systems (CVIS) [15], the Cooperative Systems for Intelligent Road Safety (COOPERS) [16], and the Compass4D [17], while the Preparing Secure Vehicle-to-X Communication Systems (PRESERVE) [18] was focusing on secure C2C and C2I communications by protecting the privacy of user data. A typical propagation scenario for C2C communications is illustrated in Fig. 1.1, where the buildings and trees can be considered as scatterers.

Figure 1.1: A typical C2C communication scenario.

The booming interest in C2C communication systems is also reflected in the allocation of the 75 MHz of spectrum in the 5.9 GHz band dedicated for short-range communications (DSRC) [19, 20]. Consequently, the IEEE 802.11p [21] standard was approved by the IEEE Task Group, which was an enhancement of the IEEE 802.11 [22] capabilities to support ITS [8]. Thus, this augmentation is called Wireless Access in Vehicular Environments (WAVE) [21]. According to the IEEE 802.11p [21], the frequency bands for DSRC will be between 5770 MHz and

5925 MHz depending on the region. Thus, several countries have allocated a DSRC frequency band. Hence, in Europe, the band $5795 - 5815$ MHz is designated for Transport and Traffic Telematics (TTT), while the USA and Japan use the frequency bands $5850 - 5925$ MHz and $5770 - 5850$ MHz, respectively.

Consequently, a large number of measurements have been carried out at different frequency bands, for example, at 2.4 MHz [23], 3.5 GHz [24], 5 GHz [25, 26], 5.2 GHz [27], and 5.9 GHz [28]. These empirical studies in the context of C2C communications have contributed to understand the properties of C2C channels. As for any communication system, the development of C2C communication systems requires a detailed knowledge of the propagation channel characteristics. In practice, highways, rural, urban, and suburban as well as tunnel environments are considered as wireless propagation environments for C2C communications, which are significantly different from traditional fixed-to-mobile (F2M) and fixed-to-fixed (F2F) communications. It is widely accepted that in C2C communications, both the mobile transmitter (MS_T) and the mobile receiver (MS_R) are in motion and equipped with multiple antenna elements, which are mostly at the same height. In addition, the propagation channel in C2C communications is dynamic and thus subject to more rapid fluctuations than traditional F2M and/or F2F channels. In this regard, accurate and proper C2C channels are required to develop, test, optimize, and analyze reliable and robust C2C communication systems.

1.2 Motivation and Contributions of the Dissertation

Developing new C2C channel models and investigating their propagation characteristics are expected to provide a foundation for the development of future ITS. From the radio propagation perspective, the scattering environment in the C2C communication channel is different from that in the F2M or F2F communication channel. Consequently, channel modeling for C2C communications has been attracting considerable attention from researchers, standardization bodies, and industrial companies.

Over the last decade, researchers have investigated a significant number of C2C channels [26, 28, 29] developed for different scattering environments. Many of them found that the C2C channel cannot be described by a single model, but must be represented by a set of many different channel models for various environments. However, there are still open problems such as developing new C2C channel models considering different geometrical propagation areas and analyzing the performance of C2C communication systems over the proposed C2C channels for further ad-

vancements in future ITS. In the literature [30–35], a large number of fundamental channel models have been proposed with various scatterer distributions and different geometrical scattering areas to study the characteristics of multipath environments and to understand the propagation characteristics of wireless channels. C2C channels addressing the multi-bounce scattering effect and non-isotropic scattering conditions, where the angle-of-departure (AOD) and the angle-of-arrival (AOA) are not uniformly distributed, have rarely been considered in the literature. To investigate and analyze the spatial and temporal characteristics of C2C channels in confined environments such as tunnels, underground roads, and parking garages are also of great importance for C2C communications. Nevertheless, there is a scarcity of literature regarding the effect of the distribution of scatterers on the spatial and temporal properties of C2C channels inside tunnel environments.

Another area that requires further attention is the performance analysis of C2C communication systems, which is of fundamental importance to provide reliable communications especially for traffic safety applications. Although there exist a number of research works focusing on the performance analysis of C2C communications [26, 36–40], there are still open problems in the analysis of C2C communication performance in different propagation scenarios and environments.

Motivated by the scarce availability of studies pertaining to the performance analysis of C2C communication systems and the need for accurate and proper C2C channel models, the main contributions of this dissertation are listed as follows:

1. Narrowband and wideband two-dimensional (2D) geometry-based stochastic C2C channel models were developed. They are able to capture the scattering effect of urban, rural, and highway propagation areas, in which straight street and curved street scenarios are taken into account;

2. C2C channel models considering single- and double-bounce scattering effects under line-of-sight (LOS) and non-LOS (NLOS) propagation conditions were developed;

3. A new wideband three-dimensional (3D) geometry-based C2C channel model was proposed for tunnel environments assuming both LOS and NLOS propagation conditions;

4. All aforementioned channel models were validated by real-world measurement campaigns.

5. The performance of space-time coded orthogonal frequency division multiplexing (OFDM) systems was analyzed over different types of wideband C2C

channels correlated in time and space.

1.3 Organization of the Dissertation

This dissertation concentrates on the comprehensive investigations of different C2C propagation scenarios. The covered topics range from developing new narrowband and wideband geometry-based MIMO C2C channel models for different propagation environments up to the analysis of the performance of C2C communication systems in terms of bit error probability (BEP). This dissertation summarizes the research work presented in five selected papers, which are included at the end of the dissertation as appendices (Appendices A-E). Papers addressing similar topics are collected together to form chapters. The rest of the dissertation is organized as follows:

- **Chapter 2** is dedicated to model and analyze 2D narrowband single-input single-output (SISO) and multiple-input multiple-output (MIMO) C2C channel models. Two different kinds of 2D geometry-based channel models, i.e., the geometrical street scattering model (rectangle model) and the geometrical curved street scattering model (curved model), are introduced in the current chapter. Furthermore, the extension from a narrowband MIMO C2C channel model to a wideband model is discussed. Consequently, the statistical characterization of the geometrical street scattering model in terms of the temporal autocorrelation function (ACF) and the space-time cross-correlation function (ST-CCF) is discussed. Afterwards, we validate the usefulness of the proposed models. Papers I – III (Appendices A – C) that are summarized in subsequent sections of Chapter 2 reveal key results pertaining to the statistical properties of the rectangle model and the curved model.

- **Chapter 3** caters for the modeling and analysis of 3D geometry-based MIMO channel models for C2C communication systems. The motivation behind modeling 3D geometry-based C2C channels with LOS components comes from the fact that such models can appropriately characterize real-life propagation channels. Here, it is necessary to point out that the C2C fading channel model illustrated in this chapter is a new 3D geometrical-semicircular-based channel model, which characterizes the fading behaviour in tunnel environments. An insightful review of Paper IV (Appendix D) is included in Chapter 3. In this paper, we have studied the statistics in terms of the space-time-frequency CCF (STF-CCF), the time-frequency CCF (TF-CCF), the temporal

ACF, the frequency correlation function (FCF), the Doppler statistics, and the delay statistics. Moreover, a validation of the proposed 3D semicircular tunnel (SCT) model by a measured channel is addressed.

- **Chapter 4** shows our efforts to analyze the performance of MIMO OFDM systems in different C2C channels. The performance analysis of Alamouti coded OFDM systems over wideband C2C channels correlated in time and space is discussed in the present chapter. A brief overview of Paper V (Appendix E) is given in this chapter, which deals with the derivation of a generalized expression for the time-variant transfer function (TVTF) and analysis of theoretical expressions for the BEP of the Alamouti coded OFDM systems. This performance analysis is carried out assuming different propagation environments, such as the rectangle model, the street line model, the curve model, and the tunnel model.

- **Chapter 5** summarizes the main contributions of this dissertation. We close this chapter by highlighting some open problems pertaining to the design and development of C2C communication systems that call for further attention.

Each chapter comprises various sections dealing with the subtopics addressed in the chapter. The outline of each chapter has the following structure:

- **Introduction** gives an overview and the state of the art of the main topic explored in the chapter.

- **Section M** presents preliminary and significant background information on the topic of interest as well as a literature review of the prior research work on the subject.

- **Section N** provides a joint discussion on the paper(s) dealing with the same subtopic. Each section has the following structure:

  - Each section begins with a brief introduction of the subject as well as the motivations to address that particular problem.
  - It then provides a problem description and elaborates the main work of the paper(s) used in this section.
  - Finally, the main results of the paper(s) are discussed and the significance of the achieved outcome(s) is highlighted.

- **Chapter Summary and Conclusion** highlights the main findings of the chapter.

Chapter 2

Statistical Modeling and Analysis of 2D Geometry-Based C2C Channel Models

2.1 Introduction

In the past decade, MIMO C2C channel modeling has been gained a fair share of attention by researchers, standardization bodies, and industries and thus many different types of MIMO C2C channel models have been proposed. These proposed several MIMO C2C channels can be classified in many different ways, for example, with respect to the frequency-selectivity, stationarity, time-variant properties, the multi-dimensional propagation environments, etc.

According to [41], there exist in general three fundamental channel modeling approaches, namely the deterministic approach, stochastic approach, and geometry-based stochastic approach [42–45]. The deterministic channel modeling approach for C2C communications has been widely investigated by Maurer *et. al* [46]. In deterministic channel modeling, the propagation environment is described in a completely deterministic manner. The deterministic approach can be classified into two different categories, the ray-tracing approach and the measurement-based approach. In the ray-tracing approach, Maxwell's equations are often solved under boundary conditions imposed by a specific wireless channel propagation environment [41]. However, the deterministic channel modeling approach requires some effort due to the intensive computations, which makes it challenging to adjust the model parameters. It is well known that the measurement-based channel models are accurate, but they are time consuming, site-specific, and costly.

In the stochastic channel modeling approach, the statistics of the propagation

channels, such as delay, Doppler shift, and angle-of-arrival are modelled. Especially, the tapped-delay-line (TDL) [47] model is widely investigated for F2M channels by assuming wide-sense stationary uncorrelated scattering (WSSUS) conditions. The TDL model for proposed for C2C channels [29, 48] has been adopted by the IEEE 802.11p standard group. However, the WSSUS condition is usually violated in C2C channels due to the high mobility of the mobile cars. Hence, the geometry-based stochastic channel models are developed to capture the non-stationary features of C2C channels. In addition, the geometry-based stochastic approach has a number of significant benefits, such as the modeling of MIMO channels, enabling to change the environment to the desired one, and time-efficient computation of the proposed channel. Original geometry-based stochastic models for C2C communications were proposed in [49, 50]. An extension of these works from 2D geometrical models towards 3D geometrical models has been done in [51], where the Doppler spectrum and the ACF are investigated. More discussions on 2D geometry-based C2C channels are provided in the following sections.

2.1.1 C2C Channel Measurements

Owing to a large difference between the F2M and the C2C channels, the channel statistics obtained from traditional F2M wireless channels cannot be directly used for C2C communication systems. Thus, in the literature, a large number of measured C2C channels have been reported for different C2C communications scenarios. Recent C2C channel measurements are classified according to frequency-selectivity, carrier frequencies, multiple antennas configurations, propagation environments, direction of motions of both the MS_T and MS_R, and channel statistics. In the literature [52], it was mentioned that the different carrier frequencies significantly affect the channel propagation even in similar environments. Thus, more measurement campaigns are required to be performed at different frequencies, such as 2.4 GHz, 5.2GHz, and 5.9 GHz for a better design of safety and non-safety applications for C2C communications. The directions of motion of the MS_T and the MS_R also affect the C2C channel statistics, such as the average Doppler shift and the Doppler spread. Several measurement campaigns have been done in [23, 27, 53] for C2C communications, where the MS_T and the MS_R are moving in the same direction, whereas C2C channel measurement for communicating cars moving in the opposite direction are reported in [29, 54, 55]. A summary of important C2C channel measurements is presented in Table 2.1.

Table 2.1: Summary of important C2C channel measurements.

Frequency-Selectivity	**Carrier Frequency**	**Antenna Configurations**	**MS$_T$/MS$_R$ Direction of Motion**	**Propagation Environment**	**Channel Statistics**
wideband	2.4 GHz [23]	SISO	same	HW/SA	PDP, DD PP
	2.4 GHz [56]	MIMO	same	HW/UA	STF CF, LCR, SDF PSD
	5 GHz [25]	SISO	same	HW/SA/UA	envelope PDF, frequency CF, PDP
	5 GHz [54]	MIMO	opposite	HW	PL, PDP, DD PP
	5.2 GHz [57]	SISO	same	HW/SA/UA	PDP, PL, RMS DS, LCR
	5.2 GHz [55]	MIMO	opposite	HW	PDP, PL, DD PP
	5.9 GHz [29]	SISO	same, opposite	HW/SA/UA	envelope PDF, DD PP
	5.9 GHz [53]	SISO	same, opposite	HW/SA/RA/UA	PDP, Doppler spread
narrowband	5.9 GHz [28]	SISO	same	SA	PL, CT, envelope PDF Doppler PSD
	5.2 GHz [27]	SISO	same	HW/SA/UA	Doppler PSD, LCR, CDF

HW: highway; SA: suburban area; RA: rural area; UA: urban area; PDP: power delay profile; DD PP: Doppler-delay power profile; PSD: power spectral density; STF: space-time-frequency; CF: correlation function; LCR: level crossing rate; SDF: space-Doppler frequency; PDF: probability density function; RMS DS: root mean squared delay spread; PL: pathloss; CDF: cumulative distribution function; CT: coherence time.

2.1.2 C2C Channel Characteristics

The knowledge of the wireless channel is of fundamental importance to the optimal design and performance of C2C communication systems. The propagation channel characterization must be as accurate as possible and easy to use in the analysis, computer simulations and empirical experiments. On the other hand, the channel characterization should not be too complex. Thus, the tradeoff between the complexity and the accuracy must be taken into account. In C2C communication systems, a transmitted signal can propagate from the MS_T to the MS_R via different paths, which involve reflection, diffraction, scattering, waveguiding, etc. Hence, the effect of propagation delays occurs due to the multipath scattering. Therefore, the C2C channel is often characterized in terms of the time-variant channel impulse response (CIR) and/or in terms of its inverse Fourier transform, i.e., the TVTF. Moreover, there have also been derived other important channel statistics, such as pathloss, amplitude distribution functions, Doppler spread and delay spread.

In [25, 28, 29], the analysis of amplitude distributions has been presented. The authors of [28] observed that the amplitude distribution of the received signal gradually changes from Ricean to Rayleigh distribution if the distance between the MS_T and the MS_R increases. Moreover, the amplitude distribution function can also be described by the Weibull distribution [25], because of high speed and low elevated antennas of the MS_T and the MS_R as well as due to the fast moving scatterers in propagation environments. Owing to the relatively high speed of the MS_T and the MS_R, the Doppler spread of C2C channels is higher than the spread of conventional cellular channels. The Doppler PSD has been studied in [27] for a narrowband C2C channel at 5.2 GHz. The joint delay and Doppler PSD measurements are available in [23, 29, 55] for wideband C2C channels.

2.2 Narrowband 2D Geometry-Based C2C Channel Models

In this section, we discuss narrowband 2D geometry-based C2C channel models derived from different geometrical street scattering environments such as straight street, cross street, and curved street scattering environments. Since the pioneering works in [49, 50], there has been a huge amount of research works investigating C2C fading channels. Research works presented in [49, 50] deal with the studies of the statistical properties of narrowband SISO mobile-to-mobile (M2M) channels under NLOS propagation conditions and provide a theoretical analysis based on

simplified assumptions. The increasing demand for high data-rate wireless communication services resulted in a significant upsurge of interest in MIMO systems, due to a remarkable gain in the spectral efficiency of wireless communication systems [58, 59]. Thus, MIMO communication systems can also be of great interest for C2C communications due to their higher throughput. In this regard, several articles have been published addressing geometry-based MIMO C2C channel models, which are developed and analyzed under different scattering conditions induced by, for example, the two-ring model [60], the elliptical model [61], the T-junction model [62], the cross-junction model [63], the rectangle mode [64], the street line model [65], and the curve model [66]. Many studies have revealed that geometry-based channel modeling is a good starting point for deriving simulation models for MIMO channels. Simulation models for narrowband MIMO M2M channels are presented in [60, 67, 68]. A generic geometry-based MIMO M2M channel model proposed in [68] combines the two-ring model and the elliptical model, where a combination of single- and double-bounce scattering under LOS propagation conditions is assumed. Geometry-based narrowband MIMO channel models are usually characterized by their spatial and temporal correlation properties. Moreover, all the aforementioned geometry-based MIMO C2C channel models are 2D channel models, i.e., transmitted signals travel only in the horizontal plane.

In Paper I, a new geometry-based model for narrowband SISO C2C channel is proposed. For our analysis, we have considered that scatterers are uniformly distributed within rectangles in the form of stripes parallel to both sides of the street as shown in Fig. 2.1. This model is called the rectangle model. The novelty of the proposed rectangle model arises from the non-isotropic scattering, which in turn results in a non-uniformly distribution of the AODs and the AOAs. The proposed model assumed single-bounce scattering under both LOS and NLOS propagation conditions. The advanced rectangle model is an extension of the channel model in [69], which is derived for indoor radio propagation environments. In [69], it has been assumed that the scatterers are uniformly distributed within the 2D horizontal plane of a room. In contrast to [69], we proposed the rectangle model for outdoor propagation environments, which is of interest for C2C communications in urban, rural, and highway environments. Moreover, the proposed rectangle model also includes the geometrical street scattering model presented in [65] as a special case if the width of the scattering area, i.e., width of the rectangle, is very small. Starting from the geometrical rectangle model, we derived a reference model by assuming an infinite number of scatterers. Analytical expressions are presented for the probability density functions (PDFs) of the AOD and the AOA as well as the Doppler

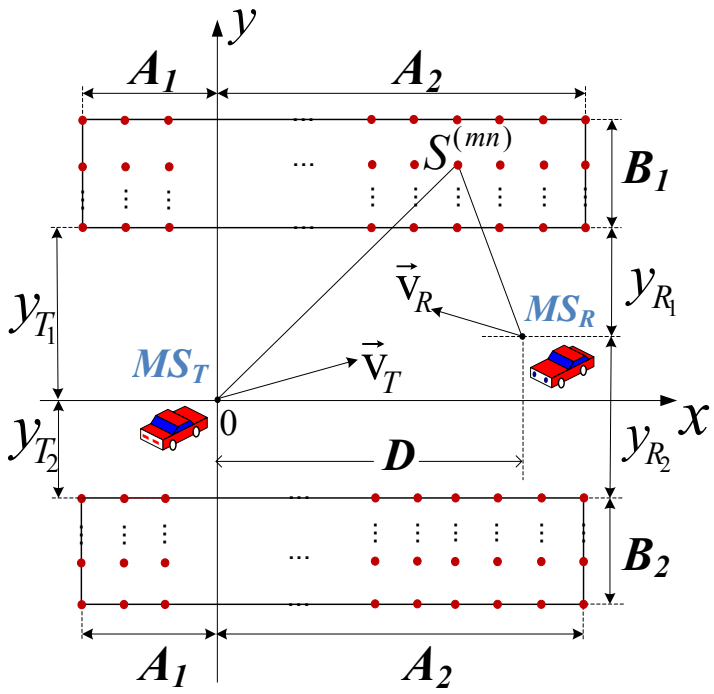

Figure 2.1: Geometrical street scattering (rectangle) model with local scatterers uniformly distributed in two rectangular areas on both sides of the street.

frequency. Furthermore, we investigated the effect of the street parameters, such as the width and the length of the rectangle, on the Doppler PSD. It was interesting to observe that the shape of the Doppler PSD resembles a Gaussian function if the width of the scattering area is very large. Finally, the proposed channel model is validated by demonstrating an excellent fit of its Doppler statistics to those of a real-world measured channel for urban and rural areas.

As alluded to earlier in the previous chapter, the roadways are considered as an important propagation environment for C2C communications. In practice, there exist many different types of roads, such as intersections, cross-junctions, T-junctions, roundabouts, and U-turns, which have different scattering environments due to their geometry. The investigation of C2C propagation channel in curved road environments is of great importance for C2C communications, especially in mountain areas, where high terrains usually block the LOS path. In this context, in Paper III (Appendix C), we presented a new narrowband MIMO C2C channel model based on the geometrical curved street scattering environment. The propagation scenario investigated in Paper III is shown in Fig. 2.2. In Paper III, we derive a reference narrowband channel model by assuming a combination of single- and double-bounce scattering under LOS and NLOS propagation conditions. It is noteworthy that the

developed reference model is an analytical model, which is based on the assumption that the number of local scatterers distributed on curves is infinite. However, using an infinite number of scatterers for the reference model makes it ideal and non-realizable. Thus, we obtain a simulation model by using the principle of deterministic channel modeling [70, Sec. 8.1], where a finite number of scatterers are considered. In the literature, several models are available that can be used for the simulation of mobile radio channels. The sum-of-cisoids (SOC) model [71, 72] is an appropriate simulation model for mobile radio channels under non-isotropic conditions. In [72], several parametrization techniques, such as the extended method of exact Doppler spread (EMEDS) [60], the L_p-norm method (LPNM) [70, Sec5.4.3], and the generalized method of equal areas (GMEA) [73], have been discussed and analyzed. In Paper III, we use the LPNM, which is a high-performance parameter computation method for the design of SOC channel simulator.

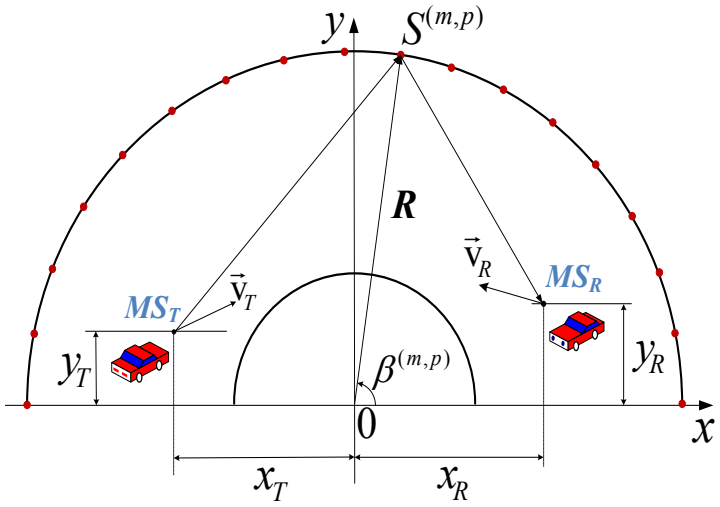

Figure 2.2: Geometrical curved street scattering (curve) model with local scatterers uniformly distributed in the outer and inner curves of the street

The significance of the works presented in Paper I and Paper III comes from the fact that the proposed channel models can be employed in analyzing the spatial and temporal behavior of C2C channels in non-isotropic propagation conditions. Thus, in Paper III, we have derived analytical expressions for the 3D ST-CCF, the temporal ACF, and the 2D space CCF. It was shown that the proposed curved model includes the well-known geometrical one-ring model [32] as a special case, which demonstrates the usefulness of the model.

2.3 Wideband 2D Geometry-Based C2C Channel Models

According to the DSRC [20] standard, 75 MHz of licensed spectrum has been allocated including seven channels, where each of them has 10 MHz bandwidth. Such C2C channels can be considered as frequency-selective, i.e., wideband channels [52]. Thus, narrowband C2C channel measurements are not sufficient for developing C2C communication services based on the DSRC standard. Wideband measured C2C channels are therefore important to understand the frequency-selectivity behavior of C2C channels and develop high-performance C2C communication systems. Therefore, most C2C measurement campaigns are based on wideband channel characterization (see Table 2.1 in Section 2.1.1). In wideband stochastic channel models, the signal bandwidth significantly exceeds the coherence bandwidth of the channel. Owing to the upsurge demand of high date-rate wideband communication systems employing MIMO technologies, such as MIMO OFDM systems, it is of fundamental importance to have accurate, proper, and realistic wideband MIMO M2M channel models. Thus, in the literature [56, 74–76], several wideband geometry-based MIMO M2M channel models have been proposed.

Paper II in Appendix B of this dissertation deals with the wideband 2D geometry-based MIMO C2C channel model, which is an extension of the rectangle model in Paper I (Appendix A) with respect to the frequency-selectivity and multiple antennas. In the proposed wideband MIMO C2C channel model, we derive the reference model by assuming an infinite number of scatterers under both LOS and NLOS propagation conditions. In the literature, there mostly two kinds of scattering, i.e., single-bounce and double-bounce scattering, are assumed during derivation of the reference channel model. From geometry point of view, in the single-bounce scattering, the channel statistics such as the AOD and the AOA are dependent, which is in contrast to the double-bounce models having independent AOD and AOA. Due to this distinction, the statistical properties of the single-bounce models and the double-bounce models are different. We derive a TVTF by taking into account a single-bounce scattering, which in turn results in that the AOD and the AOA are dependent. In the proposed model, the position of scatterers $S^{(mn)}$ [see Fig. 2.1] is determined by the Cartesian coordinates (x_m, y_n). By using the locations of the scatterers, we derive the relationship between the AOD and the AOA in terms of the coordinates (x_m, y_n) of the local scatterers $S^{(mn)}$. Analytical expressions are derived for the STF-CCF, the 2D space CCF, the 2D TF-CCF, the temporal ACF, and the FCF. It is noteworthy that the study of these correlation properties is important

for the development and analysis of C2C communication systems. As discussed in Section 2.2, in this wideband model, we also used the LPNM method to derive the simulation model. To verify the usefulness of the proposed 2D geometry-based stochastic wideband MIMO C2C channel model, its statistical characteristics need to be compared to empirical data obtained from real-world measured channels. Hence, by using the measured channel reported in [77], we computed the measurement-based parameters of the geometrical street scattering model. Finally, it was shown that the resulting mean Doppler shift and the Doppler spread of the reference model can be perfectly matched to the mean Doppler shift and the Doppler spread of the measured channel reported in [77]. It is noteworthy that the computed mean Doppler shift $B_{kl}^{(1)} = -110$ Hz and the Doppler spread $B_{kl}^{(2)} = 941$ Hz do not closely agree with measured channel ($B_{kl}^{*(1)} = -176$ Hz and $B_{kl}^{*(2)} = 978$ Hz) in case of the highway NLOS scenario. It was observed that for this scenario, a close agreement in the analytical result and the measured channel can be found for sufficiently small values of the Rice factor.

2.4 Chapter Summary and Conclusion

Increasing number of cars on traffic roads has triggered an enormous hike in the demand for C2C applications and has spurred research in channel modeling for C2C communication systems. Thus, a comprehensive as well as generic description of real-world propagation environments are required for future C2C communication systems. To achieve this goal, many geometry-based stochastic models have been published in the literature for the characterization of C2C fading channels. For this reason, the current chapter was dedicated to several 2D geometry-based C2C channel models, which are proposed and investigated in various C2C communication scenarios under different propagation conditions, such as LOS and NLOS propagation conditions. This chapter talked about both narrowband 2D geometry-based MIMO C2C channels and wideband 2D geometry-based MIMO C2C channels. Furthermore, the statistical characterization of 2D geometry-based MIMO C2C channel was addressed.

The chapter started by stressing the importance of the channel modeling in C2C communications. Thereafter, fundamental channel modeling approaches and their advantages and disadvantages were discussed. Moreover, C2C channel measurement campaigns are reviewed and listed. Therein, characteristics of the C2C channels, such as the CIR, the TVTF, and the Doppler spread were highlighted. Then, the chapter proceeded by addressing several narrowband geometry-based MIMO C2C

channel models, which are derived from different geometrical structures. The C2C channel statistics such as the Doppler PSD were discussed. The simulation model's parametrization techniques are addressed. The importance of the work provided in Papers I and III (Appendices A and C) is highlighted.

The chapter then gave the reasons behind the use of wideband C2C channel models than narrowband C2C channel models. Propelled by those reasons, in this chapter we introduced wideband geometry-based MIMO C2C channel models. Finally, the chapter ended by summing up the main findings of Paper II (Appendix B), which deal with the wideband geometry-based MIMO C2C channel model. The correlation properties of the proposed wideband MIMO C2C channels were addressed. Finally, a measurement-based validation of the usefulness of the proposed model was discussed.

Chapter 3

Statistical Modeling and Analysis of 3D Geometry-Based C2C Channel Models

3.1 Introduction

In Chapter 2, the modeling of 2D narrowband and wideband geometry-based channel models were proposed for different C2C communications scenarios. The previously reported 2D channel models for both SISO M2M channels [49, 50, 78] and MIMO M2M channels [60–62, 65, 66, 79] assume that waves travelling from the transmitter antenna to the receiver antenna propagate only in the azimuth plane, i.e., in the horizontal plane. However, this assumption is not valid for certain radio propagation environments, such as urban areas or tunnel environments because of the low-elevation antennas of the mobile transmitter and the mobile receiver. Hence, all above mentioned channel models suffer from the fundamental limitation of being 2D models. In contrast, Chapter 3 accentuates the modeling and analysis of 3D geometry-based channel models designed for C2C communication systems.

In a wireless propagation environment, the received signal is a sum of many statistically independent components, which propagate in the 3D plane through different multiple paths. Consequently, studying and analyzing more realistic 3D geometrical channel models are of fundamental importance. Thus, to improve performance of wireless communications, the channel's degrees of freedom in the vertical plane, i.e., in the elevation plane should be used. Hence, considering the elevation directions in channel modeling results in designing 3D geometry-based channel models. Moreover, 3D geometry-based channel models can easily be reduced to 2D channel models, under special conditions, for example, if the received multipath signals are

observed with fixed elevation angles [80].

Ossanna [81] was the first to propose a channel model that takes into account vertically polarized horizontally traveling waves [82]. The model proposed by Ossanna is primarily suited for suburban areas, where he assumed that both direct and reflected signals exist. In 1965, Gilbert [83] introduced three different models, which were based on multipath scattering. In [83], it was observed that for a large number N of travelling plane waves all three models are equivalent. In the second model proposed by Gilbert [83], N waves have equal and fixed amplitudes. By using this fact, Clarke proposed his well-known omnidirectional scattering mode in [84].

However, all aforementioned models have the common feature that the field incidents on the transmitter and the receiver antennas are composed of a number of waves and these waves are assumed to travel horizontally. Nevertheless, Aulin [82] questioned this basic assumption, in which the transmission between the transmitter and the receiver on an urban street would not be possible. Hence, he proposed a 3D model, which is a generalization of the Clarke model in a way that vertically polarized waves do not necessarily travel in the horizontal plane. In [82], it was found that the shape of the signal spectrum was significantly affected even for small deviations from the horizontal plane. Moreover, a PDF for the elevation angle was derived, which was easy to handle and produced the closed-form solutions. However, the proposed PDF of the elevation angle was not realistic from a physical point of view and the signal properties were determined in the horizontal plane. To fill this gap, a new 3D model was introduced in [85] for fixed-to-mobile communications, where the major characteristics of mobile radio signals, such as the autocovariance, the cross-correlation function, and the power spectral density were determined.

The remainder of this chapter is organized as follows. Section 3.2 briefly addresses the 3D geometry-based channel models. The statistical analysis of 3D geometry-based C2C channel models is described in Section 3.3. In Section 3.4, a summary of interesting results of the statistics of 3D geometrical semicircular-tunnel-based channel model is presented. Finally, the chapter summary is provided in Section 3.5.

3.2 3D Geometry-Based Channel Models

The demand for improved system performance and higher spectrum efficiency in wireless communication systems has directed recent research activities toward the development of new propagation channel models that can describe most physical phenomena related to radio propagation. A major characteristic of mobile radio

channels is the multipath propagation, which is caused by diffraction and scattering from terrain features and buildings. In this regard, the channel model should not only describe the azimuth and elevation angles as well as time-of-arrival statistics but should also consider different urban propagation environments parameters, such as building heights, their densities, and real street propagation conditions.

In [86], the first channel model was proposed based on the vertical plane launching (VPL) simulation for urban environments. However, in this model [86], the effect of the terrain features and antenna array positions with respect to the surrounding obstacles was not taken into account. Consequently, a measurement-based 3D channel model has been introduced in [87], where different propagation mechanisms have been analyzed. Obviously, an accurate prediction analysis requires performing several measurement campaigns with different calibration techniques and for different types of propagation environments. In this context, a large number of measurement campaigns were carried out in different urban street environments [86]. Consequently, a number of 3D geometry-based channel models, such as the 3D sphere model, the 3D hemisphere model [34], the 3D concentric-cylinder model [88], and the 3D tunnel model [89] have been proposed in the literature. In the following subsections, we will briefly review some of them.

3.2.1 3D Sphere Models

For a macrocellular propagation environment, a mobile station (MS) equipped with an elevated antenna, which is usually surrounded by buildings, rooftops, and other obstacles, communicates with a highly elevated base station (BS) antenna. In this situation, the major scatterers are considered to be distributed around the MS including trees, ground, rooftops, and buildings. This assumption leads to the design of 3D geometrical sphere models to investigate the spatial-temporal characteristics of the underlying propagation channel. In the literature, there exist several studies dealing with the 3D geometrical sphere model, where the scatterers are distributed inside a sphere or hemisphere, uniformly [34, 90] and Gaussian-like [91]. In [34], a 3D hemisphere model has been proposed, where the angle-of-arrival statistics of the received signals is derived. Shortly after the proposed model in [34] was published, the temporal and spatial characteristics of the received signal of 3D hemisphere model were studied in [92]. However, all these models are proposed for fixed-to-mobile communication systems. The authors of [93] have proposed a novel 3D two-sphere model for non-isotropic MIMO M2M channels, where only double-bounced scattering is assumed. Other 3D two-sphere models can be found in [80] and [94], where 2×2 dual-polarized and 4×4 spatial-polarized MIMO M2M channels are

proposed, respectively. A class of 3D sphere models is illustrated in Fig. 3.1, which includes the hemisphere model Fig. 3.1 (a), the sphere model Fig. 3.1 (b), and the two-sphere model Fig. 3.1 (c).

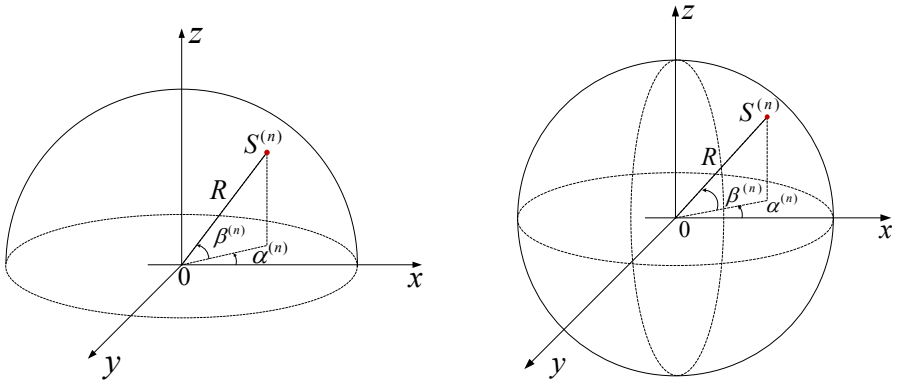

a) hemisphere model b) sphere model

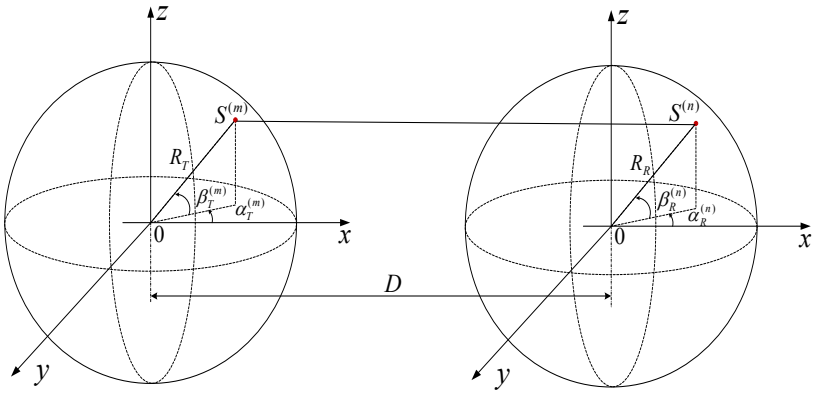

c) two-sphere model

Figure 3.1: A class of 3D sphere models.

In the 3D sphere models, it is considered that the BS and MS play the role of the transmitter and receiver, respectively, where the MS is moving horizontally, i.e., in the xy-plane. The plane waves travel via scatterer $S^{(m)}$ ($S^{(n)}$) in both vertical and horizontal directions with the corresponding elevation $\beta^{(n)}$ and azimuth $\alpha^{(n)}$ angles, respectively, inside the spheres with radius R_i ($i = T, R$). For M2M communication scenario, it is assumed that the mobile transmitter ($i = T$) and the mobile receiver ($i = R$) are placed at a certain distance D from each other.

3.2.2 3D Cylinder Models

Nowadays, high buildings, tall and wide road bridges are being deployed in modern motorways and urban streets, which make the urban street environment challenging for radio propagation. In such a wireless scattering environment, the received signal is composed of many statistically independent components, which travel in the 3D space on different paths. This type of propagation environment can be addressed as bad urban propagation environment [33]. Therefore, the 3D geometrical cylinder model has become an attractive model, because it describes the propagation environment of densely developed areas with high rise buildings. Parson [85] proposed one of the first 3D cylinder models, where a measurement-based distribution function is used for the elevation angle $\beta^{(n)}$. Consequently, for both narrowband and wideband MIMO communication systems, reference channel models are proposed based on the 3D two-cylinder model in [88] and [56], respectively. In [95] and [96], 3D three-cylinder models were proposed for narrowband and wideband MIMO M2M fading channels in relay-based amplify-and-forward (AF) cooperative networks, respectively. Fig 3.2 shows an example of a 3D two-cylinder model for M2M communication systems.

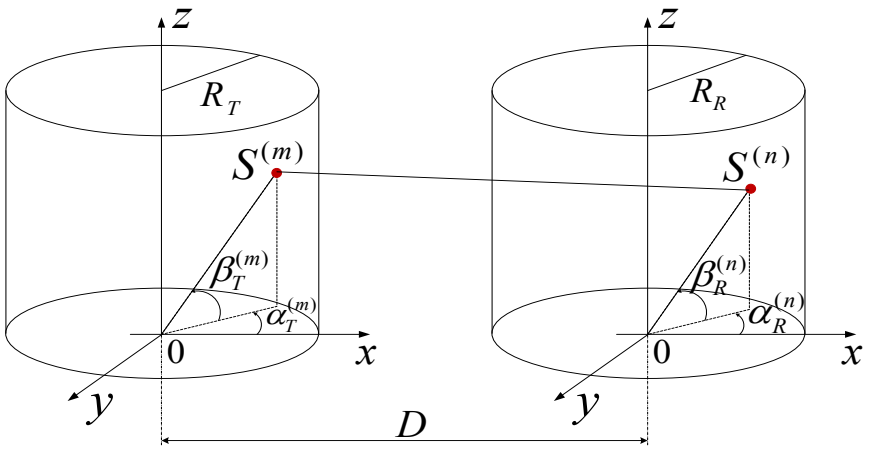

Figure 3.2: 3D two-cylinder model for M2M communication systems.

3.3 Statistical Characterization of 3D C2C Channels

In recent years, several studies have been published focusing on 3D channel modeling for M2M communications, which can also be considered for C2C and C2I communications. As discussed in Section 3.1, the existing 2D geometry-based channel models do not describe accurately the propagation conditions for C2C communica-

tion systems in urban street environments. Thus, Section 3.2 introduces some 3D geometry-based channel models developed for C2C communications. In this section, we address narrowband 3D geometry-based C2C channel models and wideband 3D geometry-based C2C channel models.

3.3.1 Narrowband 3D Geometry-Based C2C Channel Models

Narrowband 3D geometry-based channel models designed for C2C communications can be found in [88, 93, 97, 98]. In [88], the authors have developed a 3D two concentric-cylinder geometry-based stochastic model for narrowband non-isotropic scattering MIMO M2M channels. There, the spatial-temporal characteristics of the received signal have been investigated in terms of the space-time (ST) correlation function (CF). Using the sum-of-sinusoids (SOS) method, two SOS 3D channel simulators are proposed for MIMO M2M channels. Other 3D two-sphere geometry-based MIMO C2C channel models are proposed in [93, 97]. The 3D two-sphere model in [93] allows us to jointly study the impact of the elevation angle and the azimuth angle on the channel statistics. It has been shown that the proposed 3D two-sphere channel model results in lower ST-CF than the corresponding 2D model and it more accurately reflects a real propagation environment. A generalized 3D model based on a two-concentric quasi-sphere model is presented in [97], where a generalized expression is derived for the temporal ACF. A novel 3D MIMO C2C regular-shaped geometry-based stochastic model has been proposed in [98] by using a combination of a 3D two-sphere model and an elliptical-cylinder model. In the proposed model comprehensive statistical properties, such as the amplitude and phase PDFs, ST-CF, Doppler PSD, envelope level crossing rate (LCR), and the average duration of fades (ADF) are derived and investigated. The impacts of the elevation angle and the vehicular traffic density on the above mentioned the statistical properties of the channel are studied and discussed by comparing them with those of the corresponding 2D model. It has been shown that the proposed 3D model more accurately characterizes the real C2C channels.

3.3.2 Wideband 3D Geometry-Based C2C Channel Models

Wideband 3D geometry-based MIMO C2C channels have been reported in [76] and [26], in which a 3D two-concentric-cylinder model and a two-sphere model are considered, respectively. The modeling of 3D geometry-based dual-polarized and spatial-polarized MIMO M2M channel models is proposed in [80] and [94], respectively, where a joint TF-CCF has been derived to investigate the system

performance over different WSSUS channel realizations. A wideband 3D three-concentric-cylinder MIMO M2M channel model has been proposed in [96] for relay-based communications, where the WSSUS condition is assumed and straight vertical scattering surfaces are emulated.

3.4 The 3D Geometrical Semicircular-Tunnel-Based Channel Model

The radio propagation channel is the principal contributor to transmission quality degradation effects of wireless communication systems. In confined environments, such as underground tunnels, mines, and tunnel roads, wireless communications experience severe fading problems [99]. In reality, roads are often passing through tunnels, which can have various geometrical shapes [100], such as circular, semicircular, oval, rectangular, and horseshoe shapes. Owing to the scattering and reflection of incident waves on the tunnel walls, multipath propagation effects are complicated. Therefore, modeling and understanding the radio propagation in tunnel environments is of importance for C2C communication systems. In this regard, the characteristics of mobile radio channels inside a tunnel environment have been widely investigated, where a geometrical optical model [101], a wave-guide model [102], and a full wave model [36] are used. Moreover, there have been carried out many studies focusing on the wireless communications in tunnel environments and some measurement are performed, where path-loss [102, 103], delay [104], and Doppler spreads [105] are investigated. The authors of [104] measured a propagation channel inside an arched tunnel and analyzed the characteristics of the channel in terms of the delay spread. Numerical results demonstrated that more than 90 % of the extracted paths consist of single-bounce scattering and direct path, i.e., LOS component.

A theoretical analysis of radio propagation in tunnels with vehicular traffic flow has been provided in [99]. It was shown that the multipath signal propagation in tunnel environments is influenced by the number, size, and position of the mobile stations, i.e., cars, the size of the tunnel and the vehicular traffic flow. The impact of vehicular traffic density in C2C communications has also been investigated in [98], where a 3D geometry-based channel model is proposed for narrowband MIMO C2C channels. In 3D channel models, incoming multipath signals take place within both azimuth and elevation angles. Thus, the distribution of scatterers is an important part affecting the azimuth and elevation angles of departure and arrival statistics. In this regard, the knowledge of the distribution of the elevation

and azimuth angles of the transmitted plane waves is important because it allows us to investigate the spatial-temporal characteristics of the underlying fading channel. However, all aforementioned 3D channel models proposed for tunnel environments do not consider the impact of the distribution of the scatterers on the propagation channel statistics. To bridge this gap, we propose a new 3D SCT channel model for a wideband MIMO C2C channel under LOS and NLOS propagation conditions.

Paper IV presents a wideband MIMO C2C channel model based on a geometrical SCT scattering model with the purpose of characterizing fading behavior inside tunnel environments. In the designed SCT channel model, it is considered that both the MS_T and MS_R are in motion and equipped with multiple antenna elements. The geometrical SCT scattering model was originally presented in [89] for a SISO scenario. A typical propagation scenario inside an SCT is illustrated in Fig. 3.3, where scatterers are randomly distributed on the tunnel wall. Here, both the MS_T and MS_R

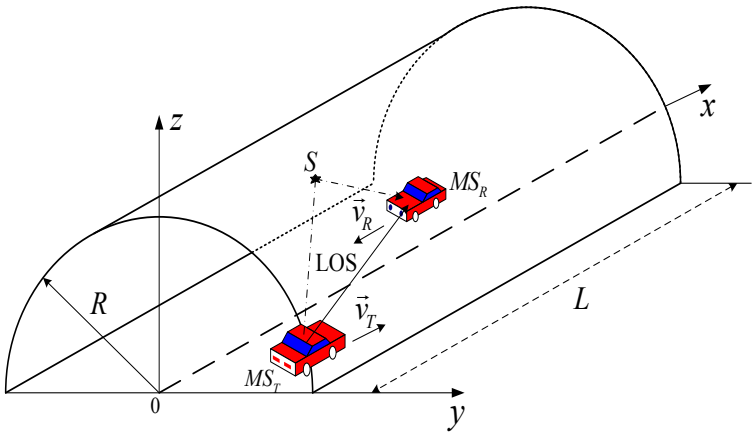

Figure 3.3: A typical propagation scenario in an SCT.

communicate with each other under LOS and NLOS propagation conditions. Moreover, the proposed SCT channel model considers single-bounce scattering, which implies that homogeneous plane waves emitted from the MS_T are first captured by scatterer S on the tunnel wall before reaching the MS_R (see Fig. 3.3). Furthermore, to simplify the mathematical analysis, we have assumed that the WSSUS assumption is valid over a short observation time interval. This assumption is supported by the study in [105], where the authors investigated the time interval over which the fading process in a tunnel environment can be considered as wide-sense stationary.

Starting from the geometrical SCT channel model, we derive the reference model in terms of the TVTF, which is a sum of the diffuse, LOS, and specular components. With respect to the position of the mobile transmitter and the mobile receiver antennas, the azimuth and elevation angles of departure and arrival are de-

rived. The analytical expression is derived for the STF-CCF of the reference model, in which the 2D time-frequency CCF, the 2D space CCF, the temporal ACF, and the FCF are included as special cases. Furthermore, we derive an efficient SOC channel simulator from the TVTF characterizing the reference model. It is shown that both the temporal ACF and the FCF of the SOC channel simulator match very well with those of the reference model. Finally, we evaluate and present the delay statistics and the Doppler statistics of the proposed SCT channel model for both LOS and NLOS propagation conditions. The usefulness of the proposed SCT channel model is validated by demonstrating an excellent match of the delay spread of the reference model to that of the measured channel reported in [104]. Numerical results also show the impact of the transmitter (receiver) antenna element spacing δ_T (δ_R) on the delay statistics, where for small values of δ_T and δ_R the delay spreads are the same for all transmission links. This means that the delay spread can be considered as independent of antenna element indices. Our work includes a discussion on the influence of the antenna element indices on the FCF of the reference model. Presented results show that the FCF has the same fluctuation curves for the transmission links $A_T^{(1)} - A_R^{(2)}$ and $A_T^{(2)} - A_R^{(1)}$, which illustrates the symmetrical positions of the mobile transmitter and the mobile receiver (see Fig. D.3 in Appendix D). Moreover, presented results demonstrate a good agreement between the FCF of the reference model and the simulation model. Furthermore, it was concluded that the proposed 3D SCT channel model could also be considered as a frequency-non-selective channel model for DSRC systems [19, 20], where the system bandwidth is 10 MHz.

The fundamental procedure presented in Paper IV for the purpose of deriving the novel 3D SCT channel model and confirming the validity of the proposed channel model is general and can be applied to other tunnel environments with different shapes. The derived SOC channel simulator can be used to study and optimize future wideband channels in tunnel environments.

3.5 Chapter Summary and Conclusion

Efficient and accurate channel models are required for evaluating, analyzing and designing future advanced C2C communication systems, which allows us to predict the spatial and temporal characteristics of the received multipath signals. In a wireless scattering environment, the received signal is composed of many statistically independent components, such as the diffuse component, specular component and the LOS component, which travel in the 3D space via different paths. In this regard, modeling and developing of 3D geometry-based channel models for C2C commu-

nications are of crucial importance. Thus, in this chapter, we propose a new 3D geometrical SCT channel model for C2C communications in tunnel environments.

The chapter began by highlighting the importance and advantages of designing 3D geometry-based channel models. The literature study revealed that 2D geometry-based channel models could not appropriately characterize the statistics of the fading channel in urban street environments. To fill this gap in research, 3D geometry-based channel models have been proposed and developed for different propagation conditions, taken into account, single- and double-bounced scattering as well as direct paths, such as the LOS component and ground specular component. Consequently, different types of 3D geometry-based channel models, such as the 3D sphere models, and the 3D cylinder models were briefly reviewed and discussed. Afterwards, we discussed and reviewed 3D geometry-based channel models derived for narrowband and wideband MIMO C2C communications. However, those 3D channel models do not investigate radio propagation in tunnel environments, which is important for countries with mountainous areas, where many traffic roads are passing through tunnels. Thus, the modeling of propagation channels in tunnel environments is of importance for C2C communications. Motivated by this fact, we proposed a 3D SCT channel model for wideband MIMO C2C channels.

The chapter then summarized the work presented in Paper IV (Appendix D), which deals with the development of a wideband 3D SCT channel model for MIMO C2C communication systems. The analytical expression for the STF-CCF has been derived, from which the spacial, temporal, and frequency correlation properties of the underlying channel are investigated. Interesting findings and the usefulness of the proposed model are highlighted.

Chapter 4

Performance Analysis of C2C Communication Systems

4.1 Introduction

Over the last few decades, there has been a growing interest in studying and developing C2C communication systems, which play a key role in ITS [8]. C2C communication systems aim to minimize traffic accidents and improve the traffic flow [4]. The design, development, performance analysis and test of C2C communication systems highly depend on a detailed understanding of the underlying propagation channel and the corresponding realistic easy-to-use channel model. In order to investigate and support C2C communications, the IEEE 802.11p [21] standard has been developed, which is directly derived from IEEE 802.11a with some modifications to adapt to vehicular environments. The IEEE 802.11p standard makes use of the OFDM physical layer and the quality of services (QoS) extension on the medium access control (MAC) layer. Nevertheless, the basic characteristics of the physical channel of C2C communications is still an open question for the research community and the industry. C2C communications are characterized by a higher mobility compared to the traditional F2M and mobile-to-fixed (M2F) communications. Specifically, in C2C communications, both the transmitter and the receiver are in motion and both may be surrounded by multiple scattering objects, which are also moving. Thus, the rate of fading can be twice as fast as in traditional cellular channels. Moreover, in C2C communication systems, both the mobile transmitter and the mobile receiver are equipped with multiple antenna arrays, where the range of the antenna height is between 1 and 6 m [106, 107]. Owing to the low-elevation antennas, the LOS paths are usually blocked in C2C communications, which may have a high risk potential for road traffic accidents with serious injuries and even

fatalities. These, antenna height differences have a major impact on the system performance. Therefore, it is of crucial importance to have accurate C2C channel models which can reflect the fading statistics of real-world channels [52, 106].

A number of authors have investigated the performance of C2C communication systems in different types of propagation environments. In [107], a geometrical blind bend model is proposed to derive a narrowband SISO C2I channel model. The blind bend model takes into account single- and double-bounce scattering. There, the performance of various digital modulations over C2I channels is evaluated by using the PDF of the fading amplitude. A geometrical curved street scattering model [66] can be considered as a blind bend environment. Paper III (Appendix C) presents a narrowband MIMO C2C channel model developed for a curved street environment where single- and double-bounce scattering are considered under LOS and NLOS propagation conditions. An extension of this narrowband MIMO C2C channel model towards frequency selectivity is introduced in Paper V (Appendix E).

The impact of fast-varying channels on C2C communication systems was studied in [37]. It was demonstrated that the channel estimation process is the most affected part due to the rapid changes of the amplitude of the channel. The performance of hybrid automatic repeat request (HARQ) with code combining (CC) and with incremental redundancy (IR) over double Rayleigh fading channels is studied in [108] and [38], respectively. In [108], analytical solutions for the characteristic quantities of double Rayleigh fading channels are derived. In both cases [38, 108], it is shown that HARQ with CC and IR enables the data rate to be close to the ergodic capacity, where the channel state information (CSI) is unavailable at the transmitter side. In [39], the frame success ratio and goodputs of C2I channels in a tunnel environment were discussed and analyzed. There, it was shown that using higher-order modulation schemes with a constant packet length results in better goodput. A summary of analyses and investigations on the system performance of C2C communications over different channel models is listed in Table 4.1.

Modeling and simulation of 2D and 3D C2C channel models were the topic of Chapter 2 and 3, respectively. Chapter 4 is devoted to assess the performance of C2C communication systems in different propagation environments. Special emphasis is placed on geometrical scattering models, such as the rectangle model [79], the curve model [66], the street line model [65], and the tunnel model [89]. In our analysis, we assume single-bounce scattering [56] in an NLOS propagation environment. In Paper II (Appendix B), we proposed a wideband MIMO C2C channel model, which is derived from the geometrical street scattering model under the assumption of single-bounce scattering in LOS and NLOS propagation environments.

In this channel model [79], the effective scatterers are located within rectangle areas on both sides of the street. For the performance evaluation of such a C2C channel model, we consider only single-bounce scattering under NLOS propagation conditions. The impact of the geometrical model parameters on the system performance is investigated in Paper V.

To the best of our knowledge, a theoretical analysis of the performance of C2C communication systems over different C2C channels under various geometrical scattering conditions has not yet been performed. In order to fill this gap in the research, we presented in this chapter our investigations on the performance of Alamouti coded OFDM systems over wideband MIMO C2C channels correlated in time and space.

The remainder of this chapter is structured as follows. Section 4.2 deals with the performance analysis of C2C communication systems. Section 4.3 summarizes the conclusions that can be drawn after exploring the performance of Alamouti coded OFDM systems over wideband C2C channels. Finally, the chapter summary is given in Section 4.4.

Table 4.1: Summary of the performance analysis of C2C communication systems.

Car-to-X Communications	Amplitude Fading	Model	Antenna Configurations	Computed Statistics
Car-to-car	Weibull [25, 26, 40]	Tapped delay line (TDL) [25, 26]	SISO [25, 26], MIMO [25]	Packet error rate (PER) [37]
			MIMO [40]	Bit error rate (BER) [40]
	Nakagami [25] [109]	TDL [25]	SISO [25]	RMS delay, PDP [25]
			MIMO [109]	BER [109]
	Rayleigh [29]	TDL [29]		PER [29, 110]
		IEEE 802.11p [21]	MIMO [111]	Average PER [111]
	Double Rayleigh [38, 108]			Outage probability, Bit error probability (BEP) [38, 108]
	Rician [112]	Two-ring, elliptical [112]	MIMO [112]	Doppler PSD, BEP [112]
		Ray tracing [113]	MIMO [113]	Average BER [113]
Car-to-infrastructure	Rayleigh [65, 66, 107, 114]		MIMO [114]	BEP [114]
		Blind bend [107]	SISO [107]	BEP [107]
		Curve [66]	MIMO [115]	BEP [115]
		Rectangle [115]	MIMO [115]	BEP [115]
		Street line [65]	MIMO [65]	BEP [115]
		Tunnel [89]	MIMO [89]	BEP [115]

4.2 STBC-OFDM Systems: Description and Prior Work

Over the last few decades, an increasing demand for high data rate wireless communication services and applications has placed high demands on reliable and robust communication link. In modern wireless communication systems, performance degradation always occurs due to severe fading of the signal envelopes caused by multipath propagation environments. In this regard, wireless communication systems with both high data rate and high quality transmission have been widely investigated [116]. In order to improve the transmission quality over fast and frequency-selective fading channels, the transmit diversity technique is a promising method to reduce fading effects in mobile wireless communication [117]. The space-time coding (STC) scheme was first defined by Tarokh *et al.* [118, 119] to describe a new 2D way of encoding and decoding transmitted signals over wireless fading channels using multiple transmit antenna arrays. In the literature, there exist two main types of STC, namely space-time block codes (STBCs) and space-time trellis codes (STTCs) [118]. STBC is a well-known spectral efficient transmit diversity technique, which has a significant performance improvements and low complexity. On the other hand OFDM is robust against frequency-selective fading and provides a relatively simpler receiver implementation. A traditional OFDM system with a sufficiently long cyclic prefix transforms the frequency-selective fading channel into a number of frequency-flat fading channels. Hence, orthogonal transmit diversity techniques, such as STBC can be applied to OFDM systems. Thus, the combination of STBC and OFDM is regarded as a promising solution to combat frequency-selective fading, which is considered for the fourth-generation wideband communication systems. OFDM has become a widely used technique for broadband wireless communication systems and has been adopted in several modern wireless communication standards, such as IEEE 802.11 (WiFi), IEEE 802.16 (WiMax), and LTE [120, 121]. Moreover, in the literature [122, 123], a number of STBC-OFDM systems have been proposed and analyzed, e.g., the simple and popular Alamouti STBC [124]. The block diagram of an Alamouti coded MIMO-OFDM system is shown in Fig. 4.1 for a 2×1 antenna configuration. The serial data bits are first passed through a serial-to-parallel converter, and then the resulted data bit is modulated by using different modulation rules. In the following, two consecutive complex data symbols S_1 and S_2 are coded by the Alamouti scheme [124]. Thereafter, the inverse Fourier transform is computed and a cyclic prefix is added to each sequence to prevent intersymbol interference between successive OFDM symbols.

Finally, the OFDM data sequences are transmitted over the MIMO channel.

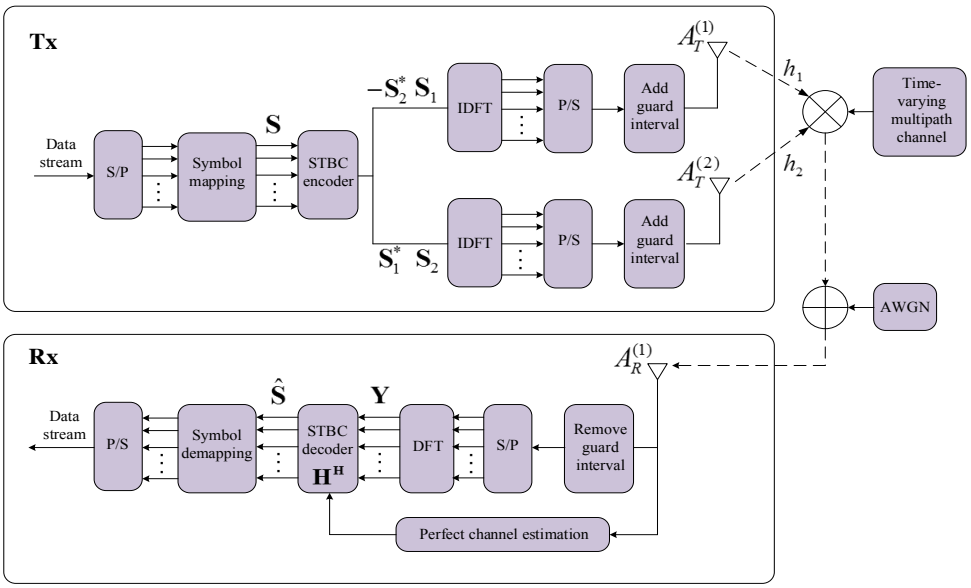

Figure 4.1: Block diagram of an STBC MIMO-OFDM system with 2×1 antennas. DFT: discrete Fourier transform; IDFT: Inverse DFT; P/S: parallel to serial; S/P: serial to parallel.

The symbols received at the time slots t_1 and t_2 can be presented as [125, p. 125]

$$y_1 = y(t_1) = g_{11}(x_1,t_1)s_1 + g_{12}(x_2,t_1)s_2 + n_1 \tag{4.1}$$

$$y_2 = y(t_2) = -g_{11}(x_1,t_2)s_2^* + g_{12}(x_2,t_2)s_1^* + n_2 \tag{4.2}$$

where $g_{1k}(x_k,t_i)$ denotes the complex channel gain in the time slot t_i $(i = 1,2)$ of the transmission link from the kth transmitting antenna $A_T^{(k)}$ located at x_k $(k = 1,2)$ to the single receive antenna $A_R^{(1)}$, where s_i stands for the OFDM symbol and n_i is the additive white Gaussian noise (AWGN) component. In the performance analysis of the Alamouti coded MIMO-OFDM system presented in Paper V (Appendix E), we have studied the effect of both the space and the time correlation functions of the underlying C2C channels on the system performance.

Recent studies have been performed on the application of STBC schemes to C2C communication systems [37, 111, 113]. The IEEE 802.11p standard is also based on OFDM. Table 4.2 lists the parameters of the IEEE 802.11p physical layer. In [112], the performance of C2C communication systems is investigated and analyzed, where a new regular-shaped geometry-based stochastic model for non-isotropic scattering wideband C2C Rician fading channels has been proposed. In order to combat intercarrier interference (ICI), a new precoding-based cancellation (PBC)

Table 4.2: Parameters of the IEEE 802.11p standard.

Parameter	**Value**
Data rates (Mb/s)	3, 4.5, 6, 9, 12, 18, 24, 27
Forward error correction (FEC) rates	1/2, 2/3, 3/4
Modulation	Binary phase-shift keying (BPSK), quaternary PSK (QPSK), Quadrature amplitude modulation (QAM)
Subcarriers	52
Bandwidth	10 MHz
Subcarrier spacing	156.25 kHz
OFDM symbol duration	8 μs
Cyclic prefix	1.6 μs
Fast Fourier transform (FFT) period	6.4 μs
Preamble	32 μs
Pilot subcarriers	± 21, ± 7

scheme has also been proposed in [112]. The impact of the Doppler shift on MIMO OFDM systems used in C2C communications is studied in [37, 109]. In [37], it was shown that the channel estimation process is most affected by rapid variations of the channel, where ICI has little impact on the system performance at small data rates. It was also shown that the use of multiple antennas improves the PER. To sum up, it can be said that MIMO-OFDM systems can be very useful for C2C communication systems due to their high spectral efficiency and their ability to mitigate multipath fading effects.

4.3 Performance Analysis of Alamouti Coded OFDM Systems over C2C Channels Correlated in Time and Space

Paper V studies the performance of Alamouti coded OFDM systems over wideband MIMO C2C channels correlated in time and space. The BEP is used to measure the error rate of the Alamouti coded OFDM system for different types of C2C channel models, such as the rectangle model [79], the tunnel model [89], the street line mode [65], and the curve model [66], which are illustrated in Fig. 4.2. The effects of the

maximum Doppler frequency and the spatial correlation on the system performance are discussed. Furthermore, the impact of the geometrical model parameters on the system performance is studied. The complete article that is summarized in this section can be found in Appendix E.

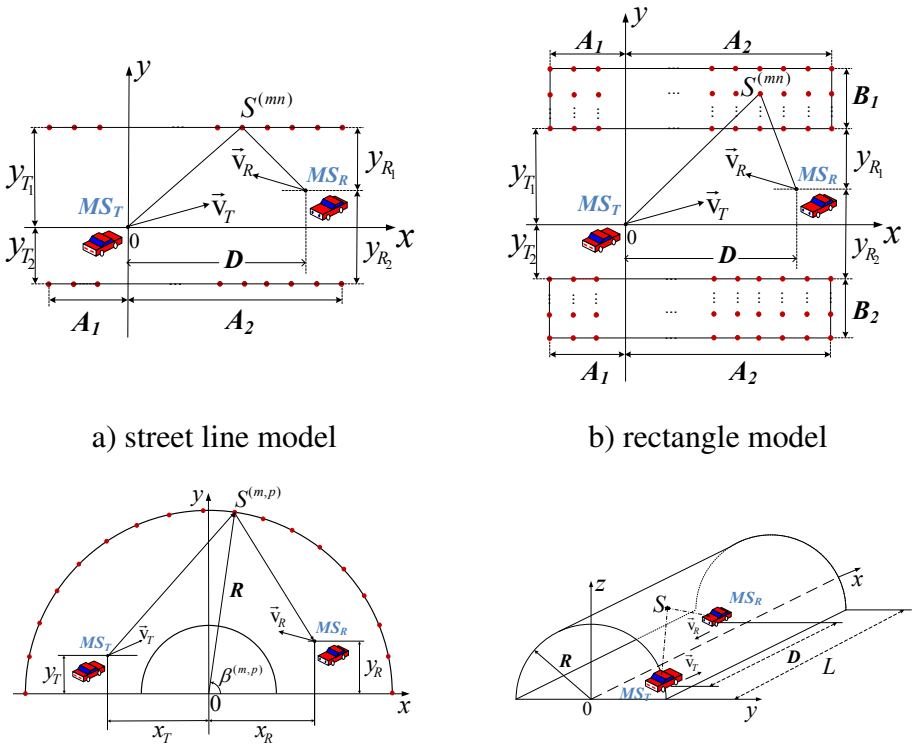

a) street line model b) rectangle model

c) curve model d) tunnel model

Figure 4.2: Typical geometrical C2C channel models for specific scenarios.

In Paper V, we presented a generalized expression of the TVTF by considering different geometrical scattering models. In C2C communications, there are mainly two classes of applications, namely safety and non-safety applications [4]. For safety applications, generally the symbol duration is long due to the short safety messages. In this case, the delay spread of the channel is such that the channel can be considered as a narrowband channel. On the contrary, the non-safety applications require high data rates, where the delay spread of the channel is in the order of the symbol duration. In this situation, the underlying channel is considered a frequency-selective channel. Therefore, to deploy high data rate non-safety applications in C2C communications, wideband MIMO C2C channels are required. In this regard, Paper V also aims at deriving a wideband MIMO C2C channel model based on the geometrical curved street scattering model, which is an extension of the narrowband MIMO C2C curve model in [66]. Moreover, MIMO communica-

tion systems can be of great interest for C2C communications, due to their higher throughput [59]. Consequently, in Paper V, we presented an extension of the SISO C2C tunnel model [89] to a MIMO C2C tunnel channel model. Taking into account all the aforementioned derivations, we presented the corresponding correlation functions of the generalized model, such as the 2D space CCF and the temporal ACF. In our analysis, it is assumed that the perfect CSI is known at the receiver side. Based on this assumption, the BEP of BPSK Alamouti coded OFDM systems over wideband MIMO C2C channels correlated in time and space is derived. Finally, a comparative study of the BEP of Alamouti coded OFDM systems is presented. In Section 4.1, it is mentioned that single-bounce scattering is assumed where the (m,n)th homogeneous plane wave emitted from the lth transmitter antenna element $A_T^{(l)}$ travels over the local scatterer $S^{(mn)}$ before impinging on the kth receiver antenna element $A_R^{(k)}$. Hence, by computing the absolute value of the TVTF $H_{k,l}(f',t)$, we can see that the envelope of the TVTFs follows the Rayleigh distribution [107] as shown in Fig. 4.3.

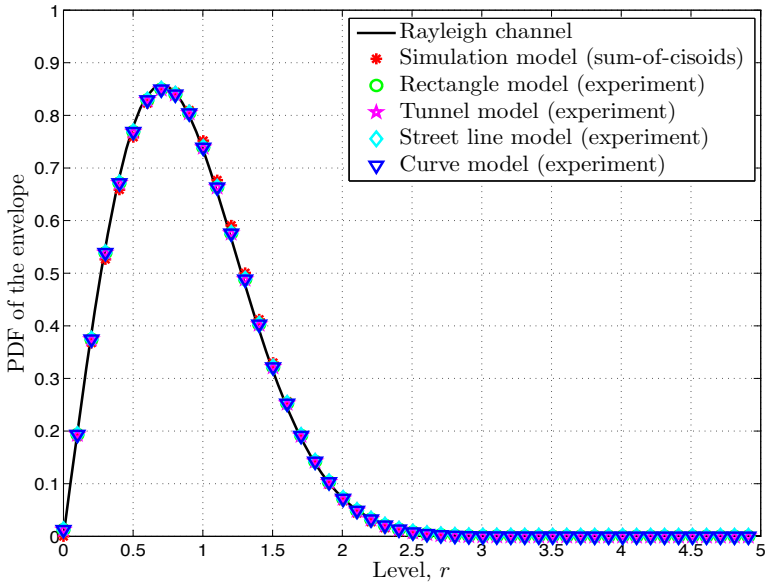

Figure 4.3: PDF of the envelope of various C2C channel models.

The BEP of Alamouti coded OFDM systems can be computed by integrating the conditional BEP over the PDF of an instantaneous output signal-to-noise ratio (SNR) [126, 127]. In our analysis, we used a binary phase-shift keying (BPSK) modulation scheme for the conditional BEP. In [114], an approximation for the instantaneous output SNR is presented. Based on this approximation an analytical expression for the PDF of the approximate instantaneous SNR is derived. Finally, the performance of Alamouti coded OFDM systems over different types of C2C

channels correlated in time and space is evaluated with the help of the BEP expression in [115, Eq. 21-22]. The influence of both the maximum Doppler frequency and the antenna element spacings on the system performance is investigated and discussed. Owing to the perfect CSI at the receiver side, the maximum Doppler frequency $f_{T_{\max}}$ ($f_{R_{\max}}$) does not affect the system performance, which is illustrated in the simulation results. It is noteworthy that all considered channel models behave in the same way. Moreover, the theoretical BEPs are validated by simulation, where an excellent fitting is demonstrated. On the contrary, the system performance can be improved even if the antenna element spacings δ_T increase. This fact shows that the spatial correlation between the TVTFs is smaller if the antenna element spacings are large. However, all considered channel models have the same BEP curves for a given antenna element spacing. The impact of the geometrical model parameters on the system performance is listed below:

- *The rectangle model*. It turns out that the system performance improves as the street length L_A increases. Nevertheless, changing the distance D [see Fig. 4.2(b)] between the mobile transmitter and the mobile receiver does not affect the system performance. Analogously, the street width B_1 and B_2 [see Fig. 4.2 (b)] does not affect the BEP performance. This fact indicates that a large number of scatterers are located on a street line.

- *The curve model*. Similarly to the system performance of the C2C tunnel channel model, the BEP performance of the C2C curved model does not change if the radius R [see Fig. 4.2(c)] of the curve varies in the considered range.

- *The tunnel model*. The effects of the radius R [see Fig. 4.2(d)] of the tunnel arch and the distance D between the mobile transmitter and the mobile receiver on the BEP performance are indistinguishable for the given antenna element spacings. On the contrary, the system performance improves if the antenna element spacings δ_T increase.

The obtained analytical results enable us to investigate the system performance using different kinds of C2C fading channels in a straightforward and time-efficient manner. Moreover, the proposed generalized channel model allows us to investigate different types of C2C channels and their spatial-temporal-frequency characteristics. Furthermore, the proposed model can be applied to other propagation environments, which results in 2D and 3D geometry-based C2C channel models, by adjusting the corresponding model parameters. Thus, this model can be used to study, investigate and optimize future C2C channels.

4.4 Chapter Summary

In the development and test of any new communication system, the thorough evaluation of its performance is imperative. It is especially required for the development of future C2C communications to design and support reliable and robust C2C safety applications. The performance analysis of C2C communications highly depends on the detailed knowledge and understanding of the underlying radio channel. The lack of performance analyses in the literature for C2C communication systems over different real life geometrical channel models motivated us to dedicate this chapter to the study and investigation of the performance of MIMO-OFDM systems over different types of C2C channels.

The chapter began with an overview of the performance analysis of C2C communication systems in different propagation environments by addressing their important statistical measures, such as the BER, PER, delay spread, Doppler spread, and BEP. Therein, the description and previous work on the STBC-OFDM systems are presented and discussed.

Thereafter, the chapter summarized the work presented in Paper V (Appendix E), where the performance of an Alamouti coded OFDM system over wideband MIMO C2C channels correlated in time and space is analyzed. The effects of temporal and spatial correlations on the system performance have been discussed. The numerical results show that the system performance of C2C communication systems is not only impacted by the temporal and spatial correlation function but also by geometrical model parameters. Finally, the chapter described the motivation behind the presented work and its advantages for future C2C communication systems.

Chapter 5

Summary of Contributions and Outlook

5.1 Major Contributions

This dissertation dealt with the exploration of various aspects of C2C communication systems. The topics covered a range from the modeling of geometry-based C2C channel models in different propagation conditions to the overall performance analysis of the system. In the following, the main contributions of this doctoral dissertation are summarized.

- A new geometry-based street scattering channel model (rectangle model) for a narrowband SISO C2C channel was proposed, where the geometrical rectangle area on both sides of the street models the scattering environment.
- A stochastic narrowband MIMO C2C reference channel model and its corresponding channel simulation model were derived based on the geometrical street scattering model. Spatial and temporal correlation functions of the reference and the simulation model were analyzed for LOS and NLOS propagation conditions.
- We have extended the geometrical street scattering (rectangle model) narrowband MIMO C2C channel model to the wideband MIMO C2C channel model. A profound statistical analysis of the wideband MIMO C2C channel model is presented by deriving analytical expressions for the STF-CCF, the temporal ACF, and the FCF as well as the Doppler statistics. Moreover, the validity of the proposed rectangle model for wideband MIMO C2C channel has been confirmed by demonstrating an excellent match of the Doppler statistics, such

as the mean Doppler shift and the Doppler spread, of the reference model to those of the real-world measured channel.

- In practice, there exist many different street types, such as intersections, U-turns, roundabouts, cross-junctions, which have different scattering environments. Thus, we proposed a novel geometrical curved street scattering model for narrowband MIMO C2C communications. The complex channel gain of the reference model was derived from the geometrical curved street scattering model by taking into account single-bounced and double-bounced scattering as well as the LOS components. Interesting findings pertaining to statistical properties, such as the 3D ST-CCF, the temporal ACF, and the 2D space-CCF were documented.

- The narrowband MIMO C2C channel model based on the curved model further extended to the wideband model, which is a special case of the generalized wideband channel model.

- The characteristics of the propagation channel in tunnel environments are of crucial importance for C2C communications. In this regard, we introduced a new wideband 3D geometrical SCT model for MIMO C2C communication systems in tunnel environments. The wideband 3D SCT C2C channel model was proposed by taking into account the diffuse, the LOS and the specular components under LOS and NLOS propagation conditions. The space, time, and frequency correlation properties were evaluated in LOS and NLOS propagation conditions. The impact of the tunnel arch radius on the correlation functions was studied. Furthermore, the validation of the proposed 3D SCT model was proven by fitting the delay spread of the reference model to that of the measured channel.

- A generalized wideband channel model for MIMO C2C communication systems was proposed in which the rectangle model, street line model, curve model, and the tunnel model are included as special cases. In the proposed wideband channel model, a generalized expression for the TVTF was derived by considering single-bounce scattering under NLOS propagation conditions.

- The performance analysis of C2C communication systems depends on the detailed knowledge of the underlying propagation channel and its statistical properties. Therefore, by using the generalized channel model, the performance analysis of Alamouti coded OFDM systems over different types of C2C channels correlated in time and space were analyzed. A generalized

expression was presented for the BEP, which will be used to investigate the performance of Alamouti coded OFDM systems over different types of C2C channel models, such as the rectangle model, street line model, tunnel model, and the curve model. The impact of the geometrical model parameters on the BEP performance was discussed and presented. The effect of the maximum Doppler shift and the antenna element spacing on the system performance was investigated.

5.2 Outlook

This dissertation was an attempt to study and investigate the issues related to the modeling and analysis of C2C fading channels considering different propagation environments and conditions in C2C communication systems. The statistical characterization and validation of the proposed C2C channel models and the performance analysis of the Alamouti coded OFDM systems over different C2C channels were also included. Although the discussion covered various aspects of C2C communication systems, there are still open problems that remained unaddressed. Some few problems are highlighted in the following.

- The entire analysis presented in this dissertation is based on the assumption that the C2C channels are wide-sense stationary uncorrelated scattering. Although the WSSUS assumption is still valid for a short observation time intervals, it is of great importance to investigate C2C communications considering the non-stationarity characteristics of C2C channels.

- The geometrical curved street scattering model for MIMO C2C communications was presented. However, measurements for curved road environments are lacking, which are required for the validation of the curved model.

- Although, we provided expressions for the statistical properties of C2C channels, further studies are needed to obtain exact, simple and closed-form solutions.

- In our performance investigations of Alamouti coded OFDM systems, we have assumed perfect channel state information (CSI), which is not always available in practice. Further research work is required to extend our performance analysis to the case of unknown CSI. Additionally, extending the Alamouti coded OFDM system to a general MIMO-OFDM system can also be investigated in future work.

- In recent years, there has been an upsurge of interest towards cooperative communications, due to many advantages such as high data rate services, diversity and multiplexing gains as well as infrastructure-less deployment. Consequently, C2C communications has recently gained much attention of researchers, standardization bodies, and industrial companies, since it offers many applications. Hence, these applications are targeted to make transportation safer, more efficient, and more environmentally friendly. In this regard, modeling and analysis of cooperative C2C communication channels are required for future C2C communications. In addition, the system performance of cooperative C2C communications should be investigated in the future.

REFERENCES

[1] F. Qu, F.-Y. Wang, and L. Yang, "Intelligent transportation spaces: vehicles, traffic, communications, and beyond," *IEEE Commun. Magazine*, vol. 48, no. 11, pp. 136–142, Nov. 2010.

[2] S. Biswas, R. Tatchikou, and F. Dion, "Vehicle-to-vehicle wireless communication protocols for enhancing highway traffic safety," *IEEE Communications Magazine*, vol. 44, no. 1, pp. 74–82, Jan. 2006.

[3] G. Karagiannis, O. Altintas, E. Ekici, G. Heijenk, B. Jarupan, K. Lin, and T. Weil, "Vehicular networking: A survey and tutorial on requirements, architectures, challenges, standards, and solutions," *IEEE Commun. Surv. Tutorials*, vol. 13, no. 4, pp. 584–616, Nov. 2011.

[4] G. Rafiq, B. Talha, M. Pätzold, J. G. Luis, G. Ripa, I. Carreras, C. Coviello, S. Marzorati, G. P. Rodriguez, G. Herrero, and M. Desaeger, "What's new in intelligent transportation systems? An overview of European projects and initiatives," *IEEE Veh. Technol. Mag.*, vol. 8, no. 4, pp. 45–69, Dec. 2013.

[5] M. Alsabaan, W. Alasmary, A. Albasir, and K. Naik, "Vehicular networks for a greener environment: A survey," *IEEE Commun. Surv. Tutorials*, vol. 15, no. 3, pp. 1372–1388, Jul. 2013.

[6] J. Zhu and S. Roy, "MAC for dedicated short range communications in intelligent transport system," *IEEE Communications Magazine*, vol. 41, no. 12, pp. 60–67, Dec. 2003.

[7] V. Gradinescu *et al.*, "Adaptive traffic lights using car-to-car communication," in *Proc. IEEE 65th Veh. Technol. Conf., VTC'07-Spring*. Dublin, Ireland, Apr. 2007, pp. 21–25, DOI 10.1109/VETECS.2007.17.

[8] Intelligent Transportation Systems (ITS) [Online]. Available: http://www.its.dot.gov.

[9] L. Angell *et al.*, "Driver workload metrics project: final report," Washington, DC: National Highway Traffic Safety Administration, Tech. Rep. DOT HS 810 635, 2006.

[10] R. Curry, J. Greenberg, and R. Kiefer, "Forward collision warning requirements project: task 4 final report," Washington, DC: National Highway Traffic Safety Administration, Tech. Rep. DOT HS 809 925, 2005.

[11] F. Ahmed-Zaid *et al.*, "Vehicle safety communications - applications (VSC-A) final report," Washington, DC: National Highway Traffic Safety Administration, Tech. Rep. DOT HS 811 492A, 2011.

[12] European Road Transport Telematics Implementation Coordinating Organization (ERTICO) [Online]. Available: http://www.ertico.com.

[13] Car-to-Car Communication Consortium (C2C-CC) [Online]. Available: http://www.car-to-car.org.

[14] A. Chelli, *Channel Modeling and system performance analysis of vehicle-to-vehicle communication systems*. Doctoral dissertation, University of Agder, Grimstad, Norway, 2013.

[15] Cooperative Vehicle-Infrastructure Systems (CVIS) [Online]. Available: http://www.cvisproject.org.

[16] Cooperative Systems for Intelligent Road Safety (COOPERS) [Online]. Available: http://www.coopers-ip.eu.

[17] Compass4D [Online]. Available: http://www.compass4d.eu.

[18] Preparing Secure Vehicle-to-X Communication Systems (PRESERVE) [Online]. Available: http://www.preserve-project.eu.

[19] *Standard Specification for Telecommunications and Information Exchange Between Roadside and Vehicle Systems - 5 GHz Band Dedicated Short Range Communications (DSRC) Medium Access Control (MAC) and Physical Layer (PHY) Specifications*, Sep. 2003, ASTM E 2213-03.

[20] J. B. Kenney, "Dedicated short-range communications (DSRC) standards in the United States," *Proceedings of the IEEE*, vol. 99, no. 7, pp. 1162–1182, Jul. 2011.

[21] "IEEE 802.11p, Part 11: Wireless LAN medium access control (MAC) and physical layer (PHY) specifications Amendment 6: Wireless access in vehicular environments, IEEE standards association," Jun. 2010.

[22] "802.11–2012 – IEEE standard for information technology–telecommunications and information exchange between systems local and metropolitan area networks–specific requirements Part 11: Wireless LAN Medium Access Control (MAC) and Physical Layer (PHY) specifications," Mar. 2012.

[23] G. Acosta, K. Tokuda, and M. A. Ingram, "Measured joind Doppler-delay power profiles for vehicle-to-vehicle communications at 2.4 GHz," in *Proc. IEEE Global Communications Conference, GLOBECOM'04, Dallas, TX*, vol. 6, Nov. 29 - Dec. 3 2004, pp. 3813–3817.

[24] P. C. F. Eggers, T. W. C. Brown, K. Olesen, and G. F. Pedersen, "Assessment of capacity support and scattering in experimental high speed vehicle to vehicle MIMO links," in *Proc. 65th IEEE Vehicular Technology Conference, VTC 2007-Spring*, Apr. 2007, pp. 466–470.

[25] I. Sen and D. W. Matolak, "Vehicle-vehicle channel models for the 5-GHz band," *IEEE Trans. Intell. Trans. Syst.*, vol. 9, no. 2, pp. 235–245, Jun. 2008.

[26] Q. Wu, D. W. Matolak, and I. Sen, "5-GHz-band vehicle-to-vehicle channels: models for multiple values of channel bandwidth," *IEEE Trans. Veh. Technol.*, vol. 59, no. 5, pp. 2620–2625, Jun. 2010.

[27] J. Maurer, T. Fügen, and W. Wiesbeck, "Narrow-band measurement and analysis of the inter-vehicle transmission channel at 5.2 GHz," in *Proc. IEEE 55th Semiannual Veh. Technol. Conf., VTC'02-Spring*, vol. 3. Birmingham, Alabama, May 2002, pp. 1274–1278.

[28] L. Cheng, B. E. Henty, D. D. Stancil, F. Bai, and P. Mudalige, "Mobile vehicle-to-vehicle narrow-band channel measurement and characterization of the 5.9 GHz dedicated short range communication (DSRC) frequency band," *IEEE J. Select. Areas Commun.*, vol. 25, no. 8, pp. 1501–1516, Oct. 2007.

[29] G. Acosta-Marum and M. A. Ingram, "Six time- and frequency-selective empirical channel models for vehicular wireless LANs," *IEEE Vehicuar Technology Magazine*, vol. 2, pp. 4–11, Dec. 2007.

[30] R. B. Ertel and J. H. Reed, "Angle and time of arrival statistics for circular and elliptical scattering models," *IEEE J. Select. Areas Commun.*, vol. 17, no. 11, pp. 1829–1840, Nov. 1999.

[31] A. Abdi and M. Kaveh, "A space-time correlation model for multielement antenna systems in mobile fading channels," *IEEE J. Select. Areas Commun.*, vol. 20, no. 3, pp. 550–560, Apr. 2002.

[32] M. Pätzold and B. O. Hogstad, "A space-time channel simulator for MIMO channels based on the geometrical one-ring scattering model," *Wireless Communications and Mobile Computing, Special Issue on Multiple-Input*

Multiple-Output (MIMO) Communications, vol. 4, no. 7, pp. 727–737, Nov. 2004.

[33] A. Y. Olenko, K. T. Wong, and S. A. Qasmi, "Distribution of the uplink multipaths' arrival delay and azimuth-elevation arrival angle because of 'bad urban' scatterers distributed cylindrically above the mobile," *Trans. Emerging Tel. Tech.*, vol. 2012, 2012, DOI 10.1002/ett.2530.

[34] R. Janaswamy, "Angle of arrival statistics for a 3-D spheroid model," *IEEE Trans. Veh. Technol.*, vol. 51, no. 5, pp. 1242–1247, Sep. 2002.

[35] Y. I. Wu and K. T. Wong, "A geometrical model for the TOA distribution of uplink/downlink multipaths, assuming scatterers with a conical spatial density," *IEEE Antennas Propag. Mag.*, vol. 50, no. 6, pp. 196–205, Dec. 2008.

[36] K. Arshad, F. Katsriku, and A. Lasebae, "Modelling obstructions in straight and curved rectangular tunnels by finite element approach," *Journal of Electrical Engineering*, vol. 59, no. 1, pp. 9–13, 2008.

[37] I. Ivan, P. Besnier, M. Crussiere, M. Drissi, L. Le Danvic, M. Huard, and E. Lardjane, "Physical layer performance analysis of V2V communications in high velocity context," in *Proc. 9th International Conference on Intelligent Transport Systems Telecommunications, ITST 2009*. Lille, France, Oct. 2009, pp. 409–414.

[38] A. Chelli and M. Pätzold, "Performance of hybrid-ARQ with incremental redundancy over double Rayleigh fading channels," in *Proc. IEEE Vehicular Technology Conference (VTC-Spring'2011)*. Budapest, Hungary, May 2011.

[39] V. Shivaldova, G. Maier, D. Smely, N. Czink, A. Alonso, A. Winkelbauer, A. Paier, and C. F. Mecklenbräuker, "Performance evaluation of IEEE 802.11p infrastructure-to-vehicle tunnel measurements," in *Proc. 7th International Wireless Communications and Mobile Computing Conference, IWCMC 2011*. Istanbul, Turkey, Jul. 2011, pp. 848–852.

[40] D. W. Matolak, Q. Wu, J. J. S. Sanchez, D. M. Jimenez, and M. C. A. Torres, "Performance of LTE in vehicle-to-vehicle channels," in *Proc. IEEE Veh. Technol. Conf., VTC-Fall 2011*. San Francisco, CA, Sep. 2011, pp. 1–4.

[41] J. Karedal, F. Tufvesson, N. Czink, A. Paier, C. Dumard, T. Zemen, and C. F. Mecklenbräuker, "A geometry-based stochastic MIMO model for vehicle-to-

vehicle communications," *IEEE Trans. Wireless Commun.*, vol. 8, no. 7, pp. 3646–3657, Jul. 2009.

[42] H. Asplund, A. A. Glazunov, K. I. Pedersen, and M. Steinbauer, "The COST259 directional channel model - II, macrocells," *IEEE Trans. Wireless Commun.*, vol. 5, pp. 3434–3450, 2006.

[43] P. Almers, E. Bonek, A. Burr, N. Czink, M. Debbah, V. Degli-Esposti, H. Hofstetter, P. Kyösti, D. Laurenson, G. Matz, A. F. Molisch, C. Oestges, and H. Özcelik, "Survey of channel and radio propagation models for wireless MIMO systems," *EURASIP J. Wireless Commun. Networking*, vol. 2007, 2007, DOI 10.1155/2007/19070.

[44] K. T. Wong, Y. I. Wu, and M. Abdulla, "Landmobile radiowave multipaths DOA-distribution: Assessing geometric models by the open literature's empirical datasets," *IEEE Trans. Antennas Propagat.*, vol. 58, no. 3, pp. 946–958, Mar. 2010.

[45] A. Borhani and M. Pätzold, "A unified disk scattering model and its angle-of-departure and time-of-arrival statistics," *IEEE Trans. Veh. Technol.*, vol. 62, no. 2, pp. 473–485, Feb. 2013.

[46] J. Maurer, T. Fügen, T. Schäfer, and W. Wiesbeck, "A new inter-vehicle communications (IVC) channel model," in *Proc. IEEE Veh. Technol. Conf., VTC'04-Fall*, vol. 1, Sep. 2004, pp. 9–13.

[47] COST 207, "Digital land mobile radio communications," *Office for Official Publications of the European Communities*, Final Report, Luxemburg, 1989.

[48] G. Acosta-Marum and M. A. Ingram, "Doubly selective vehicle-to-vehicle channel measurements and modeling at 5.9 GHz," in *Proc. Int. Symp. Wireless Personal Multimedia Commun.*, vol. 2, 2006.

[49] A. S. Akki and F. Häber, "A statistical model of mobile-to-mobile land communication channel," *IEEE Trans. Veh. Technol.*, vol. 35, no. 1, pp. 2–7, Feb. 1986.

[50] A. S. Akki, "Statistical properties of mobile-to-mobile land communication channels," *IEEE Trans. Veh. Technol.*, vol. 43, no. 4, pp. 826–831, Nov. 1994.

[51] F. Vatalaro and A. Forcella, "Doppler spectrum in mobile-to-mobile communications in the presence of three-dimensional multipath scattering," *IEEE Trans. Veh. Technol.*, vol. 46, no. 1, pp. 213 – 219, 1997.

[52] C.-X. Wang, X. Cheng, and D. I. Laurenson, "Vehicle-to-vehicle channel modeling and measurements: Recent advances and future challenges," *IEEE Communications Magazine*, vol. 47, no. 11, pp. 96–103, Nov. 2009.

[53] J. Kunisch and J. Pamp, "Wideband car-to-car radio channel measurements and model at 5.9 GHz," in *2008 IEEE 68th Vehicular Technology Conference*, Calgary, Canada, Sep. 2008, pp. 1–5.

[54] A. Paier, J. Karedal, N. Czink, H. Hofstetter, and C. Dumard, "Car-to-car radio channel measurements at 5 GHz: Pathloss, power delay profile, and Doppler delay spectra," in *Proc. 4th Int. Symp. on Wireless Communication Systems, ISWCS'07*. Trondheim, Norway, Oct. 2007, pp. 224–228.

[55] A. Paier, J. Karedal, N. Czink, C. Dumard, T. Zemen, F. Tufvesson, A. F. Molisch, and C. F. Mecklenbräuker, "Characterization of vehicle-to-vehicle radio channels from measurements at 5.2 GHz," *Wireless Pers. Commun.*, Jun. 2008.

[56] A. G. Zajić, G. L. Stüber, T. G. Pratt, and S. Nguyen, "Wideband MIMO mobile-to-mobile channels: geometry-based statistical modeling with experimental verification," *IEEE Trans. Veh. Technol.*, vol. 58, no. 2, pp. 517–534, Feb. 2009.

[57] O. Renaudin, V.-M. Kolmonen, P. Vainikainen, and C. Oestges, "Wideband measurement-based modeling of inter-vehicle channels in the 5.2 GHz band," *IEEE Trans. Veh. Technol.*, vol. 62, no. 8, pp. 3531–3540, Oct. 2013.

[58] G. J. Foschini and M. J. Gans, "On limits of wireless communications in a fading environment when using multiple antennas," *Wireless Pers. Commun.*, vol. 6, pp. 311–335, Mar. 1998.

[59] I. E. Telatar, "Capacity of multi-antenna Gaussian channels," *European Trans. Telecommun. Related Technol.*, vol. 10, pp. 585–595, 1999.

[60] M. Pätzold, B. O. Hogstad, and N. Youssef, "Modeling, analysis, and simulation of MIMO mobile-to-mobile fading channels," *IEEE Trans. Wireless Commun.*, vol. 7, no. 2, pp. 510–520, Feb. 2008.

[61] M. Pätzold and B. O. Hogstad, "A wideband MIMO channel model derived from the geometrical elliptical scattering model," *Wireless Communications and Mobile Computing*, vol. 8, pp. 597–605, May 2008.

[62] H. Zhiyi, C. Wei, Z. Wei, M. Pätzold, and A. Chelli, "Modelling of MIMO vehicle-to-vehicle fading channels in T-junction scattering environments," in *Proc. 3rd European Conference on Antennas and Propagation, EuCAP 2009*. Berlin, Germany, Mar. 2009, pp. 652–656.

[63] A. Theodorakopoulos, P. Papaioannou, T. Abbas, and F. Tufvesson, "A geometry based stochastic model for MIMO V2V channel simulation in cross-junction scenario," in *Proc. 13th International Conference on ITS Telecommunications*. Tampere, Finland, Nov. 2013.

[64] N. Avazov and M. Pätzold, "A narrowband MIMO car-to-car channel model based on the geometrical street scattering model," in *Proc. International Conference on Selected Topics in Mobile and Wireless Networking, iCOST12*. Avignon, France, Jul. 2012, pp. 18–23.

[65] A. Chelli and M. Pätzold, "A MIMO mobile-to-mobile channel model derived from a geometric street scattering model," in *Proc. 4th IEEE International Symposium on Wireless Communication Systems, ISWCS 2007*. Trondheim, Norway, Oct. 2007, pp. 792–797.

[66] N. Avazov and M. Pätzold, "A novel MIMO car-to-car channel model based on the geometrical curved street scattering model," in *Proc. Loughborough Antennas and Propagation Conference (LAPC'2012)*. Loughborough, UK, Nov. 2012, pp. 1–6.

[67] A. G. Zajić and G. L. Stüber, "Space-time correlated mobile-to-mobile channels: modelling and simulation," *IEEE Trans. Veh. Technol.*, vol. 57, no. 2, pp. 715–726, Mar. 2008.

[68] X. Cheng, C.-X. Wang, D. I. Laurenson, H.-H. Chen, and A. V. Vasilakos, "A generic geometrical-based MIMO mobile-to-mobile channel model," in *Proc. International Wireless Communications and Mobile Computing Conference, IWCMC'08*, Aug. 2008, pp. 1000 –1005.

[69] Y. Ma and M. Pätzold, "Design and simulation of narrowband indoor radio propagation channels under LOS and NLOS propagation conditions," in *Proc. IEEE 71st Vehicular Technology Conference, VTC2010-Spring*. Taipei, Taiwan, May 2010.

[70] M. Pätzold, *Mobile Radio Channels*, 2nd ed. Chichester: John Wiley & Sons, 2011, 583 pages.

[71] M. Pätzold and B. Talha, "On the statistical properties of sum-of-cisoids-based mobile radio channel simulators," in *Proc. 10th International Symposium on Wireless Personal Multimedia Communications, WPMC 2007*. Jaipur, India, Dec. 2007, pp. 394–400.

[72] C. A. Gutiérrez and M. Pätzold, "The design of sum-of-cisoids Rayleigh fading channel simulators assuming non-isotropic scattering conditions," *IEEE Trans. Wireless Commun.*, vol. 9, no. 4, pp. 1308–1314, Apr. 2010.

[73] ——, "The generalized method of equal areas for the design of sum-of-sinusoids simulators for mobile Rayleigh fading channels with arbitrary Doppler spectra," *Wireless Communications and Mobile Computing*, Jul. 2011, DOI:10.1002/wcm.1154.

[74] Y. Ma and M. Pätzold, "Wideband two-ring MIMO channel models for mobile-to-mobile communications," in *Proc. 10th International Symposium on Wireless Personal Multimedia Communications, WPMC 2007*. Jaipur, India, Dec. 2007, pp. 380–384.

[75] A. Chelli and M. Pätzold, "A wideband multiple-cluster MIMO mobile-to-mobile channel model based on the geometrical street model," in *Proc. IEEE International Symposium on Personal, Indoor and Mobile Radio Communications, PIMRC 2008*. Cannes, France, Sep. 2008, pp. 1–6.

[76] A. G. Zajić and G. L. Stüber, "Three-dimensional modeling and simulation of wideband MIMO mobile-to-mobile channels," *IEEE Trans. Wireless Commun.*, vol. 8, no. 3, pp. 1260–1275, Mar. 2009.

[77] I. Tan, T. Wanbin, K. Laberteaux, and A. Bahai, "Measurement and analysis of wireless channel impairments in DSRC vehicular communications," in *Proc. IEEE ICC'08*, May 2008, pp. 4882–4888.

[78] N. Avazov and M. Pätzold, "A geometric street scattering channel model for car-to-car communication systems," in *Proc. International Conference on Advanced Technologies for Communications, ATC 2011*. Da Nang City, Vietnam, Aug. 2011, pp. 224–230.

[79] ——, "Design of wideband MIMO car-to-car channel models based on the geometrical street scattering model," *Modeling and Simulation in Engineering*, vol. 2012, Article ID 264213, 11 pages, Sep. 2012. DOI:10.1155/2012/264213.

[80] J. Chen and T. G. Pratt, "A three-dimensional geometry-based statistical model of 2×2 dual-polarized MIMO mobile-to-mobile wideband channels," *Modelling and Simulation in Engineering*, vol. 2012, Article ID 756508, 2012.

[81] J. F. Ossana, Jr., "A model for mobile radio radio fading due to building reflections: Theoretical and experimental waveform power spectra," *Bell. Syst. Tech. J.*, vol. 43, pp. 2935–2971, Nov. 1964.

[82] T. Aulin, "A modified model for the fading signal at a mobile radio channel," *IEEE Trans. Veh. Technol.*, vol. VT-28, no. 3, pp. 182–203, Aug. 1979.

[83] E. N. Gilbert, "Energy reception for mobile radio," *Bell. Syst. Tech. J.*, vol. 44, no. 8, pp. 1779–1803, Oct. 1965.

[84] R. H. Clarke, "A statistical theory of mobile radio reception," *Bell. Syst. Tech. J.*, vol. 47, pp. 957–1000, Jul. 1968.

[85] J. D. Parsons and A. D. Turkmani, "Characteristics of mobile radio signals: model description," *IEEE Proceedings-I*, vol. 138, no. 6, pp. 549–556, Dec. 1991.

[86] C. Cheon, G. Liang, and H. L. Bertoni, "Simulating radio channel statistics for different building environments," *IEEE J. Select. Areas Commun.*, vol. 19, no. 11, pp. 2191–2200, Nov. 2001.

[87] N. Blaunstein, M. Toeltsch, C. G. Christodoulou, J. Laurila, E. Tsalolihin, E. Boenk *et al.*, "Azimuth, elevation, and time-delay distributions in wireless communication channels," *IEEE Antennas and Propagation Magazine*, vol. 48, no. 1, pp. 160–167, Feb. 2006.

[88] A. G. Zajić and G. L. Stüber, "Three-dimensional modeling, simulation, and capacity analysis of space-time correlated mobile-to-mobile channels," *IEEE Trans. Veh. Technol.*, vol. 57, no. 4, pp. 2042–2054, Jul. 2008.

[89] N. Avazov and M. Pätzold, "A wideband car-to-car channel model based on a geometrical semicircular tunnel scattering model," in *Proc. 24th IEEE Int. Symp. on Personal, Indoor and Mobile Radio Communications (PIMRC'2013)*. London, UK, Sep. 2013, pp. 248–253.

[90] S. J. Nawaz, B. H. Qureshi, and N. M. Khan, "A generalized 3-D scattering model for a macrocell environment with a directional antenna at the BS," *IEEE Trans. Veh. Technol.*, vol. 59, no. 7, pp. 3193–3204, Sep. 2010.

[91] S. J. Nawaz, M. N. Patwary, N. M. Khan, and H. Yu, "3-D Gaussian scatter density propagation model employing a directional antenna at BS," in *Advance Satellite Multimedia Systems Conference*, 2010, pp. 395–400.

[92] Q. Yao and M. Pätzold, "Spatial-temporal characteristics of a half-spheroid model and its corresponding simulation model," in *Proc. IEEE Vehicular Technology Conference, VTC 2004-Spring*, vol. 1, May 2004, pp. 147–151, DOI 10.1109/VETECS.2004.1387930.

[93] Y. Yuan, X. Cheng, C.-X. Wang, D. I. Laurenson, X. Ge, and F. Zhao, "Space-time correlation properties of a 3D two-sphere model for non-isotropic MIMO mobile-to-mobile channels," in *Proc. of the IEEE Global Telecommunications Conference (GLOBECOM'10)*, Dec. 2010, pp. 1–5.

[94] J. Chen and T. G. Pratt, "A three-dimensional geometry-based statistical modeling and performance of 4×4 spatial-polarization mobile-to-mobile wideband MIMO channels." Atlanta, GA, Dec. 2013, pp. 3936–3941, DOI 10.1109/GLOCOM.2013.6831688.

[95] E. T. Michailidis, P. Theofilakos, and A. G. Kanatas, "A 3-D model for MIMO mobile-to-mobile amplify-and-forward relay fading channels," in *Proc. 6th European Conference on Antennas and Propagation, EuCAP'2012*, vol. 3. Prague, Czech Republic, Mar. 2012, pp. 2073–2077.

[96] E. T. Michailidis and A. G. Kanatas, "A 3-D wideband MIMO channel model for mobile-to-mobile relay-based communications," in *Proc. IEEE Symp. on Personal, Indoor and Mobile Radio Communications, PIMRC 2013*. London, UK, Sep. 2013, pp. 122–126.

[97] P. T. Samarasinghe, T. A. Lamahewa, T. D. Abhayapala, and R. A. Kennedy, "3D mobile-to-mobile wireless channel model," in *Proc. of Australian Communications Theory Workshop, AusCTW 2010*. Canberra, ACT, Feb. 2010, pp. 30–34, DOI 10.1109/AUSCTW.2010.5426757.

[98] Y. Yuan, C.-X. Wang, X. Cheng, B. Ai, and D. I. Laurenson, "Novel 3D geometry-based stochastic models for non-isotropic MIMO vehicle-to-vehicle channels," *IEEE Trans. Wireless Commun.*, vol. 13, no. 1, pp. 298–309, Jan. 2014.

[99] Z. Sun and I. F. Akyildiz, "A mode-based approach for channel modeling in underground tunnels under the impact of vehicular traffic flow," *IEEE Trans. Wireless Commun.*, vol. 10, no. 10, pp. 3222–3231, Oct. 2011.

[100] Norwegian Public Roads Administration, [Online] Available: http://www.vegvesen.no, *Road Tunnels*. NPRA Printing Center, Jul. 2004, no. 0.21, ISBN 82-7207-540-7.

[101] S. F. Mahmoud and J. R. Wait, "Geometrical optical approach for electromagnetic wave propagation in rectangular mine tunnels," *Radio Science*, vol. 9, no. 12, pp. 1147–1158, Dec. 1974.

[102] D. G. Dudley, M. Liénard, S. F. Mahmoud, and P. Degauque, "Wireless propagation in tunnels," *IEEE Antennas Propagation Mag.*, vol. 49, no. 2, pp. 11–26, Apr. 2007.

[103] F. Pallares, F. Juan, and L. Juan-Llacer, "Analysis of path los and delay spread at 900 MHz and 2.1 GHz while entering tunnels," *IEEE Trans. Veh. Technol.*, vol. 50, no. 3, pp. 767–776, May 2001.

[104] G. S. Ching, M. Ghoraishi, M. Landmann, N. Lertsirisopon, J.-I. Takada, T. Imai, I. Sameda, and H. Sakamoto, "Wideband polarimetric directional propagation channel analysis inside an arched tunnel," *IEEE Trans. Antennas Propagat.*, vol. 57, no. 3, pp. 760–767, Mar. 2009.

[105] L. Bernadó, A. Roma, A. Paier, T. Zemen, N. Czink, J. Karedal, A. Thiel, F. Tufvesson, A. F. Molisch, and C. F. Mecklenbräuker, "In-tunnel vehicular radio channel characterization," in *Proc. 73rd IEEE Vehicular Technology Conference (VTC2011-Spring)*, May 2011, pp. 1–5.

[106] A. F. Molisch, F. Tufvesson, J. Karedal, and C. F. Mecklenbräuker, "A survey on vehicle-to-vehicle propagation channels," *IEEE Trans. Commun.*, vol. 16, no. 6, pp. 12–22, Dec. 2009.

[107] A. Chelli, R. Hamdi, and M.-S. Alouini, "Channel modelling and performance analysis of V2I communication systems in blind bend scattering environments," *Progress in Electromagnetics Research B*, vol. 57, pp. 233–251, 2014.

[108] A. Chelli and M. Pätzold, "On the performance of hybrid-ARQ with code combining over double Rayleigh fading channels," in *Proc. IEEE Symposium on Personal Indoor Mobile and Radio Communications (PIMRC'2011)*. Toronto, Canada, Sep. 2011.

[109] S. N. Sur and R. Bera, "Doppler shift impact on the MIMO OFDM systems in vehicular channel conditions," *International Journal of Information Technology & Computer Science*, vol. 4, no. 8, pp. 57 – 62, Jul. 2012. DOI:10.5815/ijitcs.2012.08.07.

[110] J. Nuckelt, M. Schack, and T. Kürner, "Deterministic and stochastic channel models implemented in a physical layer simulator for car-to-X communications," *Adv. Radio Sci.*, vol. 9, pp. 165–171, Jan. 2011.

[111] M. Takanashi, K. Hayakawa, K. Sanda, and T. Shibata, "Channel tracking with zero padding scheme for STBC-OFDM system under fast fading environment," in *Proc. IEEE 69th Veh. Technol. Conf., VTC-Spring 2009*. Barcelona, Spain, Apr. 2009, pp. 1–5.

[112] X. Cheng, Q. Yao, M. Wen, C.-X. Wang, L.-Y. Song, and B.-L. Jiao, "Wideband channel modeling and intercarrier interference cancellation for vehicle-to-vehicle communication systems," *IEEE J. Select. Areas Commun.*, vol. 31, no. 9, pp. 434–448, Sep. 2013.

[113] K. Ito, N. Suzuki, and Y. Karasawa, "Performance evaluation of MIMO-STBC for inter-vehicle communications in a shadowing environment generated by a large vehicle," in *Proc. 66th Vehicular Technology Conference, VTC-Fall 2007*. Baltimore, MD, Sep. 2007, pp. 758–762.

[114] Y. Ma and M. Pätzold, "Performance analysis of Alamouti coded OFDM systems over Rayleigh fading channels correlated in space and time," in *Proc. the 71st IEEE Vehicular Technology Conference, VTC2010-Spring*. Taipei, Taiwan, May 2010, pp. 1–6.

[115] N. Avazov and M. Pätzold, "Performance analysis of Alamouti coded OFDM systems over wideband MIMO car-to-car channels correlated in time and space," in *Proc. International conference on Connected Vehicles and Expo (ICCVE'2014)*. Messe Wien, Austria, Nov. 2014.

[116] J.-L. Yu and Y.-C. Lin, "Space-time-coded MIMO ZP-OFDM systems: Semiblind channel estimation and equalization," *IEEE Trans. Circuits. Syst. I.*, vol. 56, no. 7, pp. 1360–1372, Jul. 2009.

[117] H.-Y. Chen, W.-K. Chang, and S.-J. Jou, "A low-overhead interference canceller for high-mobility STBC-OFDM systems," *IEEE Trans. Circuits. Syst. I.*, vol. 60, no. 10, pp. 2763–2773, Oct. 2013.

[118] V. Tarokh, N. Seshadri, and A. R. Calderbank, "Space-time codes for high data rate wireless communication: performance criterion and code construction," *IEEE Trans. Inform. Theory*, vol. 44, no. 2, pp. 744–765, Mar. 1998.

[119] V. Tarokh, H. Jafarkhani, and A. R. Calderbank, "Space-time block coding from orthogonal design," *IEEE Trans. Inform. Theory*, vol. 45, no. 5, pp. 1456–1467, Jul. 1999.

[120] B. O'Hara and A. Petrick, Eds., *The IEEE 802.11 Handbook: A Designer's Companion*. Piscataway, NJ: IEEE Press, 1999.

[121] G. Hiertz, D. Denteneer, L. Stibor, Y. Zang, X. Costa, and B. Walke, "The IEEE 802.11 universe," *IEEE Communications Magazine*, vol. 48, no. 1, pp. 62–70, Jan. 2010.

[122] J. Cheng, H. Wang, and S. Cheng, "Space-time block coded transmit diversity OFDM system in mobile channels," in *Proc. IEEE 13th International Symposium on Personal, Indoor and Mobile Radio Communications, PIMRC 2002*, vol. 1. Lisbon, Portugal, Sep. 2002, pp. 208–211.

[123] J. Kim, R. W. Heath, Jr, and E. J. Powers, "Receiver designs for Alamouti coded OFDM systems in fast fading channels," *IEEE Trans. Wireless Commun.*, vol. 4, no. 2, pp. 550–559, Mar. 2005.

[124] S. M. Alamouti, "A simple transmit diversity technique for wireless communications," *IEEE J. Select. Areas Commun.*, vol. 16, no. 8, pp. 1451–1458, Oct. 1998.

[125] T. Brown, E. D. Carvalho, and P. Kyritsi, *Practical Guide to the MIMO Radio Channel: with MATLAB Examples*. Chichester: John Wiley & Sons, 2012, ISBN 9780470994498.

[126] A. Goldsmith, *Wireless Communications*. New York: Cambridge University Press, 2005.

[127] J. Proakis and M. Salehi, *Digital Communications*, 5th ed. New York: McGraw-Hill, 2007.

Appendices A–E

List of Publications

The purpose of this preface to Appendices A–E is to record all the articles that are an outcome of the research work carried out by the author of this dissertation.

The list of publications consists of submitted and already published papers. Firstly, the next section lists those articles which are briefly discussed in Chapters 2–4 of this dissertation and are replicated in Appendices A–E. Thereafter, the subsequent section details those papers which are published within the framework of this doctoral thesis, however they are not included in this dissertation.

Articles Included in this Dissertation

Those articles which are included in Appendices A–E of this dissertation are tabulated as follows:

Paper I [1] N. Avazov and M. Pätzold, "A geometric street scattering channel model for car-to-car communication systems," in *Proc. IEEE International Conference on Advanced Technologies for Communications, ATC 2011*, Da Nang, Vietnam, Aug. 2011, pp. 224 – 230.

Paper II N. Avazov and M. Pätzold, "Design of wideband MIMO car-to-car channel models based on the geometrical street scattering model," in *Special Issue: Modeling and Simulation in Engineering*, vol. 2012, Hindawi, 2012, ISSN: 1687-5605 (Online).

[1] This article received the Best Student Paper Award at the International Conference on Advanced Technologies for Communications, ATC 2011.

Paper III N. Avazov and M. Pätzold, "A novel MIMO car-to-car channel model based on the geometrical curved street scattering model," in *Proc. Loughborough Antennas and Propagation Conference, LAPC 2012*, Loughborough, UK, Nov. 2012, pp. 1 – 6.

Paper IV N. Avazov and M. Pätzold, "A novel wideband MIMO car-to-car channel model based on a geometrical semicircular tunnel scattering model," *IEEE Transactions on Vehicular Technology*, 2015 (in press).

Paper V N. Avazov and M. Pätzold, "Performance analysis of Alamouti coded OFDM systems over wideband MIMO car-to-car channels correlated in time and space," *IEEE the 3rd International Conference on Connected Vehicles and Expo, ICCVE 2014*, Vienna, Austria, Nov. 2014.

In the next section, those papers are listed which have not been reproduced in this paper collection.

Articles Not Included in this Dissertation

The articles pointed out in the following are also published during this PhD study and carry equal importance as the ones mentioned in previous section. However, to reduce the overlap between the articles making up the final manuscript, they are not included in this dissertation.

Paper VI N. Avazov and M. Pätzold, "Design of measurement-based correlation models for shadow fading," in *Proc. International Conference on Advanced Technologies for Communications, ATC 2010*, Ho Chi Minh City, Vietnam, Oct. 2010, pp. 133 – 138.

Paper VII N. Avazov and M. Pätzold, "Design and simulation of measurement-based correlation models for shadow fading," *REV, Journal on Electronics and Communications*, vol. 1, no. 2, April-June 2011.

Paper VIII N. Avazov and M. Pätzold, "A narrowband MIMO car-to-car channel model based on the geometrical street scattering model," in *Proc. International Conference on Selected Topics in Mobile and Wireless Networking, iCOST12*, Avignon, France, Jul. 2012, pp. 18 – 23.

Paper IX N. Avazov and M. Pätzold, " A wideband car-to-car channel model based on a geometrical semicircular tunnel scattering model," in *Proc.*

24th IEEE Int. Symp. on Personal, Indoor and Mobile Radio Communications, PIMRC 2013, London, UK, Sept. 2013, pp. 248–253, ISBN 978-1-4673-6234-4.

Appendix A

Paper I

Title:	A Geometric Street Scattering Channel Model for Car-to-Car Communication Systems
Authors:	**Nurilla Avazov** and Matthias Pätzold
Affiliation:	University of Agder, Faculty of Engineering and Science, P. O. Box 509, NO-4898 Grimstad, Norway
Conference:	*IEEE International Conference on Advance Technologies for Communications, ATC 2011*, Da Nang, Vietnam, Aug. 2011.

A Geometric Street Scattering Channel Model for Car-to-Car Communication Systems

Nurilla Avazov and Matthias Pätzold
Faculty of Engineering and Science, University of Agder,
P.O. Box 509, NO-4898 Grimstad, Norway
E-mails: {nurilla.k.avazov, matthias.paetzold}@uia.no

Abstract — **This paper presents a geometric street scattering channel model for car-to-car (C2C) communication systems under line-of-sight (LOS) and non-LOS (NLOS) propagation conditions. Starting from the geometric model, we develop a stochastic reference channel model, where the scatterers are uniformly distributed in rectangles in the form of stripes parallel to both sides of the street. We derive analytical expressions for the probability density functions (PDFs) of the angle-of-departure (AOD) and the angle-of-arrival (AOA). We also investigate the Doppler power spectral density (PSD) and the autocorrelation function (ACF) of the proposed model, assuming that the mobile transmitter (MT) and the mobile receiver (MR) are moving, while the surrounding scatterers are fixed. To validate the reference channel model, its Doppler parameters are compared to those of a real-world measured channel for urban and rural areas. The numerical results show a good fitting of the theoretical results to the computer simulations. The proposed geometry-based channel model allows to study the effects of the street scatterers on the performance of C2C communication systems.**

I. INTRODUCTION

C2C communications have recently received great attention due to some traffic telematic applications that make transportation safer, more efficient, and more environmentally friendly [1]. Robust and reliable traffic telematic applications and services require C2C wireless communication systems that can provide robust connectivity. To develop such wireless communication systems and standards, accurate channel models for the C2C communication systems are required. In this context, several mobile-to-mobile (M2M) fading channels have been proposed, for example, one-ring [2], two-ring [3], and elliptical [4] channel models. A two-dimensional (2D) reference model for a single-input single-output (SISO) M2M Rayleigh fading channel has been proposed by Akki and Haber in [5]. In [6], a three-dimensional (3D) model for wideband multiple-input multiple-output (MIMO) M2M channel is studied. Its corresponding first- and second-order channel statistics have been investigated and validated by using an experimental MIMO M2M channel sounding campaign.

In C2C communication systems, the transmitter and the receiver are in motion, in this respect the underlying radio channel model differs from the traditional cellular channels. Consequently, new channel models are required for C2C communication systems. For instance, several geometry-based street models have been studied and analyzed in [7–10]. Especially, the T-junction model has widely been investigated by assuming different scattering scenarios. In [7], a geometry-based channel model has been proposed, where scatterers are located in one line. A non-stationary MIMO vehicular-to-vehicular (V2V) channel model based on the T-junction model has been derived in [8]. The proposed channel model takes into account double-bounced scattering from fixed scatterers. To study the statistical properties of the proposed channel model, the Choi-Williams distribution has been used. In [11], a GPS-enabled channel sounding platform for measuring V2V wireless channels under LOS and NLOS propagation conditions has been presented.

In the literature, a number of fundamental channel models with different scatterer distributions, e.g., uniform, Gaussian, Laplacian, and von Mises, have been used to characterize the AOD and AOA. For example, in [12] the author discusses a Gaussian scatterer distribution model by assuming a circular scattering region around a mobile station. It has also been analyzed the spatial and temporal properties of the first arrival path in multipath environments. The authors of [13] and [14] focused on the modeling of narrowband and wideband SISO mobile fading channels for indoor radio propagation environments, respectively. It has been assumed that scatterers are uniformly distributed in the 2D horizontal plane of a room. The

base station is considered as the transmitter while the mobile station is the receiver.

In contrast to [13], in this paper, we propose a new geometric street scattering channel model for outdoor propagation environments, while both the MT and the MR are in motion. The main contribution of this paper is that it presents a geometric street model with an infinite number of scatterers, which are uniformly distributed in rectangles in the form of stripes parallel to both sides of the street. A typical propagation scenario for the proposed model is shown in Fig. A.1, where the buildings and the trees can be considered as scatterers. The analytical expressions for the PDFs of the AOD and the AOA, as well as the transmitter and the receiver Doppler frequencies have been derived. We have also investigated the Doppler PSD and the ACF of the proposed model. To confirm the correctness of the proposed model, the Doppler parameters of the reference model have been compared to those of the measured channel in [11]. The numerical results show that the statistics of the proposed model fit very well to those of the computer simulations.

The rest of this paper is organized as follows. Section II describes the geometric street scattering model. In Section III, the reference channel model is reviewed. We also study the statistical properties of the proposed geometry-based street scattering model, such as the PDFs of the AOD and the AOA. In Section IV, the parameters of a measurement-based model have been computed. The evaluation of the main statistical properties of the proposed model is the topic of Section V. Finally, Section VI provides the conclusion of the paper.

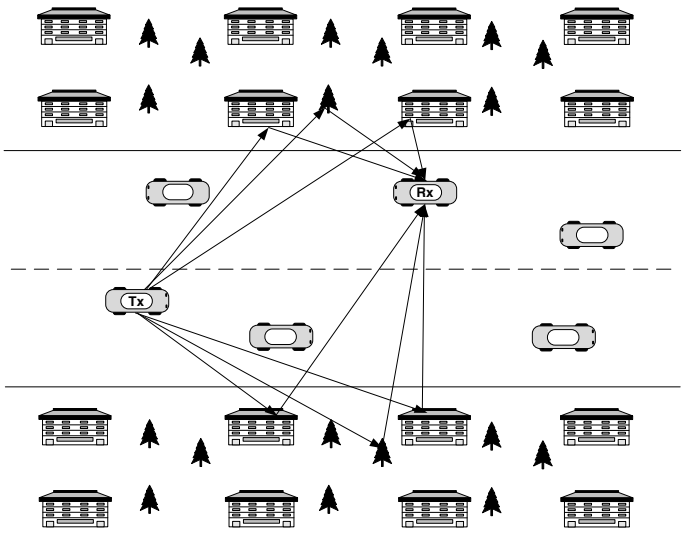

Figure A.1: A typical propagation scenario at a straight street.

II. The Geometric Street Scattering Model

We consider the geometric street scattering model as depicted in Fig. A.2. In our model, the geometric street scattering model describes the scattering environment for an M2M channel, which constitutes the starting point for the derivation of the reference model. We consider rectangle areas at both sides of the street with length A_i $(i = 1,2)$ and width B_i $(i = 1,2)$. The MT and the MR are placed in the street with distance D, denoted by $D = x_R + x_T$. We assume that the MT with coordinates (x_T, y_T), moving with speed v_T in the direction of the x-axis, is communicating with the MR with coordinates (x_R, y_R), moving with speed v_R in the opposite direction of the x-axis. The transmitter (receiver) is located at a distance y_{T_1} (y_{R_1}) from the left-hand side of the street and at a distance y_{T_2} (y_{R_2}) from the right-hand side of the street. The symbols α and β stand for the AOD and the AOA, respectively.

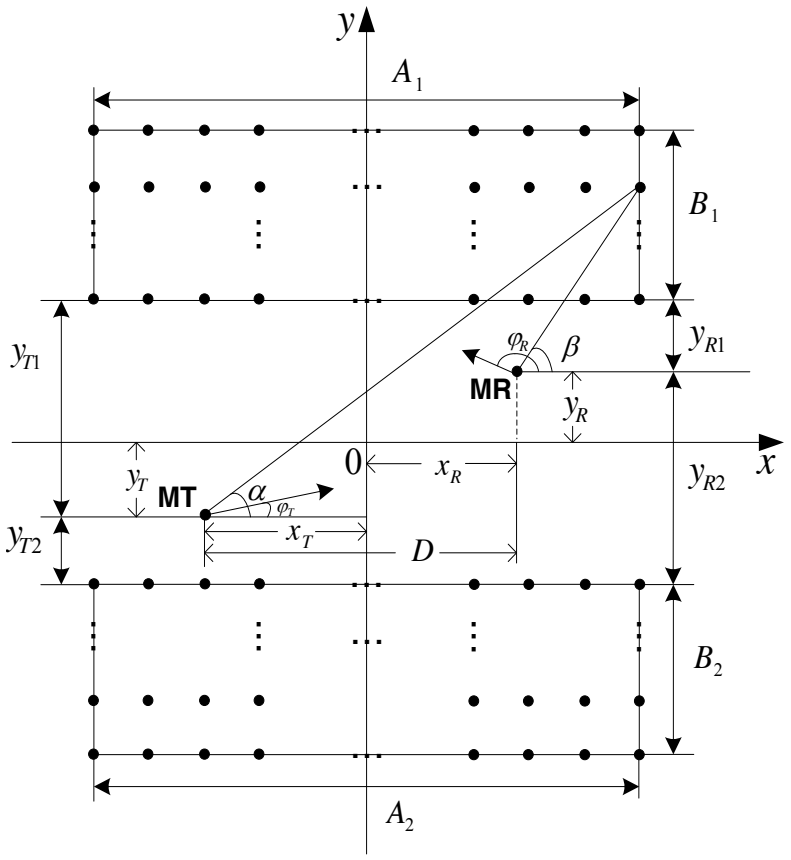

Figure A.2: Geometric street scattering model with local scatterers uniformly distributed in the rectangles at both sides of the street.

III. The Geometric Street Scattering Channel Model and Its Statistical Properties

In this section, we first review the reference channel model of M2M communication systems under LOS and NLOS propagation conditions. Then, we derive the PDFs of the AOD and the AOA. Thereafter, by using the PDFs of the AOD and the AOA, we obtain the PDFs of the transmitter and the receiver Doppler frequencies, as well as the total Doppler frequency, which enables us to analyze the Doppler PSD of the proposed geometric street scattering channel model.

A. Review of the Reference Channel Model

The reference channel model can be modeled by a complex process

$$\mu_\rho(t) = \mu(t) + m(t) \tag{A.1}$$

where $\mu(t)$ denotes the sum of the scattered components and $m(t)$ represents the LOS part. The LOS part of the received signal can generally be described by a complex sinusoid (cisoid) of the form [14]

$$m(t) = \rho e^{j(2\pi f_\rho t + \theta_\rho)}, \tag{A.2}$$

where ρ, f_ρ, and θ_ρ denote the amplitude, the Doppler frequency, and the phase of the LOS part, respectively. If not otherwise stated, then it is supposed that the parameters ρ, f_ρ, and θ_ρ are constant; meaning that the LOS part $m(t)$ is a time-variant deterministic process.

Usually, it is assumed that the real and imaginary part of the scattered component $\mu(t)$ are zero-mean Gaussian processes, each having the variance $\sigma_\mu^2/2$. The absolute value of $\mu_\rho(t)$ in (A.1) leads to the Rice process, i.e., $\xi(t) = |\mu_\rho(t)|$. Under NLOS conditions the Rice process $\xi(t)$ reduces to the Rayleigh process, i.e., $\zeta(t) = |\mu(t)|$ [15].

B. Derivation of the PDFs of the AOD and the AOA

We use boldface letters to denote random variables and normal letters for the values that the corresponding random variable can take. Let us assume that in Fig. A.2 the position of all scatterers in the rectangle is presented by (x,y). The positions of the MT and the MR are denoted by (x_T, y_T) and (x_R, y_R), respectively, each having non-zero positive value. Accordingly, the AOD $\boldsymbol{\alpha}$ and the AOA $\boldsymbol{\beta}$ can be expressed

as

$$\boldsymbol{\alpha} = \begin{cases} \arctan\frac{\boldsymbol{y}+y_T}{\boldsymbol{x}+x_T}, & \text{if } \boldsymbol{x} \geq -x_T, \\ \pi + \arctan\frac{\boldsymbol{y}+y_T}{\boldsymbol{x}+x_T}, & \text{if } \boldsymbol{x} < -x_T \text{ and } \boldsymbol{y} \geq -y_T, \\ -\pi + \arctan\frac{\boldsymbol{y}+y_T}{\boldsymbol{x}+x_T}, & \text{if } \boldsymbol{x} > -x_T \text{ and } \boldsymbol{y} < -y_T, \end{cases} \tag{A.3}$$

$$\boldsymbol{\beta} = \begin{cases} \arctan\frac{\boldsymbol{y}-y_R}{\boldsymbol{x}-x_R}, & \text{if } \boldsymbol{x} \geq x_R \\ \pi + \arctan\frac{\boldsymbol{y}-y_R}{\boldsymbol{x}-x_R}, & \text{if } \boldsymbol{x} < x_R \text{ and } \boldsymbol{y} \geq y_R, \\ -\pi + \arctan\frac{\boldsymbol{y}-y_R}{\boldsymbol{x}-x_R}, & \text{if } \boldsymbol{x} > x_R \text{ and } \boldsymbol{y} < y_R\,. \end{cases} \tag{A.4}$$

For ease of analysis of the AOD and the AOA, we shift the origin of the coordinate system to the positions where the MT and the MR are located in Figs. (A.3a) and in (A.3b), respectively. We introduce new coordinate systems for the MT and the MR, where we have $\boldsymbol{x}' = \boldsymbol{x} + x_T$, $\boldsymbol{y}' = \boldsymbol{y} + y_T$ and $\boldsymbol{x}'' = \boldsymbol{x} - x_R$, $\boldsymbol{y}'' = \boldsymbol{y} - y_R$, respectively.

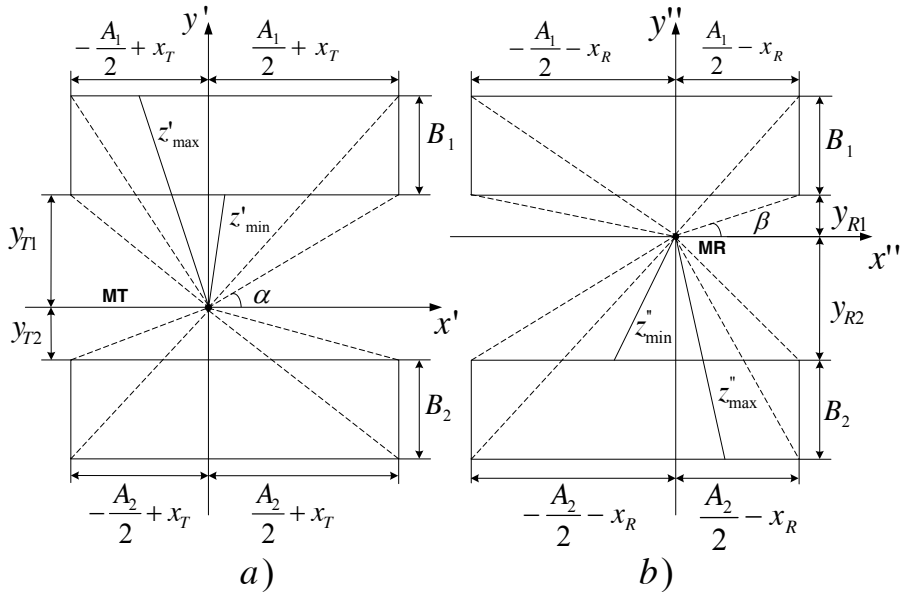

Figure A.3: Geometric street scattering model: Illustrating a) the AOD α and b) the AOA β.

It is mentioned in Section II that all scatterers are uniformly distributed in the rectangle areas at both sides of the street. Hence, the random variables $\boldsymbol{x}'$ and $\boldsymbol{x}''$ are also uniformly distributed over the ranges $[-A_i/2+x_T, A_i/2+x_T]$, $(i=1,2)$ and $[-A_i/2-x_R, A_i/2-x_R]$, $(i=1,2)$, respectively; while $\boldsymbol{y}'$ and $\boldsymbol{y}''$ follow the uniform distribution in the intervals $[y_{T_1}, B_1+y_{T_1}] \cup [-B_2-y_{T_2}, -y_{T_2}]$ and $[y_{R_1}, B_1+y_{R_1}] \cup [-B_2-y_{R_2}, -y_{R_2}]$, respectively. Thus, the densities $p_{\boldsymbol{x}'}(x')$, $p_{\boldsymbol{x}''}(x'')$, $p_{\boldsymbol{y}'}(y')$, and

$p_{\boldsymbol{y}''}(y'')$ of $\boldsymbol{x}'$, $\boldsymbol{x}''$, $\boldsymbol{y}'$, and $\boldsymbol{y}''$, respectively, are given by

$$p_{\boldsymbol{x}'}(x') = \frac{1}{A_i}, \quad \text{if} \quad \boldsymbol{y}' \in I_i,\ i = 1,2, \tag{A.5}$$

$$p_{\boldsymbol{x}''}(x'') = \frac{1}{A_i}, \quad \text{if} \quad \boldsymbol{y}'' \in J_i,\ i = 1,2, \tag{A.6}$$

$$p_{\boldsymbol{y}'}(y') = p_{\boldsymbol{y}''}(y'') = \frac{1}{B_1 + B_2}, \tag{A.7}$$

where $I_1 = [y_{T_1}, B_1 + y_{T_1}]$, $I_2 = [-B_2 - y_{T_2}, -y_{T_2}]$, $J_1 = [y_{R_1},\ B_1 + y_{R_1}]$, and $J_2 = [-B_2 - y_{R_2}, -y_{R_2}]$. Assuming that the random variables $\boldsymbol{x}'$, $\boldsymbol{x}''$, $\boldsymbol{y}'$, and $\boldsymbol{y}''$ are independent, the joint PDFs $p_{\boldsymbol{x}'\boldsymbol{y}'}(x', y') = p_{\boldsymbol{x}'}(x') \cdot p_{\boldsymbol{y}'}(y')$ and $p_{\boldsymbol{x}''\boldsymbol{y}''}(x'', y'') = p_{\boldsymbol{x}''}(x'') \cdot p_{\boldsymbol{y}''}(y'')$ of the random variables $\boldsymbol{x}'$, $\boldsymbol{y}'$ and $\boldsymbol{x}''$, $\boldsymbol{y}''$, respectively, can be expressed as

$$p_{\boldsymbol{x}'\boldsymbol{y}'}(x', y') = \frac{1}{A_i(B_1 + B_2)}, \quad \text{if} \quad \boldsymbol{y}' \in I_i,\ i = 1,2, \tag{A.8}$$

$$p_{\boldsymbol{x}''\boldsymbol{y}''}(x'', y'') = \frac{1}{A_i(B_1 + B_2)}, \quad \text{if} \quad \boldsymbol{y}'' \in J_i,\ i = 1,2. \tag{A.9}$$

The transformation of the Cartesian coordinates (x', y') and (x'', y'') into polar coordinates (z', α) and (z'', β) gives the joint PDFs $p_{\boldsymbol{z}'\boldsymbol{\alpha}}(z', \alpha)$ and $p_{\boldsymbol{z}''\boldsymbol{\beta}}(z'', \beta)$ of $\boldsymbol{z}' = \sqrt{(\boldsymbol{x}'^2 + \boldsymbol{y}'^2)}$ and $\boldsymbol{z}'' = \sqrt{(\boldsymbol{x}''^2 + \boldsymbol{y}''^2)}$ with the corresponding AOD $\boldsymbol{\alpha} = \arctan(\boldsymbol{y}'/\boldsymbol{x}')$ and AOA $\boldsymbol{\beta} = \arctan(\boldsymbol{y}''/\boldsymbol{x}'')$, respectively. Hence, the joint PDFs $p_{\boldsymbol{z}'\boldsymbol{\alpha}}(z', \alpha)$ and $p_{\boldsymbol{z}''\boldsymbol{\beta}}(z'', \beta)$ can be expressed as

$$p_{\boldsymbol{z}'\boldsymbol{\alpha}}(z', \alpha) = \frac{z'}{A_i(B_1 + B_2)}, \quad \text{if} \quad \boldsymbol{y}' \in I_i,\ i = 1,2, \tag{A.10}$$

$$p_{\boldsymbol{z}''\boldsymbol{\beta}}(z'', \beta) = \frac{z''}{A_i(B_1 + B_2)}, \quad \text{if} \quad \boldsymbol{y}'' \in J_i,\ i = 1,2. \tag{A.11}$$

By integrating the joint PDFs $p_{\boldsymbol{z}'\boldsymbol{\alpha}}(z', \alpha)$ and $p_{\boldsymbol{z}''\boldsymbol{\alpha}}(z'', \alpha)$ over z' and z'', respectively, we obtain the PDFs of the AOD $\boldsymbol{\alpha}$ and AOA $\boldsymbol{\beta}$, respectively, as

$$p_{\boldsymbol{\alpha}}(\alpha) = \frac{{z'_{\max}}^2}{2A_i(B_1 + B_2)} - \frac{{z'_{\min}}^2}{2A_i(B_1 + B_2)}, \tag{A.12}$$

$$p_{\boldsymbol{\beta}}(\beta) = \frac{{z''_{\max}}^2}{2A_i(B_1 + B_2)} - \frac{{z''_{\min}}^2}{2A_i(B_1 + B_2)}, \tag{A.13}$$

where $z'_{\max}$, $z'_{\min}$ (see Fig. (A.3a)), $z''_{\max}$, and $z''_{\min}$ (see Fig. (A.3b)) stand for the distance from the origin to the boundaries of the rectangle area.

Using the geometrical relationships, we derive an expression for $z'_{\max}$, $z'_{\min}$, $z''_{\max}$, and $z''_{\min}$ in form of a piecewise function depending on the AOD α and the AOA β,

respectively, and A_i, B_i. The AOD and AOA ranges are separated by dash lines in Figs. (A.3a) and (A.3b), respectively. For brevity, we only present here the final expressions for the PDFs of the AOD $\boldsymbol{\alpha}$ in (A.31) and the AOA $\boldsymbol{\beta}$ in (A.32), which can be found in Appendix A.A.

C. Derivation of the PDFs of the Transmitter and the Receiver Doppler Frequencies

Due to the assumption that the AOD $\boldsymbol{\alpha}$ and the AOA $\boldsymbol{\beta}$ are random variables, it follows that the corresponding transmitter and receiver Doppler frequencies defined by

$$\boldsymbol{f}_T = f_T(\boldsymbol{\alpha}) = f_{T_{\max}} \cos(\boldsymbol{\alpha} - \varphi_T), \tag{A.14}$$

$$\boldsymbol{f}_R = f_R(\boldsymbol{\beta}) = f_{R_{\max}} \cos(\boldsymbol{\beta} - \varphi_R), \tag{A.15}$$

are also random variables. The quantities $f_{T_{\max}}$ and $f_{R_{\max}}$ stand for the maximum Doppler frequencies of the transmitter and receiver, respectively, while φ_T, and φ_R denote the angles between the direction of the transmitter and receiver w.r.t the x-axis, respectively.

The PDFs of the Doppler frequencies $\boldsymbol{f}_T$ and $\boldsymbol{f}_R$, denoted by $p_{\boldsymbol{f}_T}(f_T)$ and $p_{\boldsymbol{f}_R}(f_R)$, respectively, can easily be computed by using the fundamental theorem of transformation of random variables [16]. Consequently, the PDFs $p_{\boldsymbol{f}_T}(f_T)$ and $p_{\boldsymbol{f}_R}(f_R)$ can be defined as

$$p_{\boldsymbol{f}_T}(f_T) = \sum_{l=1}^{m} \frac{p_{\boldsymbol{\alpha}}(\alpha)}{|\frac{\partial}{\partial \alpha}|_{\alpha=\alpha_l}} \tag{A.16}$$

$$p_{\boldsymbol{f}_R}(f_R) = \sum_{u=1}^{v} \frac{p_{\boldsymbol{\beta}}(\beta)}{|\frac{\partial}{\partial \beta}|_{\beta=\beta_u}}, \tag{A.17}$$

where m and v are the number of the solutions of the equations in (A.16) and (A.17), respectively, within the interval $[-\pi, \pi)$. If $f_T \leq |f_{T_{\max}}|$ and $f_R \leq |f_{R_{\max}}|$, we find two real-valued solutions within the interval, which are known as

$$\alpha_1 = -\alpha_2 = \arccos(\frac{f_T}{f_{T_{\max}}}) + \varphi_T, \tag{A.18}$$

$$\beta_1 = -\beta_2 = \arccos(\frac{f_R}{f_{R_{\max}}}) + \varphi_R, \tag{A.19}$$

so that $m = 2$ and $v = 2$. After some mathematical computations and by using (A.14)-(A.19), we find the following results for the PDFs $p_{\boldsymbol{f}_T}(f_T)$ and $p_{\boldsymbol{f}_R}(f_R)$

$$p_{\boldsymbol{f}_T}(f_T) = \frac{p_{\boldsymbol{\alpha}}(\alpha_1) + p_{\boldsymbol{\alpha}}(\alpha_2)}{\sqrt{f_{T_{\max}}^2 - f_T^2}} \, |_{\alpha_1=-\alpha_2}, \tag{A.20}$$

$$p_{\boldsymbol{f}_R}(f_R) = \frac{p_{\boldsymbol{\beta}}(\beta_1)+p_{\boldsymbol{\beta}}(\beta_2)}{\sqrt{f_{R_{\max}}^2 - f_R^2}} \,|_{\beta_1=-\beta_2}\,. \tag{A.21}$$

The final expressions for the densities $p_{\boldsymbol{f}_T}(f_T)$ [see (A.33)] and $p_{\boldsymbol{f}_R}(f_R)$ [see (A.34)] are given in Appendix A.A.

Now, we introduce the total Doppler frequency, defined by $\boldsymbol{f} = \boldsymbol{f}_T + \boldsymbol{f}_R$, of the geometric street scattering model. Consequently, the PDF $p_{\boldsymbol{f}}(f)$ of the sum $\boldsymbol{f} = \boldsymbol{f}_T + \boldsymbol{f}_R$ of two independent random variables, $\boldsymbol{f}_T$ and $\boldsymbol{f}_R$ is equal to the convolution of their densities. To obtain the PDF $p_{\boldsymbol{f}}(f)$ of $\boldsymbol{f}$ we use the characteristic functions $\Phi_{\boldsymbol{f}_T}(\omega)$ and $\Phi_{\boldsymbol{f}_R}(\omega)$ of $\boldsymbol{f}_T$ and $\boldsymbol{f}_R$, respectively, which are defined as

$$\Phi_{\boldsymbol{f}_T}(\omega) = E\left\{e^{j\omega \boldsymbol{f}_T}\right\} = \int_{-\infty}^{\infty} p_{\boldsymbol{f}_T}(f_T) e^{j\omega f_T} df_T\,, \tag{A.22}$$

$$\Phi_{\boldsymbol{f}_R}(\omega) = E\left\{e^{j\omega \boldsymbol{f}_R}\right\} = \int_{-\infty}^{\infty} p_{\boldsymbol{f}_R}(f_R) e^{j\omega f_R} df_R\,. \tag{A.23}$$

By using (A.22) and (A.23), we can find the characteristic function $\Phi_{\boldsymbol{f}}(\omega)$ of the total Doppler frequency $\boldsymbol{f}$ by the product of two characteristic functions as

$$\Phi_{\boldsymbol{f}}(\omega) = \Phi_{\boldsymbol{f}_T}(\omega) \cdot \Phi_{\boldsymbol{f}_R}(\omega)\,. \tag{A.24}$$

Consequently, by using the Fourier transform inversion formula for (A.24), we can derive the PDF $p_{\boldsymbol{f}}(f)$ of $\boldsymbol{f}$ as

$$p_{\boldsymbol{f}}(f) = \frac{1}{2\pi} \int_{-\infty}^{\infty} \Phi_{\boldsymbol{f}}(\omega) e^{-j\omega f} d\omega\,. \tag{A.25}$$

Since no closed-form solution exists for the PDF $p_{\boldsymbol{f}}(f)$ in (A.25), this integral has to be solved numerically.

D. Derivation of the Doppler PSD and the ACF

The Doppler PSD $S_{\mu_\rho\mu_\rho}(f)$ of the process $\mu_\rho(t)$ in (A.1) can be presented as,

$$S_{\mu_\rho\mu_\rho}(f) = S_{\mu\mu}(f) + \rho^2 \delta(f - f_\rho) \tag{A.26}$$

which is the sum of the Doppler PSD $S_{\mu\mu}(f)$ of $\mu(t)$ and a weighted delta function at $f = f_\rho$. In our model, we consider that the number of scatterers is infinite; therefore, the Doppler PSD $S_{\mu\mu}(f)$ of the scattered component $\mu(t)$ is continuous. According to [15], the mean power within an infinitesimal frequency interval

df can be represented by $S_{\mu\mu}(f)df$. Therefore, due to $\int_{-\infty}^{\infty} S_{\mu\mu}(f)df = \sigma_\mu^2$ and $\int_{-\infty}^{\infty} p_{\boldsymbol{f}}(f)df = 1$, it follows the relation

$$S_{\mu\mu}(f) = \sigma_\mu^2 p_{\boldsymbol{f}}(f). \tag{A.27}$$

By taking (A.27) into account and using (A.31), (A.32), (A.33), (A.34), and (A.25) we compute the Doppler PSD $S_{\mu\mu}(f)$ of $\mu(t)$. Thus, the Doppler PSD $S_{\mu_\rho\mu_\rho}(f)$ of $\mu_\rho(t)$ can easily be derived by substituting (A.27) into (A.26).

From the $S_{\mu\mu}(f)$, we can directly compute the ACF of the scattered components $\mu(t)$ by taking the inverse Fourier transform of the Doppler PSD $S_{\mu\mu}(f)$, i.e., $r_{\mu\mu}(\tau) = \int_{-\infty}^{\infty} S_{\mu\mu}(f)e^{j2\pi f\tau}df$. Consequently, we can express the ACF $r_{\mu_\rho\mu_\rho}(\tau)$ in terms of the ACF $r_{\mu\mu}(\tau)$ of $\mu(t)$ as follows

$$r_{\mu_\rho\mu_\rho}(\tau) = r_{\mu\mu}(\tau) + \rho^2 e^{j2\pi f_\rho \tau}. \tag{A.28}$$

IV. Measurement-Based Model Parameters

The objective of this section is to compute the model parameters A_i, B_i, y_{Ti}, y_{Ri}, $(i = 1,2)$, x_R, x_T, $f_{T_{\max}}$, and $f_{R_{\max}}$ such that the average Doppler shift $B^{(1)}_{\mu_\rho\mu_\rho}$ and the Doppler spread $B^{(2)}_{\mu_\rho\mu_\rho}$ of the reference model are close to those $\left(B^{\star(1)}_{\mu_\rho\mu_\rho}\right.$ and $\left.B^{\star(2)}_{\mu_\rho\mu_\rho}\right)$ of the measured channel reported in [11]. To solve this parameter computation problem, we compute the model parameters such that the following errors

$$E_{B^{(1)}_{\mu_\rho\mu_\rho}} = \left|B^{\star(1)}_{\mu_\rho\mu_\rho} - B^{(1)}_{\mu_\rho\mu_\rho}\right| \tag{A.29}$$

$$E_{B^{(2)}_{\mu_\rho\mu_\rho}} = \left|B^{\star(2)}_{\mu_\rho\mu_\rho} - B^{(2)}_{\mu_\rho\mu_\rho}\right| \tag{A.30}$$

become a minimum. Finally, measurement-based model parameters and the corresponding Doppler parameters are listed in Table A.1.

V. Numerical Results

In this section, we will discuss the main theoretical results by evaluating the Doppler PSD and the ACF of the proposed model. We consider a rectangle area at both sides of the street with length $A_1 = A_2 = 200$ m and width $B_1 = B_2 = 40$ m as our outdoor street model. All theoretical results have been obtained by choosing $\sigma^2_{\mu_\rho} = \sigma^2_\mu + \rho^2 = 1$, $f_\rho = 65$ Hz, $\theta_\rho = 0^\circ$, $\varphi_T = 0^\circ$, $\varphi_R = 180^\circ$, and $f_{\max} = 182$ Hz. The Rice factor $c_R = \rho^2/\sigma^2_\mu$ was chosen from the set $\{0,2,4\}$.

The theoretical results for the Doppler PSD $S_{\mu\mu}(f)$ in (A.27) of the channel's scattered component $\mu(t)$ are presented in Figs. A.4 and A.5 for the different length

Table A.1: Measurement-based parameters of the geometrical street scattering channel model and its Doppler statistics.

Model parameters	**Propagation Environment**		
	Urban LOS	**Urban NLOS**	**Rural LOS**
A_1 (A_2) (m)	993 (992)	1027 (1007)	1014 (957)
B_1 (B_2) (m)	50 (50)	51 (50)	5 (5)
$f_{T_{\max}}$ $(f_{R_{\max}})$ (Hz)	165 (165)	144 (164)	523 (574)
x_T (x_R) (m)	101 (103)	109 (169)	51 (51)
y_{T1} (y_{T2}) (m)	12 (8)	13 (8)	12 (8)
y_{R1} (y_{R2}) (m)	8 (12)	8 (12)	8 (12)
ρ^2	0.8	-	0.8
f_ρ (Hz)	65	-	66
σ_μ^2	0.2	-	0.2
Measured average Doppler shift $B^{\star(1)}_{\mu_\rho\mu_\rho}$ (Hz)	-20 [11]	103 [11]	201 [11]
Theoretical average Doppler shift $B^{(1)}_{\mu_\rho\mu_\rho}$ (Hz)	-20	103	201

Model parameters	**Propagation Environment**		
	Urban LOS	**Urban NLOS**	**Rural LOS**
A_1 (A_2) (m)	3814 (3446)	418 (421)	1206 (1399)
B_1 (B_2) (m)	46 (43)	51 (47)	5 (5)
$f_{T_{\max}}$ $(f_{R_{\max}})$ (Hz)	164 (153)	152 (162)	482 (581)
x_T (x_R) (m)	105 (93)	209 (386)	51 (52)
y_{T1} (y_{T2}) (m)	12 (8)	3 (12)	12 (8)
y_{R1} (y_{R2}) (m)	7 (12)	7 (8)	8 (12)
ρ^2	0.9	-	0.8
f_ρ (Hz)	59	-	67
σ_μ^2	0.2	-	0.2
Measured Doppler spread $B^{\star(2)}_{\mu_\rho\mu_\rho}$ (Hz)	341 [11]	298 [11]	782 [11]
Theoretical Doppler spread $B^{(2)}_{\mu_\rho\mu_\rho}$ (Hz)	340.9	298	780

and width of the rectangles at both sides of the street. Figure A.4 illustrates that by increasing the length $A_i,\ (i=1,2)$, the shape of the Doppler PSD at $f>0$ becomes a U shape. The Doppler PSD $S_{\mu\mu}$ for different values of the area width $B_i,\ (i=1,2)$

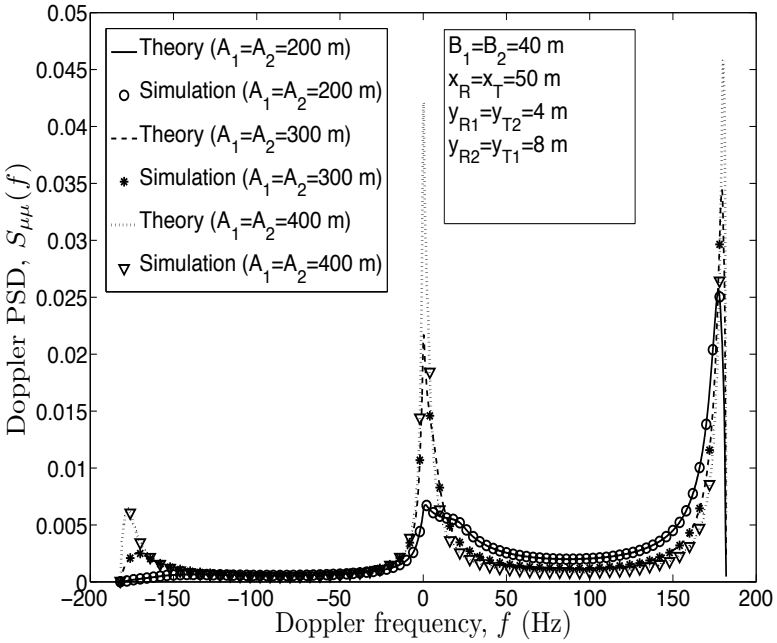

Figure A.4: Doppler PSD $S_{\mu\mu}(f)$ of $\mu(t)$ for different values of the area length $A_1=A_2$ ($B_1=B_2=40$ m, $x_R=x_T=50$ m, $y_{R1}=y_{T2}=4$ m, and $y_{R2}=y_{T1}=8$ m).

are demonstrated in Fig. A.5. It shows that for different B_i values, the Doppler PSD gets its maximum peaks at $f = f_{\max}$. The shape of the Doppler PSD resembles a Gaussian shape when the length of B_i is very large.

The theoretical results demonstrated in Figs. A.4 and A.5 are also confirmed by simulations. In the simulation, we generate the scatterers, which are uniformly randomly distributed in the rectangles. The locations of the scatterers have been determined by outcomes of a random generator with uniform distribution in the intervals $[-A_i/2+x_T, A_i/2+x_T]$, $(i=1,2)$ ($[-A_i/2-x_R, A_i/2-x_R]$, $(i=1,2)$) and $[y_{T_1}, B_1+y_{T_1}]\cup[-B_2-y_{T_2}, -y_{T_2}]$ ($[y_{R_1}, B_1+y_{R_1}]\cup[-B_2-y_{R_2}, -y_{R_2}]$). By using (A.3), (A.4), (A.14), and (A.15), we can obtained the densities of the transmitter (receiver) Doppler frequencies. Thereafter, we can find the total Doppler frequencies, i.e., $f=f_T+f_R$. Finally, we can numerically compute the Doppler PSD by means of (A.27).

Figure A.6 shows the absolute value of the ACF $r_{\mu_\rho\mu_\rho}(\tau)$ of the process $\mu_\rho(t)$ by considering different values for the Rice factor c_R. As shown in Fig. A.6, under NLOS condition ($c_R=0$) the curve of the ACF fluctuates with less peaks by gradually decreasing while the time lag increases. The obtained theoretical results in Fig.

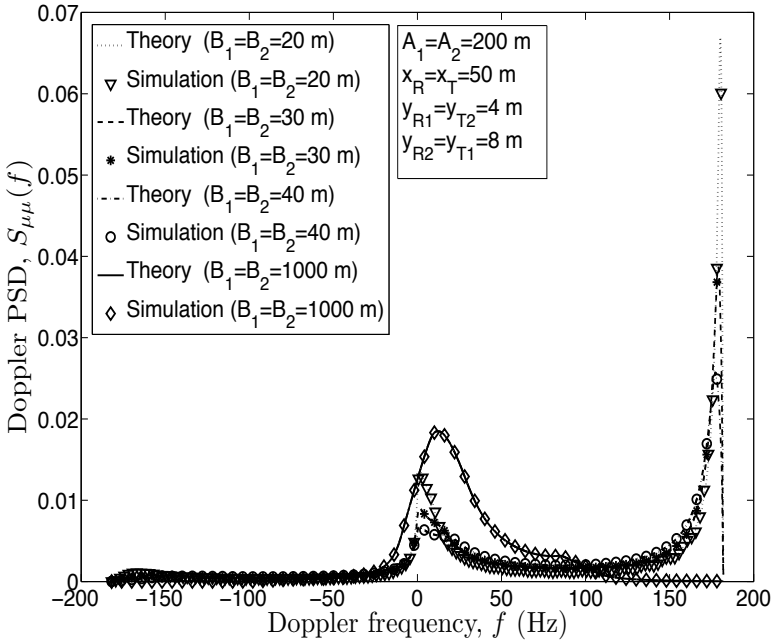

Figure A.5: Doppler PSD $S_{\mu\mu}(f)$ of $\mu(t)$ for different values of the area width $B_1 = B_2$ ($A_1 = A_2 = 200$ m, $x_R = x_T = 50$ m, $y_{R1} = y_{T2} = 4$ m, and $y_{R2} = y_{T1} = 8$ m).

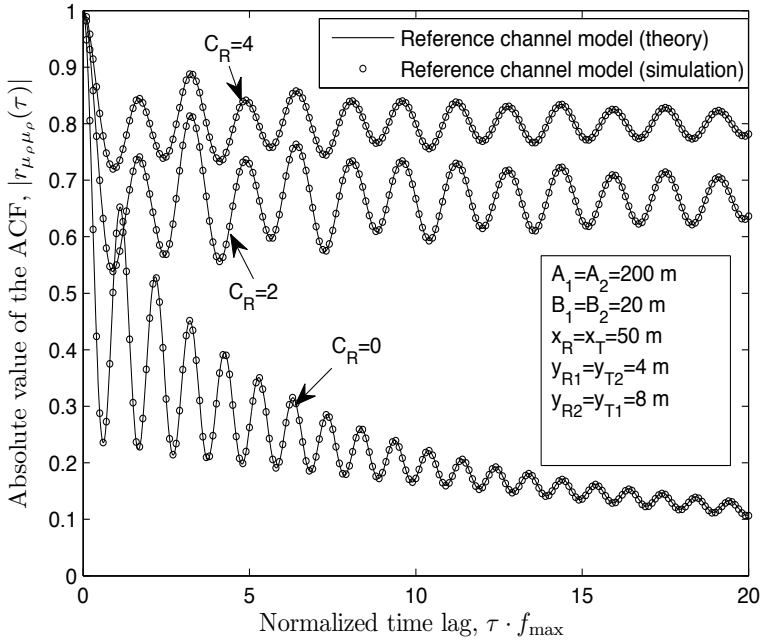

Figure A.6: The absolute value of the ACF $r_{\mu_\rho\mu_\rho}(\tau)$ of the reference channel model ($A_1 = A_2 = 200$ m, $B_1 = B_2 = 20$ m, $x_R = x_T = 50$ m, $y_{R1} = y_{T2} = 4$ m, and $y_{R2} = y_{T1} = 8$ m).

A.6 have also been confirmed by computer simulations.

VI. Conclusion

We designed the geometric street scattering channel model with local scatterers, which are uniformly distributed in the rectangles in the form of stripes parallel to both sides of the street. We have derived analytical expressions for the PDFs of the AOD (AOA) and the transmitter (receiver) Doppler frequencies. By obtaining the PDF of the total Doppler frequency, we have numerically computed the Doppler PSD and the ACF of the proposed geometric street scattering model. For the different size of scattering ranges we have studied the Doppler PSD of the proposed model. We have also validated our model by fitting the Doppler parameters of the reference model to those of the measured one. Numerical results show that the theoretical results of the proposed model fit very well to the computer simulations. To design an efficient C2C channel model, the properties of the wireless multipath environments are of great importance. Therefore, the distribution behavior of the scatterers and scattering regions play a key role in the design of future C2C communication systems.

APPENDIX A.A

In this appendix, we provide the final results for the PDFs of the AOD $\boldsymbol{\alpha}$ and the AOA $\boldsymbol{\beta}$, as well as the transmitter and the receiver Doppler frequencies $\boldsymbol{f}_T$ and $\boldsymbol{f}_R$, respectively.

THE FINAL EXPRESSIONS FOR THE PDFS OF THE AOD $\boldsymbol{\alpha}$ AND THE AOA $\boldsymbol{\beta}$

$$p_{\boldsymbol{\alpha}}(\alpha)=\begin{cases}\frac{(A_1+2x_T)^2}{4A_1g_1(\alpha)}-\frac{y_{T1}^2}{A_1g_2(\alpha)}, & \text{if } \arctan\frac{2y_{T1}}{A_1+2x_T}<\alpha\leq\arctan\frac{2B_1+2y_{T1}}{A_1+2x_T}\\ \frac{(B_1+y_{T1})^2}{A_1g_2(\alpha)}-\frac{y_{T1}^2}{A_1g_2(\alpha)}, & \text{if } \arctan\frac{2B_1+2y_{T1}}{A_1+2x_T}<\alpha\leq\pi-\arctan\frac{2B_1+2y_{T1}}{A_1-2x_T}\\ \frac{(A_1-2x_T)^2}{4A_1g_1(\alpha)}-\frac{y_{T1}^2}{A_1g_2(\alpha)}, & \text{if } \pi-\arctan\frac{2B_1+2y_{T1}}{A_1-2x_T}<\alpha\leq\pi-\arctan\frac{2y_{T1}}{A_1-2x_T}\\ \frac{(A_2-2x_T)^2}{4A_2g_1(\alpha)}-\frac{y_{T2}^2}{A_2g_2(\alpha)}, & \text{if } -\pi+\arctan\frac{2y_{T2}}{A_2-2x_T}<\alpha\leq-\pi+\arctan\frac{2B_2+2y_{T2}}{A_2-2x_T}\\ \frac{(B_2+y_{T2})^2}{A_2g_2(\alpha)}-\frac{y_{T2}^2}{A_2g_2(\alpha)}, & \text{if } -\pi+\arctan\frac{B_2+2y_{T2}}{A_2-2x_T}<\alpha\leq-\arctan\frac{2B_2+2y_{T2}}{A_2+2x_T}\\ \frac{(A_2+2x_T)^2}{4A_2g_1(\alpha)}-\frac{y_{T2}^2}{A_2g_2(\alpha)}, & \text{if } -\arctan\frac{2B_2+2y_{T2}}{A_2+2x_T}<\alpha\leq-\arctan\frac{2y_{T2}}{A_2+2x_T}\end{cases} \tag{A.31}$$

where $g_1(\alpha)=2(B_1+B_2)\cos^2(\alpha)$ and $g_2(\alpha)=2(B_1+B_2)\sin^2(\alpha)$.

$$p_{\boldsymbol{\beta}}(\beta)=\begin{cases}\frac{(A_1-2x_R)^2}{4A_1g_1(\beta)}-\frac{y_{R1}^2}{A_1g_2(\beta)}, & \text{if } \arctan\frac{2y_{R1}}{A_1-2x_R}<\beta\leq\arctan\frac{2B_1+2y_{R1}}{A_1-2x_R}\\ \frac{(B_1+y_{R1})^2}{A_1g_2(\beta)}-\frac{y_{R1}^2}{A_1g_2(\beta)}, & \text{if } \arctan\frac{2B_1+2y_{R1}}{A_1-2x_R}<\beta\leq\pi-\arctan\frac{2B_1+2y_{R1}}{A_1+2x_R}\\ \frac{(A_1+2x_R)^2}{4A_1g_1(\beta)}-\frac{y_{R1}^2}{A_1g_2(\beta)}, & \text{if } \pi-\arctan\frac{2B_1+2y_{R1}}{A_1+2x_R}<\beta\leq\pi-\arctan\frac{2y_{R1}}{A_1+2x_R}\\ \frac{(A_2+2x_R)^2}{4A_2g_1(\beta)}-\frac{y_{R2}^2}{A_2g_2(\beta)}, & \text{if } -\pi+\arctan\frac{2y_{R2}}{A_2+2x_R}<\beta\leq-\pi+\arctan\frac{2B_2+2y_{R2}}{A_2+2x_R}\\ \frac{(B_2+y_{R2})^2}{A_2g_2(\beta)}-\frac{y_{R2}^2}{A_2g_2(\beta)}, & \text{if } -\pi+\arctan\frac{B_2+2y_{R2}}{A_2+2x_R}<\beta\leq-\arctan\frac{2B_2+2y_{R2}}{A_2-2x_R}\\ \frac{(A_2-2x_R)^2}{4A_2g_1(\beta)}-\frac{y_{R2}^2}{A_2g_2(\beta)}, & \text{if } -\arctan\frac{2B_2+2y_{R2}}{A_2-2x_R}<\beta\leq-\arctan\frac{2y_{R2}}{A_2-2x_R}\end{cases} \tag{A.32}$$

where $g_1(\beta)=2(B_1+B_2)\cos^2(\beta)$ and $g_2(\beta)=2(B_1+B_2)\sin^2(\beta)$.

THE FINAL EXPRESSIONS FOR THE PDFS OF THE TRANSMITTER AND THE RECEIVER DOPPLER FREQUENCIES

$$p_{\boldsymbol{f}_T}(f_T)=\begin{cases}
\frac{A_1}{D}\left[(G_{T2}^k)^2F_T-4y_{T2}^2f_T^2\right]f_{T_{\max}}^2, \\
\qquad \text{if } -\frac{G_{T2}^k f_{T_{\max}}}{\sqrt{(G_{T2}^k)^2+4y_{T2}^2}}<(-1)^k f_T\le -\frac{G_{T1}^k f_{T_{\max}}}{\sqrt{(G_{T1}^k)^2+4y_{T1}^2}}, k=0,1 \\
\frac{1}{D}\left[(A_2(G_{T1}^k)^2+A_1(G_{T2}^k)^2)F_T-4C_Tf_T^2\right]f_{T_{\max}}^2, \\
\qquad \text{if } -\frac{(G_{T1}^k) f_{T_{\max}}}{\sqrt{(G_{T1}^k)^2+4y_{T1}^2}}<(-1)^k f_T\le -\frac{(G_{T2}^k) f_{T_{\max}}}{\sqrt{(G_{T2}^k)^2+4E_{T2}^2}}, k=0,1 \\
\frac{1}{D}\left[(A_2F_T(G_{T1}^k)^2-4f_T^2(C_T-A_1E_{T2}^2)\right]f_{T_{\max}}^2, \\
\qquad \text{if} -\frac{G_{T2}^k f_{T_{\max}}}{\sqrt{(G_{T2}^k)^2+4E_{T2}^2}}<(-1)^k f_T\le -\frac{G_{T1}^k f_{T_{\max}}}{\sqrt{(G_{T1}^k)^2+4E_{T1}^2}}, k=0,1 \\
\frac{1}{F_T^{3/2}}\left[(A_2E_{T1}^2+A_1E_{T2}^2)-C_T\right]f_{T_{\max}}^2, \\
\qquad \text{if } -\frac{\left(\frac{A_1}{2}-x_T\right)f_{T_{\max}}}{\sqrt{\left(\frac{A_1}{2}-x_T\right)^2+E_{T1}^2}}<f_T\le\frac{\left(\frac{A_1}{2}+x_T\right)f_{T_{\max}}}{\sqrt{\left(\frac{A_1}{2}+x_T\right)^2+E_{T1}^2}},
\end{cases} \tag{A.33}$$

where $C_T=A_2y_{T1}^2+A_1y_{T2}^2$, $D=8A_1A_2(B_1+B_2)f_T^2(f_{T_{\max}}^2-f_T^2)^{3/2}$, $E_{T1}=B_1+y_{T1}$, $E_{T2}=B_2+y_{T2}$, $F_T=(f_{T_{\max}}^2-f_T^2)$, $G_{T1}^k=A_1-(-1)^k2x_T$, and $G_{T2}^k=A_2-(-1)^k2x_T$.

$$p_{\boldsymbol{f}_R}(f_R)=\begin{cases}
\frac{A_2}{D}\left[(G_{R1}^k)^2F_R-4y_{R1}^2f_R^2\right]f_{R_{\max}}^2, \\
\qquad \text{if } -\frac{G_{R1}^k f_{R_{\max}}}{\sqrt{(G_{R1}^k)^2+4y_{R1}^2}}<(-1)^k f_R\le -\frac{G_{R2}^k f_{R_{\max}}}{\sqrt{(G_{R2}^k)^2+4y_{R2}^2}}, k=0,1 \\
\frac{1}{D}\left[(A_2(G_{R1}^k)^2+A_1(G_{R2}^k)^2)F_R-4C_Rf_R^2\right]f_{R_{\max}}^2, \\
\qquad \text{if } -\frac{(G_{R2}^k) f_{R_{\max}}}{\sqrt{(G_{R2}^k)^2+4y_{R1}^2}}<(-1)^k f_R\le -\frac{G_{R1}^k f_{R_{\max}}}{\sqrt{(G_{R1}^k)^2+4E_{R1}^2}}, k=0,1 \\
\frac{1}{D}\left[4f_R^2(A_2E_{R1}^2-C_R)-A_1F_R(G_{R2}^k)^2\right]f_{R_{\max}}^2, \\
\qquad \text{if} -\frac{G_{R1}^k f_{R_{\max}}}{\sqrt{(G_{R1}^k)^2+E_{R1}^2}}<(-1)^k f_R\le -\frac{G_{R2}^k f_{R_{\max}}}{\sqrt{(G_{R2}^k)^2+4E_{R2}^2}}, k=0,1 \\
\frac{4f_R^2}{D}\left[(A_2E_{R1}^2+A_1E_{R2}^2)-C_R\right]f_{R_{\max}}^2, \\
\qquad \text{if } -\frac{\left(\frac{A_2}{2}-x_R\right)f_{R_{\max}}}{\sqrt{\left(\frac{A_1}{2}-x_R\right)^2+E_{R2}^2}}<f_R\le\frac{\left(\frac{A_2}{2}+x_R\right)f_{R_{\max}}}{\sqrt{\left(\frac{A_2}{2}+x_R\right)^2+E_{R2}^2}},
\end{cases} \tag{A.34}$$

where $C_R=A_2y_{R1}^2+A_1y_{R2}^2$, $D=8A_1A_2(B_1+B_2)f_R^2(f_{R_{\max}}^2-f_R^2)^{3/2}$, $E_{R1}=B_1+y_{R1}$, $E_{R2}=B_2+y_{R2}$, $F_R=(f_{R_{\max}}^2-f_R^2)$, $G_{R1}^k=A_1-(-1)^k2x_R$, and $G_{R2}^k=A_2-(-1)^k2x_R$.

REFERENCES

[1] F. Qu, F.-Y. Wang, and L. Yang, "Intelligent transportation spaces: vehicles, traffic, communications, and beyond," *IEEE Commun. Magazine*, vol. 48, no. 11, pp. 136–142, Nov. 2010.

[2] M. Pätzold and B. O. Hogstad, "A space-time channel simulator for MIMO channels based on the geometrical one-ring scattering model," in *Proc. 60th IEEE Semiannual Veh. Technol. Conf., VTC 2004-Fall. Los Angeles, CA, USA*, vol. 1, Sept. 2004, pp. 144–149.

[3] M. Pätzold, B. O. Hogstad, N. Youssef, and D. Kim, "A MIMO mobile-to-mobile channel model: Part I — the reference model," in *Proc. 16th IEEE Int. Symp. on Personal, Indoor and Mobile Radio Communications, PIMRC 2005. Berlin, Germany*, Sept. 2005, pp. 573–578.

[4] M. Pätzold and B. O. Hogstad, "A wideband MIMO channel model derived from the geometrical elliptical scattering model," *Wireless Communications and Mobile Computing*, vol. 8, pp. 597–605, May 2008.

[5] A. S. Akki and F. Haber, "A statistical model of mobile-to-mobile land communication channel," *IEEE Trans. Veh. Technol.*, vol. 35, no. 1, pp. 2–7, Feb. 1986.

[6] A. G. Zajić, G. L. Stüber, T. G. Pratt, and S. Nguyen, "Wideband mimo mobile-to-mobile channels: geometry-based statistical modeling with experimental verification," *IEEE Trans. Veh. Technol.*, vol. 58, no. 2, pp. 517–534, Feb. 2009.

[7] A. Chelli and M. Pätzold, "A MIMO mobile-to-mobile channel model derived from a geometric street scattering model," in *Proc. 4th IEEE International Symposium on Wireless Communication Systems, ISWCS 2007*. Trondheim, Norway, Oct. 2007, pp. 792–797.

[8] ——, "A non-stationary MIMO vehicle-to-vehicle channel model based on the geometrical T-junction model," in *Proc. International Conference on Wireless Communications and Signal Processing, WCSP 2009*. Nanjing, China, Nov. 2009.

[9] C. Wei, H. Zhiyi, X. Tao, and Z. Wei, "A novel isotropic scatter distribution wideband MIMO M2M fading channel model," in *Proc. 7th Annual Commu-*

nication Networks and Services Research Conference, CNSR'09., May 2009, pp. 443 –445.

[10] X. Cheng, C.-X. Wang, D. I. Laurenson, S. Salous, and A. V. Vasilakos, "An adaptive geometry-based stochastic model for non-isotropic MIMO mobile-to-mobile channels," *IEEE Trans. Wireless Commun.*, vol. 8, no. 9, pp. 4824–4835, Sep. 2009.

[11] I. Tan, T. Wanbin, K. Laberteaux, and A. Bahai, "Measurement and analysis of wireless channel impairments in DSRC vehicular communications," in *Proc. IEEE ICC'08*, May 2008, pp. 4882–4888.

[12] S. H. Kong, "TOA and AOD statistics for down link Gaussian scatterer distribution model," *IEEE Trans. Wireless Commun.*, vol. 8, no. 5, pp. 2609–2617, May 2009.

[13] Y. Ma and M. Pätzold, "Modelling and statistical characterization of wideband indoor radio propagation channels," in *Proc. International Congress on Ultra Modern Telecommunications and Control Systems and Workshops, ICUMT 2010*. Moscow, Russia, Oct. 2010, pp. 777–783.

[14] ——, "Design and simulation of narrowband indoor radio propagation channels under LOS and NLOS propagation conditions," in *Proc. IEEE 71st Vehicular Technology Conference, VTC2010-Spring*. Taipei, Taiwan, May 2010.

[15] M. Pätzold, *Mobile Fading Channels*. Chichester: John Wiley & Sons, 2002.

[16] A. Papoulis and S. U. Pillai, *Probability, Random Variables and Stochastic Processes*, 4th ed. New York: McGraw-Hill, 2002.

Appendix B

Paper II

Title:	Design of Wideband MIMO Car-to-Car Channel Models Based on the Geometrical Street Scattering Model
Authors:	**Nurilla Avazov** and Matthias Pätzold
Affiliation:	University of Agder, Faculty of Engineering and Science, P. O. Box 509, NO-4898 Grimstad, Norway
Journal:	*Special Issue: Modelling and Simulation in Engineering*, vol. 2012, Hindawi, 2012, ISSN:1687-5605 (Online).

Design of Wideband MIMO Car-to-Car Channel Models Based on the Geometrical Street Scattering Model

Nurilla Avazov and Matthias Pätzold
Faculty of Engineering and Science, University of Agder,
P.O. Box 509, NO-4898 Grimstad, Norway
E-mails: {nurilla.k.avazov, matthias.paetzold}@uia.no

Abstract — **In this paper, we propose a wideband multiple-input multiple-output (MIMO) car-to-car (C2C) channel model based on the geometrical street scattering model. Starting from the geometrical model, a MIMO reference channel model is derived under the assumption of single-bounce scattering in line-of-sight (LOS) and non-LOS (NLOS) propagation environments. The proposed channel model assumes an infinite number of scatterers, which are uniformly distributed in two rectangular areas located on both sides of the street. Analytical solutions are presented for the space-time-frequency cross-correlation function (STF-CCF), the two-dimensional (2D) space CCF, the time-frequency CCF (TF-CCF), the temporal autocorrelation function (ACF), and the frequency correlation function (FCF). An efficient sum-of-cisoids (SOC) channel simulator is derived from the reference model. It is shown that the temporal ACF and the FCF of the SOC channel simulator fit very well to the corresponding correlation functions of the reference model. To validate the proposed channel model, the mean Doppler shift and the Doppler spread of the reference model have been matched to real-world measurement data. The comparison results demonstrate an excellent agreement between theory and measurements, which confirms the validity of the derived reference model. The proposed geometry-based channel simulator allows us to study the effect of nearby street scatterers on the performance of C2C communication systems.**

I. INTRODUCTION

C2C communications is an emerging technology, which receives considerable attention due to new traffic telematic applications that improve the efficiency of traffic flow and reduce the number of road accidents [1]. The development of C2C communication technologies is supported in Europe by respected organizations, such as the European Road Transport Telematics Implementation Coordinating Organization (ERTICO) [2] and the C2C Communication Consortium (C2C-CC) [3]. In this context, a large number of research projects focussing on C2C communications are currently being carried out throughout the world.

In C2C communication systems, the underlying radio channel differs from traditional fixed-to-mobile and mobile-to-fixed channels in the way that both the transmitter and the receiver are in motion. In this connection, robust and reliable traffic telematic systems have to be developed and tested, which calls for new channel models for C2C communication systems. Furthermore, MIMO communication systems can also be of great interest for C2C communications due to their higher throughput [4]. In this regard, several MIMO mobile-to-mobile (M2M) channel models have been developed and analyzed under different scattering conditions imposed, for example, by the two-ring model [5], the elliptical model [6], the T-junction model [7], and the geometrical street model [8, 9]. A 2D reference model for narrowband single-input single-output (SISO) M2M Rayleigh fading channels has been proposed by Akki and Haber in [10, 11]. Simulation models for SISO M2M channels have been reported in [12] and [13]. In [5, 14, 15], the 2D reference and simulation models have been presented for narrowband MIMO M2M channels. The proposed model in [15] combines the two-ring model and the elliptical model, where a combination of single- and double-bounce scattering in LOS propagation environments is assumed.

All aforementioned channel models are narrowband M2M channel models. In contrast with narrowband channels, a channel is called a wideband channel or frequency-selective channel if the signal bandwidth significantly exceeds the coherence bandwidth of the channel. Owing to increasing demands for high data rate wideband communication systems employing MIMO technologies, such as MIMO orthogonal frequency division multiplexing (OFDM) systems, it is of crucial importance to have accurate and realistic wideband MIMO M2M channel models. According to IEEE 802.11p [16], the dedicated frequency bands for short range communications [17] will be between 5770 MHz and 5925 MHz depending on the region. The range 5795–5815 MHz will be devoted to Europe, while 5850–5925 MHz and 5770–5850 MHz will be assigned to North America and Japan, respec-

tively. Consequently, a large number of C2C channel measurements have been carried out at different frequency bands, for example, at 2.4 GHz [18], 3.5 GHz [19], 5 GHz [20, 21], 5.2 GHz [22], and 5.9 GHz [23]. Real-world measurement campaigns for wideband C2C channels can be found in [24–27]. In the literature, there exist several papers [28–30] with the focus on the modeling of wideband MIMO M2M channels. A reference model derived from the geometrical T-junction scattering model has been proposed in [7] for wideband MIMO vehicle-to-vehicle (V2V) fading channels. In [29], a three-dimensional (3D) model for a wideband MIMO M2M channel has been studied. Its corresponding first- and second-order statistics have been investigated and validated on the basis of real-world measurement data. In the same paper, it has been shown that 3D scattering scenarios are more realistic than 2D scattering scenarios. However, 2D scattering models are more complexity efficient and they provide a good approximation to 3D scattering models [31]. For those reasons, we propose in our paper a 2D street scattering model.

In the literature, numerous fundamental channel models with different scatterer distributions, such as the uniform, Gaussian, Laplacian, and von Mises distribution, have been proposed to characterize the angle-of-departure (AOD) and the angle-of-arrival (AOA) statistics. In [32], the author studied the effect of Gaussian distributed scatterers on the channel characteristics in a circular scattering region around a mobile station. The spatial and temporal properties of the first arrival path in multipath environments have also been analyzed in [32]. The authors of [9] assume rectangular scattering areas on both sides of the street, in which an infinite number of scatterers are uniformly distributed. It has been observed that the shape of the Doppler power spectral density (PSD) resembles a Gaussian function if the width of the scattering area is very large.

In contrast to our previous work in [9], where the focus was on the derivation of a reference channel model for a narrowband SISO C2C channels, we design in this paper a wideband MIMO C2C channel model by starting from the same geometrical street scattering model. We focus on the statistical characterization of a wideband reference channel model assuming that an infinite number of scatterers are uniformly distributed within two rectangular areas. The radio propagation phenomena in street environments are modelled by a wide-sense stationary uncorrelated scattering process, where in addition a LOS component is taken into account. The reference model has been derived from the geometrical street scattering model assuming that the AOD and the AOA are dependent due to single-bounce scattering. To account for the nature of C2C channels, we take the mobility of both the transmitter and the receiver for granted.

In our model, we consider a 2D street scattering environment to reduce the computational cost by still guaranteeing a good match between the reference model and measured channels. A typical propagation scenario for the proposed model is illustrated in Fig. B.1, where the buildings and the trees are considered as scattering objects. Such a typical densely urban environment scenario allows us to assume that the local scatterers are uniformly distributed in a specific area. An analytical expression will be derived for the STF-CCF from which the 2D space CCF, the TF-CCF, the temporal ACF, and the FCF can be obtained directly. To validate the proposed reference model, the mean Doppler shift and the Doppler spread of the reference model have been matched to the corresponding quantities of the measured channel described in [25] for different propagation environments, such as urban, rural, and highway areas. Furthermore, we have derived an SOC channel simulator from the reference model. It is shown that the designed channel simulator matches the underlying reference model with respect to the temporal ACF and the FCF.

The rest of this paper is organized as follows. Section II describes the geometrical street scattering model. In Section III, the reference channel model is derived from the geometrical street model. Section IV analyzes the correlation properties of the reference model, such as the STF-CCF, the 2D space CCF, the TF-CCF, the temporal ACF, and the FCF. The computation of the measurement-based model parameters and the characteristic quantities describing the Doppler effect are discussed in Section V. Section VI describes briefly the simulation model derived from the reference model. The illustration of some numerical results found for the correlation functions of the reference model and the corresponding simulation model is the topic of Section VII. Finally, Section VIII draws the conclusion of the paper.

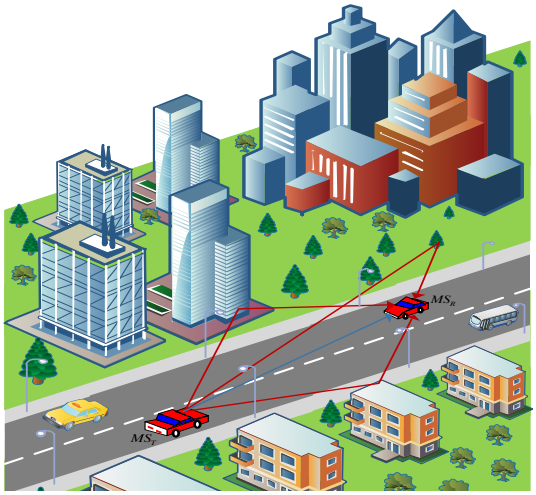

Figure B.1: A typical propagation scenario along a straight street in urban areas.

II. The Geometrical Street Scattering Model

This section briefly describes the geometrical street scattering model for wideband MIMO C2C channels. The proposed geometrical model describes the scattering environment in an urban area, where the scatterers are located in two rectangular areas on both sides of the street as illustrated in Fig. B.2. We consider rectangular grids formed by rows and columns, where the length and the width of the rectangular grids are denoted by $L_A = A_1 + A_2$ and B_i $(i = 1,2)$, respectively. The scatterer located in the mth column of the nth row is denoted by $S^{(mn)}$ $(m = 1,2,\ldots,M,\ n = 1,2,\ldots,N)$. It is assumed that the local scatterers $S^{(mn)}$ are uniformly distributed in the rectangles. The symbols MS_T and MS_R in Fig. B.2 stand for the mobile transmitter and the mobile receiver, respectively. The symbol D represents the scalar projection of the distance between the transmitter and the receiver onto the x-axis. The transmitter (receiver) is located at a distance y_{T_1} (y_{R_1}) from the left-hand side of the street and at a distance y_{T_2} (y_{R_2}) from the right-hand side of the street. Both

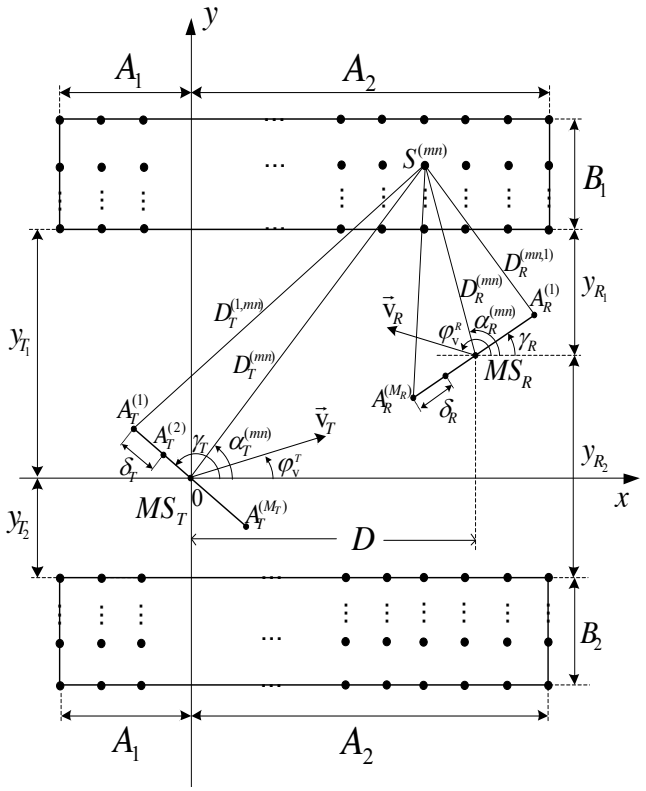

Figure B.2: Geometrical street scattering model with local scatterers uniformly distributed in two rectangular areas on both sides of the street.

the transmitter and the receiver are in motion and equipped with M_T transmitter antenna elements and M_R receiver antenna elements, respectively. The antenna ele-

ment spacings at the transmitter and the receiver are denoted by δ_T and δ_R, respectively. The symbols $\alpha_T^{(mn)}$ and $\alpha_R^{(mn)}$ denote the AOD and the AOA, respectively. The angle γ_T (γ_R) describes the tilt angle of the transmitter (receiver) antenna array. Moreover, it is assumed that the transmitter (receiver) moves with speed v_T (v_R) in the direction determined by the angle of motion φ_{v}^T (φ_{v}^R).

III. The Reference Model

A. Derivation of the Reference Model

In this section, we derive the reference model for the MIMO C2C channel under the assumption of LOS and NLOS propagation conditions. From Fig. B.2, we can realize that the (mn)th homogeneous plane wave emitted from the lth antenna element $A_T^{(l)}$ ($l = 1,\ 2,\ldots,\ M_T$) of the transmitter travels over the local scatterer $S^{(mn)}$ before impinging on the kth antenna element $A_R^{(k)}$ ($k = 1,\ 2,\ldots,\ M_R$) of the receiver. The reference model is based on the assumption that the number of local scatterers within both rectangular areas is infinite, i.e., $M,N \to\ \infty$. The temporal, spatial, and frequency characteristics of the reference model are determined by the $M_R \times M_T$ channel matrix $\boldsymbol{H}(f',t) = [H_{kl}(f',t)]_{M_R \times M_T}$, where $H_{kl}(f',t)$ denotes the time-variant transfer function (TVTF) of the channel for the link between the lth transmitter antenna element $A_T^{(l)}$ and the kth receiver antenna element $A_R^{(k)}$. The TVTF $H_{kl}(f',t)$ can be expressed as a superposition of the diffuse component and the LOS component as follows

$$H_{kl}(f',t) \;\; = \;\; H_{kl}^{\mathrm{DIF}}(f',t) + H_{kl}^{\mathrm{LOS}}(f',t) \tag{B.1}$$

where $H_{kl}^{\mathrm{DIF}}(f',t)$ and $H_{kl}^{\mathrm{LOS}}(f',t)$ represent the diffuse and the LOS components of the channel, respectively.

Note that the single-bounce scattering components bear more energy than the double-bounce scattering components. Hence, in our analysis, we model the diffuse component $H_{kl}^{\mathrm{DIF}}(f',t)$ by only taking into account the single-bounce scattering effects, which is in accordance with the assumptions made in [28, 33]. From the geometrical street scattering model shown in Fig. B.2, we can derive the TVTF of the diffuse component, which results in the following expression

$$\begin{aligned} H_{kl}^{\mathrm{DIF}}(f',t) \;\; = \;\; & \lim_{M,N\to\infty} \frac{1}{\sqrt{(c_R+1)MN}} \sum_{m,n=1}^{M,N} a_{l,mn} b_{k,mn} c_{mn} \\ & \cdot e^{j\left[\theta_{mn} + 2\pi\left(f_T^{(mn)} + f_R^{(mn)}\right)t - 2\pi f' \tau_{kl}^{\prime(mn)}\right]} \end{aligned} \tag{B.2}$$

where

$$a_{l,mn} = e^{j\pi(\delta_T/\lambda)(M_T-2l+1)\cos\left(\alpha_T^{(mn)}-\gamma_T\right)} \tag{B.3}$$

$$b_{k,mn} = e^{j\pi(\delta_R/\lambda)(M_R-2k+1)\cos\left(\alpha_R^{(mn)}-\gamma_R\right)} \tag{B.4}$$

$$c_{mn} = e^{-j\frac{2\pi}{\lambda}\left(\frac{y_{T_1}}{\sin\left(\alpha_T^{(mn)}\right)}+\frac{y_{R_1}}{\sin\left(\alpha_R^{(mn)}\right)}\right)} \tag{B.5}$$

$$f_T^{(mn)} = f_{T_{\max}}\cos\left(\alpha_T^{(mn)}-\varphi_{\mathrm{v}}^T\right) \tag{B.6}$$

$$f_R^{(mn)} = f_{R_{\max}}\cos\left(\alpha_R^{(mn)}-\varphi_{\mathrm{v}}^R\right) \tag{B.7}$$

$$\tau_{kl}'^{(mn)} = \frac{1}{c_0}\left[D_T^{(l,mn)}+D_R^{(mn,k)}\right]. \tag{B.8}$$

In (B.6) and (B.7), the symbols $f_{T_{\max}} = \mathrm{v}_T/\lambda$ and $f_{R_{\max}} = \mathrm{v}_R/\lambda$ denote the maximum Doppler frequencies associated with the movement of the transmitter and the receiver, respectively, and λ is the wavelength. The symbol c_R in (B.2) represents the Rice factor, which is defined as the ratio of the power of the LOS component to the power of the diffuse component, i.e., $c_R = E\{|\,H_{kl}^{\mathrm{LOS}}(f,'t)\,|^2\}/E\{|\,H_{kl}^{\mathrm{DIF}}(f,'t)\,|^2\}$. The phases θ_{mn} in (B.2) denote the phase shift introduced by the scatterer $S^{(mn)}$. It is assumed that the phases θ_{mn} are independent, identically distributed (i.i.d.) random variables, which are uniformly distributed over the interval $[0,2\pi)$. The symbols $\tau_{kl}'^{(mn)}$ and c_0 represent the propagation delays of the diffuse component and the speed of light, respectively. In (B.8), the quantity $D_T^{(l,mn)}$ stands for the distance from the lth transmitter antenna element $A_T^{(l)}$ to the scatterer $S^{(mn)}$, while $D_R^{(mn,k)}$ is the distance between the scatterer $S^{(mn)}$ and the kth receiver antenna element $A_R^{(k)}$. It is assumed that $(M_T-1)\delta_T \ll \min\{y_{T1},y_{T2}\}$ and $(M_R-1)\delta_R \ll \min\{y_{R1},y_{R2}\}$. These assumptions, together with the approximation $\sqrt{1+x}\approx 1+x/2$ $(x\ll 1)$, allow us to approximate the two distances $D_T^{(l,mn)}$ and $D_R^{(mn,k)}$ as follows

$$D_T^{(l,mn)} \approx D_T^{(mn)} - (M_T-2l+1)(\delta_T/2)\cos\left(\alpha_T^{(mn)}-\gamma_T\right) \tag{B.9}$$

$$D_R^{(mn,k)} \approx D_R^{(mn)} - (M_R-2k+1)(\delta_R/2)\cos\left(\alpha_R^{(mn)}-\gamma_R\right) \tag{B.10}$$

where $D_T^{(mn)}$ and $D_R^{(mn)}$ are given by $D_T^{(mn)} = \frac{y_{T_1}}{\sin(\alpha_T^{(mn)})}$ and $D_R^{(mn)} = \frac{y_{R_1}}{\sin(\alpha_R^{(mn)})}$, respectively.

It is noteworthy that one can also find articles [11, 34], in which only double-bounce scattering is assumed for M2M communications. However, by following a similar approach as in [15], one can easily extend our analysis on the basis of single-bounce scattering to the case of double-bounce scattering, and thus also to a

combination of single- and double-bounce scattering.

The TVTF of the LOS component is given by

$$H_{kl}^{\mathrm{LOS}}(f',t) = \sqrt{\frac{c_R}{(c_R+1)}} e^{j\left[2\pi(f_T^{(0)}+f_R^{(0)})t-\frac{2\pi}{\lambda}D_{kl}-2\pi f'\tau_{kl}'^{(0)}\right]} \tag{B.11}$$

where

$$f_T^{(0)} = f_{T_{\max}} \cos\left(\alpha_T^{(0)} - \varphi_{\mathrm{v}}^T\right) \tag{B.12}$$

$$f_R^{(0)} = f_{R_{\max}} \cos\left(\alpha_R^{(0)} - \varphi_{\mathrm{v}}^R\right) \tag{B.13}$$

$$\begin{aligned} D_{kl} &= D_0 - (M_T - 2l + 1)\frac{\delta_R}{2}\cos(\gamma_T) \\ &\quad + (M_R - 2k + 1)\frac{\delta_R}{2}\cos(\gamma_R) \end{aligned} \tag{B.14}$$

$$D_0 = \sqrt{D^2 + (y_{T_1} - y_{R_1})^2} \tag{B.15}$$

In (B.11), $f_T^{(0)}$ and $f_R^{(0)}$ denote the Doppler shifts of the LOS component caused by the movement of the transmitter and the receiver, respectively. The symbols $\alpha_T^{(0)}$ and $\alpha_R^{(0)}$ in (B.12) and (B.13) represent the AOD and the AOA of the LOS component, respectively. Finally $\tau_{kl}'^{(0)}$ denotes the propagation delay of the LOS component. The delay of the LOS component is defined by $\tau_{kl}'^{(0)} = D_{kl}/c_0$ with D_{kl} being the length of the direct path from the lth transmitter antenna element $A_T^{(l)}$ to the kth receiver antenna element $A_R^{(k)}$. The symbol D_0 in (B.14) denotes the Euclidean distance between the transmitter and the receiver. According to [35], the LOS component $H_{kl}^{\mathrm{LOS}}(f',t)$ is assumed to be a deterministic process, while the diffuse component $H_{kl}^{\mathrm{DIF}}(f',t)$ is a stochastic process.

B. Derivation of the AOD and the AOA

The position of all local scatterers $S^{(mn)}$ is described by the Cartesian coordinates (x_m, y_n). In the reference model, the coordinates x_m and y_n are independent random variables, which are determined by the distribution of the local scatterers. With reference to Fig. B.2, we take into account that due to single-bounce scattering the AOD $\alpha_T^{(mn)}$ and the AOA $\alpha_R^{(mn)}$ are dependent. By using the trigonometric identities, we can express the AOD $\alpha_T^{(mn)}$ and the AOA $\alpha_R^{(mn)}$ in terms of the coordinates (x_m, y_n) of the local scatterers $S^{(mn)}$ as follows

$$\alpha_T^{(mn)}(x_m,y_n) = \begin{cases} g(x_m,y_n), & \text{if } y_n \in J_i,\ x_m \in [0, A_2] \\ (-1)^{i+1}\pi + g(x_m,y_n), & \text{if } y_n \in J_i,\ x_m \in [-A_1, 0] \end{cases} \tag{B.16}$$

$$\alpha_R^{(mn)}(x_m,y_n)=\begin{cases} f(x_m,y_n), & \text{if } y_n\in J_i,\ x_m\in[D,A_2] \\ (-1)^{i+1}\pi+f(x_m,y_n), & \text{if } y_n\in J_i,\ x_m\in[-A_1,D] \end{cases} \quad \text{(B.17)}$$

for $i=1,2$, where $J_1=[y_{T_1},y_{T_1}+B_1]$, $J_2=[-y_{T_2}-B_2,-y_{T_2}]$, and

$$g(x_m,y_n) = \arctan\frac{y_n}{x_m} \quad \text{(B.18)}$$

$$f(x_m,y_n) = \arctan\frac{y_n-y_{T_1}+y_{R_1}}{x_m-D}. \quad \text{(B.19)}$$

IV. Correlation Properties of the Reference Model

In this section, we derive a general analytical solution for the STF-CCF, from which other correlation functions, such as the 2D space CCF, the TF-CCF, the temporal ACF, and the FCF can easily be derived.

A. Derivation of the STF-CCF

According to [10], the STF-CCF of the links $A_T^{(l)}-A_R^{(k)}$ and $A_T^{(l')}-A_R^{(k')}$ is defined as the correlation between the channel transfer functions $H_{kl}(f',t)$ and $H_{k'l'}(f',t)$, i.e.,

$$\begin{aligned}\rho_{kl,k'l'}(\delta_T,\delta_R,\nu',\tau) &= E\{H_{kl}^*(f',t)H_{k'l'}(f'+\nu',t+\tau)\} \\ &= \rho_{kl,k'l'}^{\text{DIF}}(\delta_T,\delta_R,\nu',\tau)+\rho_{kl,k'l'}^{\text{LOS}}(\delta_T,\delta_R,\nu',\tau) \quad \text{(B.20)}\end{aligned}$$

where $(*)$ denotes the complex conjugate operator and $E\{\cdot\}$ stands for the expectation operator that applies to all random variables: the phases $\{\theta_{mn}\}$ and the coordinates (x_m,y_n) of the scatterers $S^{(mn)}$. The first term $\rho_{kl,k'l'}^{\text{DIF}}(\delta_T,\delta_R,\tau,\nu')$ represents the STF-CCF of the diffuse component. This correlation function can be expressed, after substituting (B.2) in (B.20), by

$$\begin{aligned}\rho_{kl,k'l'}^{\text{DIF}}(\delta_T,\delta_R,\nu',\tau) &= \lim_{M,N\to\infty}\frac{1}{(c_R+1)MN}\sum_{m,n=1}^{M,N}E\Big\{c_{ll'}^{(mn)}\,d_{kk'}^{(mn)} \\ &\quad \cdot e^{j2\pi\left[\left(f_T^{(mn)}+f_R^{(mn)}\right)\tau-\nu'\tau_{kl}^{\prime(mn)}\right]}\Big\} \quad \text{(B.21)}\end{aligned}$$

where

$$c_{ll'}^{(mn)} = e^{j2\pi(\delta_T/\lambda)(l-l')\cos\left(\alpha_T^{(mn)}-\gamma_T\right)} \quad \text{(B.22)}$$

$$d_{kk'}^{(mn)} = e^{j2\pi(\delta_R/\lambda)(k-k')\cos\left(\alpha_R^{(mn)}-\gamma_R\right)}. \quad \text{(B.23)}$$

The quantities $f_T^{(mn)}$, $f_R^{(mn)}$, and $\tau_{kl}^{\prime(mn)}$ are given by (B.6), (B.7), and (B.8), respectively. We recall that the AOD $\alpha_T^{(mn)}$ and the AOA $\alpha_R^{(mn)}$ can be expressed in terms of the random variables x_m and y_n according to (B.16) and (B.17), respectively.

In Section II, it has been mentioned that all scatterers are uniformly distributed in the two rectangular areas on both sides of the street, as illustrated in Fig. B.2. Hence, the random variables x_m and y_n are also uniformly distributed over the rectangular areas. If the number of scatterers tends to infinity, i.e., $M,N \to \infty$, then the discrete random variables x_m and y_n become continuous random variables denoted by x and y, respectively. Thus, the probability density functions (PDFs) $p_x(x)$ and $p_y(y)$ of x and y, respectively, are given by

$$p_x(x) = \frac{1}{L_A}, \text{ if } x \in [-A_1, A_2] \tag{B.24}$$

$$p_y(y) = \begin{cases} \frac{1}{2B_1}, & \text{if } y \in [y_{T_1}, B_1 + y_{T_1}] \\ \\ \frac{1}{2B_2}, & \text{if } y \in [-B_2 - y_{T_2}, -y_{T_2}] \end{cases} \tag{B.25}$$

where $L_A = A_1 + A_2$. Assuming that the random variables x and y are independent, the joint PDF $p_{xy}(x,y)$ of the random variables x and y can be expressed as a product of the marginal PDFs $p_x(x)$ and $p_y(y)$, i.e.,

$$\begin{aligned} p_{xy}(x,y) &= p_x(x) \cdot p_y(y) \\ &= \begin{cases} \frac{1}{2L_A B_1}, \text{ if } x \in [-A_1, A_2],\ y \in [y_{T_1}, B_1 + y_{T_1}] \\ \\ \frac{1}{2L_A B_2}, \text{ if } x \in [-A_1, A_2],\ y \in [-B_2 - y_{T_2}, -y_{T_2}]. \end{cases} \end{aligned} \tag{B.26}$$

The infinitesimal power of the diffuse component corresponding to the differential axes dx and dy is proportional to $p_{xy}(x,y)dxdy$. As $M,N \to \infty$, this infinitesimal contribution must be equal to $1/MN = p_{xy}(x,y)dxdy$. Consequently, it follows from (B.21) that the STF-CCF of the diffuse component can be expressed as

$$\begin{aligned} \rho_{kl,k'l'}^{\mathrm{DIF}}(\delta_T, \delta_R, \nu', \tau) &= \frac{1}{2L_A B_1 (c_R + 1)} \int_{y_{T_1}}^{y_{T_1}+B_1} \int_{-A_1}^{A_2} c_{ll'}^{\mathrm{DIF}}(\delta_T, x, y) d_{kk'}^{\mathrm{DIF}}(\delta_R, x, y) \\ &\quad \cdot e^{j2\pi\left[(f_T(x,y)+f_R(x,y))\tau - \nu'\tau'_{kl}(x,y)\right]} dxdy \\ &\quad + \frac{1}{2L_A B_2 (c_R + 1)} \int_{-B_2-y_{T_2}}^{-y_{T_2}} \int_{-A_1}^{A_2} c_{ll'}^{\mathrm{DIF}}(\delta_T, x, y) d_{kk'}^{\mathrm{DIF}}(\delta_R, x, y) \\ &\quad \cdot e^{j2\pi\left[(f_T(x,y)+f_R(x,y))\tau - \nu'\tau'_{kl}(x,y)\right]} dxdy \end{aligned} \tag{B.27}$$

where

$$c_{ll'}^{\mathrm{DIF}}(\delta_T,x,y) = e^{j2\pi(\delta_T/\lambda)(l-l')\cos(\alpha_T(x,y)-\gamma_T)} \quad \text{(B.28)}$$

$$d_{kk'}^{\mathrm{DIF}}(\delta_R,x,y) = e^{j2\pi(\delta_R/\lambda)(k-k')\cos(\alpha_R(x,y)-\gamma_R)} \quad \text{(B.29)}$$

$$f_T(x,y) = f_{T_{\max}}\cos\left(\alpha_T(x,y)-\varphi_{\mathrm{v}}^T\right) \quad \text{(B.30)}$$

$$f_R(x,y) = f_{R_{\max}}\cos\left(\alpha_R(x,y)-\varphi_{\mathrm{v}}^R\right) \quad \text{(B.31)}$$

$$\tau'_{kl}(x,y) = \frac{1}{c_0}\left[D_T^{(l)}(x,y)+D_R^{(k)}(x,y)\right]. \quad \text{(B.32)}$$

Using the functions in (B.9) and (B.10), the distances $D_T^{(l)}(x,y)$ and $D_R^{(k)}(x,y)$ can be expressed as

$$D_T^{(l)}(x,y) \approx \frac{y_{T_1}}{\sin\left(\alpha_T(x,y)\right)} - (M_T-2l+1)(\delta_T/2)\cos\left(\alpha_T(x,y)-\gamma_T\right) \quad \text{(B.33)}$$

$$D_R^{(k)}(x,y) \approx \frac{y_{R_1}}{\sin\left(\alpha_R(x,y)\right)} - (M_R-2k+1)(\delta_R/2)\cos\left(\alpha_R(x,y)-\gamma_R\right). \quad \text{(B.34)}$$

In (B.20), the quantity $\rho_{kl,k'l'}^{\mathrm{LOS}}(\delta_T,\delta_R,\tau,\nu')$, which represents the STF-CCF of the LOS component, can be written as

$$\begin{aligned}\rho_{kl,k'l'}^{\mathrm{LOS}}(\delta_T,\delta_R,\nu',\tau) &= \frac{c_R}{(c_R+1)}c_{ll'}^{(0)}(\delta_T)d_{kk'}^{(0)}(\delta_R) \\ &\quad \cdot e^{j2\pi\left[\left(f_T^{(0)}+f_R^{(0)}\right)\tau-\nu'\tau_{kl}'^{(0)}\right]}\end{aligned} \quad \text{(B.35)}$$

where

$$c_{ll'}^{(0)}(\delta_T) = e^{j2\pi(\delta_T/\lambda)(l-l')\cos(\gamma_T)} \quad \text{(B.36)}$$

$$d_{kk'}^{(0)}(\delta_R) = e^{-j2\pi(\delta_R/\lambda)(k-k')\cos(\gamma_R)}. \quad \text{(B.37)}$$

The Doppler shifts $f_T^{(0)}$ and $f_R^{(0)}$ are given by (B.12) and (B.13), respectively.

B. Derivation of the 2D Space CCF

The 2D space CCF $\rho_{kl,k'l'}(\delta_T,\delta_R)$ is defined as $\rho_{kl,k'l'}(\delta_T,\delta_R)=E\{H_{kl}^*(f',t)H_{k'l'}(f',t)\}$, which is equal to the STF-CCF $\rho_{kl,k'l'}(\delta_T,\delta_R,\nu',\tau)$ in (B.20) by setting ν' and τ to zero, i.e.,

$$\begin{aligned}\rho_{kl,k'l'}(\delta_T,\delta_R) &= \rho_{kl,k'l'}(\delta_T,\delta_R,0,0) \\ &= \frac{1}{2L_AB_1(c_R+1)}\int_{y_{T_1}}^{y_{T_1}+B_1}\int_{-A_1}^{A_2} c_{ll'}^{\mathrm{DIF}}(\delta_T,x,y)d_{kk'}^{\mathrm{DIF}}(\delta_R,x,y)dxdy\end{aligned}$$

$$+\frac{1}{2L_AB_2(c_R+1)}\int_{-B_2-y_{T_2}}^{-y_{T_2}}\int_{-A_1}^{A_2} c_{ll'}^{\mathrm{DIF}}(\delta_T,x,y)d_{kk'}^{\mathrm{DIF}}(\delta_R,x,y)dxdy$$
$$+\frac{c_R}{(c_R+1)}c_{ll'}^{(0)}(\delta_T)d_{kk'}^{(0)}(\delta_R)\,. \qquad \text{(B.38)}$$

C. Derivation of the TF-CCF

The TF-CCF of the transmission link from $A_T^{(l)}$ $(l=1,2,\ldots,M_T)$ to $A_R^{(k)}$ $(k=1,2,\ldots,M_R)$ is defined by $r_{kl}(\nu',\tau):=E\{H_{kl}^*(f',t)H_{kl}(f'+\nu',t+\tau)\}$ [36]. The TF-CCF can be obtained directly from the STF-CCF [see (B.20)] by setting the antenna element spacings δ_T and δ_R to zero, i.e.,

$$\begin{aligned} r_{kl}(\nu',\tau) &= \rho_{kl,k'l'}^{\mathrm{DIF}}(0,0,\nu',\tau)+\rho_{kl,k'l'}^{\mathrm{LOS}}(0,0,\nu',\tau) \\ &= \frac{1}{2L_AB_1(c_R+1)}\int_{y_{T_1}}^{y_{T_1}+B_1}\int_{-A_1}^{A_2} e^{j2\pi\left[(f_T(x,y)+f_R(x,y))\tau-\nu'\tau'_{kl}(x,y)\right]}dxdy \\ &\quad +\frac{1}{2L_AB_2(c_R+1)}\int_{-B_2-y_{T_2}}^{-y_{T_2}}\int_{-A_1}^{A_2} e^{j2\pi\left[(f_T(x,y)+f_R(x,y))\tau-\nu'\tau'_{kl}(x,y)\right]}dxdy \\ &\quad +\frac{c_R}{(c_R+1)}e^{j2\pi\left(f_T^{(0)}+f_R^{(0)}\right)\tau}e^{-j2\pi\nu'\tau_{kl}'^{(0)}}\,. \end{aligned} \qquad \text{(B.39)}$$

D. Derivation of the Temporal ACF and the Doppler PSD

The temporal ACF of the transmission link from $A_T^{(l)}$ $(l=1,2,\ldots,M_T)$ to $A_R^{(k)}$ $(k=1,2,\ldots,M_R)$ is defined by $r_{kl}(\tau):=E\{H_{kl}^*(f',t)H_{kl}(f',t+\tau)\}$ [36, p. 376]. The temporal ACF can be obtained directly from the TF-CCF [see (B.39)] by setting at ν' to zero, i.e., $r_{kl}(\tau)=r_{kl}(\tau,0)$, which gives

$$\begin{aligned} r_{kl}(\tau) &= \frac{1}{2L_AB_1(c_R+1)}\int_{y_{T_1}}^{y_{T_1}+B_1}\int_{-A_1}^{A_2} e^{j2\pi[f_T(x,y)+f_R(x,y)]\tau}dxdy \\ &\quad +\frac{1}{2L_AB_2(c_R+1)}\int_{-B_2-y_{T_2}}^{-y_{T_2}}\int_{-A_1}^{A_2} e^{j2\pi[f_T(x,y)+f_R(x,y)]\tau}dxdy \\ &\quad +\frac{c_R}{(c_R+1)}e^{j2\pi\left(f_T^{(0)}+f_R^{(0)}\right)\tau}. \end{aligned} \qquad \text{(B.40)}$$

Notice that the expression in (B.40) reveals that the ACF $r_{kl}(\tau)$ is independent of k and l.

Computing the Fourier transform of the temporal ACF $r_{kl}(\tau)$ results in the Doppler PSD $S_{kl}(f)$, i.e.,

$$S_{kl}(f) = \int_{-\infty}^{\infty} r_{kl}(\tau) e^{-j2\pi f\tau} d\tau \,. \tag{B.41}$$

The two most important statistical quantities characterizing the Doppler PSD $S_{kl}(f)$ are the average Doppler shift $B_{kl}^{(1)}$ and the Doppler spread $B_{kl}^{(2)}$ [35]. The average Doppler shift $B_{kl}^{(1)}$ is defined as the first moment of $S_{kl}(f)$, which can be expressed as follows

$$B_{kl}^{(1)} = \frac{\int_{-\infty}^{\infty} f S_{kl}(f) df}{\int_{-\infty}^{\infty} S_{kl}(f) df} \,. \tag{B.42}$$

The Doppler spread $B_{kl}^{(2)}$ is defined as the square root of the second central moment of $S_{kl}(f)$, which can be written as

$$B_{kl}^{(2)} = \sqrt{\frac{\int_{-\infty}^{\infty} \left(f - B_{kl}^{(1)}\right)^2 S_{kl}(f) df}{\int_{-\infty}^{\infty} S_{kl}(f) df}} \,. \tag{B.43}$$

E. Derivation of the FCF

The frequency characteristics of the reference model are described by the FCF $r_{kl}(\nu')$. The FCF $r_{kl}(\nu')$ of the transmission link from $A_T^{(l)}$ to $A_R^{(k)}$ is defined by $r_{kl}(\nu') := E\{H_{kl}^*(f',t) H_{kl}(f'+\nu',t)\}$ for all $l = 1,2,\ldots,M_T$ and $k = 1,2,\ldots,M_R$. This function can be obtained directly from the TF-CCF [see (B.39)] by setting τ to zero, i.e., $r_{kl}(\nu') = r_{kl}(0,\nu')$, which results in

$$\begin{aligned} r_{kl}(\nu') \;=\; & \frac{1}{2L_A B_1 (c_R+1)} \int_{y_{T_1}}^{y_{T_1}+B_1} \int_{-A_1}^{A_2} e^{-j2\pi\nu'\tau'_{kl}(x,y)} dx dy \\ & + \frac{1}{2L_A B_2 (c_R+1)} \int_{-B_2-y_{T_2}}^{-y_{T_2}} \int_{-A_1}^{A_2} e^{-j2\pi\nu'\tau'_{kl}(x,y)} dx dy \\ & + \frac{c_R}{(c_R+1)} e^{-j2\pi\nu'\tau_{kl}'^{(0)}} \,. \end{aligned} \tag{B.44}$$

In contrast to the temporal ACF $r_{kl}(\tau)$, the FCF $r_{kl}(\nu')$ depends on k and l.

V. Measurement-Based Computation of the Model Parameters

The objective of this section is to determine the set of model parameters $\mathscr{P} = \{A_1, A_2, B_1, B_2, \ y_{T_1}, y_{T_2}, y_{R_1}, y_{R_2}, D, f_{T_{\max}}, f_{R_{\max}}, c_R\}$ describing the reference model in such a way that the average Doppler shift $B_{kl}^{(1)}$ and the Doppler spread $B_{kl}^{(2)}$ of the reference model match the corresponding quantities $\left(B_{kl}^{\star(1)} \text{ and } B_{kl}^{\star(2)}\right)$ of the measured channel reported in [25]. To determine the set of model parameters $\mathscr{P}$, we minimize the following error

$$E_{\min} = W_1 E_{B_{kl}^{(1)}} + W_2 E_{B_{kl}^{(2)}} \tag{B.45}$$

where W_1 and W_2 denote the weighting factors. The symbols $E_{B_{kl}^{(1)}}$ and $E_{B_{kl}^{(2)}}$ in (B.45) stand for the absolute errors of the average Doppler shift and Doppler spread, respectively, which are defined as

$$E_{B_{kl}^{(1)}} = \arg\min_{\mathscr{P}} \left| B_{kl}^{\star(1)} - B_{kl}^{(1)} \right| \tag{B.46}$$

$$E_{B_{kl}^{(2)}} = \arg\min_{\mathscr{P}} \left| B_{kl}^{\star(2)} - B_{kl}^{(2)} \right| . \tag{B.47}$$

In (B.46) and (B.47), the notation $\arg\min_x f(x)$ stands for the argument of the minimum, which is the set of points of the given argument for which $f(x)$ reaches its minimum value. At the beginning of the optimization procedure, the weighting factors W_1 and W_2 are selected arbitrarily, but such that they satisfy the equality $W_1 + W_2 = 1$. If the error $E_{B_{kl}^{(i)}}$ $(i = 1, 2)$ in (B.45) is large, then we reduce the corresponding weighting factor W_i and vice versa. We continue the optimization procedure until the result in (B.45) reaches an error floor, meaning that the average Doppler shift and the Doppler spread of the reference model match best the measured average Doppler shift and the measured Doppler spread, respectively.

For the measured channels in [25], the resulting optimized model parameters and the corresponding average Doppler shift and Doppler spread are listed in Table B.1. The results found for the reference model demonstrate an excellent fitting to real-world measured channels for rural, urban, and highway propagation areas, which validates the usefulness of the proposed reference model. It is worth mentioning that the computed average Doppler shift $B_{kl}^{(1)} = -110$ Hz and the Doppler spread $B_{kl}^{(2)} = 941$ Hz do not closely agree with the measured channel ($B_{kl}^{\star(1)} = -176$ Hz and $B_{kl}^{\star(2)} = 978$ Hz) in case of the highway NLOS scenario. For this scenario, a close agreement can be found for sufficiently small values of $c_R \neq 0$.

Table B.1: Measurement-based parameters of the geometrical street scattering model and the resulting average Doppler shift and the Doppler spread.

Model Parameters	**Propagation Environment**				
	Urban LOS	**Urban NLOS**	**Rural LOS**	**Highway LOS**	**Highway NLOS**
A_1 (A_2) (m)	546.28 (1249)	537.03 (908.3)	546.52 (1236)	547.69 (1207)	546.88 (1193)
B_1 (B_2) (m)	198.96 (198.77)	76.46 (1.1113)	20.89 (18.25)	199.8 (200)	0.01 (0.01)
$f_{T_{\max}}$ $(f_{R_{\max}})$ (Hz)	223.55 (219.77)	262.1 (209.97)	463.72 (491.65)	511.68 (442.62)	491.67 (481.97)
y_{T1} (y_{T2}) (m)	10.42 (7)	2.12 (1.18)	15.28 (4.63)	17.62 (19.78)	1.3 (1.3)
y_{R1} (y_{R2}) (m)	19.82 (6.6)	20 (7.06)	14.57 (9.4)	19.63 (25)	20 (9.4)
D (m)	238.6	236.7	186.77	896.7	749.6
c_R	0.485	0	0.27	0.4	0
Measured average Doppler shift $B_{kl}^{\star(1)}$ (Hz) [25]	-20	103	201	209	-176
Theoretical average Doppler shift $B_{kl}^{(1)}$ (Hz)	-20	102.67	200.55	208.8	-110
Measured Doppler spread $B_{kl}^{\star(2)}$ (Hz) [25]	341	298	782	761	978
Theoretical Doppler spread $B_{kl}^{(2)}$ (Hz)	341	298	782.03	760.88	941

VI. The Simulation Model

The reference model described above is a theoretical model, which is based on the assumption that the number of scatterers (M,N) is infinite. Owing to an infinite realization complexity, the reference model is non-realizable. However, the reference model can serve as a ground for the derivation of stochastic and deterministic simulation models. According to the generalized principle of deterministic channel modeling [35, Sec. 8.1], a stochastic simulation model can be derived from the reference model introduced in (B.1) by using only a finite number of scatterers. In the literature, several different models exist that allow for a proper simulation of mobile channels. The SOC model is an appropriate simulation model for mobile radio channels under non-isotropic scattering conditions. A detailed description and the design of SOC models can be found in [37] and [38], respectively. In [38], several parametrization techniques for SOC models have been discussed and analyzed. Here, we use the L_p-norm method (LPNM), which is a high-performance parameter computation method for the design of SOC channel simulators.

VII. Numerical Results

This section illustrates the analytical results given by (B.38), (B.39), (B.40), and (B.44). The correctness of the analytical results will be verified by simulations. The performance of the channel simulator has been assessed by comparing its temporal ACF and the FCF to the corresponding system functions of the reference model [see (B.40) and (B.44)].

As an example for our geometrical street scattering model, we consider rectangular scattering areas on both sides of the street with a length of $L_A = A_1 + A_2$, where $A_1 = 50\,\text{m}$ and $A_2 = 450$ m, and a width of $B_1 = B_2 = 100$ m. With reference to Fig. B.2, the position of the transmitter and the receiver are defined by the distances $D = 400\,\text{m}$, $y_{T_1} = y_{R_2} = 20\,\text{m}$, and $y_{T_2} = y_{R_1} = 10\,\text{m}$. For the reference model, all theoretical results have been obtained by choosing the following parameters: $\gamma_T = 90^\circ$, $\gamma_R = 90^\circ$, $\varphi_{\text{v}}^T = 0^\circ$, $\varphi_{\text{v}}^R = 180^\circ$, and $f_{T_{\max}} = f_{R_{\max}} = 91$ Hz. The Rice factor c_R was chosen from the set $\{0, 0.5, 1\}$. The scatterers are uniformly distributed over the considered rectangular areas. The L_p-norm method has been applied to optimize the simulation model parameters by using a finite number of scatterers (cisoids). For the simulation model, we use $M \times N = 50 \times 25$ scatterers (cisoids) within the rectangle on the left-hand side as well as on the right-hand side.

In Fig. B.3, the absolute value of the 2D space CCF $|\rho_{11,22}(\delta_T, \delta_R)|$ of the reference model is presented for the NLOS propagation scenario ($c_R = 0$). The results have been obtained by using (B.38). From Fig. B.3, we can observe that the 2D

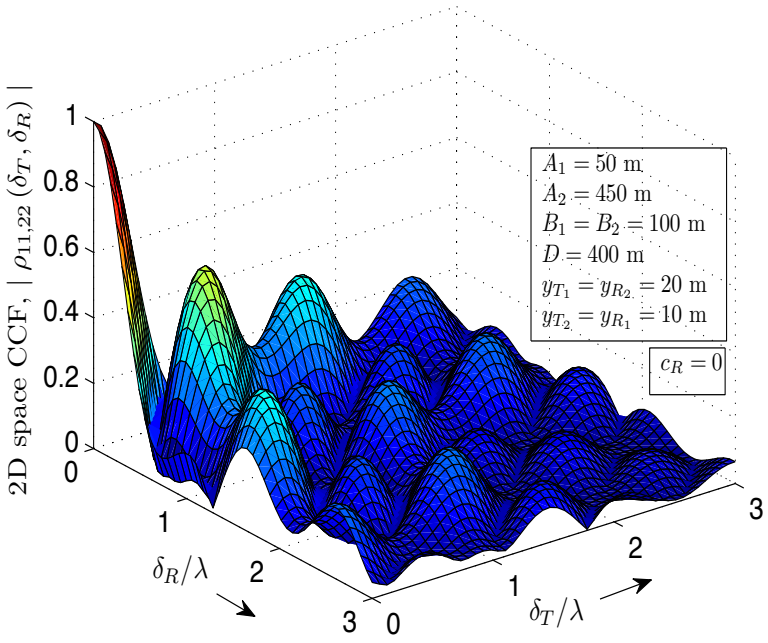

Figure B.3: Absolute value of the 2D space CCF $|\rho_{11,22}(\delta_T,\delta_R)|$ of the reference model for an NLOS propagation scenario ($c_R = 0$).

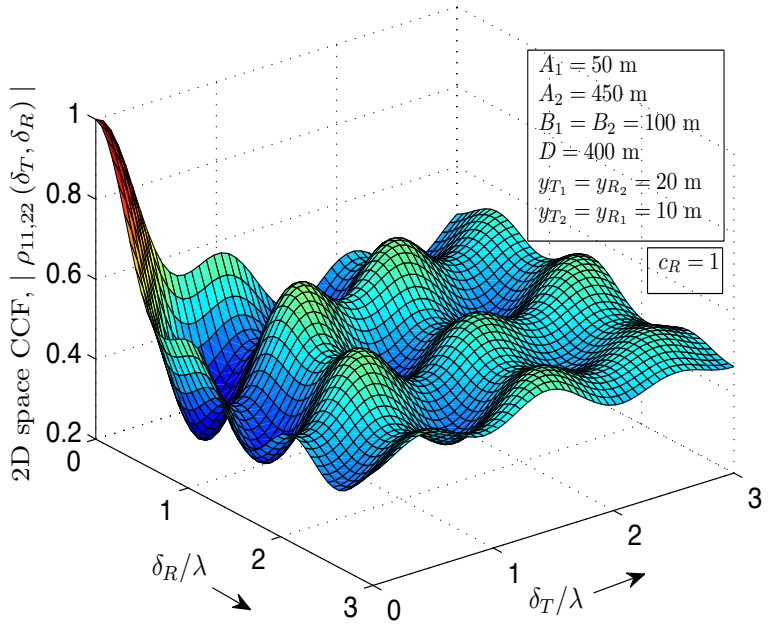

Figure B.4: Absolute value of the 2D space CCF $|\rho_{11,22}(\delta_T,\delta_R)|$ of the reference model for a LOS propagation scenario ($c_R = 1$).

space CCF decreases as the antenna element spacings increase. For the comparison reasons, the absolute value of the 2D space CCF $|\rho_{11,22}(\delta_T,\delta_R)|$ is depicted in Fig. B.4 for a LOS propagation scenario ($c_R = 1$). From Fig. B.4, one can see that the channel transfer functions $H_{kl}(f',t)$ and $H_{k'l'}(f',t)$ are highly correlated over a large range of antenna element spacings δ_T and δ_R. This can be concluded from the fact that even for large antenna element spacings, e.g., $\delta_T = \delta_R = 3\lambda$, the absolute value of the 2D space CCF $|\rho_{11,22}(\delta_T,\delta_R)|$ equals approximately one half of its maximum value. Comparing Figs. B.3 and B.4 shows that by increasing the Rice factor c_R, the 2D space CCF also increases.

Figs. B.5 and B.6 illustrate the TF-CCFs of the reference model under NLOS and LOS propagation conditions, respectively. From Fig. B.5, we can observe that the TF-CCF decreases as the time and frequency lags increase in NLOS propagation environments. A comparison of Fig. B.5 and Fig. B.6 shows that the absolute value of the TF-CCF is under LOS conditions in general higher than under NLOS.

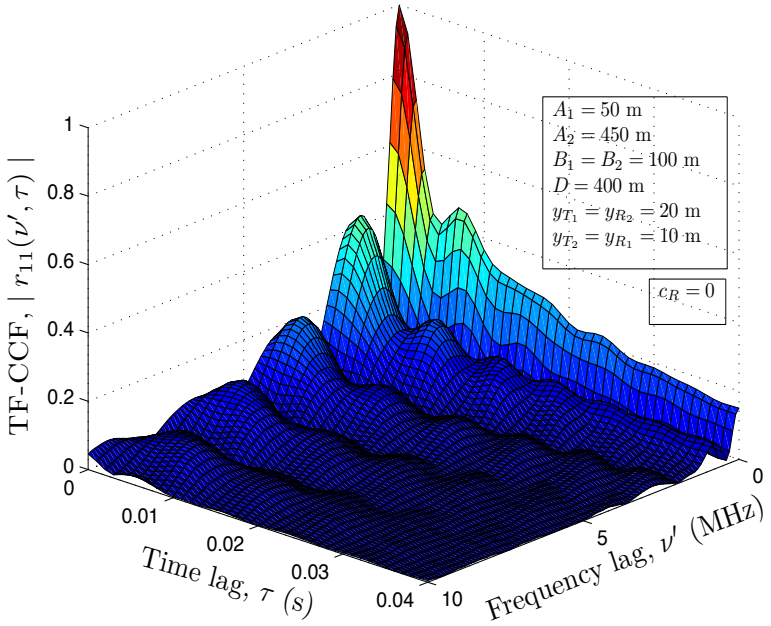

Figure B.5: Absolute value of the TF-CCF $|r_{11}(\nu',\tau)|$ of the reference model for an NLOS propagation scenario ($c_R = 0$).

Figure B.7 depicts the absolute value of the temporal ACF $|r_{kl}(\tau)|$ according to (B.40) if both the transmitter and the receiver are moving towards each other. A good match between the temporal ACF of the reference model and that of the simulation model can be observed in Fig. B.7. This figure demonstrates also that the experimental simulation results of the temporal ACF match very well with the theoretical results.

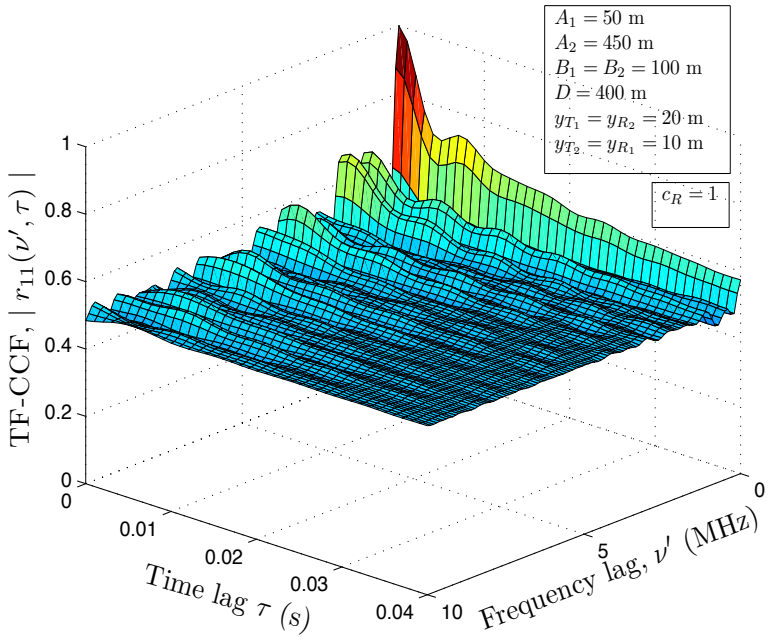

Figure B.6: Absolute value of the TF-CCF $|r_{11}(\nu', \tau)|$ of the reference model for a LOS propagation scenario ($c_R = 1$).

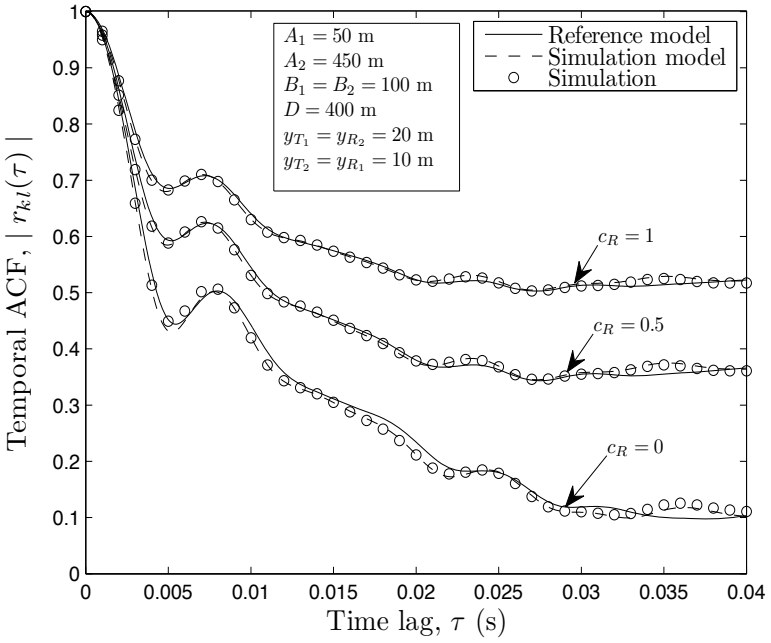

Figure B.7: Absolute values of the ACFs $|r_{kl}(\tau)|$ (reference model) and $|\hat{r}_{kl}(\tau)|$ (simulation model) for different values of the Rice factor $c_R \in \{0, 0.5, 1\}$.

Finally, Fig. B.8 illustrates the absolute value of the FCF $|r_{kl}(\nu')|$ for different Rice factors $c_R = \{0, 0.5, 1\}$ if both the transmitter and the receiver are moving towards each other. A close agreement between the reference model and the simulation model can be seen in Fig. B.8 for all chosen Rice factors. One can realize that the experimental simulation results of the FCF match very well with the theoretical results.

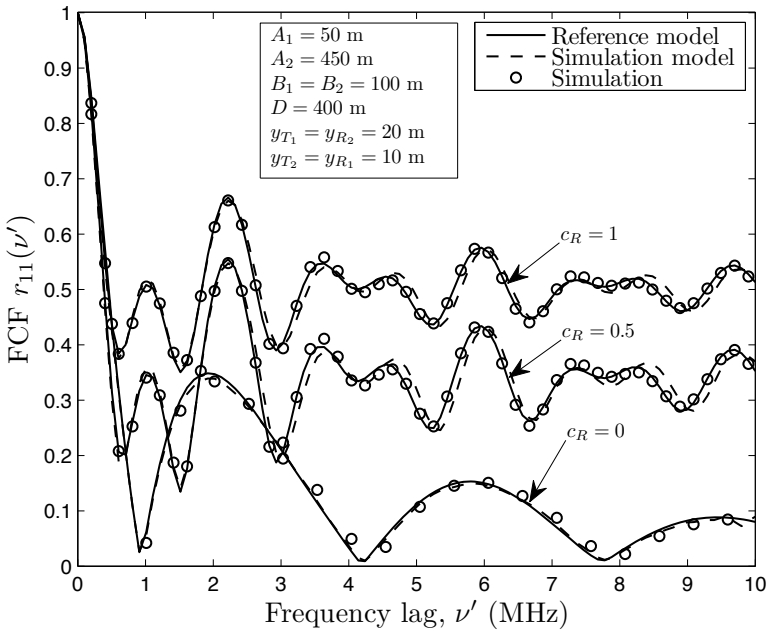

Figure B.8: Absolute values of the FCFs $|r_{11}(\nu')|$ (reference model) and $|\hat{r}_{11}(\nu')|$ (simulation model) for different values of the Rice factor $c_R \in \{0, 0.5, 1\}$.

VIII. Conclusion

In this paper, a reference model for a wideband MIMO C2C channel has been derived by starting from the geometrical street scattering model. Taking both LOS and NLOS propagation conditions into account, we have analyzed the 2D space CCF and the TF-CCF of the reference model. To find a proper simulation model, the SOC principle has been applied. It has been shown that the SOC channel simulator approximates the reference model with high accuracy with respect to the temporal ACF and the FCF. An excellent fitting of the average Doppler shift and the Doppler spread of the reference model to the corresponding quantities of measured channels has validated the usefulness of the proposed reference model. Further extensions of the proposed wideband MIMO C2C channel model incorporating the non-stationarity properties of real-world C2C channels are planned for future work.

REFERENCES

[1] F. Qu, F.-Y. Wang, and L. Yang, "Intelligent transportation spaces: vehicles, traffic, communications, and beyond," *IEEE Commun. Magazine*, vol. 48, no. 11, pp. 136–142, Nov. 2010.

[2] http://www.ertico.com.

[3] http://www.car-to-car.org.

[4] I. E. Telatar, "Capacity of multi-antenna Gaussian channels," *European Trans. Telecommun. Related Technol.*, vol. 10, no. 6, pp. 585–595, Nov./Dec. 1999.

[5] M. Pätzold, B. O. Hogstad, and N. Youssef, "Modeling, analysis, and simulation of MIMO mobile-to-mobile fading channels," *IEEE Trans. Wireless Commun.*, vol. 7, no. 2, pp. 510–520, Feb. 2008.

[6] M. Pätzold and B. O. Hogstad, "A wideband MIMO channel model derived from the geometrical elliptical scattering model," *Wireless Communications and Mobile Computing*, vol. 8, pp. 597–605, May 2008.

[7] H. Zhiyi, C. Wei, Z. Wei, M. Pätzold, and A. Chelli, "Modelling of MIMO vehicle-to-vehicle fading channels in T-junction scattering environments," in *Proc. 3rd European Conference on Antennas and Propagation, EuCAP 2009*. Berlin, Germany, Mar. 2009, pp. 652–656.

[8] A. Chelli and M. Pätzold, "A MIMO mobile-to-mobile channel model derived from a geometric street scattering model," in *Proc. 4th IEEE International Symposium on Wireless Communication Systems, ISWCS 2007*. Trondheim, Norway, Oct. 2007, pp. 792–797.

[9] N. Avazov and M. Pätzold, "A geometric street scattering channel model for car-to-car communication systems," in *Proc. International Conference on Advanced Technologies for Communications, ATC 2011*. Da Nang City, Vietnam, Aug. 2011, pp. 224–230.

[10] A. S. Akki and F. Haber, "A statistical model of mobile-to-mobile land communication channel," *IEEE Trans. Veh. Technol.*, vol. 35, no. 1, pp. 2–7, Feb. 1986.

[11] A. S. Akki, "Statistical properties of mobile-to-mobile land communication channels," *IEEE Trans. Veh. Technol.*, vol. 43, no. 4, pp. 826–831, Nov. 1994.

[12] R. Wang and D. Cox, "Channel modeling for ad hoc mobile wireless networks," in *Proc. the 55th IEEE Veh. Technol. Conf., VTC 2002-Spring, Birmingham, AL*, vol. 1, May 2002, pp. 21 – 25.

[13] C. S. Patel, G. L. Stüber, and T. G. Pratt, "Simulation of Rayleigh-faded mobile-to-mobile communication channels," *IEEE Trans. Commun.*, vol. 53, no. 11, pp. 1876–1884, Nov. 2005.

[14] A. G. Zajic and G. L. Stübber, "Space-time correlated mobile-to-mobile channels: Modelling and simulation," *IEEE Trans. Veh. Technol.*, vol. 57, no. 2, pp. 715 –726, Mar. 2008.

[15] X. Cheng, C. X. Wang, D. I. Laurenson, H. H. Chen, and A. V. Vasilakos, "A generic geometrical-based MIMO mobile-to-mobile channel model," in *Proc. International Wireless Communications and Mobile Computing Conference, IWCMC'08*, Aug. 2008, pp. 1000 –1005.

[16] "IEEE 802.11p, Part 11: Wireless LAN medium access control (MAC) and physical layer (PHY) specifications Amendment 6: Wireless access in vehicular environments, IEEE standards association," Jun. 2010.

[17] "Standard specification for telecommunications and information exchange between roadside and vehicle systems – 5 GHz band dedicated short range communications (DSRC) medium access control (MAC) and physical layer (PHY) specifications," ASTM E2213-03, Sep. 2003.

[18] G. Acosta, K. Tokuda, and M. A. Ingram, "Measured joind doppler-delay power profiles for vehicle-to-vehicle communications at 2.4 GHz," in *Proc. IEEE Global Communications Conference, GLOBECOM'04, Dallas, TX*, vol. 6, Nov. 29 - Dec. 3 2004, pp. 3813–3817.

[19] P. C. F. Eggers, T. W. C. Brown, K. Olesen, and G. F. Pedersen, "Assessment of capacity support and scattering in experimental high speed vehicle-to-vehicle MIMO links," in *Proc. 65th IEEE Vehicular Technology Conference, VTC 2007-Spring*, Apr. 2007, pp. 466–470.

[20] I. Sen and D. W. Matolak, "Vehicle-to-vehicle channel models for 5-GHz band," *Trans. Intell. Transp. Sys.*, vol. 9, no. 2, pp. 235–245, Jun. 2008.

[21] Q. Wu, D. W. Matolak, and I. Sen, "5-GHz-band vehicle-to-vehicle channels: models for multiple values of channel bandwidth," *IEEE Trans. Veh. Technol.*, vol. 59, no. 5, pp. 2620–2625, Jun. 2010.

[22] J. Maurer, T. Fügen, and W. Wiesbeck, "Narrow-band measurement and analysis of the inter-vehicle transmission channel at 5.2 GHz," in *Proc. 55th IEEE Veh. Technol. Conf., VTC 2002-Spring, Birmingham, AL*, vol. 3, May 2002, pp. 1274 – 1278.

[23] L. Cheng, B. Henty, D. D. Stancil, F. Bai, and P. Mudalige, "Mobile vehicle-to-vehicle narrow-band channel measurement and characterization of the 5.9 GHz dedicated short range communication (DSRC) frequency band," *IEEE J. Select. Areas Commun.*, vol. 25, no. 8, pp. 1501–1516, Oct. 2007.

[24] A. Paier, J. Karedal, N. Czink, H. Hofstetter, and C. Dumard, "Car-to-car radio channel measurements at 5 GHz: Pathloss, power delay profile, and doppler delay spectra," in *Proc. 4th Int. Symp. on Wireless Communication Systems, ISWCS'07, Trondheim, Norway*, Oct. 2007, pp. 224–228.

[25] I. Tan, T. Wanbin, K. Laberteaux, and A. Bahai, "Measurement and analysis of wireless channel impairments in DSRC vehicular communications," in *Proc. IEEE International Communications Conference, ICC'08*, May 2008, pp. 4882–4888.

[26] J. Kunisch and J. Pamp, "Wideband car-to-car radio channel measurements and model at 5.9 GHz," in *Proc. 68th IEEE Veh. Technol. Conf., VTC 2008-Fall*, Sept. 2008, pp. 1–5.

[27] O. Renaudin, V.-M. Kolmonen, P. Vainikainen, and C. Oestges, "Wideband measurement-based modeling of inter-vehicle channels in the 5 GHz band," in *Proc. 5th European Conference on Antennas and Propagation, EUCAP'11*, Apr. 2011, pp. 2881 –2885.

[28] A. Chelli and M. Pätzold, "A wideband multiple-cluster MIMO mobile-to-mobile channel model based on the geometrical street model," in *Proc. IEEE International Symposium on Personal, Indoor and Mobile Radio Communications, PIMRC 2008*. Cannes, France, Sep. 2008, pp. 1–6.

[29] A. G. Zajic, G. L. Stüber, T. G. Pratt, and S. T. Nguyen, "Wideband MIMO mobile-to-mobile channels: geometry-based statistical modeling with experimental verification," *IEEE Trans. Veh. Technol.*, vol. 58, no. 2, pp. 517–534, Feb. 2009.

[30] X. Cheng, C. X. Wang, D. I. Laurenson, S. Salous, and A. V. Vasilakos, "An adaptive geometry-based stochastic model for non-isotropic MIMO mobile-

to-mobile channels," *IEEE Trans. Wireless Commun.*, vol. 8, no. 9, pp. 4824–4835, Sept. 2009.

[31] G. D. Durgin, *Space-Time Wireless Channels*. Prentice Hall, 203, 345 pages.

[32] S. H. Kong, "TOA and AOD statistics for down link Gaussian scatterer distribution model," *IEEE Trans. Wireless Commun.*, vol. 8, no. 5, pp. 2609–2617, May 2009.

[33] Y. Ma and M. Pätzold, "A wideband one-ring MIMO channel model under non-isotropic scattering conditions," in *Proc. 67th IEEE Vehicular Technology Conference, VTC 2008-Spring, Singapore*, May 2008, pp. 424–429.

[34] F. Vatalaro and A. Forcella, "Doppler spectrum in mobile-to-mobile communications in the precense of three-dimensional multipath scattering," *IEEE Trans. Veh. Technol.*, vol. 46, no. 1, pp. 213–219, Feb. 1997.

[35] M. Pätzold, *Mobile Radio Channels*, 2nd ed. Chichester: John Wiley & Sons, 2011, 583 pages.

[36] A. Papoulis and S. U. Pillai, *Probability, Random Variables and Stochastic Processes*, 4th ed. New York: McGraw-Hill, 2002.

[37] M. Pätzold and B. Talha, "On the statistical properties of sum-of-cisoids-based mobile radio channel simulators," in *Proc. 10th International Symposium on Wireless Personal Multimedia Communications, WPMC 2007*. Jaipur, India, Dec. 2007, pp. 394–400.

[38] C. A. Gutiérrez and M. Pätzold, "The design of sum-of-cisoids Rayleigh fading channel simulators assuming non-isotropic scattering conditions," *IEEE Trans. Wireless Commun.*, vol. 9, no. 4, pp. 1308–1314, Apr. 2010.

Appendix C

Paper III

Title:	A Novel MIMO Car-to-Car Channel Model Based on the Geometrical Curved Street Scattering Model
Authors:	**Nurilla Avazov** and Matthias Pätzold
Affiliation(s):	University of Agder, Faculty of Engineering and Science, P. O. Box 509, NO-4898 Grimstad, Norway
Conference:	*Loughborough Antennas and Propagation Conference, LAPC 2012*, Loughborough, UK, Nov. 2012.

A Novel MIMO Car-to-Car Channel Model Based on the Geometrical Curved Street Scattering Model

Nurilla Avazov and Matthias Pätzold
Faculty of Engineering and Science, University of Agder
Servicebox 509, NO-4898 Grimstad, Norway
E-mails: {nurilla.k.avazov, matthias.paetzold}@uia.no

Abstract — **This paper introduces a novel multiple-input multiple-output (MIMO) car-to-car (C2C) channel model, which is based on a geometrical curved street scattering model. Starting from the geometrical model, a MIMO reference channel model is derived under the assumption of a combination of single- and double-bounce scattering in line-of-sight (LOS) and non-LOS (NLOS) propagation environments. The proposed channel model assumes an infinite number of scatterers, which are uniformly distributed on the outer and inner curves of the street. Expressions are presented for the three-dimensional (3D) space-time cross-correlation function (CCF), the temporal autocorrelation function (ACF), and the two-dimensional (2D) space CCF. An efficient sum-of-cisoids (SOC) channel simulator is derived from the reference model. It is shown that the temporal ACF of the SOC channel simulator fits very well to that of the reference model. The validity of the derived reference model has been verified by demonstrating an excellent match between the temporal ACF of the reference model with that of the one-ring model.**

I. Introduction

C2C communication systems are a cornerstone of the envisioned intelligent transportation systems (ITS) [1] because of their key benefits in safety and traveling ease. In C2C communication systems, both the transmitter and the receiver are in motion, which makes the underlying channels different from the traditional fixed-to-mobile or mobile-to-fixed channels in which the base-station is stationary and elevated [2]. For the development of future C2C communication systems, it is necessary to have a detailed knowledge of the statistical properties of the underlying fading channel. Furthermore, C2C communication systems are usually equipped with low elevation antennas. MIMO systems can also be of great benefit for C2C communications due to their higher throughput [3].

In the literature, several MIMO mobile-to-mobile (M2M) channel models have been proposed, such as the one-ring model [4], the two-ring model [5, 6], the elliptical model [7], the T-junction model [8], and the geometrical street model [9]. Simulation models for single-input single-output (SISO) M2M channels have been presented in [10, 11]. A narrowband SISO C2C channel model based on the geometrical street scattering model has been introduced in [9]. A generic and adaptive geometry-based stochastic model for non-isotropic MIMO M2M channels has been proposed in [12], where a combination of single- and double-bounce scattering phenomena have been assumed under LOS propagation conditions. Real-world channel measurements conducted for narrowband and wideband M2M communications have been reported in [13] and [14], respectively. Finally, we mention that 3D reference models for narrowband and wideband MIMO M2M channels have been proposed in [15] and [16], respectively.

In practice, there exist many different street types [17], such as intersections, T-junctions, roundabouts, and U-turns, which have different scattering environments according to their geometry. There are also roads passing through different types of tunnels, which can have the shape of a rectangle or a semi-circle. M. Nilsson *et al.* [18] suggested a simulation model to investigate radio propagation in curved road tunnels at a carrier frequency of 925 MHz. The proposed simulation model rests upon both waveguide methods and geometrical optics. In this paper, we propose a novel geometrical curved street scattering model, which can be used as a starting point for the development of curved, arch, and U-turn street scattering models.

This paper focuses on the statistical characterization of a narrowband reference channel model assuming that an infinite number of scatterers is uniformly distributed on outer and inner curves of the street. The reference model will be derived from the geometrical curved street scattering model assuming that the angle-of-departure (AOD) and the angle-of-arrival (AOA) are dependent in case of single-bounce scattering and independent for the double-bounce scattering components. Moreover, it is assumed that both the mobile transmitter and the mobile receiver are in motion. Expressions of the 3D space-time CCF, the temporal ACF, and the 2D space CCF are derived. The validity of the proposed model is verified by fitting the temporal ACF of the reference model to that of the one-ring model [4]. Furthermore, we derive an SOC channel simulator from the reference model by using the concept [19, Sec. 8.1]. It is shown that the designed channel simulator matches very good the underlying reference model with respect to the temporal ACF.

The rest of this paper is organized as follows. Section II describes the geometrical curved street scattering model. In Section III, the reference channel model is

derived from the geometrical curved street model. Section IV analyzes the correlation properties of the reference model, such as the 3D space-time CCF, the temporal ACF, and the 2D space CCF. Section V describes briefly the simulation model derived from the reference model. The illustration of the numerical results found for the correlation functions of the reference and simulation models are the topic of Section VI. Finally, Section VII draws the conclusions of the paper.

II. The Geometrical Curved Street Scattering Model

In this section, we briefly describe the geometrical curved street scattering model for narrowband MIMO C2C channels shown in Fig. C.1. The proposed geometrical curved street model is the starting point for the derivation of a reference channel model. We assume that the scatterers are uniformly distributed on the outer and the inner curves of the street as illustrated in Fig. C.1. The symbols MS_T and MS_R in Fig. C.1 stand for the mobile transmitter and the mobile receiver, respectively. With regard to MS_T, we suppose that there are M_p scatterers located on the outer

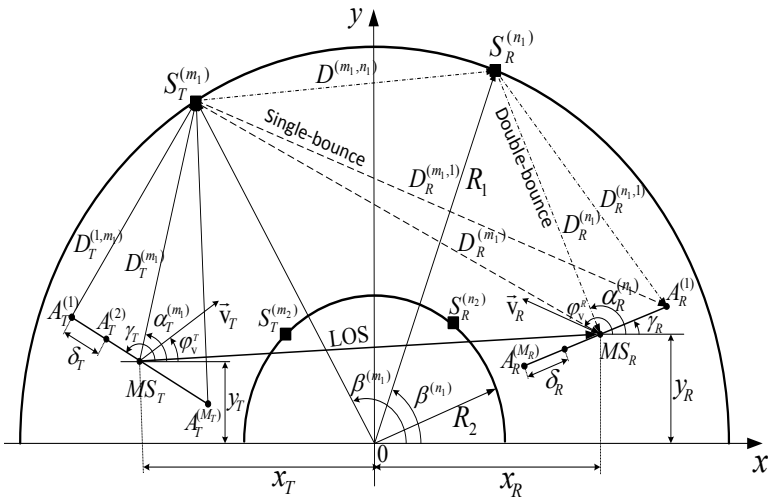

Figure C.1: Geometrical curved street scattering model with single-bounce ($- - -$), double-bounce ($-\cdot-$), and LOS (—-) components for MIMO C2C channels.

$(p=1)$ and the inner $(p=2)$ semi-circles with radii R_1 and R_2, where the m_pth $(m_p = 1,2,\ldots,M_p)$ effective scatterer is denoted by $S_T^{(m_p)}$. Analogously, with regard to MS_R, we assume that there are N_q scatterers located on the outer $(q=1)$ and the inner $(q=2)$ semi-circles with radii R_1 and (R_2), where the n_qth $(n_q = 1,2,\ldots,N_q)$ effective scatterer is denoted by $S_R^{(n_q)}$. The symbol $\beta^{(m_p)}$ $(\beta^{(n_q)})$ denotes the angle-of-scatterer (AOS) associated with the scatterer $S_T^{(m_p)}$ $(S_R^{(n_q)})$. The transmitter (receiver) is located at the position x_T and y_T (x_R and y_R). Both the transmitter and the receiver are in motion and equipped with M_T transmitter antenna elements and M_R

receiver antenna elements, respectively. The antenna element spacings at the transmitter and the receiver are denoted by δ_T and δ_R, respectively. The symbols $\alpha_T^{(m_p)}$ and $\alpha_R^{(n_q)}$ denote the AOD and the AOA, respectively. The angle γ_T (γ_R) describes the tilt angle of the transmitter (receiver) antenna array. Furthermore, it is assumed that the transmitter (receiver) moves with speed v_T (v_R) in the direction determined by the angle-of-motion φ_{v}^T (φ_{v}^R).

III. The Reference Model

This section presents the reference model for the MIMO C2C channel by considering a combination of single- and double-bounce scattering under the assumption of LOS and NLOS propagation conditions shown in Fig. C.1. From Fig. C.1, we can observe that the complex channel gain $g_{kl}(t)$ of the link between the lth transmitter antenna element $A_T^{(l)}$ ($l = 1,2,\ldots,M_T$) and the kth receiver antenna element $A_R^{(k)}$ ($k = 1,2,\ldots,M_R$) can be expressed as a superposition of single-bounce, double-bounce, and LOS components as follows

$$g_{kl}(t) = g_{kl}^{\mathrm{SB}}(t) + g_{kl}^{\mathrm{DB}}(t) + g_{kl}^{\mathrm{LOS}}(t) \tag{C.1}$$

where $g_{kl}^{\mathrm{SB}}(t)$, $g_{kl}^{\mathrm{DB}}(t)$ and $g_{kl}^{\mathrm{LOS}}(t)$ denote the single-bounce, the double-bounce, and the LOS components of the complex channel gain $g_{kl}(t)$, respectively.

A. Derivation of the Double-Bounce Scattering Component

In this subsection, we derive the double-bounce scattering component $g_{kl}^{\mathrm{DB}}(t)$ of the complex channel gain. As shown in Fig. C.1, we realize that the m_pth homogeneous plane wave emitted from the lth antenna element $A_T^{(l)}$ of the transmitter travels over the local scatterers $S_T^{(m_p)}$ and $S_R^{(n_q)}$ on the outer ($p = q = 1$) and the inner ($p = q = 2$) semi-circles before impinging on the kth antenna element $A_R^{(k)}$ of the receiver. The reference model is based on the assumption that the number of local scatterers on the outer and the inner semi-circles are infinite, i.e., $M_p, N_q \to \infty$. Under the flat-fading channel assumption, the double-bounce scattering component $g_{kl}^{\mathrm{DB}}(t)$ of the link between the lth transmitter antenna element $A_T^{(l)}$ and the kth receiver antenna element $A_R^{(k)}$ can be expressed as a superposition of the double-bounce scattering components from the outer and the inner semi-circles

$$g_{kl}^{\mathrm{DB}}(t) \;=\; \sum_{p,q=1}^{2} g_{kl}^{\mathrm{DB},p,q}(t) \tag{C.2}$$

where

$$g_{kl}^{\mathrm{DB},p,q}(t) = \lim_{M_p,N_q\to\infty} \frac{1}{\sqrt{(c_R+1)M_pN_q}} \sum_{m_p,n_q=1}^{M_p,N_q} a_l^{(m_p)} b_k^{(n_q)} c_{m_pn_q} \cdot e^{j\left[2\pi\left(f_T^{(m_p)}+f_R^{(nq)}\right)t+\theta_{m_pn_q}\right]} \tag{C.3}$$

and

$$a_l^{(m_p)} = e^{j\pi(\delta_T/\lambda)(M_T-2l+1)\cos\left(\alpha_T^{(m_p)}-\gamma_T\right)} \tag{C.4}$$

$$b_k^{(n_q)} = e^{j\pi(\delta_R/\lambda)(M_R-2k+1)\cos\left(\alpha_R^{(nq)}-\gamma_R\right)} \tag{C.5}$$

$$c_{m_pn_q} = e^{-j\frac{2\pi}{\lambda}\left(D_T^{(m_p)}+D_R^{(nq)}\right)} \tag{C.6}$$

$$f_T^{(m_p)} = f_{T\max}\cos\left(\alpha_T^{(m_p)}-\varphi_{\mathrm{v}}^T\right) \tag{C.7}$$

$$f_R^{(n_q)} = f_{R\max}\cos\left(\alpha_R^{(n_q)}-\varphi_{\mathrm{v}}^R\right). \tag{C.8}$$

In (C.7) and (C.8), the symbols $f_{T\max} = \mathrm{v}_T/\lambda$ and $f_{R\max} = \mathrm{v}_R/\lambda$ denote the maximum Doppler frequencies, and λ is the wavelength. The symbol c_R in (C.3) represents the Rice factor, which is defined as the ratio of the power of the LOS component to the power of the sum of single- and double-bounce components, i.e., $c_R = E\{|g_{kl}^{\mathrm{LOS}}(t)|^2\}/E\{|g_{kl}^{\mathrm{SB}}(t)+g_{kl}^{\mathrm{DB}}(t)|^2\}$. In our model, we assume that the scatterers $S_T^{(m_p)}$ and $S_R^{(n_q)}$ introduce the phase shifts θ_{m_p} and θ_{n_q}, respectively. The phase shifts θ_{m_p} and θ_{n_q} are assumed to be independent, identically distributed (i.i.d.) random variables, which are uniformly distributed over the interval $[0,2\pi)$. Hence, the joint phase $\theta_{m_pn_q}$ in (C.3) can be expressed in the following form [5]

$$\theta_{m_pn_q} = \theta_{m_p}+\theta_{n_q}. \tag{C.9}$$

B. Derivation of the Single-Bounce Scattering Component

In Fig. C.1, the single-bounce scattering path from the scatterer $S_T^{(m_p)}$ to the kth antenna element $A_R^{(k)}$ of the receiver is denoted by a dashed line. In case of single-bounce scattering, the m_pth homogeneous plane wave emitted from the lth antenna element $A_T^{(l)}$ of the transmitter travels over the local scatterer $S_T^{(m_p)}$ before impinging on the kth antenna element $A_R^{(k)}$ of the receiver. Hence, the single-bounce scattering component of the complex channel gain $g_{kl}^{\mathrm{SB}}(t)$ can be obtained by considering only

the effective scatterers $S_T^{(m_p)}$ [see Fig. C.1], for $n_q = m_p$ and $q = p$, as

$$g_{kl}^{\mathrm{SB}}(t) = \sum_{p=1}^{2} \lim_{M_p \to \infty} \frac{1}{\sqrt{(c_R+1)M_p}} \sum_{m_p=1}^{M_p} a_l^{(m_p)} b_k^{(m_p)} c_{m_p} \cdot e^{j\left[2\pi\left(f_T^{(m_p)} + f_R^{(m_p)}\right)t + \theta_{m_p}\right]} \tag{C.10}$$

where

$$a_l^{(m_p)} = e^{j\pi(\delta_T/\lambda)(M_T-2l+1)\cos\left(\alpha_T^{(m_p)}-\gamma_T\right)} \tag{C.11}$$

$$b_k^{(m_p)} = e^{j\pi(\delta_R/\lambda)(M_R-2k+1)\cos\left(\alpha_R^{(m_p)}-\gamma_R\right)} \tag{C.12}$$

$$c_{m_p} = e^{-j\frac{2\pi}{\lambda}\left(D_T^{(m_p)}+D_R^{(m_p)}\right)} \tag{C.13}$$

$$f_T^{(m_p)} = f_{T_{\max}} \cos\left(\alpha_T^{(m_p)} - \varphi_{\mathrm{v}}^T\right) \tag{C.14}$$

$$f_R^{(m_p)} = f_{R_{\max}} \cos\left(\alpha_R^{(m_p)} - \varphi_{\mathrm{v}}^R\right). \tag{C.15}$$

C. The LOS Component

The LOS component $g_{kl}^{\mathrm{LOS}}(t)$ in (C.1) is given by

$$g_{kl}^{\mathrm{LOS}}(t) = \sqrt{\frac{c_R}{(c_R+1)}} a_l^{(0)} b_k^{(0)} c^{(0)} e^{j2\pi\left(f_T^{(0)}+f_R^{(0)}\right)t} \tag{C.16}$$

where

$$a_l^{(0)} = e^{j\pi(\delta_T/\lambda)(M_T-2l+1)\cos(\gamma_T)} \tag{C.17}$$

$$b_k^{(0)} = e^{-j\pi(\delta_R/\lambda)(M_R-2k+1)\cos(\gamma_R)} \tag{C.18}$$

$$c^{(0)} = e^{-j\frac{2\pi}{\lambda}\sqrt{(y_R-y_T)^2+(x_T+x_R)^2}} \tag{C.19}$$

$$f_T^{(0)} = f_{T_{\max}} \cos\left(\alpha_T^{(0)} - \varphi_{\mathrm{v}}^T\right) \tag{C.20}$$

$$f_R^{(0)} = f_{R_{\max}} \cos\left(\alpha_R^{(0)} - \varphi_{\mathrm{v}}^R\right). \tag{C.21}$$

In (C.16), $f_T^{(0)}$ and $f_R^{(0)}$ denote the Doppler shifts of the LOS component caused by the movement of the transmitter and the receiver, respectively. The symbols $\alpha_T^{(0)}$ and $\alpha_R^{(0)}$ in (C.20) and (C.21), respectively, represent the AOD and the AOA of the LOS component.

D. Derivation of the AOD and the AOA

The position of all local scatterers $S_T^{(m_p)}$ and $S_R^{(n_q)}$ is described by the AOSs $\beta^{(m_p)}$ and $\beta^{(n_q)}$, respectively. With reference to Fig. C.1 and by using elementary

trigonometric identities, we can express the relationships between the AOD $\alpha_T^{(m_p)}$ and the AOS $\beta^{(m_p)}$ as well as between the AOA $\alpha_R^{(n_q)}$ and the AOS $\beta^{(n_q)}$. Hence, by using the following two functions

$$g_T(\beta^{(m_p)}) = \arctan\left(\frac{\frac{R_p}{\sqrt{x_T^2+y_T^2}}\sin\beta^{(m_p)} - \sin\alpha_T'}{\cos\alpha_T' + \frac{R_p}{\sqrt{x_T^2+y_T^2}}\cos\beta^{(m_p)}}\right) \tag{C.22}$$

$$g_R(\beta^{(n_q)}) = \arctan\left(\frac{\frac{R_q}{\sqrt{x_R^2+y_R^2}}\sin\beta^{(n_q)} - \sin\alpha_R'}{\frac{R_q}{\sqrt{x_R^2+y_R^2}}\cos\beta^{(n_q)} - \cos\alpha_R'}\right) \tag{C.23}$$

where $\alpha_T' = \arctan(y_T/x_T)$ and $\alpha_R' = \arctan(y_R/x_R)$, we can express the AOD $\alpha_T^{(m_p)}(\beta^{(m_p)})$ and the AOA $\alpha_R^{(n_q)}(\beta^{(n_q)})$ for the outer ($p=q=1$) and the inner ($p=q=2$) semi-circles as follows:

1) Outer semi-circle

$$\alpha_T^{(m_1)}(\beta^{(m_1)}) = \begin{cases} g_T(\beta^{(m_1)}), & \text{if} \quad 0 \le \beta^{(m_1)} \le \pi - \arccos(\frac{x_T}{R_1}) \\ \pi + g_T(\beta^{(m_1)}), & \text{if} \quad \pi - \arccos(\frac{x_T}{R_1}) < \beta^{(m_1)} \le \pi \end{cases} \tag{C.24}$$

$$\alpha_R^{(n_1)}(\beta^{(n_1)}) = \begin{cases} g_R(\beta^{(n_1)}), & \text{if} \quad 0 \le \beta^{(n_1)} \le \arccos(\frac{x_R}{R_1}) \\ \pi + g_R(\beta^{(n_1)}), & \text{if} \quad \arccos(\frac{x_R}{R_1}) < \beta^{(n_1)} \le \pi\,. \end{cases} \tag{C.25}$$

2) Inner semi-circle

$$\begin{aligned} \alpha_T^{(m_2)}(\beta^{(m_2)}) &= g_T(\beta^{(m_2)}), \quad \text{if } 0 \le \beta^{(m_2)} \le \pi \\ \alpha_R^{(n_2)}(\beta^{(n_2)}) &= \pi + g_R(\beta^{(n_2)}), \text{ if } 0 \le \beta^{(n_2)} \le \pi\,. \end{aligned} \tag{C.26}$$

(C.27)

IV. Correlation Properties of the Reference Model

In this section, we derive a general analytical solution for the 3D space-time CCF from which other correlation functions, such as the temporal ACF and the 2D space CCF can easily be derived.

A. Derivation of the 3D Space-Time CCF

According to [2], the 3D space-time CCF of the links $A_T^{(l)} - A_R^{(k)}$ and $A_T^{(l')} - A_R^{(k')}$ is defined as the correlation between the complex channel gains $g_{kl}(t)$ and $g_{k'l'}(t)$, i.e.,

$$\begin{aligned} \rho_{kl,k'l'}(\delta_T,\delta_R,\tau) &:= E\{g_{kl}^*(t)g_{k'l'}(t+\tau)\} \\ &= \rho_{kl,k'l'}^{\mathrm{SB}}(\delta_T,\delta_R,\tau)+\rho_{kl,k'l'}^{\mathrm{DB}}(\delta_T,\delta_R,\tau) \\ &\quad +\rho_{kl,k'l'}^{\mathrm{LOS}}(\delta_T,\delta_R,\tau) \end{aligned} \tag{C.28}$$

where $(*)$ denotes the complex conjugate operator, and $E\{\cdot\}$ stands for the expectation operator that applies to all random variables, namely the phases $\theta_{m_p n_q}$ and the AOSs $\beta^{(m_p)}$ and $\beta^{(n_q)}$. The symbols $\rho_{kl,k'l'}^{\mathrm{SB}}(\delta_T,\delta_R,\tau)$, $\rho_{kl,k'l'}^{\mathrm{DB}}(\delta_T,\delta_R,\tau)$, and $\rho_{kl,k'l'}^{\mathrm{LOS}}(\delta_T,\delta_R,\tau)$ represent the 3D space-time CCF of the single-bounce, the double-bounce, and LOS components, respectively.

The 3D space-time CCF $\rho_{kl,k'l'}^{\mathrm{DB}}(\delta_T,\delta_R,\tau)$ of the double-bounce scattering component $g_{k,l}^{\mathrm{DB}}(t)$ is given by

$$\rho_{kl,k'l'}^{\mathrm{DB}}(\delta_T,\delta_R,\tau) = \sum_{p,q=1}^{2} \rho_{kl,k'l'}^{\mathrm{DB},p,q}(\delta_T,\delta_R,\tau) \tag{C.29}$$

where

$$\begin{aligned} \rho_{kl,k'l'}^{\mathrm{DB},p,q}(\delta_T,\delta_R,\tau) = \lim_{M_pN_q\to\infty} \frac{1}{(c_R+1)M_pN_q} \sum_{m_p,n_q=1}^{M_p,N_q} E\Big\{ c_{ll'}^{(m_p)} d_{kk'}^{(n_q)} \\ \cdot e^{j2\pi\left(f_T^{(m_p)}+f_R^{(n_q)}\right)\tau} \Big\} \end{aligned} \tag{C.30}$$

and

$$c_{ll'}^{(m_p)} = e^{j2\pi(\delta_T/\lambda)(l-l')\cos\left(\alpha_T^{(m_p)}-\gamma_T\right)} \tag{C.31}$$

$$d_{kk'}^{(n_q)} = e^{j2\pi(\delta_R/\lambda)(k-k')\cos\left(\alpha_R^{(n_q)}-\gamma_R\right)}. \tag{C.32}$$

The quantities $f_T^{(m_p)}$ and $f_R^{(n_q)}$ are given by (C.7) and (C.8), respectively. We recall that the AOD $\alpha_T^{(m_p)}$ and the AOA $\alpha_R^{(n_q)}$ can be expressed in terms of the random variables $\beta^{(m_p)}$ and $\beta^{(n_q)}$ by using (C.22) and (C.23), respectively.

The 3D space-time CCF $\rho^{\mathrm{SB}}_{kl,k'l'}(\delta_T,\delta_R,\tau)$ of the single-bounce scattering component $g^{\mathrm{SB}}_{k,l}(t)$ can be obtained by considering only the effective scatterers $S^{(m_p)}$, for $n_q = m_p$ and $q = p$, as

$$\begin{aligned}\rho^{\mathrm{SB}}_{kl,k'l'}(\delta_T,\delta_R,\tau) \;=\; \sum_{p=1}^{2} \lim_{M_p\to\infty} \frac{1}{(c_R+1)M_p} \sum_{m_p=1}^{M_p} E\Big\{ c_{ll'}^{(m_p)} d_{kk'}^{(m_p)} \\ \cdot e^{j2\pi\left(f_T^{(m_p)}+f_R^{(m_p)}\right)\tau}\Big\}\end{aligned} \tag{C.33}$$

where

$$c_{ll'}^{(m_p)} \;=\; e^{j2\pi(\delta_T/\lambda)(l-l')\cos\left(\alpha_T^{(m_p)}-\gamma_T\right)} \tag{C.34}$$

$$d_{kk'}^{(m_p)} \;=\; e^{j2\pi(\delta_R/\lambda)(k-k')\cos\left(\alpha_R^{(m_p)}-\gamma_R\right)}. \tag{C.35}$$

The Doppler frequencies $f_T^{(m_p)}$ and $f_R^{(m_p)}$ are given by (C.14) and (C.15), respectively.

In Section II, it has been mentioned that all scatterers are uniformly distributed on the outer and inner semi-circles [see Fig. C.1]. Hence, the random variables $\beta^{(m_p)}$ and $\beta^{(n_q)}$ are also uniformly distributed over the intervals $[\beta^{(p)}_{\min},\beta^{(p)}_{\max}]$ and $[\beta^{(q)}_{\min},\beta^{(q)}_{\max}]$, respectively. If the number of scatterers tends to infinity, i.e., $M_p, N_q \to \infty$, then the discrete random variables $\beta^{(m_p)}$ and $\beta^{(n_q)}$ become continuous random variables denoted by $\beta^{(p)}$ and $\beta^{(q)}$, respectively. Thus, the probability density functions (PDFs) $p_{\beta^{(p)}}(\beta^{(p)})$ and $p_{\beta^{(q)}}(\beta^{(q)})$ of $\beta^{(p)}$ and $\beta^{(q)}$, respectively, are given by

$$p_{\beta^{(p)}}(\beta^{(p)}) \;=\; \frac{1}{\beta^{(p)}_{\max}-\beta^{(p)}_{\min}}, \quad \beta^{(p)} \in [\beta^{(p)}_{\min},\beta^{(p)}_{\max}] \tag{C.36}$$

$$p_{\beta^{(q)}}(\beta^{(q)}) \;=\; \frac{1}{\beta^{(q)}_{\max}-\beta^{(q)}_{\min}}, \quad \beta^{(q)} \in [\beta^{(q)}_{\min},\beta^{(q)}_{\max}]. \tag{C.37}$$

The infinitesimal power of the diffuse component corresponding to the differential angles $d\beta^{(p)}$ and $d\beta^{(q)}$ is proportional to $p_{\beta^{(p)}}(\beta^{(p)})p_{\beta^{(q)}}(\beta^{(q)})d\beta^{(p)}d\beta^{(q)}$. As $M_p, N_q \to \infty$, this infinitesimal contribution must be equal to $1/(M_pN_q) = p_{\beta^{(p)}}(\beta^{(p)})p_{\beta^{(q)}}(\beta^{(q)})d\beta^{(p)}d\beta^{(q)}$. Consequently, it follows that (C.30) can be ex-

pressed as

$$\rho^{\mathrm{DB},p,q}_{kl,k'l'}(\delta_T,\delta_R,\tau) = \frac{1}{(c_R+1)}\int_{\beta^{(p)}_{\min}}^{\beta^{(p)}_{\max}}\int_{\beta^{(q)}_{\min}}^{\beta^{(q)}_{\max}} c^{(p)}_{ll'}(\delta_T,\beta^{(p)})d^{(q)}_{kk'}(\delta_R,\beta^{(q)}) \cdot e^{j2\pi\left(f^{(p)}_T(\beta^{(p)})+f^{(q)}_R(\beta^{(q)})\right)\tau} p_{\beta^{(p)}}(\beta^{(p)}) \cdot p_{\beta^{(q)}}(\beta^{(q)})d\beta^{(p)}d\beta^{(q)} \quad \text{(C.38)}$$

where

$$c^{(p)}_{ll'}(\delta_T,\beta^{(p)}) = e^{j2\pi\frac{\delta_T}{\lambda}(l-l')\cos\left(\alpha_T(\beta^{(p)})-\gamma_T\right)} \quad \text{(C.39)}$$

$$d^{(q)}_{kk'}(\delta_R,\beta^{(q)}) = e^{j2\pi\frac{\delta_R}{\lambda}(k-k')\cos\left(\alpha_R(\beta^{(q)})-\gamma_R\right)} \quad \text{(C.40)}$$

$$f^{(p)}_T(\beta^{(p)}) = f_{T_{\max}}\cos\left(\alpha^{(p)}_T(\beta^{(p)})-\varphi^T_{\mathrm{v}}\right) \quad \text{(C.41)}$$

$$f^{(q)}_R(\beta^{(q)}) = f_{R_{\max}}\cos\left(\alpha^{(q)}_R(\beta^{(q)})-\varphi^R_{\mathrm{v}}\right). \quad \text{(C.42)}$$

In (C.41) and (C.42), we recall that the AOD $\alpha^{(p)}_T(\beta^{(p)})$ and the AOA $\alpha^{(q)}_R(\beta^{(q)})$ are functions of the AOSs $\beta^{(p)}$ and $\beta^{(q)}$ according to (C.24)–(C.27). Thus, after substituting (C.38) in (C.29), we can express the 3D space-time CCF of the double-bounce scattering component in integral form.

The 3D space-time CCF of the single-bounce scattering component is given by

$$\rho^{\mathrm{SB}}_{kl,k'l'}(\delta_T,\delta_R,\tau) = \frac{1}{(c_R+1)}\sum_{p=1}^{2}\int_{\beta^{(p)}_{\min}}^{\beta^{(p)}_{\max}} c^{(p)}_{ll'}(\delta_T,\beta^{(p)})d^{(p)}_{kk'}(\delta_R,\beta^{(p)}) \cdot e^{j2\pi\left(f^{(p)}_T(\beta^{(p)})+f^{(p)}_R(\beta^{(p)})\right)\tau} p_{\beta^{(p)}}(\beta^{(p)})d\beta^{(p)}. \quad \text{(C.43)}$$

Finally, the 3D space-time CCF $\rho^{\mathrm{LOS}}_{kl,k'l'}(\delta_T,\delta_R,\tau)$ of the LOS component $g^{\mathrm{LOS}}_{kl}(t)$ is obtained as

$$\rho^{\mathrm{LOS}}_{kl,k'l'}(\delta_T,\delta_R,\tau) = \frac{c_R}{(c_R+1)}c^{(0)}_{ll'}(\delta_T)d^{(0)}_{kk'}(\delta_R)e^{j2\pi\left(f^{(0)}_T+f^{(0)}_R\right)\tau} \quad \text{(C.44)}$$

where

$$c^{(0)}_{ll'}(\delta_T) = e^{j2\pi(\delta_T/\lambda)(l-l')\cos(\gamma_T)} \quad \text{(C.45)}$$

$$d^{(0)}_{kk'}(\delta_R) = e^{-j2\pi(\delta_R/\lambda)(k-k')\cos(\gamma_R)}. \quad \text{(C.46)}$$

The Doppler shifts $f_T^{(0)}$ and $f_R^{(0)}$ are given by (C.20) and (C.21), respectively.

B. The 2D Space CCF

The 2D space CCF $\rho_{kl,k'l'}(\delta_T,\delta_R)$ is defined as $\rho_{kl,k'l'}(\delta_T,\delta_R) := E\{g_{kl}^*(t)g_{k'l'}(t)\}$, which equals the 3D space-time CCF $\rho_{kl,k'l'}(\delta_T,\delta_R,\tau)$ at $\tau = 0$, i.e.,

$$\begin{aligned}\rho_{kl,k'l'}(\delta_T,\delta_R) &= \rho_{kl,k'l'}^{\mathrm{SB}}(\delta_T,\delta_R,0)+\rho_{kl,k'l'}^{\mathrm{DB}}(\delta_T,\delta_R,0)\\ &\quad +\rho_{kl,k'l'}^{\mathrm{LOS}}(\delta_T,\delta_R,0)\,. \end{aligned} \tag{C.47}$$

C. The Temporal ACF

The temporal ACF of the complex channel gain $g_{kl}(t)$ of the transmission link from $A_T^{(l)}$ $(l = 1,2,\ldots,M_T)$ to $A_R^{(k)}$ $(k = 1,2,\ldots,M_R)$ is defined by $r_{g_{kl}}(\tau) := E\{g_{kl}^*(t)g_{kl}(t+\tau)\}$ [20, p. 376]. The temporal ACF can directly be obtained from the 3D space-time CCF [see (C.28)] by setting the antenna element spacings δ_T and δ_R to zero. By using (C.29), (C.38), (C.43), and (C.44), this results in

$$\begin{aligned}r_{g_{kl}}(\tau) &= \rho_{kl,k'l'}^{\mathrm{SB}}(0,0,\tau)+\rho_{kl,k'l'}^{\mathrm{DB}}(0,0,\tau)\\ &\quad +\rho_{kl,k'l'}^{\mathrm{LOS}}(0,0,\tau)\,. \end{aligned} \tag{C.48}$$

V. The Simulation Model

The reference model described above can serve as basis for the derivation of stochastic and deterministic simulation models [19, Sec. 8.1]. In the literature, a large number of models exist that allow for a proper simulation of mobile channels. The SOC model is an appropriate simulation model for mobile radio channels under non-isotropic scattering conditions. A detailed description and design concept of SOC models can be found in [21] and [22], respectively. For our model, we use the L_p-norm method (LPNM) [19, Sec. 5.4.3], which is a high-performance parameter computation method for the design of SOC channel simulators.

VI. Performance Evaluation

This section illustrates the results in (C.47) and (C.48). The performance of the channel simulator has been assessed by comparison of its temporal ACF to that of the reference model in (C.48). As our geometrical curved street scattering model, we consider semi-circles with radii $R_1 = 14$ m and $R_2 = 8$ m for the outer and the inner semi-circles, respectively. With reference to Fig. C.1, the positions of the transmitter and the receiver are defined by the distances $(x_T, y_T) = (10\text{ m}, 2\text{ m})$, and $(x_R, y_R) = (12\text{ m}, 4\text{ m})$, respectively. For the reference model, all theoretical results have been obtained by choosing the following parameters: $\gamma_T = 90^\circ$, $\gamma_R = 90^\circ$,

$\varphi_{\mathrm{v}}^{T} = 90^{\circ}$, $\varphi_{\mathrm{v}}^{R} = 90^{\circ}$, $\beta^{(p)} \in [0, 180^{\circ}]$ $(p = 1,2)$, $\beta^{(q)} \in [0, 180^{\circ}]$ $(q = 1,2)$, and $f_{T_{\max}} = f_{R_{\max}} = 91$ Hz. The Rice factor c_R was chosen from the set $\{0, 0.5, 1\}$. The scatterers are uniformly distributed on semi-circles. The L_p-norm method [19, Sec. 5.4.3] has been used to optimize the simulation model parameters by assuming a finite number of scatterers (cisoids). For the simulation model, we use $M_1 = N_1 = 50$ scatterers (cisoids) on the outer semi-circle and $M_2 = N_2 = 50$ on the inner semi-circle.

Fig. C.2 illustrates the absolute value of the temporal ACF $|r_{g_{11}}(\tau)|$ for the case that both the transmitter and the receiver are moving towards each other. A good fitting between the temporal ACF of the reference model and that of the simulation model can be observed. This figure demonstrates also that the experimental simulation results of the temporal ACF match very well with the theoretical results. From Fig. C.2, we can observe that the approximation error caused by a limited number of scatterers (cisoids) M_p, N_q can in general be ignored if $M_p \geq 50$ and $N_q \geq 50$.

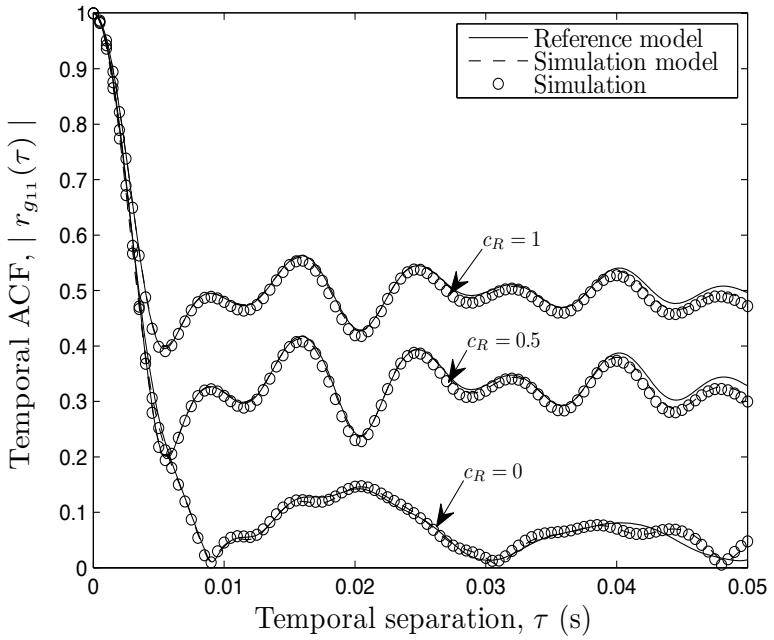

Figure C.2: Absolute values of the ACFs $|r_{g_{11}}(\tau)|$ (reference model) and $|\tilde{r}_{g_{11}}(\tau)|$ (simulation model) for different Rice factors ($c_R = \{0, 0.5, 1\}$, $R_1 = 14$ m, $R_2 = 8$ m, $x_T = 10$ m, $x_R = 12$ m, $y_T = 2$ m, and $y_R = 4$ m).

Fig. C.3 presents the temporal ACF $r_{g_{11}}(\tau)$ of the reference model given by (C.48) under certain geometrical conditions, which meet the geometry of the one-ring model [4, Eq. (9)], i.e., $R_1 = 14$ m, $R_2 = 0$ m, $x_T = 420$ m, $y_T = 0$ m, $x_R = 0$ m, and $y_R = 0$ m . A perfect fitting between the temporal ACF of the proposed reference model and that of the one-ring model can be observed in Fig. C.3, which validates

the usefulness of the proposed model and demonstrates that the proposed model includes the one-ring model as a special case.

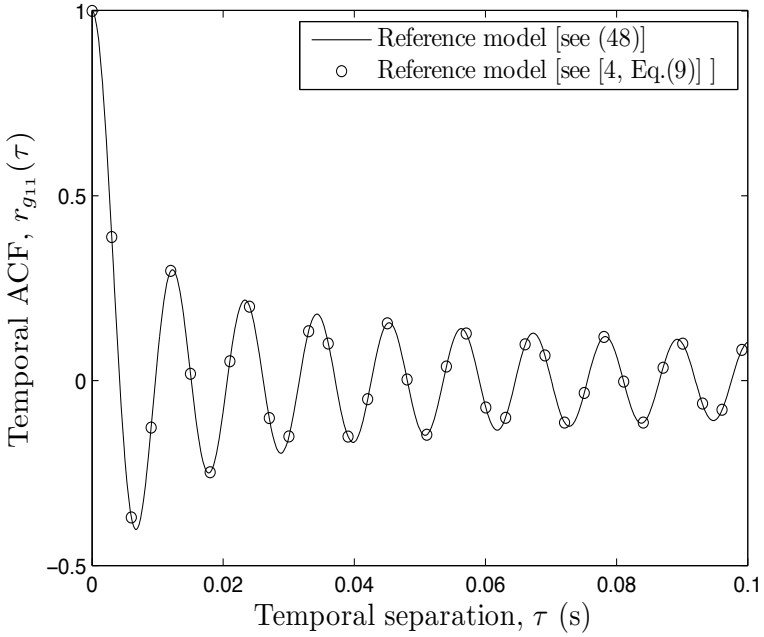

Figure C.3: Temporal ACF $r_{g_{11}}(\tau)$ of the reference model [see (C.48)] in comparison with the temporal ACF of the one-ring model [4, Eq. (9)] for a NLOS propagation scenario ($c_R = 0$, $R_1 = 14$ m, $R_2 = 0$ m, $x_T = 420$ m, $x_R = 0$ m, $y_T = 0$ m, and $y_R = 0$ m).

In Fig. C.4, the absolute value of the 2D space CCF $|\rho_{11,22}(\delta_T, \delta_R)|$ of the reference model is presented for a LOS propagation scenario ($c_R = 1$). The result has been obtained using (C.47). From Fig. C.4, we can realize that the complex channel gains $g_{kl}(t)$ and $g_{k'l'}(t)$ are highly correlated even for relatively large antenna element spacings.

VII. Conclusion

In this paper, a novel MIMO C2C channel model has been developed based on the geometrical curved street scattering model. By a combination of single- and double-bounce scattering components, we have analyzed the temporal ACF and the 2D space CCF of the reference model under both LOS and NLOS propagation conditions. To find a proper simulation model, the SOC principle has been applied. It has been shown that the SOC channel simulator approximates the reference model with respect to the temporal ACF with high accuracy. The usefulness of the proposed model has been validated by demonstrating a perfect fit between the ACF of

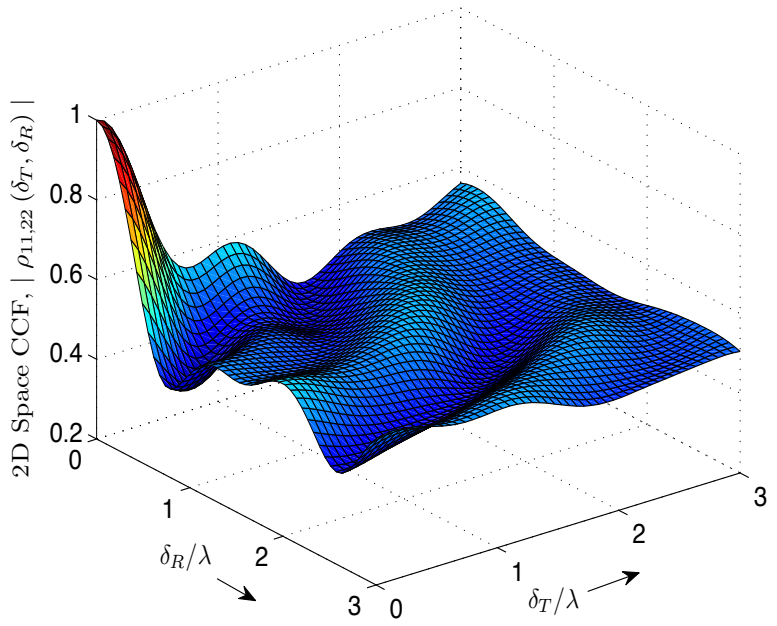

Figure C.4: Absolute value of the 2D space CCF $|\rho_{11,22}(\delta_T,\delta_R)|$ of the reference model for a LOS propagation scenario ($c_R = 1$, $R_1 = 14$ m, $R_2 = 8$ m, $x_T = 10$ m, $x_R = 12$ m, $y_T = 2$ m, and $y_R = 4$ m).

the reference model and that of the one-ring model. Further investigations focusing on the effect of moving scatterers on the statistics of MIMO C2C channels are planned in our future work.

REFERENCES

[1] ITS project, http://www.its.dot.gov/index.htm,, Nov. 2007.

[2] A. S. Akki and F. Haber, "A statistical model of mobile-to-mobile land communication channel," *IEEE Trans. Veh. Technol.*, vol. 35, no. 1, pp. 2–7, Feb. 1986.

[3] I. E. Telatar, "Capacity of multi-antenna Gaussian channels," *European Trans. Telecommun. Related Technol.*, vol. 10, no. 6, pp. 585–595, Nov./Dec. 1999.

[4] M. Pätzold and B. O. Hogstad, "A space-time channel simulator for MIMO channels based on the geometrical one-ring scattering model," in *Proc. 60th IEEE Semiannual Veh. Technol. Conf., VTC 2004-Fall. Los Angeles, CA, USA*, vol. 1, Sept. 2004, pp. 144–149.

[5] M. Pätzold, B. O. Hogstad, and N. Youssef, "Modeling, analysis, and simulation of MIMO mobile-to-mobile fading channels," *IEEE Trans. Wireless Commun.*, vol. 7, no. 2, pp. 510–520, Feb. 2008.

[6] A. G. Zajic and G. L. Stüber, "Space-time correlated mobile-to-mobile channels: modelling and simulation," *IEEE Trans. Veh. Technol.*, vol. 57, no. 2, pp. 715–726, Mar. 2008.

[7] M. Pätzold and B. O. Hogstad, "A wideband MIMO channel model derived from the geometrical elliptical scattering model," *Wireless Communications and Mobile Computing*, vol. 8, pp. 597–605, May 2008.

[8] H. Zhiyi, C. Wei, Z. Wei, M. Pätzold, and A. Chelli, "Modelling of MIMO vehicle-to-vehicle fading channels in T-junction scattering environments," in *Proc. 3rd European Conference on Antennas and Propagation, EuCAP 2009*. Berlin, Germany, Mar. 2009, pp. 652–656.

[9] N. Avazov and M. Pätzold, "A geometric street scattering channel model for car-to-car communication systems," in *Proc. International Conference on Advanced Technologies for Communications, ATC 2011*. Da Nang City, Vietnam, Aug. 2011, pp. 224–230.

[10] R. Wang and D. Cox, "Channel modeling for ad hoc mobile wireless networks," in *Proc. the 55th IEEE Veh. Technol. Conf., VTC 2002-Spring, Birmingham, AL*, vol. 1, May 2002, pp. 21 – 25.

[11] C. S. Patel, G. L. Stüber, and T. G. Pratt, "Simulation of Rayleigh-faded mobile-to-mobile communication channels," *IEEE Trans. Commun.*, vol. 53, no. 11, pp. 1876–1884, Nov. 2005.

[12] X. Cheng, C. X. Wang, D. I. Laurenson, S. Salous, and A. V. Vasilakos, "An adaptive geometry-based stochastic model for non-isotropic MIMO mobile-to-mobile channels," *IEEE Trans. Wireless Commun.*, vol. 8, no. 9, pp. 4824–4835, Sept. 2009.

[13] J. Maurer, T. Fügen, and W. Wiesbeck, "Narrow-band measurement and analysis of the inter-vehicle transmission channel at 5.2 ghz," in *Proc. 55th IEEE Veh. Technol. Conf., VTC 2002-Spring, Birmingham, AL*, vol. 3, May 2002, pp. 1274 – 1278.

[14] J. Kunish and J. Pamp, "Wideband car-to-car radio channel measurements and model at 5.9 GHz," in *Proc. 68th IEEE Veh. Technol. Conf., VTC 2008-Fall*, Sept. 2008, pp. 1–5.

[15] A. G. Zajic and G. L. Stüber, "A three-dimensional MIMO mobile-to-mobile channel model," Mar. 2007, pp. 1883–1887.

[16] ——, "A three-dimensional parametric model for wideband MIMO mobile-to-mobile channels," Nov. 2007, pp. 3760–3764.

[17] G. Morrish, *Street Design Guidelines*. Landcom Project., 2006, 41 pages.

[18] M. Nilsson, J. Slettenmark, and C. Beckman, "Wave propagation in curved road tunnels," in *IEEE Antennas and Propagation Society International Symposium, 1998*, vol. 4, June 1998, pp. 1876–1879.

[19] M. Pätzold, *Mobile Radio Channels*, 2nd ed. Chichester: John Wiley & Sons, 2011, 583 pages.

[20] A. Papoulis and S. U. Pillai, *Probability, Random Variables and Stochastic Processes*, 4th ed. New York: McGraw-Hill, 2002.

[21] M. Pätzold and B. Talha, "On the statistical properties of sum-of-cisoids-based mobile radio channel simulators," in *Proc. 10th International Symposium on Wireless Personal Multimedia Communications, WPMC 2007*. Jaipur, India, Dec. 2007, pp. 394–400.

[22] C. A. Gutiérrez and M. Pätzold, "The design of sum-of-cisoids Rayleigh fading channel simulators assuming non-isotropic scattering conditions," *IEEE Trans. Wireless Commun.*, vol. 9, no. 4, pp. 1308–1314, Apr. 2010.

Appendix D

Paper IV

Title:	A Novel Wideband MIMO Car-to-Car Channel Model Based on a Geometrical Semicircular Tunnel Scattering Model
Authors:	**Nurilla Avazov** and Matthias Pätzold
Affiliation(s):	University of Agder, Faculty of Engineering and Science, P. O. Box 509, NO-4898 Grimstad, Norway
Conference:	*IEEE Transactions on Vehicular Technology*, 2015 (in press).

A Novel Wideband MIMO Car-to-Car Channel Model Based on a Geometrical Semi-Circular Tunnel Scattering Model

Nurilla Avazov and Matthias Pätzold
Faculty of Engineering and Science, University of Agder
P.O. Box 509, NO-4898 Grimstad, Norway
E-mails: {nurilla.k.avazov, matthias.paetzold}@uia.no

Abstract — **In this paper, we present a wideband multiple-input multiple-output (MIMO) car-to-car (C2C) channel model based on a geometrical semi-circular tunnel (SCT) scattering model. From the geometrical SCT scattering model, a reference channel model is derived under the assumption of single-bounce scattering in line-of-sight (LOS) and non-LOS (NLOS) propagation environments. In the proposed reference channel model, it is assumed that an infinite number of scatterers are randomly distributed on the tunnel wall. Starting from the geometrical scattering model, the time-variant transfer function (TVTF) is derived, and its correlation properties in time, frequency, and space are studied. Expressions are presented for the space-time-frequency cross-correlation function (STF-CCF), the two-dimensional (2D) space CCF, the 2D time-frequency CCF (TF-CCF), the temporal autocorrelation function (ACF), and the frequency correlation function (FCF). Owing to the semi-circular geometry, we reduced the originally threefold integrals to double integrals in the computations of the correlation functions, which simplifies the numerical analysis considerably. From the TVTF characterizing the reference model, an efficient sum-of-cisoids (SOC) channel simulator is derived. Numerical results show that both the temporal ACF and the FCF of the SOC channel simulator match very well with those of the reference model. A validation of the proposed model has been done by fitting the delay spread of the reference model to that of the measured channel, which demonstrates an excellent agreement. The proposed channel simulator allows us to evaluate the performance of C2C communication systems in tunnel environments.**

Index Terms — **Angle-of-arrival (AOA), angle-of-departure (AOD), car-to-car (C2C), delay spread, diffuse component, frequency correlation function (FCF), line-of-sight (LOS) component, semi-circular tunnel (SCT) scattering model, time-variant transfer function (TVTF).**

I. INTRODUCTION

In recent years, there has been an increased interest in developing car-to-car (C2C) communication systems that offer new traffic telematic applications for improving safety and mobility on roads. Efficient C2C communication systems integrate information and communication technology into transport infrastructures, cars, and end-user devices [1]. To improve safety in C2C communication environments, many research projects have been carried out throughout the world, for example, the C2C Communication Consortium [2], the European Road Transport Telematics Implementation Coordinating Organization (ERTICO) [3] in Europe and the Intelligent Transportation Systems (ITS) [4] in the United States. Despite many research and technological development activities, C2C communication systems still face some challenges, induced by safety requirements and wireless channel conditions. One of the most important issues in C2C communications is the channel congestion, causing the loss of safety messages [5].

To achieve the best performance of future C2C communication systems, it is important to have a detailed knowledge of the statistical properties of the underlying radio channel. Numerous mobile-to-mobile (M2M) channel models have been developed based on different geometrical scattering models, such as the two-ring model [6], the elliptical model [7], the rectangular model [8], the T-junction model [9], the cross-junction model [10], and the curve model [11]. Narrowband multiple-input multiple-output (MIMO) C2C channel models can be found in [12, 13] for 5.9 GHz, which is the carrier frequency in dedicated short-range communication (DSRC) [14] systems. However, all these models are 2D models, which have been proposed for certain environments, such as suburban and rural areas. To provide more appropriate radio propagation models for urban areas, three-dimensional (3D) MIMO M2M channel models have been developed and studied in [15–17]. A 3D geometrical scattering model based on concentric spheres at the transmitter and the receiver is assumed in [16, 17]. In [17], a 3D parametric reference model for 2×2 M2M wideband dual-polarized multipath fading channels has been developed. In [18], the importance of different propagation mechanisms in non-line-of-sight (NLOS) propagation conditions are highlighted for merging lanes on highways and four-way cross-junction scenarios. For vehicle-to-vehicle (V2V) communications, new wideband single-input single-output (SISO) and MIMO channel models based on measurement campaigns carried out at 5.2 GHz have been presented in [19] and [20], respectively.

To characterize propagation channels and to evaluate the performance of wireless communication systems, it is important to distinguish between slow and fast

fading. For example, it is well-known that the Doppler spread can be computed from the temporal autocorrelation function (ACF). The Doppler spread is one of the most important characteristic quantities of C2C channels. In the literature [12, 21–23], several C2C channel measurements have been carried out to investigate the Doppler spread of C2C channels. One advantage of geometry-based stochastic channel models is that their spatial and temporal correlation properties can be studied analytically. Thus, the temporal and spatial correlation properties of C2C channels influence the performance of C2C communication systems [24]. The effect of the temporal and spatial correlation properties of C2C channels on the system performance (bit error probability) of Alamouti-coded orthogonal frequency division multiplexing (OFDM) systems has been studied in [25].

In [19], the geometry-based stochastic model (GBSM) approach [20] has been used to model the discrete scattering component under the assumption that the underlying V2V channel is non-stationary. In general, C2C channels are non-stationary in nature. However, for non-stationary channels, it has been reported in the literature [19, 20, 26] that the wide-sense stationary uncorrelated scattering (WSSUS) assumption is still valid for short observation time intervals, commonly referred to as stationary intervals [27]. The performance of C2C communication systems has recently been studied in [28], where a new regular-shaped GBSM for non-isotropic scattering wideband C2C Rician channels has been proposed.

Roads are often passing through tunnels, which can have different geometrical shapes [29, p. 31], such as rectangular, horseshoe, oval, circular, and semi-circular shapes. Modelling of channels in tunnel environments is of importance for the development of C2C communication systems. It is especially important for countries with mountainous areas, where many roads are passing through tunnels. The characteristics of mobile radio channels inside a tunnel environment have been widely investigated by using a geometrical optical model [30], a wave guide model [31], and a full wave model [32]. A theoretical analysis of the wireless channel in tunnels with vehicular traffic flow has been introduced in [33]. It has been shown that the signal propagation in these tunnels is influenced by the number, size, and position of the vehicles, the size of the tunnel, and the vehicular traffic load. In [34], a ray-tube tracing method has been presented to simulate the wave propagation in curved road tunnels. A parametric study has been carried out to investigate the influence of the tunnel geometry and the carrier frequency on the path loss. A geometrical stochastic channel model for train-to-train communications has been derived based on the WINNER model in [35]. There, it has been shown that the channel statistics of the WINNER-based model are close to the deterministic one, which are obtained

from a 3D ray tracing simulator. In [36], a channel inside an arched tunnel was measured and the radio propagation channel in terms of the delay spread and dominant scatterers was analyzed. The investigations showed that more than 90% of the extracted paths consist of LOS and single-bounce scattering components.

In channel modelling, the distribution of the scatterers is an important aspect affecting the angle-of-departure (AOD) and the angle-of-arrival (AOA) statistics. In 3D scattering models, the knowledge of the distributions of the elevation and azimuth angles of the transmitted and the received plane waves is important, as it allows us to investigate the temporal, frequency, and spatial correlation properties of the underlying fading channel. In this regard, the proposed models for tunnel environments [30–34] do *not* consider the impact of the distributions of the scatterers on the statistics of the azimuth AOD (AAOD), azimuth AOA (AAOA), elevation AOD (EAOD), and the elevation AOA (EAOA). To fill this gap, we have recently proposed a wideband SISO C2C channel model based on a geometrical semi-circular tunnel (SCT) scattering model [37].

In this paper, we expand the channel model proposed in [37] by considering the effect of multiple antennas at both the mobile transmitter and the mobile receiver. In this regard, we derive a wideband MIMO C2C channel model from the geometrical SCT scattering model, in which the effect of LOS and NLOS propagation conditions is taken into account.

To simplify the mathematical analysis, we have assumed that the WSSUS assumption is valid over a short observation time interval. This assumption is supported by the study in [26], where the authors investigated the time interval over which the fading process in a tunnel environment can be considered as wide-sense stationary. The analysis of the measurement data in [26] has revealed that the mean stationary intervals in LOS and LOS delay compensated tunnel scenarios are 0.97 s and 1.6 s, respectively.

We study the statistical characteristics of a wideband reference channel model assuming that an infinite number of scatterers are randomly distributed on the SCT wall. Starting from the geometrical SCT scattering model, we derive the TVTF of the reference model assuming single-bounce scattering. An analytical expression is presented for the space-time-frequency (STF) cross-correlation function (STF-CCF) from which the 2D space CCF, the 2D time-frequency (TF) CCF, the temporal ACF, and the frequency correlation function (FCF) are derived directly. Furthermore, we derive an sum-of-cisoid (SOC) channel simulator from the reference model. For deriving our SOC channel simulator, we have used the L_p-norm method (LPNM) [38, Sec. 5.4.3] to compute the model parameters. According to the study

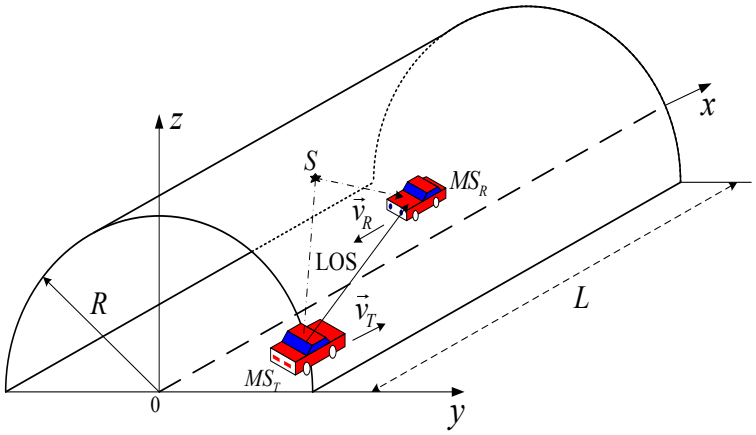

Figure D.1: A typical propagation scenario in an SCT.

in [39], the LPNM has the best performance among the five alternative methods.

It is shown that the designed channel simulator matches closely the underlying reference model with respect to the temporal ACF and the FCF. Finally, we evaluate and present the Doppler statistics and the delay statistics of the proposed SCT channel model. The usefulness of the proposed reference model is validated by demonstrating an excellent match between the delay spread of the reference model and the one of the measured channel reported in [36].

The reminder of this paper is organized as follows. Section II describes the geometrical SCT scattering model. In Section III, the reference channel model is derived from the geometrical SCT scattering model. Section IV analyzes the correlation functions of the reference model, such as the STF-CCF, the 2D space CCF, the 2D TF-CCF, the temporal ACF, and the FCF. In Section V, the simulation model is briefly discussed and a measurement-based computation of the proposed model parameters is presented. The illustration of the numerical results found for the correlation functions characterizing the reference and simulation models is the topic of Section VI. Finally, Section VII provides the conclusion of the paper.

II. The Geometrical SCT Scattering Model

Here, we briefly describe the geometrical SCT scattering model for a wideband MIMO C2C channel. A typical propagation scenario in a tunnel is illustrated in Fig. D.1. The proposed geometrical SCT scattering model describes the scattering environment inside a tunnel with a length of L. It is assumed that the cross-section of the tunnel is a semi-circle with radius R. We assume that the scatterers are randomly distributed on the tunnel wall as shown in Fig. D.2.

The geometrical SCT scattering model is shown in Fig. D.3, where we use the Cartesian coordinate system (x, y, z) to describe the position of the scatterers $S^{(mn)}$

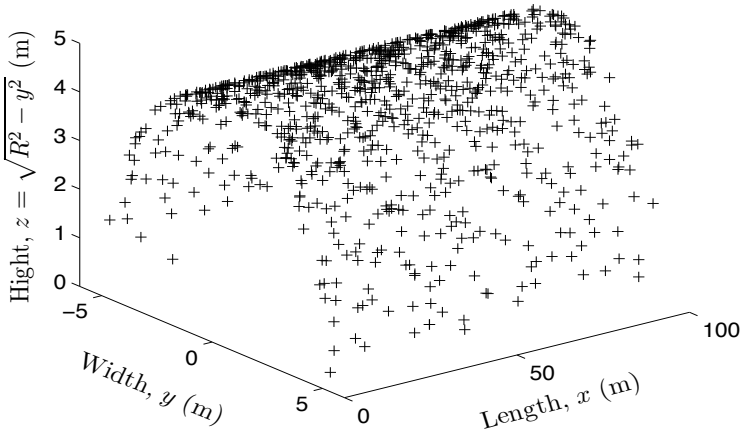

Figure D.2: Randomly distributed scatterers (+) on a tunnel wall with radius $R = 5$ m and length $L = 100$ m.

for $m = 1,2,\ldots,M$ and $n = 1,2,\ldots,N$. Owing to the semi-circular shape of the tunnel, we can describe the z-axis in terms of the y-axis as $z = \sqrt{R^2 - y^2}$. This allows us to present the position of the scatterers $S^{(mn)}$ in the 3D plane by $(x_m, y_n, \sqrt{R^2 - y_n^2})$, where x_m and y_n are random variables. Hence, the distribution of the scatterers $S^{(mn)}$ is completely determined by the distribution of x_m and y_n.

The symbols MS_T and MS_R in Fig. D.3 stand for the mobile transmitter and the mobile receiver, respectively. We assume that the mobile transmitter (receiver) is equipped with a uniform linear antenna array consisting of M_T (M_R) antenna elements. The spacings between the antenna elements at the transmitter and the receiver antennas are denoted by δ_T and δ_R, respectively. The orientations of the

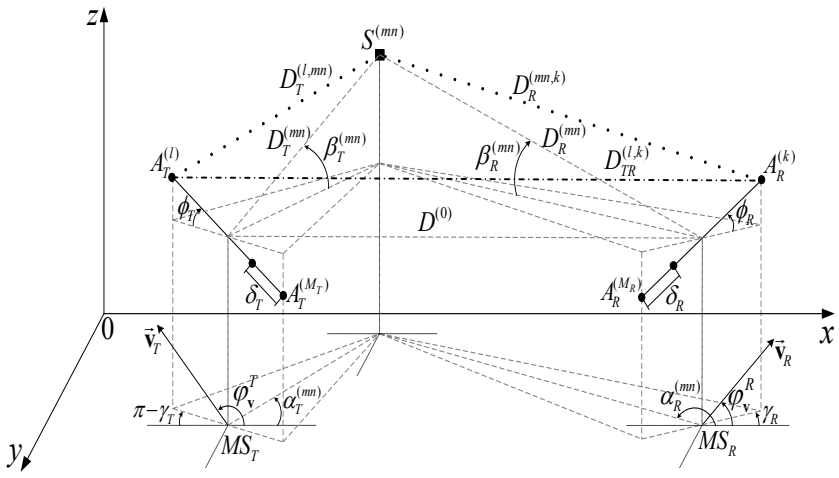

Figure D.3: Geometrical SCT scattering model with single-bounce components $(\cdots)$ and a LOS component $(-\cdot-)$ for an $M_T \times M_R$ MIMO C2C channel.

transmitter and the receiver antenna elements in the xy-plane relative to the x-axis

are described by the angles γ_T and γ_R, respectively. Similarly, the elevation angles of the transmitter and the receiver antenna arrays with respect to the xy-plane are denoted by ϕ_T and ϕ_R, respectively. The positions of the antenna arrays of the mobile transmitter MS_T and the mobile receiver MS_R are determined by (x_T, y_T, z_T) and (x_R, y_R, z_R), respectively. It is supposed that the mobile transmitter MS_T and the mobile receiver MS_R are inside the tunnel, such that $0 \leq x_T \leq x_R \leq L$ and $-R < y_T \leq y_R < R$. It is assumed that there is a LOS path between the mobile transmitter and the mobile receiver. The angles $\alpha_T^{(mn)}$, $\alpha_R^{(mn)}$, $\beta_T^{(mn)}$, and $\beta_R^{(mn)}$ denote the AAOD, AAOA, EAOD, and the EAOA, respectively. Moreover, it is assumed that both the transmitter and the receiver move with speeds v_T and v_R in the direction determined by the angles of motion φ_{v}^T and φ_{v}^R, respectively. The distance $D_T^{(l,mn)}$ denotes the path length between the lth transmitter antenna $A_T^{(l)}$ $(l = 1, 2, \ldots, M_T)$ and the scatterer $S^{(mn)}$, whereas $D_R^{(mn,k)}$ is the distance from the scatterer $S^{(mn)}$ to the kth receiver antenna $A_R^{(k)}$ $(k = 1, 2, \ldots, M_R)$. Finally, the symbol $D_{TR}^{(l,k)}$ denotes the length of the LOS path from the lth transmitter antenna to the kth receiver antenna. In our analysis, we assume single-bounce scattering and consider the scattering effects only from the scatterers which are located between the transmitter and receiver. These scatterers are addressed as *effective scatterers*.

III. Reference Model

Here, we present the reference model for the MIMO C2C channel under LOS and NLOS propagation conditions. From the geometrical SCT scattering model the TVTF will be derived and presented as a sum of diffuse, LOS, and specular components.

A. The TVTF

The propagation environment inside the tunnel is characterized by 3D scattering, where $M \cdot N$ effective scatterers $S^{(mn)}$ are randomly distributed on the tunnel wall. The reference model is based on the assumption that the number of local scatterers on the tunnel wall is infinite, i.e., $M, N \to \infty$. The MIMO C2C channel can be described by an $M_R \times M_T$ channel matrix $\mathbf{H}(\tau', t) = [h_{kl}(\tau', t)]_{M_R \times M_T}$, where $h_{kl}(\tau', t)$ denotes the time-variant impulse response. The time-variant impulse response of the reference model can be expressed as

$$h_{kl}(\tau', t) = h_{kl}^{\mathrm{DIF}}(\tau', t) + h_{kl}^{\mathrm{LOS}}(\tau', t) + h_{kl}^{\mathrm{SPE}}(\tau', t) \tag{D.1}$$

where $h_{kl}^{\mathrm{DIF}}(\tau', t)$, $h_{kl}^{\mathrm{LOS}}(\tau', t)$, and $h_{kl}^{\mathrm{SPE}}(\tau', t)$ denote the impulse responses of the diffuse, LOS, and specular components, respectively.

To further simplify the analysis, we will use the TVTF instead of the impulse response. The TVTF is the Fourier transform of the time-variant impulse response $h_{kl}(\tau',t)$ with respect to the propagation delay τ', i.e., $H_{kl}(f',t) = \mathscr{F}_{\tau'}\{h_{kl}(\tau',t)\}$ [38, p. 59]. With reference to (D.1), $H_{kl}(f',t)$ can be presented as

$$H_{kl}(f',t) = H_{kl}^{\mathrm{DIF}}(f',t) + H_{kl}^{\mathrm{LOS}}(f',t) + H_{kl}^{\mathrm{SPE}}(f',t) \tag{D.2}$$

where $H_{kl}^{\mathrm{DIF}}(f',t)$, $H_{kl}^{\mathrm{LOS}}(f',t)$, and $H_{kl}^{\mathrm{SPE}}(f',t)$ denote the diffuse, LOS, and specular components of the TVTF, respectively.

From investigations in [40], it is known that single-bounce scattering components carry more energy than double-bounce scattering components. Therefore, in our analysis, we model the diffuse component $H_{kl}^{\mathrm{DIF}}(f',t)$ by only considering the single-bounce scattering effects. From the geometrical SCT scattering model shown in Fig. D.3, we can observe that the (m,n)th homogeneous plane wave emitted from the lth transmitter antenna element $A_T^{(l)}$ travels over the local scatterer $S^{(mn)}$ before impinging on the kth receiver antenna element $A_R^{(k)}$. Hence, the diffuse component $H_{kl}^{\mathrm{DIF}}(f',t)$ of the TVTF of the link from $A_T^{(l)}$ to $A_R^{(k)}$ can be derived as

$$\begin{aligned} H_{kl}^{\mathrm{DIF}}(f',t) \;=\; & \lim_{\substack{M\to\infty \\ N\to\infty}} \frac{1}{\sqrt{(c_R+1)MN}} \sum_{m,n=1}^{M,N} e^{-j\frac{2\pi}{\lambda}D_{kl}^{(mn)}} \\ & \times e^{j\left[2\pi f^{(mn)}t + \theta^{(mn)} - 2\pi\tau_{kl}^{\prime(mn)}f'\right]} \end{aligned} \tag{D.3}$$

where

$$D_{kl}^{(mn)} \;=\; D_T^{(l,mn)} + D_R^{(mn,k)} \tag{D.4}$$

$$f^{(mn)} \;=\; f_T^{(mn)} + f_R^{(mn)} \tag{D.5}$$

$$f_T^{(mn)} \;=\; f_{T_{\max}} \cos\left(\alpha_T^{(mn)} - \varphi_{\mathrm{v}}^T\right) \cos\left(\beta_T^{(mn)}\right) \tag{D.6}$$

$$f_R^{(mn)} \;=\; f_{R_{\max}} \cos\left(\alpha_R^{(mn)} - \varphi_{\mathrm{v}}^R\right) \cos\left(\beta_R^{(mn)}\right). \tag{D.7}$$

The symbol $D_{kl}^{(mn)}$ in (D.3) denotes the total distance, which a plane wave travels from the lth transmitter antenna element to the kth receiver antenna element via the scatterer $S^{(mn)}$. The total distance $D_{kl}^{(mn)}$ is determined by (D.4) in which the distances $D_T^{(l,mn)}$ and $D_R^{(mn,k)}$ are given by

$$\begin{aligned} D_T^{(l,mn)} \;=\; & D_T^{(mn)} - (M_T - 2l + 1)\frac{\delta_T}{2}\left[\cos\phi_T \cos\left(\beta_T^{(mn)}\right)\cos\left(\gamma_T - \alpha_T^{(mn)}\right)\right. \\ & \left. + \sin\phi_T \sin\left(\beta_T^{(mn)}\right)\right] \end{aligned} \tag{D.8}$$

$$D_R^{(mn,k)} = D_R^{(mn)} - (M_R - 2k + 1)\frac{\delta_R}{2}\left[\cos\phi_R \cos\left(\beta_R^{(mn)}\right)\cos\left(\gamma_R - \alpha_R^{(mn)}\right) + \sin\phi_R \sin\left(\beta_R^{(mn)}\right)\right] \quad \text{(D.9)}$$

respectively, where

$$D_T^{(mn)} = \left[(x_m - x_T)^2 + (y_n - y_T)^2 + (\sqrt{R^2 - y_n^2} - z_T)^2\right]^{\frac{1}{2}} \quad \text{(D.10)}$$

$$D_R^{(mn)} = \left[(x_m - x_R)^2 + (y_n - y_R)^2 + (\sqrt{R^2 - y_n^2} - z_R)^2\right]^{\frac{1}{2}}. \quad \text{(D.11)}$$

In (D.6) and (D.7), the symbols $f_{T_{\max}} = \mathrm{v}_T/\lambda$ and $f_{R_{\max}} = \mathrm{v}_R/\lambda$ denote the maximum Doppler frequencies associated with the transmitter and the receiver, respectively, where λ is the wavelength. The symbol c_R in (D.3) is the summation of the Rice factors c_R^{LOS} and c_R^{SPE}, i.e., $c_R = c_R^{\mathrm{LOS}} + c_R^{\mathrm{SPE}}$. The Rice factors c_R^{LOS} and c_R^{SPE} will be defined in the paragraphs after (D.17) and (D.23), repectively. The phase $\theta^{(mn)}$ in (D.3) denotes the phase shift caused by the interaction of the transmitted plane wave and the effective scatterers $S^{(mn)}$. It is assumed that the phases $\theta^{(mn)}$ are independent, identically distributed (i.i.d.) random variables, which are uniformly distributed over the interval $[0, 2\pi)$. Finally, the symbol $\tau_{kl}^{\prime(mn)}$ in (D.3) denotes the propagation delay of the diffuse component. Using $D_{kl}^{(mn)}$ in (D.4), the propagation delays $\tau_{kl}^{\prime(mn)}$ can be computed as $\tau_{kl}^{\prime(mn)} = D_{kl}^{(mn)}/c_0$, where c_0 is the speed of light. It is worth mentioning that one can easily extend our analysis on the basis of single-bounce scattering to the case of double-bounce scattering by following a similar approach as in [11].

In an analogous manner, the LOS component $H_{kl}^{\mathrm{LOS}}(f', t)$ of the TVTF can be written as

$$H_{kl}^{\mathrm{LOS}}(f', t) = \sqrt{\frac{c_R^{\mathrm{LOS}}}{c_R + 1}} e^{-j\frac{2\pi}{\lambda} D_{TR,\mathrm{LOS}}^{(l,k)}} e^{j2\pi\left[f^{(0)}t - \tau_{kl}^{\prime(0)} f'\right]} \quad \text{(D.12)}$$

where

$$D_{TR,\mathrm{LOS}}^{(l,k)} = D^{(0)} - (M_T - 2l + 1)\frac{\delta_T}{2}\cos\phi_T \cos\gamma_T - (M_R - 2k + 1)\frac{\delta_R}{2}\cos\phi_R \cos\left(\alpha_T^{(0)} - \gamma_R\right) \quad \text{(D.13)}$$

$$D^{(0)} = \left[(x_R - x_T)^2 + (y_R - y_T)^2 + (z_R - z_T)^2\right]^{\frac{1}{2}} \quad \text{(D.14)}$$

$$f^{(0)} = f_T^{(0)} + f_R^{(0)} \quad \text{(D.15)}$$

$$f_T^{(0)} = f_{T_{\max}} \cos\left(\alpha_T^{(0)} - \varphi_{\mathrm{v}}^T\right) \cos\left(\beta_T^{(0)}\right) \tag{D.16}$$

$$f_R^{(0)} = f_{R_{\max}} \cos\left(\alpha_R^{(0)} - \varphi_{\mathrm{v}}^R\right) \cos\left(\beta_R^{(0)}\right). \tag{D.17}$$

In (D.15), $f_T^{(0)}$ and $f_R^{(0)}$ denote the Doppler shifts of the LOS component caused by the movement of the transmitter and the receiver, respectively. The angles $\alpha_T^{(0)}$ ($\beta_T^{(0)}$) and $\alpha_R^{(0)}$ ($\beta_R^{(0)}$) in (D.16) and (D.17) represent the AAOD (EAOD) and the AAOA (EAOA) of the LOS component, respectively. The symbol c_R^{LOS} in (D.12) represents the Rice factor, which is defined as the ratio of the mean power of the LOS component to the mean power of the diffuse component, i.e., $c_R^{\mathrm{LOS}} = E\{|H_{kl}^{\mathrm{LOS}}(f',t)|^2\}/E\{|H_{kl}^{\mathrm{DIF}}(f',t)|^2\}$. In (D.12), the symbol $\tau_{kl}^{\prime(0)}$ stands for the propagation delay of the LOS component. This quantity is given by $\tau_{kl}^{\prime(0)} = D_{TR}^{(l,k)}/c_0$.

Similarly to the LOS component, the specular component $H_{kl}^{\mathrm{SPE}}(f',t)$ of the TVTF $H_{kl}(f',t)$ in (D.2) can be presented as

$$H_{kl}^{\mathrm{SPE}}(f',t) = \sqrt{\frac{c_R^{\mathrm{SPE}}}{c_R+1}} e^{-j\frac{2\pi}{\lambda} D_{TR,\mathrm{SPE}}^{(l,k)}} e^{j2\pi\left[f^{(1)}t - \tau_{kl}^{\prime(1)} f'\right]} \tag{D.18}$$

where

$$\begin{aligned} D_{TR,\mathrm{SPE}}^{(l,k)} = {} & D^{(1)} - (M_T - 2l + 1)\frac{\delta_T}{2}\cos\phi_T \cos\gamma_T \\ & - (M_R - 2k + 1)\frac{\delta_R}{2}\cos\phi_R \cos\left(\alpha_T^{(1)} - \gamma_R\right) \end{aligned} \tag{D.19}$$

$$\begin{aligned} D^{(1)} = {} & \left[(x_s - x_T)^2 + (y_s - y_T)^2 + (\sqrt{R^2 - y_n^2} - z_s)^2\right]^{\frac{1}{2}} \\ & + \left[(x_s - x_R)^2 + (y_s - y_R)^2 + (\sqrt{R^2 - y_n^2} - z_s)^2\right]^{\frac{1}{2}} \end{aligned} \tag{D.20}$$

$$f^{(1)} = f_T^{(1)} + f_R^{(1)} \tag{D.21}$$

$$f_T^{(1)} = f_{T_{\max}} \cos\left(\alpha_T^{(1)} - \varphi_{\mathrm{v}}^T\right) \cos\left(\beta_T^{(1)}\right) \tag{D.22}$$

$$f_R^{(1)} = f_{R_{\max}} \cos\left(\alpha_R^{(1)} - \varphi_{\mathrm{v}}^R\right) \cos\left(\beta_R^{(1)}\right). \tag{D.23}$$

The symbol c_R^{SPE} in (D.18) represents the Rice factor, which is defined as the ratio of the mean power of the specular component to the mean power of the diffuse

component, i.e., $c_R^{\mathrm{SPE}} = E\{|H_{kl}^{\mathrm{SPE}}(f',t)|^2\}/E\{|H_{kl}^{\mathrm{DIF}}(f',t)|^2\}$. The symbol $D_{TR,\mathrm{SPE}}^{(l,k)}$ in (D.18) denotes the travelling distance of the plane wave from the lth transmitter antenna element to the kth receiver antenna element via the specular reflection point $S^{(1)}$. The position of the specular reflection point $S^{(1)}$ is determined by (x_s, y_s, z_s). The symbols $f_T^{(1)}$ and $f_R^{(1)}$ in (D.21) denote the Doppler shifts of the specular component. The angles $\alpha_T^{(1)}$ ($\beta_T^{(1)}$) and $\alpha_R^{(1)}$ ($\beta_R^{(1)}$) in (D.22) and (D.23) represent the AAOD (EAOD) and the AAOA (EAOA) of the specular component, respectively. The symbol $\tau_{kl}^{\prime(1)}$ in (D.18) stands for the propagation delay of the specular component, which is given by $\tau_{kl}^{\prime(1)} = D_{TR,\mathrm{SPE}}^{(l,k)}/c_0$. In analogy to [38, p. 61], the LOS component $H_{kl}^{\mathrm{LOS}}(f',t)$ and the specular component $H_{kl}^{\mathrm{SPE}}(f',t)$ of the TVTF are deterministic processes, while the diffuse component $H_{kl}^{\mathrm{DIF}}(f',t)$ is a stochastic process.

B. The Elevation and the Azimuth Angles

In the reference model, the position of all effective scatterers $S^{(mn)}$ is described by the Cartesian coordinates (x_m, y_n). With reference to Fig. D.3, we take into account that the AAOD $\alpha_T^{(mn)}$ and the AAOA $\alpha_R^{(mn)}$ are dependent. By using trigonometric identities, we can express the AAOD $\alpha_T^{(mn)}$, AAOA $\alpha_R^{(mn)}$, EAOD $\beta_T^{(mn)}$, and EAOA $\beta_R^{(mn)}$ in terms of the coordinates (x_m, y_n) of the position of the scatterers $S^{(mn)}$ as follows:

$$\alpha_i(x_m, y_n) = \begin{cases} f(x_m, y_n), \text{ if } y_n \geq y_i \\ -f(x_m, y_n), \text{ if } y_n < y_i \end{cases} \tag{D.24}$$

$$\beta_i(x_m, y_n) = \begin{cases} -g(x_m, y_n), \text{ if } \sqrt{R^2 - y_n^2} < z_i \\ g(x_m, y_n), \text{ if } \sqrt{R^2 - y_n^2} \geq z_i \end{cases} \tag{D.25}$$

where the index i refers to the transmitter (receiver) if $i = T$ ($i = R$). The functions $f(x,y)$ and $g(x,y)$ are given by

$$f(x_m, y_n) = \arccos\left(\frac{(x_m - x_i)}{\sqrt{(x_m - x_i)^2 + (y_n - y_i)^2}}\right) \tag{D.26}$$

and

$$g(x_m, y_n) = \arccos\left(\frac{\sqrt{(x_m - x_i)^2 + (y_n - y_i)^2}}{\sqrt{(x_m - x_i)^2 + (y_n - y_i)^2 + (\sqrt{R^2 - y_n^2} - z_i)^2}}\right) \tag{D.27}$$

respectively.

IV. Correlation Properties of the Reference Model

Here, we derive a general analytical solution for the STF-CCF, which will then be used to compute the 2D space CCF, the 2D TF-CCF, the temporal ACF, and the FCF.

A. The STF-CCF

Using (D.2), the STF-CCF between the TVTFs $H_{kl}(f',t)$ and $H_{k'l'}(f',t)$ can be expressed as

$$\begin{aligned}\rho_{kl,k'l'}(\delta_T,\delta_R,\nu',\tau) &:= E\{H^*_{kl}(f',t)H_{k'l'}(f'+\nu',t+\tau)\}\\ &= \rho^{\mathrm{DIF}}_{kl,k'l'}(\delta_T,\delta_R,\nu',\tau)+\rho^{\mathrm{LOS}}_{kl,k'l'}(\delta_T,\delta_R,\nu',\tau)\\ &\quad+\rho^{\mathrm{SPE}}_{kl,k'l'}(\delta_T,\delta_R,\nu',\tau) \qquad \text{(D.28)}\end{aligned}$$

where $(*)$ denotes the complex conjugate, and $E\{\cdot\}$ stands for the expectation operator that applies to all random variables: The phases $\theta^{(mn)}$ and the coordinates x_m and y_n defining the position of the scatterers $S^{(mn)}$.

Using (D.3), the STF-CCF $\rho^{\mathrm{DIF}}_{kl,k'l'}(\delta_T,\delta_R,\nu',\tau)$ of the diffuse component $H^{\mathrm{DIF}}_{kl}(f',t)$ can be expressed as

$$\begin{aligned}\rho^{\mathrm{DIF}}_{kl,k'l'}(\delta_T,\delta_R,\nu',\tau) &= \lim_{\substack{M\to\infty\\N\to\infty}}\frac{1}{(c_R+1)MN}\sum_{m,n=1}^{M,N}E\Big\{c^{(mn)}_{ll'}d^{(mn)}_{kk'}\\ &\quad\times e^{j2\pi\left[f^{(mn)}\tau-\tau'^{(mn)}_{kl}\nu'\right]}\Big\} \qquad \text{(D.29)}\end{aligned}$$

where

$$\begin{aligned}c^{(mn)}_{ll'} &= e^{j2\pi\frac{\delta_T}{\lambda}(l-l')\cos\phi_T\cos\left(\beta^{(mn)}_T\right)\cos\left(\gamma_T-\alpha^{(mn)}_T\right)}\\ &\quad\times e^{j2\pi\frac{\delta_T}{\lambda}(l-l')\sin\phi_T\sin\left(\beta^{(mn)}_T\right)} \qquad \text{(D.30)}\\ d^{(mn)}_{kk'} &= e^{j2\pi\frac{\delta_R}{\lambda}(k-k')\cos\phi_R\cos\left(\beta^{(mn)}_R\right)\cos\left(\gamma_R-\alpha^{(mn)}_R\right)}\\ &\quad\times e^{j2\pi\frac{\delta_R}{\lambda}(k-k')\sin\phi_R\sin\left(\beta^{(mn)}_R\right)}. \qquad \text{(D.31)}\end{aligned}$$

The expression above has been obtained by averaging over the random phases $\theta^{(mn)}$. Here, it is important to note that the quantities $c^{(mn)}_{ll'}$, $d^{(mn)}_{kk'}$, $f^{(mn)}$ and $\tau'^{(mn)}_{kl}$ are functions of the coordinates x_m and y_n. The random variables x_m and y_n are supposed to be uniformly i.i.d., such that their probability density functions (PDFs)

are given by [37]

$$p_{x_m}(x) = \frac{1}{(x_R - x_T)}, \text{ if } x \in [x_T, x_R] \tag{D.32}$$

$$p_{y_n}(y) = \frac{1}{2R}, \qquad \text{if } y \in (-R, R) \tag{D.33}$$

respectively. Hence, the joint PDF $p_{x_m y_n}(x,y)$ of the random variables x_m and y_n can be expressed as the product of the marginal PDFs $p_{x_m}(x)$ and $p_{y_n}(y)$, i.e.,

$$\begin{aligned} p_{x_m y_n}(x,y) &= p_{x_m}(x) \cdot p_{y_n}(y) \\ &= \frac{1}{2R(x_R - x_T)}, \text{ if } x \in [x_T, x_R],\ y \in (-R, R). \end{aligned} \tag{D.34}$$

The infinitesimal power of the diffuse component corresponding to the differential coordinates dx and dy is proportional to $p_{x_m y_n}(x,y)dxdy$. In the limit as $M, N \to \infty$, this infinitesimal contribution must be equal to $1/(MN)$, i.e., $1/(MN) = p_{x_m y_n}(x,y)dxdy$. Consequently, the STF-CCF $\rho^{\text{DIF}}_{kl,k'l'}(\delta_T, \delta_R, \nu', \tau)$ of the diffuse component in (D.29) can be written as

$$\begin{aligned} \rho^{\text{DIF}}_{kl,k'l'}(\delta_T, \delta_R, \nu', \tau) = \frac{1}{2R(x_R - x_T)(c_R + 1)} \int_{-R}^{R} \int_{x_T}^{x_R} & c_{ll'}(x,y) d_{kk'}(x,y) \\ & \times e^{j2\pi\left[f(x,y)\tau - \tau'_{kl}(x,y)\nu'\right]} dxdy \end{aligned} \tag{D.35}$$

where

$$c_{ll'}(x,y) = e^{j2\pi \frac{\delta_T}{\lambda}(l-l')\cos\phi_T \cos(\beta_T(x,y))\cos(\gamma_T - \alpha_T(x,y))} \times e^{j2\pi \frac{\delta_T}{\lambda}(l-l')\sin\phi_T \sin(\beta_T(x,y))} \tag{D.36}$$

$$d_{kk'}(x,y) = e^{j2\pi \frac{\delta_R}{\lambda}(k-k')\cos\phi_R \cos(\beta_R(x,y))\cos(\gamma_R - \alpha_R(x,y))} \times e^{j2\pi \frac{\delta_R}{\lambda}(k-k')\sin\phi_R \sin(\beta_R(x,y))} \tag{D.37}$$

$$f(x,y) = f_T(x,y) + f_R(x,y) \tag{D.38}$$

$$f_T(x,y) = f_{T_{\max}} \cos\left(\alpha_T(x,y) - \varphi_{\text{v}}^T\right) \cos(\beta_T(x,y)) \tag{D.39}$$

$$f_R(x,y) = f_{R_{\max}} \cos\left(\alpha_R(x,y) - \varphi_{\text{v}}^R\right) \cos(\beta_R(x,y)) \tag{D.40}$$

$$\tau'_{kl}(x,y) = \frac{1}{c_0}\left(D_T^{(l)}(x,y) + D_R^{(k)}(x,y)\right). \tag{D.41}$$

By using the functions in (D.8) and (D.9), the distances $D_T^{(l)}(x,y)$ and $D_R^{(k)}(x,y)$ in (D.35) can be expressed as

$$D_T^{(l)}(x,y) = D_T(x,y) - (M_T - 2l + 1)\frac{\delta_T}{2}\Big[\cos\phi_T \cos\left(\beta_T(x,y)\right)\cos\left(\gamma_T - \alpha_T(x,y)\right) + \sin\phi_T \sin\left(\beta_T(x,y)\right)\Big] \tag{D.42}$$

$$D_R^{(k)}(x,y) = D_R(x,y) - (M_R - 2k + 1)\frac{\delta_R}{2}\Big[\cos\phi_R \cos\left(\beta_R(x,y)\right)\cos\left(\gamma_R - \alpha_R(x,y)\right) + \sin\phi_R \sin\left(\beta_R(x,y)\right)\Big] \tag{D.43}$$

respectively, where

$$D_T(x,y) = \left[(x - x_T)^2 + (y - y_T)^2 + (\sqrt{R^2 - y^2} - z_T)^2\right]^{\frac{1}{2}} \tag{D.44}$$

$$D_R(x,y) = \left[(x - x_R)^2 + (y - y_R)^2 + (\sqrt{R^2 - y^2} - z_R)^2\right]^{\frac{1}{2}}. \tag{D.45}$$

In (D.39) and (D.40), we recall that the AAOD (AAOA) $\alpha_T(x,y)$ ($\alpha_R(x,y)$) and the EAOD (EAOA) $\beta_T(x,y)$ ($\beta_R(x,y)$) are functions of the coordinates (x,y) of the scatterers according to (D.24) and (D.25), respectively.

The STF-CCF $\rho_{kl,k'l'}^{\mathrm{LOS}}(\delta_T, \delta_R, \nu', \tau)$ of the LOS component can be expressed as

$$\rho_{kl,k'l'}^{\mathrm{LOS}}(\delta_T, \delta_R, \nu', \tau) = \frac{c_R}{c_R + 1} c_{ll'}^{(0)} d_{kk'}^{(0)} e^{j2\pi\left(f^{(0)}\tau - \tau_{kl}'^{(0)}\nu'\right)} \tag{D.46}$$

where

$$c_{ll'}^{(0)} = e^{j2\pi\frac{\delta_T}{\lambda}(l - l')\cos\phi_T \cos\gamma_T} \tag{D.47}$$

$$d_{kk'}^{(0)} = e^{j2\pi\frac{\delta_R}{\lambda}(k - k')\cos\phi_R \cos\left(\alpha_R^{(0)} - \gamma_R\right)}. \tag{D.48}$$

Analogously to the LOS component, the STF-CCF $\rho_{kl,k'l'}^{\mathrm{SPE}}(\delta_T, \delta_R, \nu', \tau)$ of the specular component can be presented as

$$\rho_{kl,k'l'}^{\mathrm{SPE}}(\delta_T, \delta_R, \nu', \tau) = \frac{c_R^{\mathrm{SPE}}}{c_R + 1} c_{ll'}^{(1)} d_{kk'}^{(1)} e^{j2\pi\left(f^{(1)}\tau - \tau_{kl}'^{(1)}\nu'\right)} \tag{D.49}$$

where

$$c_{ll'}^{(1)} = e^{j2\pi\frac{\delta_T}{\lambda}(l - l')\cos\phi_T \cos\gamma_T} \tag{D.50}$$

$$d_{kk'}^{(1)} = e^{j2\pi\frac{\delta_R}{\lambda}(k - k')\cos\phi_R \cos\left(\alpha_R^{(1)} - \gamma_R\right)}. \tag{D.51}$$

B. 2D Space CCF

The 2D space CCF $\rho_{kl,k'l'}(\delta_T,\delta_R)$ is defined as $\rho_{kl,k'l'}(\delta_T,\delta_R) := E\{H^*_{kl}(f',t)\ H_{k'l'}(f',t)\}$, which is equal to the STF-CCF $\rho_{kl,k'l'}(\delta_T,\delta_R,\nu',\tau)$ at $\nu'=0$ and $\tau=0$, i.e., $\rho_{kl,k'l'}(\delta_T,\delta_R)=\rho_{kl,k'l'}(\delta_T,\delta_R,0,0)$. Hence, the 2D space CCF can be presented as

$$\begin{aligned}\rho_{kl,k'l'}(\delta_T,\delta_R) \;=\; & \frac{1}{2R(x_R-x_T)(c_R+1)}\int_{-R}^{R}\int_{x_T}^{x_R} c_{ll'}(x,y)d_{kk'}(x,y)dxdy \\ & +\frac{c_R^{\mathrm{LOS}}}{c_R+1}c_{ll'}^{(0)}d_{kk'}^{(0)}+\frac{c_R^{\mathrm{SPE}}}{c_R+1}c_{ll'}^{(1)}d_{kk'}^{(1)}. \end{aligned} \tag{D.52}$$

C. The 2D TF-CCF

The 2D TF-CCF of the reference model is defined as the correlation of the TVTFs $H_{kl}(f',t)$ and $H_{kl}(f',t)$, i.e., $\rho_{kl}(\nu',\tau) := E\{H^*_{kl}(f',t)\ H_{kl}(f'+\nu',t+\tau)\}$. The 2D TF-CCF $\rho_{kl}(\nu',\tau)$ can easily be obtained from the STF-CCF $\rho_{kl,k'l'}(\delta_T,\delta_R,\nu',\tau)$ by setting the antenna element spacings δ_T and δ_R to zero, i.e., $\rho_{kl}(\nu',\tau)=\rho_{kl,k'l'}(0,0,\nu',\tau)$. Thus,

$$\begin{aligned}\rho_{kl}(\nu',\tau) \;=\; & \frac{1}{2R(x_R-x_T)(c_R+1)}\int_{-R}^{R}\int_{x_T}^{x_R} e^{j2\pi\left(f(x,y)\tau-\tau'_{kl}(x,y)\nu'\right)}dxdy \\ & +\frac{c_R^{\mathrm{LOS}}}{c_R+1}e^{j2\pi\left(f^{(0)}\tau-\tau_{kl}'^{(0)}\nu'\right)}+\frac{c_R^{\mathrm{SPE}}}{c_R+1}e^{j2\pi\left(f^{(1)}\tau-\tau_{kl}'^{(1)}\nu'\right)}. \end{aligned} \tag{D.53}$$

From the 2D TF-CCF two further correlation functions can be derived, such as the temporal ACF and the FCF.

D. Temporal ACF

The temporal ACF of the TVTF $H(f',t)$ of the transmission link from $A_T^{(l)}$ $(l=1,2,\ldots,M_T)$ to $A_R^{(k)}$ $(k=1,2,\ldots,M_R)$ is defined by $r_{kl}(\tau) := E\{H^*_{kl}(f',t)H_{kl}(f',t+\tau)\}$ [41, p. 376]. Alternatively, the temporal ACF $r_{kl}(\tau)$ can be obtained directly from the 2D TF-CCF $\rho_{kl}(\nu',\tau)$ by setting the frequency separation variable ν' to zero, i.e., $r_{kl}(\tau)=\rho_{kl}(0,\tau)$. In both cases, we obtain

$$\begin{aligned} r_{kl}(\tau) \;=\; & \frac{1}{2R(x_R-x_T)(c_R+1)}\int_{-R}^{R}\int_{x_T}^{x_R} e^{j2\pi f(x,y)\tau}dxdy \\ & +\frac{c_R^{\mathrm{LOS}}}{c_R+1}e^{j2\pi f^{(0)}\tau}+\frac{c_R^{\mathrm{SPE}}}{c_R+1}e^{j2\pi f^{(1)}\tau} \end{aligned} \tag{D.54}$$

for $k = 1,2,\ldots,M_R$ and $l = 1,2,\ldots,M_T$. Note that the temporal ACF $r_{kl}(\tau)$ in (D.54) is independent of k and l, which means that all TVTFs $H_{kl}(f',t)$ modelling the link from $A_T^{(l)}$ to $A_R^{(k)}$ are characterized by the same temporal ACF $r_{kl}(\tau)$ for all $k = 1,2,\ldots,M_R$ and $l = 1,2,\ldots,M_T$.

E. The FCF

The FCF of the TVTFs $H_{kl}(f',t)$ and $H_{kl}(f'+\nu',t)$ is defined by $r_{kl}(\nu') := E\{H_{kl}^*(f',t)H_{kl}(f'+\nu',t)\}$ [41, p. 376], which is equal to the 2D TF-CCF $\rho_{kl}(\nu',\tau)$ at $\tau = 0$, i.e., $r_{kl}(\nu') = \rho_{kl}(\nu',0)$. Thus, the FCF can be written as

$$\begin{aligned} r_{kl}(\nu') \;=\; & \frac{1}{2R(x_R - x_T)(c_R+1)} \int_{-R}^{R} \int_{x_T}^{x_R} e^{-j2\pi\tau'_{kl}(x,y)\nu'} dxdy \\ & + \frac{c_R^{\mathrm{LOS}}}{c_R+1} e^{-j2\pi\tau_{kl}^{\prime(0)}\nu'} + \frac{c_R^{\mathrm{SPE}}}{c_R+1} e^{-j2\pi\tau_{kl}^{\prime(1)}\nu'}. \end{aligned} \tag{D.55}$$

In contrast to the temporal ACF $r_{kl}(\tau)$, the FCF $r_{kl}(\nu')$ depends on k and l due to the propagation delays $\tau'_{kl}(x,y)$, $\tau_{kl}^{\prime(0)}$, and $\tau_{kl}^{\prime(1)}$. However, by assuming that the antenna element spacing of the transmitter (receiver) antenna array δ_T (δ_R) is small in comparison to the radius R of the tunnel arch, we can take profit from the inequality $\max\{\delta_T,\delta_R\} \ll R$. Consequently, the total travelling distance $D_{kl}^{(mn)}$ in (D.4) can be approximated as

$$D_{kl}^{(mn)} \;\approx\; D_T^{(mn)} + D_R^{(mn)} \tag{D.56}$$

where $D_T^{(mn)}$ and $D_R^{(mn)}$ are given in (D.10) and (D.11), respectively. Thus, the propagation delays $\tau'_{kl}(x,y)$, $\tau_{kl}^{\prime(0)}$, and $\tau_{kl}^{\prime(1)}$ will be independent of k and l.

F. The Doppler power spectral density

The Doppler power spectral density (PSD) is the Fourier transform of the temporal ACF $r_{kl}(\tau)$ with respect to τ, i.e., $S_f(f) = \mathscr{F}_\tau\{r_{kl}(\tau)\}$ [38, Sec. 3.3]. Hence, the Doppler PSD can be presented as

$$S_f(f) = \int_{-\infty}^{\infty} r_{kl}(\tau) e^{-j2\pi f\tau} d\tau. \tag{D.57}$$

The two most important statistical quantities characterizing the Doppler PSD $S_f(f)$ are the *average Doppler shift* $B_f^{(1)}$ and the *Doppler spread* $B_f^{(2)}$ [38, Sec. 3.3]. The average Doppler shift $B_f^{(1)}$ describes the average frequency shift that a carrier frequency experiences during the transmission over a multipath fading channel. The average Doppler shift is defined as the first moment of $S_f(f)$, which can be

expressed as follows

$$B_f^{(1)} = \frac{\int_{-\infty}^{\infty} f S_f(f) df}{\int_{-\infty}^{\infty} S_f(f) df}. \tag{D.58}$$

The Doppler spread $B_f^{(2)}$ describes the frequency spread that a carrier frequency experiences during the transmission over a multipath fading channel. The Doppler spread is defined as the square root of the second central moment of $S_f(f)$, i.e.,

$$B_f^{(2)} = \sqrt{\frac{\int_{-\infty}^{\infty} \left(f - B_f^{(1)}\right)^2 S_f(f) df}{\int_{-\infty}^{\infty} S_f(f) df}}. \tag{D.59}$$

According to [38, Sec. 3.3], the average Doppler shift $B_f^{(1)}$ and the Doppler spread $B_f^{(2)}$ can alternatively be computed by using Fourier transform techniques enabling to express these quantities in terms of the ACF $r_{kl}(\tau)$ and its first and second time derivatives at the origin as follows:

$$B_f^{(1)} = \frac{1}{2\pi j} \cdot \frac{\dot{r}_{kl}(0)}{r_{kl}(0)} \tag{D.60}$$

$$B_f^{(2)} = \frac{1}{2\pi} \sqrt{\left(\frac{\dot{r}_{kl}(0)}{r_{kl}(0)}\right)^2 - \frac{\ddot{r}_{kl}(0)}{r_{kl}(0)}}. \tag{D.61}$$

G. Power Delay Profile

The power delay profile (PDP) measures the average power associated with a given multipath delay τ'_{kl}. The PDP is the inverse Fourier transform of the FCF with respect to ν', i.e., $S_{\tau'_{kl}}(\tau'_{kl}) = \mathscr{F}_{\nu'}^{-1}\{r_{kl}(\nu')\}$ [38, Sec. 7.3]. Hence, the PDP can be expressed as

$$S_{\tau'_{kl}}(\tau'_{kl}) = \int_{-\infty}^{\infty} r_{kl}(\nu') e^{j2\pi\nu'\tau'_{kl}} d\nu'. \tag{D.62}$$

From the PDP $S_{\tau'_{kl}}(\tau'_{kl})$, we can derive two other important characteristic quantities, namely the *average delay* and the *delay spread*. The average delay is denoted by

$B^{(1)}_{\tau'_{kl}}$ and defined as the first moment of the PDP $S_{\tau'_{kl}}(\tau'_{kl})$, i.e.,

$$B^{(1)}_{\tau'_{kl}} = \frac{\int_0^\infty \tau'_{kl} S_{\tau'_{kl}}(\tau'_{kl}) d\tau'_{kl}}{\int_0^\infty S_{\tau'_{kl}}(\tau'_{kl}) d\tau'_{kl}}. \tag{D.63}$$

The delay spread is denoted by $B^{(2)}_{\tau'_{kl}}$ and defined by the square root of the second central moment of $S_{\tau'_{kl}}(\tau'_{kl})$, i.e.,

$$B^{(2)}_{\tau'_{kl}} = \sqrt{\frac{\int_0^\infty \left(\tau'_{kl} - B^{(1)}_{\tau'_{kl}}\right)^2 S_{\tau'_{kl}}(\tau'_{kl}) d\tau'_{kl}}{\int_0^\infty S_{\tau'_{kl}}(\tau'_{kl}) d\tau'_{kl}}}. \tag{D.64}$$

Alternatively, the equivalent expressions for $B^{(1)}_{\tau'_{kl}}$ and $B^{(2)}_{\tau'_{kl}}$ can be obtained by using Fourier transform techniques, which allows us to present the average delay $B^{(1)}_{\tau'_{kl}}$ and the delay spread $B^{(2)}_{\tau'_{kl}}$ in terms of the FCF $r_{kl}(\nu')$ as well as its first and second frequency derivative at the origin as [38, p. 64]

$$B^{(1)}_{\tau'_{kl}} = \frac{1}{2\pi j} \cdot \frac{\dot{r}_{kl}(0)}{r_{kl}(0)} \tag{D.65}$$

and

$$B^{(2)}_{\tau'_{kl}} = \frac{1}{2\pi} \sqrt{\left(\frac{\dot{r}_{kl}(0)}{r_{kl}(0)}\right)^2 - \frac{\ddot{r}_{kl}(0)}{r_{kl}(0)}}. \tag{D.66}$$

It is worth mentioning that owing to the inequality $\max\{\delta_T, \delta_R\} \ll R$, both the average delay $B^{(1)}_{\tau'_{kl}}$ and the delay spread $B^{(2)}_{\tau'_{kl}}$ can be independent of k and l.

V. Simulation Model

Here, we describe the simulation model and we provide some background information on the parametrization methods usually used to determine the parameters of the simulation model. Furthermore, we also present a measurement-oriented method for the computation of the model parameters.

A. Description of the Simulation Model

The reference model presented in Section III is an analytical model, which assumes an infinite number of scatterers ($M, N \to \infty$). Owing to the practical imple-

mentation complexity, the reference model is non-realizable. However, the reference model described in Section III can serve as a starting point for the derivation of stochastic and deterministic simulation models. Using the generalized principle of deterministic channel modelling [38, Sec. 8.1], a stochastic simulation model can be obtained from the reference model described by (D.2) by using only a finite number of scatterers. By employing this concept, an accurate and efficient channel simulator can be designed, which allows us to reproduce the statistical properties of the reference model with high accuracy controlled by M and N. Several different models are available that can be used for the simulation of mobile radio channels. Here, we have used an SOC model, which allows the efficient modelling and simulation of mobile radio channels under realistic nonisotropic scattering conditions. A detailed description of SOC models can be found in [42] and [43]. In the literature, several parametrization techniques for SOC models have been proposed, such as the extended method of exact Doppler spread (EMEDS) [6], the LPNM [42], and the generalized method of equal areas (GMEA) [44]. In our proposed model, we computed the model parameters by using the LPNM, which is one of the best parameter computation methods for the design of SOC channel simulators.

B. The Measurement-Based Computation of the Model Parameters

In this section, we determine the set of model parameters $\mathscr{P} = \{R, x_T, y_T, z_T, x_R, y_R, z_R, c_R\}$ describing the SCT scattering model in such a way that the Doppler spread $B_f^{(2)}$ and the delay spread $B_{\tau_{kl}}^{(2)}$ of the reference model in (D.61) and (D.66) match the corresponding Doppler spread $B_f^{\star(2)}$ and delay spread $B_{\tau_{kl}}^{\star(2)}$ of the measured channel, respectively. To find the set of model parameters $\mathscr{P}$, we minimize the error function

$$E_{\min} = W_1 E_1 + W_2 E_2 \tag{D.67}$$

where W_1 and W_2 denote the weighting factors. The symbols E_1 and E_2 in (D.67) stand for the absolute errors of the Doppler spread and the delay spread, respectively, which are defined as

$$E_1 = \arg\min_{\mathscr{P}} \left| B_f^{\star(2)} - B_f^{(2)} \right| \tag{D.68}$$

$$E_2 = \arg\min_{\mathscr{P}} \left| B_{\tau_{kl}'}^{\star(2)} - B_{\tau_{kl}'}^{(2)} \right| . \tag{D.69}$$

In (D.68) and (D.69), the notation $\arg\min_x f(x)$ denotes the set of elements that achieve the global minimum of $f(x)$. At the beginning of the optimization proce-

dure, the weighting factors W_1 and W_2 are selected such that they satisfy the equality $W_1 + W_2 = 1$. There is a scarcity of measured channels with respect to both delay statistics and the Doppler statistics in tunnel environments. Therefore, we use only the delay spread of the measured channel reported in [36]. Thus, we have set the weighting factor W_1 to zero, implying that the error function $E_{\min}$ in (D.67) equals $E_{\min} = E_2$.

By using the measured channel in [36], we have computed the measurement-based model parameters under two different scenarios, called Scenarios I and II. Scenarios I and II stand for the cases where the transmitter antenna height $z_T^\star$ is set to 8 and 2.5 m, respectively, while the receiver antenna height $z_R^\star$ equals 2.5 m for both cases. For Scenario I, two points were used for the mobile receiver MS_R in the x-axis, i.e., $x_R^\star = \{25, 50\}$. However, for Scenario II, we have considered only one point for MS_R in the x-axis, where MS_T and MS_R were separated from each other by 50 m, i.e., $x_R^\star = 50$. For the computation of the model parameters, we have considered 200 scatterers (cisoids), i.e., $M \times N = 10 \times 20$. For the measured channels in [36], the measured delay spreads $B^{\star(2)}_{\tau'_{kl}}$ are presented for two different scenarios in Table D.1. In the same table, we have also presented the resulting optimized model parameters and the corresponding delay spreads $B^{(2)}_{\tau'_{kl}}$. From the results found for the simulation model, we observe an excellent fitting of delay spreads of the simulation model to those of the measured channel, which proves the validity of the proposed SCT scattering C2C channel simulator. It is worth mentioning that not only the delay spreads but also the transmitter and receiver antenna heights closely agree with those used in the measured equipment (see Table D.1).

VII. Numerical Results

Here, we present numerical results obtained by evaluating (D.52)–(D.55) and (D.66). The correctness of the analytical results will be verified by simulations. The performance of the tunnel channel simulator has been assessed by comparing the temporal ACF and the FCF with the corresponding correlation functions of the reference model described by (D.54) and (D.55), respectively.

As our geometrical scattering model, we consider a SCT with a radius of $R = 5\,\mathrm{m}$ and a length of $L = 100\,\mathrm{m}$. With reference to Fig. D.3, the locations of the transmitter and the receiver are defined by the Cartesian coordinates $(x_T, y_T, z_T) = (20\,\mathrm{m}, 2\,\mathrm{m}, 1\mathrm{m})$ and $(x_R, y_R, z_R) = (40\,\mathrm{m}, 2\,\mathrm{m}, 1\,\mathrm{m})$, respectively. For the reference model, all numerical results have been obtained by choosing the following parameters: $\varphi_{\mathrm{v}}^T = \varphi_{\mathrm{v}}^R = 0^\circ$, $\phi_T = \phi_R = 45^\circ$, $\gamma_T = \gamma_R = 45^\circ$, and $f_{T_{\max}} = f_{R_{\max}} = 91\,\mathrm{Hz}$.

Table D.1: Measurement-based parameters of the SCT scattering model and the resulting delay spread.

SCT model parameters	**Scenario I** $z_T^\star = 8$ m $z_R^\star = 2.5$ m [36]		**Scenario II** $z_T^\star = 2.5$ m $z_R^\star = 2.5$ m [36]
	$x_R^\star = 25$ m	$x_R^\star = 50$ m	$x_R^\star = 50$ m
R (m)	9.87	6.83	7.14
x_T (m)	0.01	0.01	0.012
y_T (m)	0.01	0.01	0.01
z_T (m)	8.2	7.9	2.57
x_R (m)	22.4	54.66	53.9
y_R (m)	0.01	0.01	0.01
z_R (m)	2.7	2.64	2.62
c_R	0.5	0.51	0.52
Measured delay spread $B_{\tau'_{kl}}^{\star(2)}$ (ns) [36]	10	5	5
Theoretical delay spread $B_{\tau'_{kl}}^{(2)}$ (ns)	10	5	5

In [20], it is stated that the LOS component may contain more than just the true LOS signal, for example, the ground specular component. In our numerical studies, for the sake of simplicity, we do not take into account the effect of the specular component, i.e., c_R^{SPE} is set to zero. Thus, the Rice factor c_R equals $c_R = c_R^{\mathrm{LOS}} + c_R^{\mathrm{SPE}} = c_R^{\mathrm{LOS}}$, which was chosen from the set $\{0, 0.5, 1\}$. The effective scatterers are randomly distributed on the SCT wall over a length of $x_R - x_T = 20\,\mathrm{m}$. The LPNM has been used to optimize the parameters of the simulation model by assuming a finite number of scatterers (cisoids). For the simulation model, the number of scatterers was set to $M \times N = 30 \times 20$.

The absolute value of the 2D space CCF $|\rho_{11,22}(\delta_T, \delta_R)|$ of the reference model has been computed by using (D.52). The obtained results are illustrated in Fig. D.4 for an NLOS ($c_R = 0$) propagation scenario. We can observe that the 2D space CCF $|\rho_{11,22}(\delta_T, \delta_R)|$ decreases as the antenna element spacings δ_T and δ_R increase. For comparison reasons, the absolute value of the 2D space CCF is depicted in

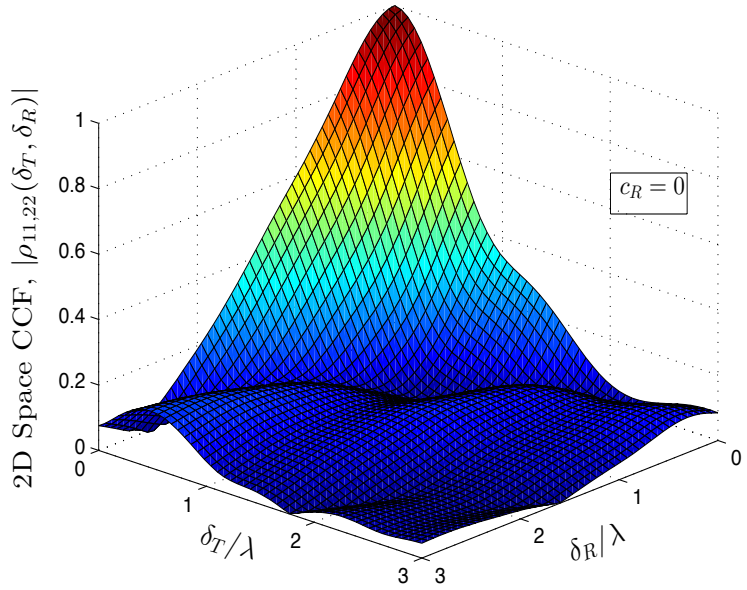

Figure D.4: Absolute value of the 2D space CCF $|\rho_{1122}(\delta_T,\delta_R)|$ of the reference model for an NLOS propagation scenario ($c_R = 0$).

Fig. D.5 for a LOS ($c_R = 1$) propagation scenario. As can be seen in Fig. D.5, under LOS propagation conditions, the TVTFs $H(f',t)$ and $H(f'+\nu',t+\tau)$ are highly correlated even for relatively large antenna element spacings.

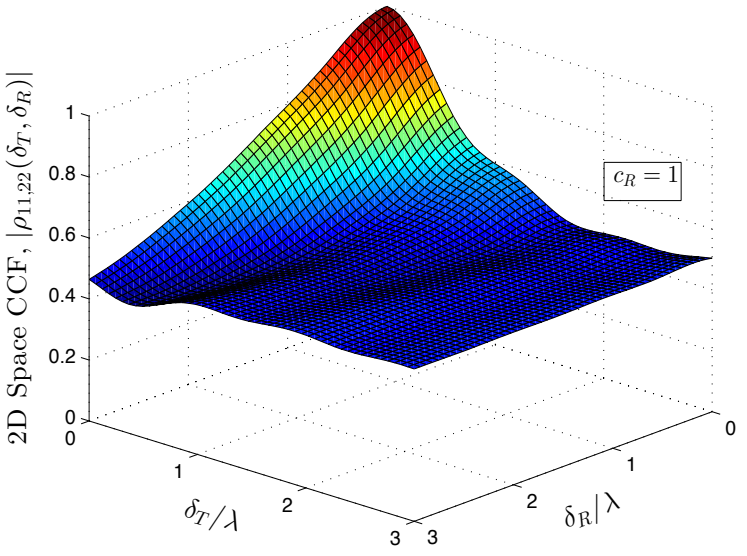

Figure D.5: Absolute value of the 2D space CCF $|\rho_{1122}(\delta_T,\delta_R)|$ of the reference model for a LOS propagation scenario ($c_R = 1$).

Similarly, the absolute value of the 2D TF-CCF $|\rho_{11}(\nu',\tau)|$ of the reference model has been evaluated by using (D.53). Figs. D.6 and D.7 illustrate the results

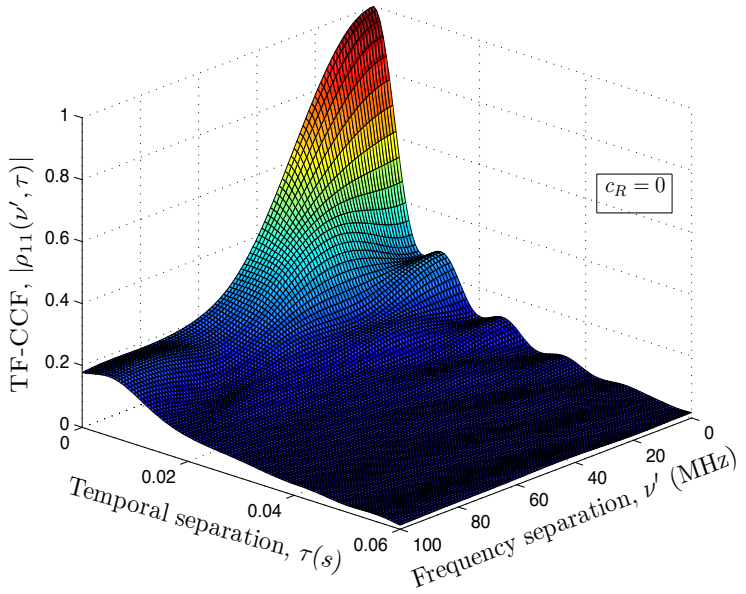

Figure D.6: Absolute value of the 2D TF-CCF $|\rho_{11}(\nu',\tau)|$ of the reference model for an NLOS propagation scenario ($c_R = 0$).

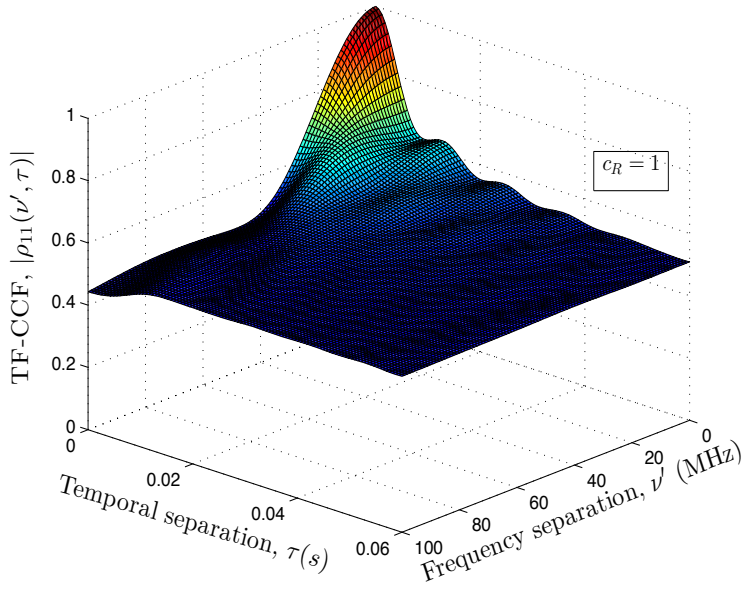

Figure D.7: Absolute value of the 2D TF-CCF $|\rho_{11}(\nu',\tau)|$ of the reference model for a LOS propagation scenario ($c_R = 1$).

for NLOS ($c_R = 0$) and LOS propagation scenarios. Regarding the influence of a LOS component, the 2D TF-CCF $|\rho_{11}(\nu',\tau)|$ behaves similar as the 2D space CCF.

Fig. D.8 shows the absolute value of the temporal ACF $|r_{kl}(\tau)|$ for the case that the transmitter and the receiver are moving with the same speed in the same direction. A good match between the temporal ACF of the reference model and the

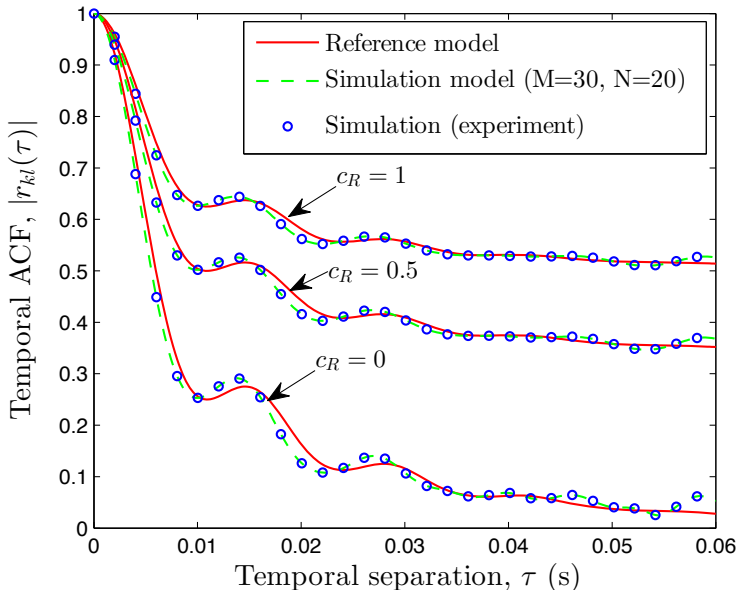

Figure D.8: Absolute value of the temporal ACF $|r_{kl}(\tau)|$ of the reference model and the temporal ACF of the simulation model for different Rice factors c_R.

simulation model can be observed. Fig. D.8 demonstrates also that the experimental simulation results of the temporal ACF match very well with the theoretical results. The experimental results have been obtained by computing the time average of the deterministic SCT simulation model making use of MATLAB function *xcorr.m*.

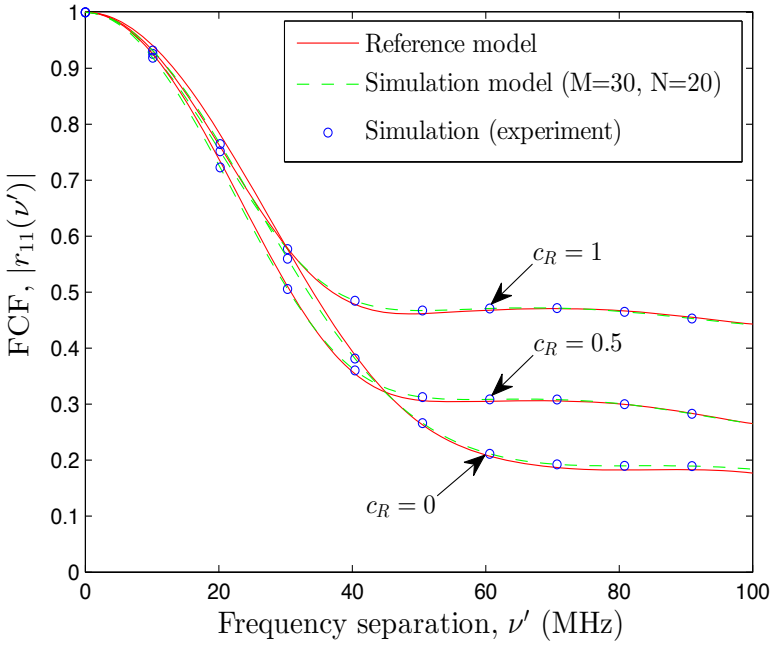

Figure D.9: Absolute value of the FCF $|r_{11}(\nu')|$ of the reference model and the FCF of the simulation model for different Rice factors c_R.

Fig. D.9 shows the absolute value of the FCF $|r_{11}(\nu')|$ for the same scenario. A good agreement between the FCF of the reference model and the simulation model can be seen. Again, it can be observed that the experimental simulation results of the FCF match very well with the theoretical ones. From Fig. D.9, we can conclude that our proposed SCT scattering model can be considered as a frequency-nonselective channel model for dedicated short-range communications (DSRC) systems [14], where the system bandwidth is 10 MHz. In both Figs. D.8 and D.9, we can observe that the approximation errors caused by a limited number of scatterers (cisoids) M and N can in general be neglected in the presented domains of τ and ν' if $M \geq 30$ and $N \geq 20$.

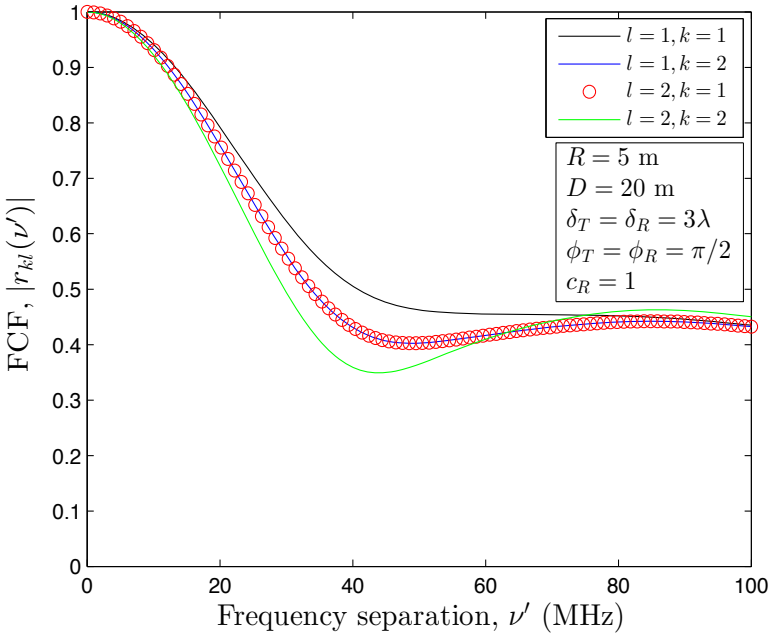

Figure D.10: Absolute value of the FCF $|r_{kl}(\nu')|$ of the reference model for different transmission links $A_T^{(l)} - A_R^{(k)}$ $(l,k = 1,2)$ under LOS propagation conditions ($c_R = 1$).

In Fig. D.10, the absolute value of the FCF $|r_{kl}(\nu')|$ is shown for different transmission links $A_T^{(l)} - A_R^{(k)}$ $(l,k = 1,2)$ under LOS propagation conditions. It is interesting to see that the FCF $|r_{kl}(\nu')|$ has the same curves for the transmission links $A_T^{(1)} - A_R^{(2)}$ and $A_T^{(2)} - A_R^{(1)}$, which shows the symmetrical positions of the mobile transmitter and the mobile receiver.

Figures D.11 and D.12 present the delay spread $B_{\tau'_{kl}}^{(2)}$ evaluated by using (D.66) for different values of the SCT arch radius R under NLOS and LOS propagation conditions, respectively. By increasing the tunnel arch radius R from 5 to 8 m, we can observe that the delay spread increases. By comparing Figs. D.11 and D.12,

we can see that the delay spread under LOS propagation conditions is smaller than the one under NLOS conditions. This fact can be attributed to the presence of a strong direct path.

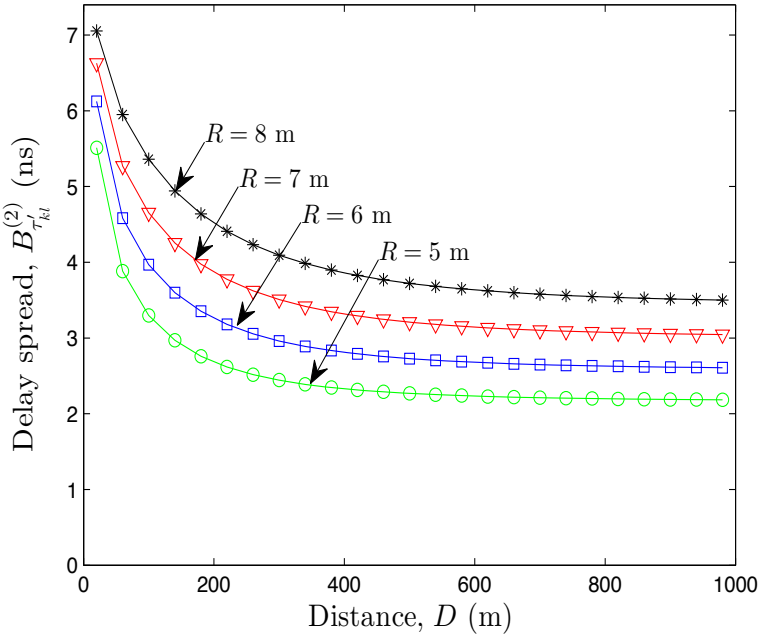

Figure D.11: Delay spread $B^{(2)}_{\tau'_{kl}}$ of the reference model for different values of the radius R of the tunnel arch under NLOS propagation conditions ($c_R = 0$).

Figure D.13 shows the delay spread $B^{(2)}_{\tau_{kl}}$ for different transmission links from $A^{(l)}_T$ to $A^{(k)}_R$ under NLOS propagation conditions, where the transmitter (receiver) antenna element spacing δ_T (δ_R) is in the order of the tunnel radius R, such as $\delta_T = \delta_R = 3\lambda$. Similarly to Fig. D.10, from Fig. D.13 it can be observed that the delay spread $B^{(2)}_{\tau_{kl}}$ has identical graphs for the transmission links $A^{(1)}_T - A^{(2)}_R$ and $A^{(2)}_T - A^{(1)}_R$, which attributes to the symmetrical positions of the mobile transmitter and the mobile receiver. For comparison reasons, in Fig. D.14, we present the delay spreads $B^{(2)}_{\tau_{kl}}$ for small values of δ_T and δ_R, i.e., $\delta_T = \delta_R = 0.3\lambda$. One can see that the delay spreads $B^{(2)}_{\tau_{kl}}$ are the same for all transmission links from $A^{(l)}_T$ to $A^{(k)}_R$ ($l,k = 1,2$), which means that the delay spread $B^{(2)}_{\tau_{kl}}$ can be considered as independent of l and k if the inequality $\max\{\delta_T, \delta_R\} \ll R$ holds.

VIII. Conclusion

In this paper, a reference model for a wideband MIMO C2C channel has been derived by starting from the geometrical SCT scattering model. In this model, it has been assumed that the scatterers are randomly distributed on the wall of an

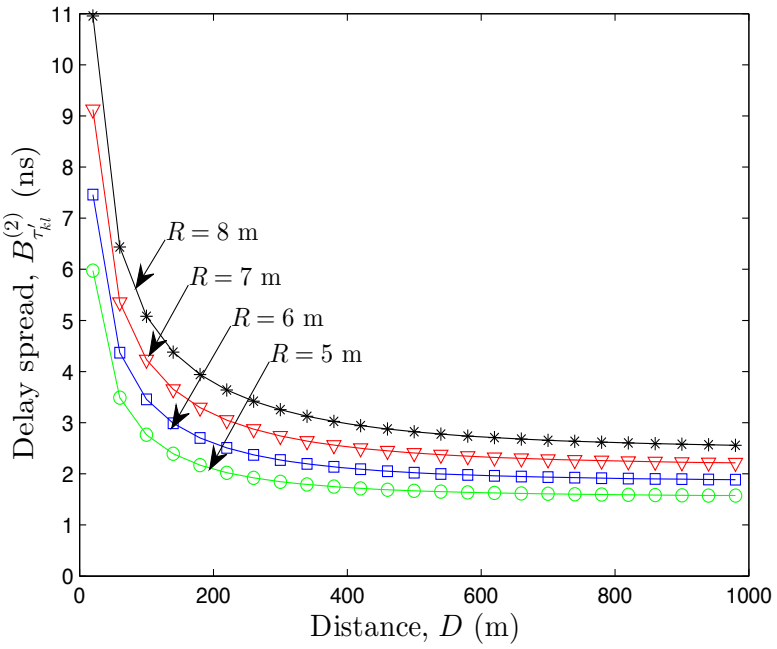

Figure D.12: Delay spread $B^{(2)}_{\tau'_{kl}}$ of the reference model for different values of the radius R of the tunnel arch under LOS propagation conditions ($c_R = 1$).

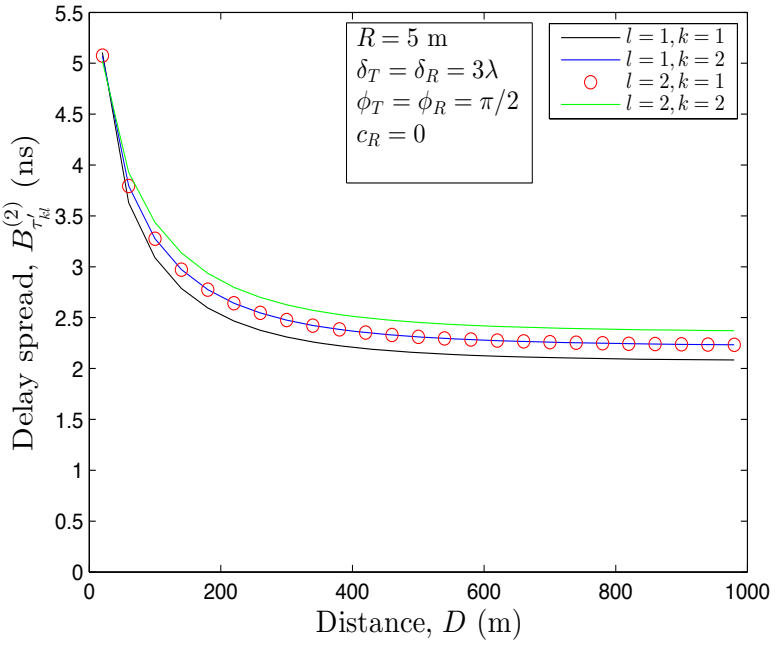

Figure D.13: Delay spread $B^{(2)}_{\tau'_{kl}}$ of the reference model for different transmission links from $A^{(l)}_T$ to $A^{(k)}_R$ $(l,k = 1,2)$ under NLOS propagation conditions ($c_R = 0$), if $\delta_T = \delta_R = 3\lambda$.

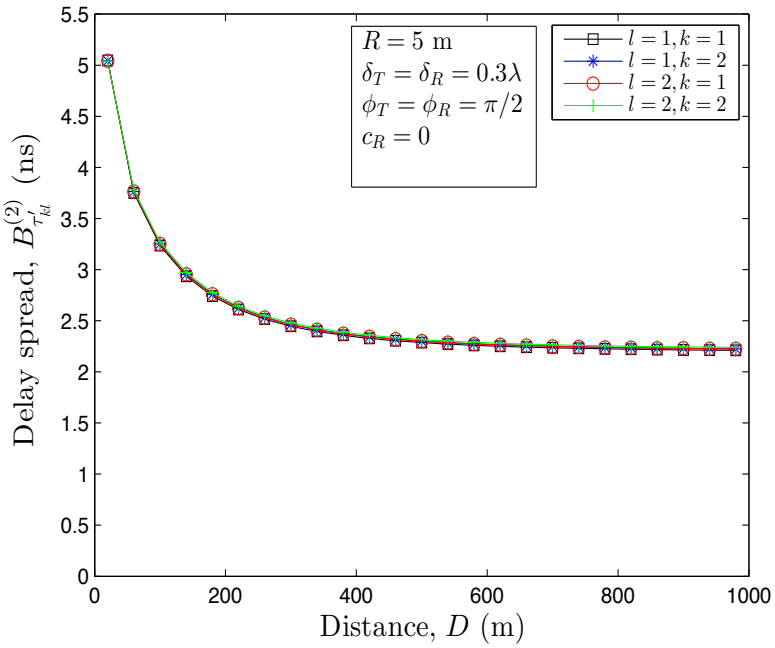

Figure D.14: Delay spread $B^{(2)}_{\tau'_{kl}}$ of the reference model for different transmission links from $A^{(l)}_T$ to $A^{(k)}_R$ $(l,k = 1,2)$ under NLOS propagation conditions ($c_R = 0$), if $\delta_T = \delta_R = 0.3\lambda$.

SCT. Taking into account single-bounce scattering under LOS and NLOS propagation conditions, we have analyzed the STF-CCF of the reference model. To find a proper simulation model, the SOC principle has been applied. It has been shown that the designed SOC channel simulator approximates closely the reference model with respect to the temporal ACF and the FCF. Moreover, the delay spread of the reference channel model has been evaluated and presented for both LOS and NLOS propagation environments. A validation of the usefulness of the proposed model has been done by demonstrating an excellent fitting of the delay spreads of the reference model to those of measured channels. Validating the proposed channel model with respect to the other channel statistical quantities could be a topic for future studies, if the required measured data is available. Numerical results have shown that the proposed model can be considered as a narrowband model for DSRC systems, where the system bandwidth is 10 MHz. The proposed channel model allows us to study the effect of multipath propagation on the performance of future C2C communication systems under propagation conditions, which are typical for tunnels.

REFERENCES

[1] G. Rafiq, B. Talha, M. Pätzold, J. G. Luis, G. Ripa, I. Carreras, C. Coviello, S. Marzorati, G. P. Rodrigues, G. Herrero, and M. Desaeger, "What's new in intelligent transportation systems? An overview of European projects and initiatives," *IEEE Veh. Technol. Mag.*, vol. 8, no. 4, pp. 45–69, Dec. 2013.

[2] Car-to-Car Communication Consortium (C2C-CC) [Online]. Available: http://www.car-to-car.org.

[3] European Road Transport Telematics Implementation Coordinating Organization (ERTICO) [Online]. Available: http://www.ertico.com.

[4] Intelligent Transportation Systems (ITS) [Online]. Available: http://www.its.dot.gov.

[5] G. Bansal and J. B. Kenney, "Controlling congestion in safety-message transmissions: a philosophy for vehicular DSRC systems," *IEEE Veh. Technol. Mag.*, vol. 8, no. 4, pp. 20–26, Dec. 2013.

[6] M. Pätzold, B. O. Hogstad, and N. Youssef, "Modeling, analysis, and simulation of MIMO mobile-to-mobile fading channels," *IEEE Trans. Wireless Commun.*, vol. 7, no. 2, pp. 510–520, Feb. 2008.

[7] M. Pätzold and B. O. Hogstad, "A wideband MIMO channel model derived from the geometrical elliptical scattering model," *Wireless Communications and Mobile Computing*, vol. 8, pp. 597–605, May 2008.

[8] N. Avazov and M. Pätzold, "Design of wideband MIMO car-to-car channel models based on the geometrical street scattering model," *Special Issue: Modeling and Simulation in Engineering*, vol. 2012, Sept. 2012.

[9] H. Zhiyi, C. Wei, Z. Wei, M. Pätzold, and A. Chelli, "Modelling of MIMO vehicle-to-vehicle fading channels in T-junction scattering environments," in *Proc. 3rd European Conference on Antennas and Propagation, EuCAP 2009*. Berlin, Germany, Mar. 2009, pp. 652–656.

[10] A. Theodorakopoulos, P. Papaioannou, T. Abbas, and F. Tufvesson, "A geometry based stochastic model for MIMO V2V channel simulation in cross-junction scenario," in *Proc. 13th International Conference on ITS Telecommunications*. Tampere, Finland, Nov. 2013.

[11] N. Avazov and M. Pätzold, "A novel MIMO car-to-car chanel model based on the geometrical curved street scattering model," in *Proc. Loughborough Antennas and Propagation Conference (LAPC'2012), Loughborough, UK*, Nov. 2012, pp. 1–6.

[12] L. Cheng, B. E. Henty, D. D. Stancil, F. Bai, and P. Mudalige, "Mobile vehicle-to-vehicle narrow-band channel measurement and characterization of the 5.9 GHz dedicated short range communication (DSRC) frequency band," *IEEE J. Select. Areas Commun.*, vol. 25, no. 8, pp. 1501–1516, Oct. 2007.

[13] X. Cheng, C.-X. Wang, D. I. Laurenson, S. Salous, and A. V. Vasilakos, "An adaptive geometry-based stochastic model for non-isotropic MIMO mobile-to-mobile channels," *IEEE Trans. Wireless Commun.*, vol. 8, no. 9, pp. 4824–4835, Sept. 2009.

[14] J. B. Kenney, "Dedicated short-range communications (DSRC) standards in the United States," *Proceedings of the IEEE*, vol. 99, no. 7, pp. 1162–1182, July 2011.

[15] A. G. Zajić, G. L. Stüber, T. G. Pratt, and S. T. Nguyen, "Wideband MIMO mobile-to-mobile channels: geometry-based statistical modeling with experimental verification," *IEEE Trans. Veh. Technol.*, vol. 58, no. 2, pp. 517–534, Feb. 2009.

[16] Y. Yuan, X. Cheng, C.-X. Wang, D. I. Laurenson, X. Ge, and F. Zhao, "Space-time correlation properties of a 3D two-sphere model for non-isotropic MIMO mobile-to-mobile channels," in *Proc. of the IEEE Global Telecommunications Conference (GLOBECOM'10)*, Dec 2010, pp. 1–5.

[17] J. Chen and T. G. Pratt, "A three-dimensional geometry-based statistical model of 2×2 dual-polarized MIMO mobile-to-mobile wideband channels," *Modelling and Simulation in Engineering*, vol. 2012, Article ID 756508, 2012.

[18] T. Abbas, L. Bernado, A. Thiel, C. Mecklenbräuker, and F. Tufvesson, "Radio channel properties for vehicular communication: merging lanes versus urban intersections," *IEEE Veh. Technol. Mag.*, vol. 8, no. 4, pp. 27–34, Dec. 2013.

[19] O. Renaudin, V.-M. Kolmonen, P. Vainikainen, and C. Oestges, "Wideband measurement-based modeling of inter-vehicle channels in the 5.2 GHz band," *IEEE Trans. Veh. Technol.*, vol. 62, no. 8, pp. 3531–3540, Oct. 2013.

[20] J. Karedal, F. Tufvesson, N. Czink, A. Paier, C. Dumard, T. Zemen, and C. F. Mecklenbräuker, "A geometry-based stochastic MIMO model for vehicle-to-vehicle communications," *IEEE Trans. Wireless Commun.*, vol. 8, no. 7, pp. 3646–3657, July 2009.

[21] J. Maurer, T. Fügen, and W. Wiesbeck, "Narrow-band measurement and analysis of the inter-vehicle transmission channel at 5.2 GHz," in *Proc. IEEE 55th Semiannual Veh. Technol. Conf., VTC'02-Spring*, vol. 3. Birmingham, Alabama, May 2002, pp. 1274–1278.

[22] G. Acosta, K. Tokuda, and M. A. Ingram, "Measured joind Doppler-delay power profiles for vehicle-to-vehicle communications at 2.4 GHz," in *Proc. IEEE Global Communications Conference, GLOBECOM'04, Dallas, TX*, vol. 6, Nov. 29 - Dec. 3 2004, pp. 3813–3817.

[23] J. Kunisch and J. Pamp, "Wideband car-to-car radio channel measurements and model at 5.9 GHz," in *2008 IEEE 68th Vehicular Technology Conference*, Calgary, Canada, Sep. 2008, pp. 1–5.

[24] Y. Ma and M. Pätzold, "Performance analysis of Alamouti coded OFDM systems over Rayleigh fading channels correlated in space and time," in *Proc. the 71st IEEE Vehicular Technology Conference, VTC2010-Spring, Taipei*, May 2010, pp. 1–6.

[25] N. Avazov and M. Pätzold, "Performance analysis of Alamouti coded OFDM systems over wideband MIMO car-to-car channels correlated in time and space," in *Proc. International conference on Connected Vehicles and Expo (ICCVE'2014), Vienna, Austria*, Nov. 2014.

[26] L. Bernadó, A. Roma, A. Paier, T. Zemen, N. Czink, J. Karedal, A. Thiel, F. Tufvesson, A. F. Molisch, and C. F. Mecklenbräuker, "In-tunnel vehicular radio channel characterization," in *Proc. 73rd IEEE Vehicular Technology Conference (VTC2011-Spring)*, May 2011, pp. 1–5.

[27] D. Umansky and M. Pätzold, "Stationarity test for wireless communication channels," in *Proc. IEEE Global Communications Conference (GLOBECOM'2009), Honolulu, Hawaii, USA*, Nov. 2009.

[28] X. Cheng, Q. Yao, M. Wen, C.-X. Wang, L.-Y. Song, and B.-L. Jiao, "Wideband channel modeling and intercarrier interference cancellation for vehicle-to-vehicle communication systems," *IEEE J. Select. Areas Commun.*, vol. 31, no. 9, pp. 434–448, Sept. 2013.

[29] *Norwegian Public Road Administration, Road Tunnels*. NPRA Printing Center, Apr. 2004.

[30] S. F. Mahmoud and J. R. Wait, "Geometrical optical approach for electromagnetic wave propagation in rectangular mine tunnels," *Radio Science*, vol. 9, no. 12, pp. 1147–1158, Dec. 1974.

[31] D. G. Dudley, M. Liénard, S. F. Mahmoud, and P. Degauque, "Wireless propagation in tunnels," *IEEE Antennas Propagation Mag.*, vol. 49, no. 2, pp. 11–26, Apr. 2007.

[32] K. Arshad, F. Katsriku, and A. Lasebae, "Modelling obstructions in straight and curved rectangular tunnels by finite element approach," *Journal of Electrical Engineering*, vol. 59, no. 1, pp. 9–13, 2008.

[33] Z. Sun and I. F. Akyildiz, "A mode-based approach for channel modeling in underground tunnels under the impact of vehicular traffic flow," *IEEE Trans. Wireless Commun.*, vol. 10, no. 10, pp. 3222–3231, Oct. 2011.

[34] T.-S. Wang and C.-F. Yang, "Simulations and measurements of wave propagations in curved road tunnels for signals from GSM base stations," *IEEE Trans. Antennas Propag.*, vol. 54, no. 9, pp. 2577–2584, Sept. 2006.

[35] S. Hairoud, P. Combeau, Y. Pousset, Y. Cocheril, and M. Berbineau, "WINNER model for subway tunnel at 5.8 GHz," Nov. 2012, pp. 743–747.

[36] G. S. Ching, M. Ghoraishi, M. Landmann, N. Lertsirisopon, J. i. Takada, T. Imai, I. Sameda, and H. Sakamoto, "Wideband polarimetric directional propagation channel analysis inside an arched tunnel," *IEEE Trans. Antennas Propag.*, vol. 57, no. 3, pp. 760–767, March 2009.

[37] N. Avazov and M. Pätzold, "A wideband car-to-car channel model based on a geometrical semicircular tunnel scattering model," in *Proc. 24th IEEE Int. Symp. on Personal, Indoor and Mobile Radio Communications (PIMRC'2013), London, UK*, Sept. 2013, pp. 248–253.

[38] M. Pätzold, *Mobile Radio Channels*, 2nd ed. Chichester: John Wiley & Sons, 2011, 583 pages.

[39] M. Pätzold, A. Szczepanski, and N. Youssef, "Methods for modeling of specified and measured multipath power-delay profiles," *IEEE Trans. Veh. Technol.*, vol. 51, no. 5, pp. 978–988, 2002.

[40] A. G. Zajić, G. L. Stüber, T. G. Pratt, and S. Nguyen, "Statistical modeling and experimental verification of wideband MIMO mobile-to-mobile channels in highway environments," in *Proc. IEEE 19th International Symposium on Personal, Indoor and Mobile Radio Communications, PIMRC 2008*, Sept. 2008, pp. 1–5.

[41] A. Papoulis and S. U. Pillai, *Probability, Random Variables and Stochastic Processes*, 4th ed. New York: McGraw-Hill, 2002.

[42] M. Pätzold and B. Talha, "On the statistical properties of sum-of-cisoids-based mobile radio channel simulators," in *Proc. 10th International Symposium on Wireless Personal Multimedia Communications, WPMC 2007*. Jaipur, India, Dec. 2007, pp. 394–400.

[43] C. A. Gutiérrez and M. Pätzold, "The design of sum-of-cisoids Rayleigh fading channel simulators assuming non-isotropic scattering conditions," *IEEE Trans. Wireless Commun.*, vol. 9, no. 4, pp. 1308–1314, Apr. 2010.

[44] ——, "The generalized method of equal areas for the design of sum-of-sinusoids simulators for mobile Rayleigh fading channels with arbitrary Doppler spectra," *Wireless Communications and Mobile Computing*, 2011, doi:10.1002/wcm.1154.

Appendix E

Paper V

Title:	Performance Analysis of Alamouti Coded OFDM Systems over Wideband MIMO Car-to-Car Channels Correlated in Time and Space
Authors:	**Nurilla Avazov** and Matthias Pätzold
Affiliation:	University of Agder, Faculty of Engineering and Science, P. O. Box 509, NO-4898 Grimstad, Norway
Conference:	*IEEE the 3rd International Conference on Connected Vehicles and Expo, ICCVE 2014*, Vienna, Austria, Nov. 2014.

Performance Analysis of Alamouti Coded OFDM Systems over Wideband MIMO Car-to-Car Channels Correlated in Time and Space

Nurilla Avazov and Matthias Pätzold
Faculty of Engineering and Science, University of Agder
P.O. Box 509, NO-4898 Grimstad, Norway
E-mails: {nurilla.k.avazov, matthias.paetzold}@uia.no

Abstract — **In this paper, the performance of Alamouti coded orthogonal frequency division multiplexing (OFDM) systems over car-to-car (C2C) fading channels correlated in time and space is analyzed. Taking different geometrical scattering models into account, a generalized expression of the time-variant transfer function (TVTF) is derived for wideband multiple-input multiple-output (MIMO) C2C channels. We present a generalized expression for the bit error probability (BEP), which will be used to describe the performance of Alamouti coded OFDM systems over different types of C2C channel models, such as the rectangle model, the tunnel model, the street model, and the curve model. The effect of the maximum Doppler frequency and the antenna element spacing on the system performance is discussed. Furthermore, the proposed generalized model allows us to study the impact of the parameters of the geometrical model on the BEP. The proposed procedure enables us to investigate the system performance using different kinds of C2C fading channel models in a straightforward and time-efficient manner.**

I. Introduction

Over the past few decades, there has been an increased interest in studying and developing C2C communication systems, which offer numerous traffic safety applications to reduce the number of road accidents and to improve traffic flow. In this regard, a large number of research projects focusing on C2C communication systems have been carried out in Europe [1–3].

The development of C2C communication systems highly depends on a detailed knowledge of the underlying radio channel. In the literature, numerous C2C channel models have been developed and analyzed, such as the street line model [4], the rectangle model [5], the cross-junction model [6], the curve model [7], and the tunnel model [8]. The time-frequency selective properties of C2C channels are significantly different from those of traditional fixed-to-mobile or mobile-to-fixed

channels. Using OFDM systems can be of great advantage for C2C communications due to their high spectral efficiency and their ability to mitigate multipath fading effects.

In [9, 10], the performance of car-to-infrastructure (C2I) communication systems is analyzed. The frame success ratios and goodputs of C2I channels in a tunnel environment were discussed and analyzed in [9], where it was shown that the use of higher-order modulation schemes with constant packet length is more beneficial to the total goodput than an increase in packet length. In [10], a narrowband single-input single-output (SISO) C2I channel model for blind bent environments has been derived. The authors of [10] studied the performance of different digital modulation schemes over channels modelled by a sum of singly and doubly scattered components. A computationally low-cost packet error model has been proposed for C2I communications in [11], where the performance influence of different system configurations and components were analyzed jointly.

The performance of C2C communication systems was analyzed in [12, 13]. The impact of fast-varying channels on the C2C system performance was studied in [12]. It was shown that the channel estimation process is the most affected part due to the rapid changes of the channel. In [13], the performance evaluation of the long term evolution (LTE) technology in a C2C communication system was conducted. The obtained results in [13] show the feasibility of broadband wireless access at data rates of several Mbit/s. Another, recently published work dealing with the performance analysis of C2C communications can be found in [14], where a new regular shaped geometry-based stochastic model for non-isotropic scattering wideband C2C Rician fading channels has been proposed. There, to combat intercarrier interference (ICI), the authors proposed a new ICI cancellation scheme, called precoding-based cancellation (PBC) scheme. Real-world measurement-based performance results of C2C communications in various road configurations under varying LOS conditions were presented in [15]. There, the effect of objects blocking the LOS path on the range of C2C communications was analyzed. Tapped delay line C2C channel models have been designed in [16] based on the bit error rate (BER) performance.

To the best of the authors' knowledge, a theoretical analysis of the performance of C2C communication systems over C2C channels under different scattering conditions, as described in [4–8] has not been performed yet. Therefore, to fill this gap, we have analyzed the performance of an Alamouti coded [17] OFDM system over different C2C channel models, such as the rectangle model [5], the tunnel model [8], the street line model [4], and the curve model [7].

The main contributions and novelties of this paper are as follows:

1) We combine all abovementioned channel models [4, 5, 7, 8] to a generalized wideband MIMO C2C channel model assuming single-bounce scattering. The proposed model includes as special cases the rectangle model, the tunnel model, the street line model, and the curve model.

2) We extend the wideband SISO C2C tunnel model in [8] to a MIMO C2C tunnel channel model.

3) We also provide an extension of the narrowband MIMO C2C curve model towards frequency selectivity.

4) Furthermore, we represent the corresponding correlation functions of the proposed generalized model, such as the two-dimensional (2D) space cross-correlation function (CCF) and the temporal autocorrelation function (ACF).

5) Finally, a comparative study of the BEP of Alamouti coded OFDM systems is presented by using all abovementioned channel models [4, 5, 7, 8].

The rest of this paper is organized as follows. Section II describes the generalized reference model. In Section III, the correlation functions of the reference channel model, such as the 2D space CCF and the temporal ACF are briefly described. Analytical expressions for the BEP of Alamouti coded OFDM systems are presented in Section IV. The illustration of the numerical results found for the BEP is the topic of Section V. Finally, Section VI provides the conclusions of the paper.

II. A Generalized Wideband MIMO C2C Channel Model

In this section, we present a generalized reference channel model for a wideband MIMO C2C channel assuming single-bounce scattering. The proposed generalized reference channel model can be used to describe the geometrical rectangle model and the tunnel model, as well as the street line model and the curve model as a special case. The reference model is obtained by assuming that the number of scatterers is infinite. The reference model serves as a basis for the derivation of efficient MIMO channel simulators. In our proposed generalized channel model, we consider two models, i.e., the rectangle model and the tunnel model, where the positions of the scatterers $S^{(mn)}$ for $m = 1,2,\ldots,M$ and $n = 1,2,\ldots,N$ are described as shown in [5, Fig. 2] and [8, Fig. 3], respectively. In both models, Cartesian coordinates (x_m, y_n) are used to desribe the positions of the scatterers $S^{(mn)}$, where x_m and y_n are random variables. The distribution of the scatterers $S^{(mn)}$ is completely

determined by the distributions of x_m and y_n. In the following, we use the notation and the definitions of the model parameters in [5, Fig. 2] and [8, Fig. 3], which are summarized in Table E.1.

Table E.1: Definition of the parameters used in [5, Fig. 2] and [8, Fig. 3].

L	The length of the tunnel.
R	The radius of the semicircle tunnel.
(x_T, y_T, z_T)	The position of the mobile transmitter (MS_T).
(x_R, y_R, z_R)	The position of the mobile receiver (MS_R).
D	The distance between the MS_T and the MS_R.
$L_A = A_1 + A_2$	The length of the rectangular grids.
B_1, B_2	The width of the rectangular grids.
y_{T_1} (y_{R_1})	The distance from the left-hand side of the street to the MS_T (MS_R).
y_{T_2} (y_{R_2})	The distance from the right-hand side of the street to the MS_T (MS_R).
γ_T (γ_R)	The orientation of the transmitter (receiver) antenna array in the xy-plane relative to the x-axis.
ϕ_T (ϕ_R)	The elevation angle of the transmitter (receiver) antenna array w.r.t. the xy-plane.
δ_T (δ_R)	The spacing between the antenna elements at the transmitter (receiver) antenna.
v_T (v_R)	The speed of the mobile transmitter (receiver).
φ_{v}^T (φ_{v}^R)	The angle of motion of the MS_T (MS_R).
$\alpha_T^{(mn)}$, $\alpha_R^{(mn)}$	The azimuth angle of departure (AAOD) and the azimuth angle of arrival (AAOA).
$\beta_T^{(mn)}$, $\beta_R^{(mn)}$	The elevation angle of departure (EAOD) and the elevation angle of arrival (EAOA).
$D_T^{(l,mn)}$, $D_R^{(mn,k)}$, $D_{TR}^{(l,k)}$,	The Euclidean distances $d\left(A_T^{(l)}, S^{(mn)}\right)$, $d\left(S^{(mn)}, A_R^{(k)}\right)$, and $d\left(A_T^{(l)}, A_R^{(k)}\right)$.

A. A Generalized TVTF

Let us assume a wideband MIMO C2C communication system employing M_T transmitter antennas and M_R receiver antennas. The wideband MIMO C2C channel can be described by the channel matrix $\mathbf{H}_p(f',t) = [H_{kl,p}(f',t)]_{M_R \times M_T}$, where

$H_{kl,p}(f',t)$ denotes the TVTF of the link from the lth transmitter antenna $A_T^{(l)}$ ($l = 1,2,\ldots,M_T$) to the kth receiver antenna $A_R^{(k)}$ ($k = 1,2,\ldots,M_R$), and the index p indicates the type of the geometrical channel model. We consider a rectangle model if $p = 1$ and a tunnel model if $p = 2$. The TVTF $H_{kl,p}(f',t)$ of the pth channel model for the link $A_T^{(l)} - A_R^{(k)}$ can be expressed as

$$H_{kl,p}(f',t) = \lim_{\substack{M\to\infty \\ N\to\infty}} \frac{1}{\sqrt{MN}} \sum_{m,n=1}^{M,N} e^{-j\frac{2\pi}{\lambda}D_{kl,p}^{(mn)}} e^{j\left[2\pi f_p^{(mn)}t + \theta^{(mn)} - 2\pi\tau_{kl,p}^{\prime(mn)}f'\right]} \quad \text{(E.1)}$$

where

$$D_{kl,p}^{(mn)} = D_{T,p}^{(l,mn)} + D_{R,p}^{(mn,k)},\ p \in \{1,2\} \quad \text{(E.2)}$$

$$f_p^{(mn)} = f_{T,p}^{(mn)} + f_{R,p}^{(mn)},\ p \in \{1,2\} \quad \text{(E.3)}$$

$$f_{T,p}^{(mn)} = f_{T_{\max}} \cos\left(\alpha_{T,p}^{(mn)} - \varphi_{\mathrm{v}}^{T}\right) \cos\left((p-1)\beta_T^{(mn)}\right) \quad \text{(E.4)}$$

$$f_{R,p}^{(mn)} = f_{R_{\max}} \cos\left(\alpha_{R,p}^{(mn)} - \varphi_{\mathrm{v}}^{R}\right) \cos\left((p-1)\beta_R^{(mn)}\right). \quad \text{(E.5)}$$

The symbols $D_{kl.p}^{(mn)}$, $f_p^{(mn)}$, $\theta^{(mn)}$, and $\tau_{kl,p}^{\prime(mn)}$ in (E.1) denote the total path length, the Doppler frequency, the phase, and the propagation delay of the reference model. The distance $D_{kl,p}^{(mn)}$ is determined by (E.2) in which the distances $D_{T,p}^{(l,mn)}$ and $D_{R,p}^{(mn,k)}$ are given by

$$\begin{aligned} D_{T,p}^{(l,mn)} = {} & D_{T,p}^{(mn)} - (M_T - 2l + 1)\frac{\delta_T}{2}\left[\cos\left((p-1)\phi_T\right)\cos\left((p-1)\beta_T^{(mn)}\right)\right. \\ & \left.\cdot\cos\left(\gamma_T - \alpha_{T,p}^{(mn)}\right) + (p-1)\sin\left(\phi_T\right)\sin\left(\beta_T^{(mn)}\right)\right],\ p \in \{1,2\} \end{aligned} \quad \text{(E.6)}$$

$$\begin{aligned} D_{R,p}^{(mn,k)} = {} & D_{R,p}^{(mn)} - (M_R - 2k + 1)\frac{\delta_R}{2}\left[\cos\left((p-1)\phi_R\right)\cos\left((p-1)\beta_R^{(mn)}\right)\right. \\ & \left.\cdot\cos\left(\gamma_R - \alpha_{R,p}^{(mn)}\right) + (p-1)\sin\left(\phi_R\right)\sin\left(\beta_R^{(mn)}\right)\right],\ p \in \{1,2\} \end{aligned} \quad \text{(E.7)}$$

respectively, where

$$D_{T,p}^{(mn)} = \left[(x_m - (p-1)x_T)^2 + (y_n - (p-1)y_T)^2 + (p-1)(\sqrt{R^2 - y_n^2} - z_T)^2\right]^{\frac{1}{2}} \quad \text{(E.8)}$$

$$\begin{aligned} D_{R,p}^{(mn)} = {} & \left[(x_m - (p-1)x_R + (p-2)D_x)^2 + (y_n - (p-1)y_R + (p-2)D_y)^2\right. \\ & \left. + (p-1)(\sqrt{R^2 - y_n^2} - z_R)^2\right]^{\frac{1}{2}}. \end{aligned} \quad \text{(E.9)}$$

The symbols D_x and D_y in (E.9) are defined as $D_x = D$ and $D_y = y_{T_1} - y_{R_1}$, respectively (see [5, Fig. 2]). It is assumed that the phases $\theta^{(mn)}$ are independent, identically distributed (i.i.d.) random variables, which are uniformly distributed over the interval $[0, 2\pi)$. Using the distance $D_{kl,p}^{(mn)}$ in (E.2), the propagation delays $\tau_{kl,p}^{\prime(mn)}$ in (E.1) can be computed as $\tau_{kl,p}^{\prime(mn)} = D_{kl,p}^{(mn)}/c_0$, where c_0 is the speed of light. It is noteworthy that we have extended in this paper the SISO C2C semicircle tunnel model in [8] to a MIMO model.

The proposed generalized channel model also includes the street line model ($p = 3$) and the curve model ($p = 4$) as special cases. In these models, it is assumed that an infinite number of scatterers are uniformly distributed on a street line (street line model) [4] or on a curve (curve model) [7]. Hence, the double-sum in (E.1) will be reduced to a single-sum, i.e., $N = 1$, by only taking into account the effect of the scatterers $S^{(m)}$. Thus, the TVTF $H_{kl,p}(f',t)$ of the reference model can be represented as

$$H_{kl,p}(f',t) \;=\; \lim_{M\to\infty} \frac{1}{\sqrt{M}} \sum_{m=1}^{M} e^{-j\frac{2\pi}{\lambda} D_{kl,p}^{(m)}} e^{j\left[2\pi f_p^{(m)} t + \theta^{(m)} - 2\pi\tau_{kl,p}^{\prime(m)} f'\right]} \qquad \text{(E.10)}$$

where

$$D_{kl,p}^{(m)} \;=\; D_{T,p}^{(l,m)} + D_{R,p}^{(m,k)},\; p \in \{3,4\} \qquad \text{(E.11)}$$

$$D_{T,p}^{(l,m)} = D_{T,p}^{(m)} - (M_T - 2l + 1)\frac{\delta_T}{2}\cos\left(\alpha_{T,p}^{(m)} - \gamma_T\right) \qquad \text{(E.12)}$$

$$D_{R,p}^{(m,k)} = D_{R,p}^{(m)} - (M_R - 2k + 1)\frac{\delta_R}{2}\cos\left(\alpha_{R,p}^{(m)} - \gamma_R\right) \qquad \text{(E.13)}$$

$$f_p^{(m)} \;=\; f_{T,p}^{(m)} + f_{R,p}^{(m)},\; p \in \{3,4\} \qquad \text{(E.14)}$$

$$f_{T,p}^{(m)} \;=\; f_{T_{\max}} \cos\left(\alpha_{T,p}^{(m)} - \varphi_{\mathrm{v}}^{T}\right) \qquad \text{(E.15)}$$

$$f_{R,p}^{(m)} \;=\; f_{R_{\max}} \cos\left(\alpha_{R,p}^{(m)} - \varphi_{\mathrm{v}}^{R}\right). \qquad \text{(E.16)}$$

The symbols $D_{T,p}^{(m)}$ and $D_{R,p}^{(m)}$ in (E.12) and (E.13), respectively, can be found in [4] for $p = 3$ and in [7] if $p = 4$, respectively.

B. Angle of Departure (AOD) and Angle of Arrival (AOA)

In the generalized reference model, the positions of all scatterers $S^{(mn)}$ are described by the Cartesian coordinates (x_m, y_n) if $p \in \{1,2\}$. For the special cases $p \in \{3,4\}$, the position of each scatterer is defined by the AOD and/or the angle of scatterer (AOS). Thus, the angles $\alpha_{T,p}^{(mn)}$ ($\alpha_{R,p}^{(mn)}$) [see (E.4) and (E.5)] and $\alpha_{T,p}^{(m)}$ ($\alpha_{R,p}^{(m)}$) [see (E.15) and (E.16)] are listed in Table E.2. According to [8, Eq. (15)],

Table E.2: AODs and AOAs of the reference model

Geometrical Model	**AOD**	**AOA**
Rectangle Model ($p=1$)	$\alpha_{T,1}^{(mn)}$ given in [5, Eq. (16)]	$\alpha_{R,1}^{(mn)}$ given in [5, Eq. (17)]
Tunnel Model ($p=2$)	$\alpha_{T,2}^{(mn)}$ given in [8, Eq. (15)]	$\alpha_{R,2}^{(mn)}$ given in [8, Eq. (15)]
Street Line Model ($p=3$)	$\alpha_{T,3}^{(m)}$ given in [4]	$\alpha_{R,3}^{(m)}$ given in [4, Eq. (14)]
Curve Model ($p=4$)	$\alpha_{T,4}^{(m)}$ given in [7, Eq. (24)]	$\alpha_{R,4}^{(m)}$ given in [7, Eq. (25)]

the EAOD $\beta_T^{(mn)}$ and the EAOA $\beta_R^{(mn)}$ can be expressed in terms of the coordinates of the position (x_m, y_n) of the scatterer $S^{(mn)}$. In the curved street scattering model, the position of the scatterer $S^{(m)}$ is described by the AOS $\beta^{(m)}$. Hence, for $p=4$, the angle $\alpha_{T,4}^{(m)}$ ($\alpha_{R,4}^{(m)}$) is defined in terms of the AOS as given in [7, Eq. (24)-(25)].

III. Correlation Properties of the Reference Model

In [18], it was shown that the performance of Alamouti coded OFDM systems depends on the temporal and spatial correlation properties of the underlying channel. In this regard, we will briefly review the main correlation functions, such as the 2D space CCF and the temporal ACF.

Starting from the derivation of the analytical expression for the space-time-frequency CCF (STF-CCF) of the Type p C2C (C2C$_p$) channel model, we will compute the corresponding 2D space CCF and the temporal ACF. The STF-CCF of the TVTFs $H_{kl,p}(f',t)$ and $H_{k'l',p}(f',t)$ is defined as $\rho_{kl,k'l',p}(\delta_T,\delta_R,\nu',\tau) := E\{H_{kl,p}^*(f',t)H_{k'l',p}(f'+\nu',t+\tau)\}$. From the STF-CCF, we can obtain the 2D space CCF $\rho_{kl,k'l',p}(\delta_T,\delta_R)$ of the reference model by setting $\tau=0$ and $\nu'=0$. The 2D space CCF for $p=1$, $p=3$, and $p=4$ can be found in [5, Eq. (30)], [4, Eq. (27)], and [7, Eq. (47)], respectively. The 2D space CCF $\rho_{kl,k'l',p}(\delta_T,\delta_R)$ of the reference model for $p=2$, i.e., for the tunnel model, can be expressed as

$$\rho_{kl,k'l',2}(\delta_T,\delta_R) = \int_{-R}^{R}\int_{x_T}^{x_R} p_{x_m y_n}(x,y)c_{ll'}(x,y)d_{kk'}(x,y)dxdy \tag{E.17}$$

where

$$\begin{aligned} c_{ll'}(x,y) &= e^{j2\pi\frac{\delta_T}{\lambda}(l-l')\cos\phi_T\cos(\beta_T(x,y))\cos(\gamma_T-\alpha_T(x,y))} \\ &\quad \cdot e^{j2\pi\frac{\delta_T}{\lambda}\sin\phi_T\sin(\beta_T(x,y))} \end{aligned} \tag{E.18}$$

$$\begin{aligned} d_{kk'}(x,y) &= e^{j2\pi\frac{\delta_R}{\lambda}(k-k')\cos\phi_R\cos(\beta_R(x,y))\cos(\gamma_R-\alpha_R(x,y))} \\ &\quad \cdot e^{j2\pi\frac{\delta_R}{\lambda}\sin\phi_R\sin(\beta_R(x,y))} \end{aligned} \tag{E.19}$$

and $p_{x_m y_n}(x,y)$ denotes the joint probability density function of the random variables x_m and y_n [8, Eq. (23)].

The temporal ACF $r_{kl,p}(\tau)$ of the TVTF of the transmission link $A_T^{(l)} - A_R^{(k)}$ is defined by $r_{kl,p}(\tau) := E\{H_{kl,p}^*(f',t)H_{kl,p}(f',t+\tau)\}$ [19, p. 376]. By making use of the results in [5, Eq. (32)], [8, Eq. (32)], [4, Eq. (26)], and [7, Eq. (48)], the temporal ACF $r_{kl,p}(\tau)$ can be expressed for all considered C2C$_p$ channel models.

IV. BEP of Alamouti Coded OFDM Systems

In this section, we present the expression of the BEP for Alamouti coded OFDM systems over C2C$_p$ channels correlated in time and space. The BEP of Alamouti coded OFDM systems can be computed as

$$P_b = \int_0^\infty P_{\gamma_\Sigma}(\gamma)\cdot P_{b|\gamma_\Sigma}(\gamma)d\gamma \tag{E.20}$$

where $P_{\gamma_\Sigma}(\gamma)$ denotes the joint PDF given by [18, Eq. (24)], and $P_{b|\gamma_\Sigma}(\gamma)$ is the conditional BEP of a digital modulation scheme for a given value of the signal-to-noise ratio (SNR) γ. For example, for the binary phase-shift keying (BPSK) modulation scheme, the conditional BEP equals $P_{b|\gamma_\Sigma}(\gamma) = \operatorname{erfc}\left(\sqrt{\gamma}\right)/2$.

Under the assumption of perfect channel state information (CSI), the BEP $P_{b,p}$ of BPSK Alamouti coded OFDM systems over C2C$_p$ channels correlated in time can be written as [18, Eq. (27)]

$$\begin{aligned} P_{b,p} &= \frac{2\sigma_0^2}{16(\sigma_0^4-\rho_{T,p}^2)^2\bar{\gamma}}\int_0^\infty\int_0^\infty\int_0^w\int_0^{z_2}\frac{z_2 z_3(w-z_3)}{z_4(z_2-z_4)w} \\ &\quad \cdot e^{-\frac{\sigma_0^2}{2(\sigma_0^4-\rho_{T,p}^2)}\left[\frac{(w-z_3)^2}{z_4}+z_2+\frac{z_3^2}{z_2-z_4}\right]}\operatorname{erfc}(\sqrt{\gamma}) \\ &\quad \cdot I_0\left(\frac{z_3\rho_{T,p}}{\sigma_0^4-\rho_{T,p}^2}\right)I_0\left(\frac{(w-z_3)\rho_{T,p}}{\sigma_0^4-\rho_{T,p}^2}\right)dz_4dz_3dz_2d\gamma \end{aligned} \tag{E.21}$$

where σ_0^2 is one half of the mean power of the received scattered components, the upper limit w is given by $w = \sqrt{2\sigma_0^2\gamma z_2/\bar{\gamma}}$, and $\rho_{T,p} = r_{kl,p}(T_s)/2$, where T_s is the symbol duration.

In an analogous manner, the BEP $P_{b,p}$ of a BPSK Alamouti coded OFDM system over C2C$_p$ channels correlated in space can be expressed as [18, Eq. (28)]

$$\begin{aligned} P_{b,p} \;=\; & \frac{2\sigma_0^2}{16(\sigma_0^4-\rho_{\Delta,p}^2)^2\bar{\gamma}} \int_0^{\infty}\int_0^{\infty}\int_0^{w}\int_0^{z_2} \frac{z_2 z_3 (w-z_3)}{z_4(z_2-z_4)w} \\ & \cdot e^{-\frac{\sigma_0^2}{2(\sigma_0^4-\rho_{\Delta,p}^2)}\left[\frac{(w-z_3)^2}{z_4}+z_2+\frac{z_3^2}{z_2-z_4}\right]} \operatorname{erfc}\left(\sqrt{\gamma}\right) \\ & \cdot I_0\left(\frac{z_3\sqrt{z_4}\rho_{\Delta,p}}{(\sigma_0^4-\rho_{\Delta,p}^2)\sqrt{z_2-z_4}}\right) \\ & \cdot I_0\left(\frac{(w-z_3)\sqrt{z_2-z_4}\rho_{T,p}}{(\sigma_0^4-\rho_{T,p}^2)\sqrt{z_4}}\right) dz_4 dz_3 dz_2 d\gamma \end{aligned} \tag{E.22}$$

where $\rho_{\Delta,p} = \rho_{kl,k'l',p}(\delta_T, 0)/2$.

V. Performance Analysis

This section presents the theoretical BEP results obtained by evaluating (E.21) and (E.22). The correctness of the analytical results will be confirmed by system simulations. For the system simulations, we consider an OFDM system with $K = 64$ subcarriers and $T_s = 8\mu s$. The geometrical model parameters used for computing the BEP in (E.21) and (E.22) are presented in Table E.3. For the reference model, all numerical results have been obtained by choosing the following parameters: $\varphi_{\mathrm{v}}^T =$

Table E.3: Model parameters.

Model parameters	Value and unit
R	5 m
(x_T, y_T, z_T)	(20 m, 2 m, 1 m)
(x_R, y_R, z_R)	(40 m, 2 m, 1 m)
D	400 m [5]
$L_A = A_1 + A_2$	500 m [5]
B_1, B_2	100 m
y_{T_1} (y_{R_1})	20 m (10 m)
y_{T_2} (y_{R_2})	10 m (20 m)

$\varphi_{\mathrm{v}}^{R}=0^{\circ}$, $\phi_T=\phi_R=45^{\circ}$, $\gamma_T=\gamma_R=45^{\circ}$, and $f_{T_{\max}}=f_{R_{\max}}=100\,\mathrm{Hz}$. The corresponding MIMO channel simulator has been designed by using the L_p-norm method, such that the resulting simulation model is ergodic [20], i.e., the statistical average equals the time average. This allows us to compute the BEP from single runs. For each single run, we have generated 10^6 data symbols.

In Fig. E.1, the BEP of an Alamouti coded OFDM system over different C2C fading channels correlated in time versus the SNR has been illustrated. In our analysis, as mentioned in Section IV, it has been assumed that the CSI is known at the receiver side. Hence, from Fig. E.1, we can conclude that the maximum Doppler frequency $f_{T_{\max}}$ ($f_{R_{\max}}$) does not affect the system performance if $f_{T_{\max}}$ ($f_{R_{\max}}$) changes over the range from 100 Hz to 500 Hz. It is worth mentioning that all considered C2C channels behave in the same manner, as the same BEP is demonstrated. Moreover, it should be mentioned that the system simulation results match those of the theoretical BEPs.

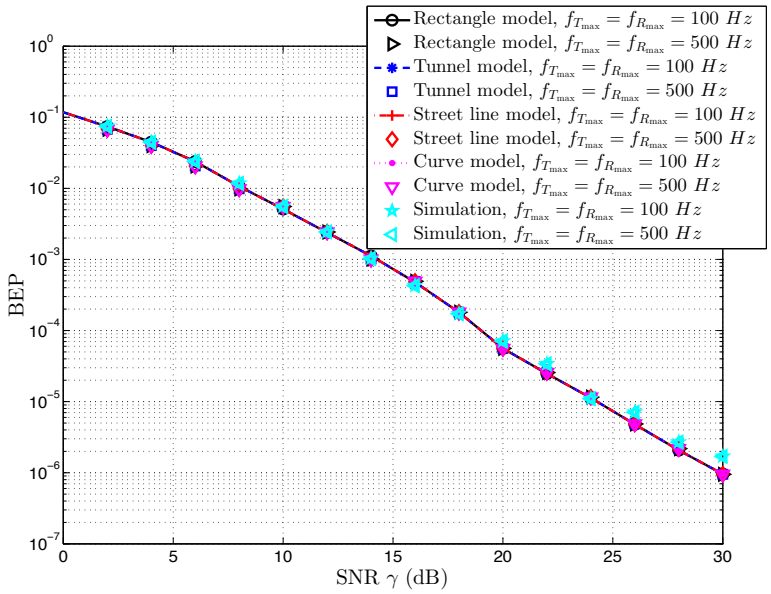

Figure E.1: BEP performance of an Alamouti coded OFDM system over different C2C fading channels correlated in time.

Figure E.2 shows the BEP performance over different C2C fading channels correlated in space for $\delta_T=0.1\lambda$ and $\delta_T=3\lambda$. From this figure, we can conclude that the system performance can be improved by increasing the antenna spacings. This fact indicates that the spatial correlation between TVTFs $H_{kl,p}(f',t)$ and $H_{k'l',p}(f',t)$ is smaller if the antenna element spacings are large. Similarly to Fig. E.1, the curves obtained for the BEP are approximately the same for different C2C channel models.

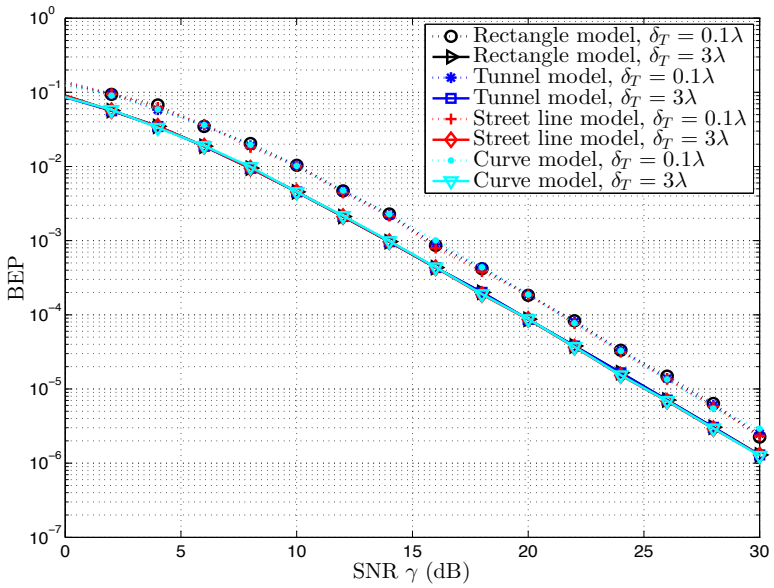

Figure E.2: BEP performance of an Alamouti coded OFDM system over different C2C fading channels correlated in space with $\delta_T = 0.1\lambda$ and $\delta_T = 3\lambda$.

Figure E.3 shows the effect of the street length L_A and the distance D between MS_T and MS_R on the BEP performance. The system performance improves as the length of the street L_A increases. However, the BEP performance does not change for different values of the distance between MS_T and MS_R. The change of the street width B_1 and B_2 does not affect the BEP performance, which can be seen in Fig. E.4. This fact can be attributed to the presence of a large number of scatterers located on a street line. Nevertheless, the system performance can be improved by increasing antenna spacings δ_T from 0.1λ to 3λ.

The effect of the tunnel model parameters, i.e., the radius R of the tunnel arch and the distance D between MS_T and MS_R, on the performance of C2C communication systems has been demonstrated for different antenna element spacings δ_T in Fig. E.5. We can see the same performance in terms of the BEP for different values of R and D, which means that small changes in R and D do not affect the system performance. From Fig. E.5, one can see the effect of the antenna spacings δ_T, in which the system performance is improved by increasing δ_T.

Finally in Fig. E.6, the system performance of the C2C channel model based on the curve model is shown. Similarly to Fig. E.5, the BEP performance does not change if the radius R of the curve varies in the considered range.

VI. Conclusion

In this paper, a generalized reference model for wideband MIMO C2C channels has been derived by assuming single-bounce scattering. An extension from the

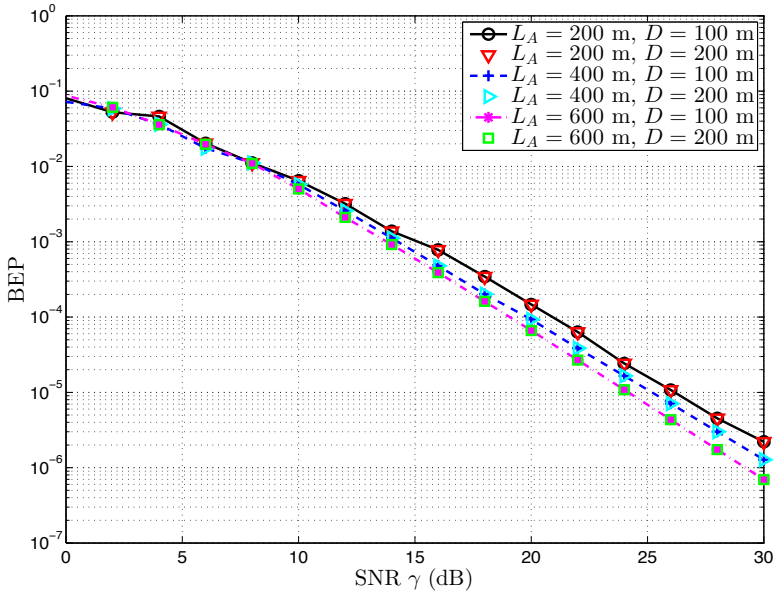

Figure E.3: BEP performance of an Alamouti coded OFDM system over a C2C channel (rectangle model) for different values of L_A and D.

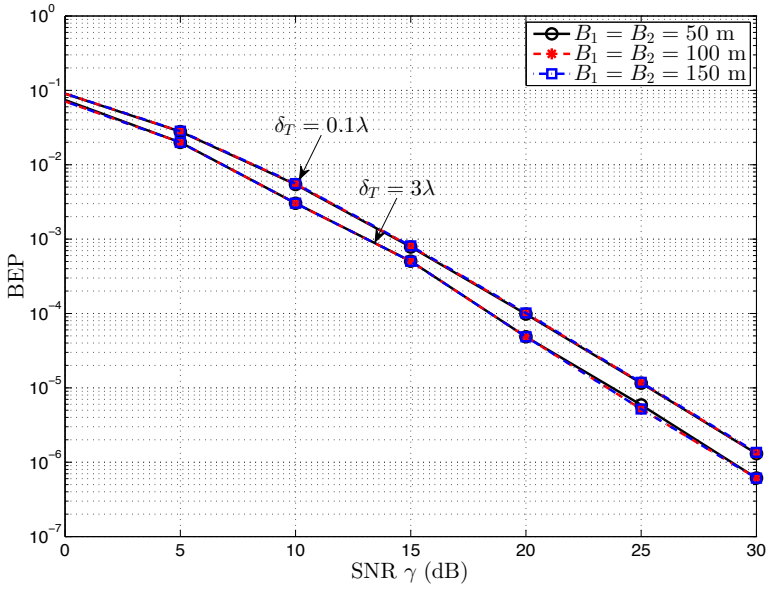

Figure E.4: BEP performance of an Alamouti coded OFDM system over a C2C channel (rectangle model) for different values of B_1 and B_2.

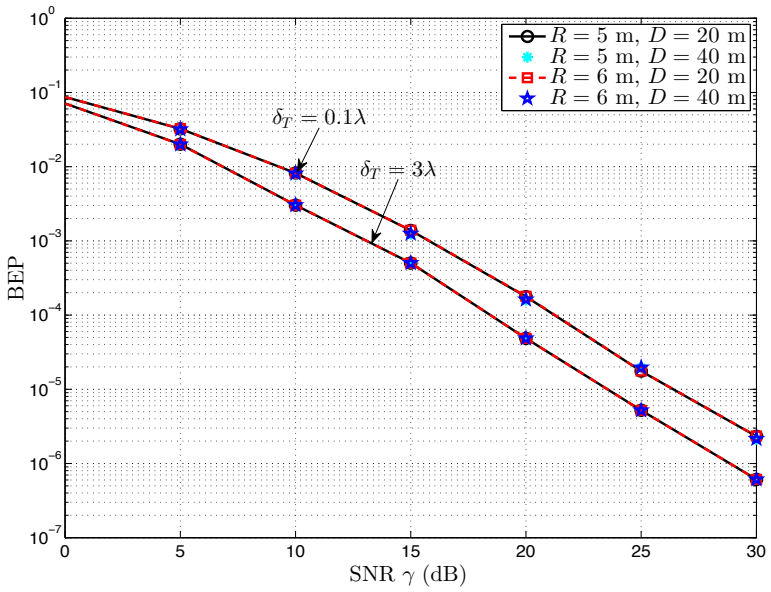

Figure E.5: BEP performance of an Alamouti coded OFDM system over a C2C channel (tunnel model) for different values of R and D.

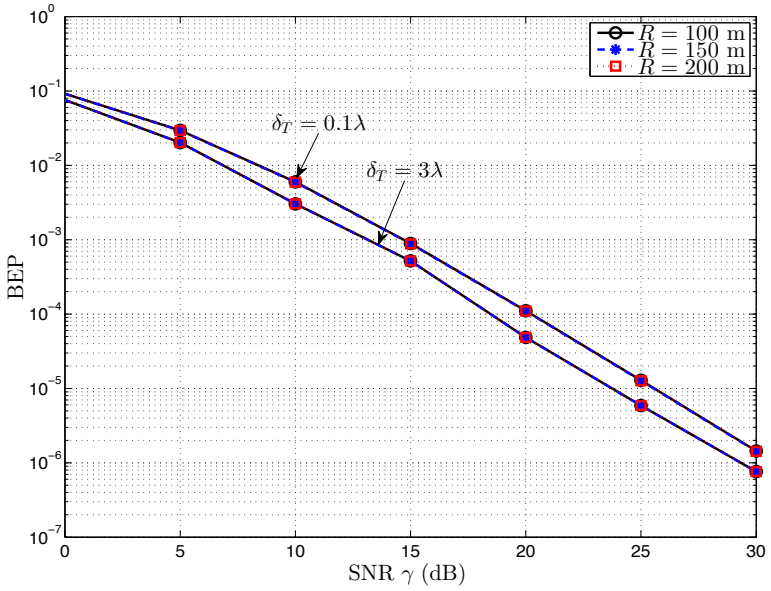

Figure E.6: BEP performance of an Alamouti coded OFDM system over a C2C channel (curve model) for different values of the curve radius R.

SISO C2C tunnel model to the MIMO case has been performed. Furthermore, an extension of the narrowband MIMO C2C channel model based on the curve model to the wideband model has been provided. An analytical expression has been presented for the BEP of Alamouti coded OFDM systems over generalized C2C channels. The effect of the geometrical model parameters of the propagation area on the system performance has been studied and discussed. It has been shown that using large antenna element spacings improves the system performance. The proposed generalized C2C channel model can serve as a highly flexible C2C channel simulator, which allows system developers to simulate a variety of C2C channels and to evaluate their performance under different propagation conditions.

REFERENCES

[1] G. Rafiq, B. Talha, M. Pätzold, J. G. Luis, G. Ripa, I. Carreras, C. Coviello, S. Marzorati, G. P. Rodrigues, G. Herrero, and M. Desaeger, "What's new in intelligent transportation systems? An overview of European projects and initiatives," *IEEE Veh. Technol. Mag.*, vol. 8, no. 4, pp. 45–69, Dec. 2013.

[2] Car-to-Car Communication Consortium (C2C-CC) [Online]. Available: http://www.car-to-car.org.

[3] European Road Transport Telematics Implementation Coordinating Organization (ERTICO) [Online]. Available: http://www.ertico.com.

[4] A. Chelli and M. Pätzold, "A MIMO mobile-to-mobile channel model derived from a geometric street scattering model," in *Proc. 4th IEEE International Symposium on Wireless Communication Systems, ISWCS 2007, Trondheim, Norway*, Oct. 2007, pp. 792–797.

[5] N. Avazov and M. Pätzold, "Design of wideband MIMO car-to-car channel models based on the geometrical street scattering model," *Special Issue: Modelling and Simulation in Engineering*, vol. 2012, Sept. 2012.

[6] A. Theodorakopoulos, P. Papaioannou, T. Abbas, and F. Tufvesson, "A geometry based stochastic model for MIMO V2V channel simulation in cross-junction scenario," in *Proc. 13th International Conference on ITS Telecommunications, Tampere, Finland*, Nov. 2013, pp. 290–295.

[7] N. Avazov and M. Pätzold, "A novel MIMO car-to-car channel model based on the geometrical curved street scattering model," in *Proc. Loughborough An-*

tennas and Propagation Conference, LAPC'2012, Loughborough, UK, Nov. 2012, pp. 1–6.

[8] ——, "A wideband car-to-car channel model based on a geometrical semi-circular tunnel scattering model," in *Proc. 24th IEEE Int. Symp. on Personal, Indoor and Mobile Radio Communications, PIMRC 2013, London, UK*, Sept. 2013, pp. 253–258.

[9] V. Shivaldova, G. Maier, D. Smely, N. Czink, A. Alonso, A. Winkelbauer, A. Paier, and C. F. Mecklenbräuker, "Performance evaluation of IEEE 802.11p infrastructure-to-vehicle tunnel measurements," in *Proc. 7th International Wireless Communications and Mobile Computing Conference, IWCMC 2011, Istanbul, Turkey*, Jul. 2011, pp. 848–852.

[10] A. Chelli, R. Hamdi, and M.-S. Alouini, "Channel modelling and performance analysis of V2I communication systems in blind bend scattering environments," *Progress in Electromagnetics Research B*, vol. 57, pp. 233–251, 2014.

[11] V. Shivaldova, A. Winkelbauer, and C. F. Mecklenbräuker, "Vehicular link performance: From real-world experiments to reliability models and performance analysis," *IEEE Veh. Technol. Mag.*, vol. 8, no. 4, pp. 35–44, Dec. 2013.

[12] I. Ivan, P. Besnier, M. Crussiere, M. Drissi, L. Le Danvic, M. Huard, and E. Lardjane, "Physical layer performance analysis of V2V communications in high velocity context," in *Proc. 9th International Conference on Intelligent Transport Systems Telecommunications, ITST 2009, Lille, France*, Oct. 2009, pp. 409–414.

[13] D. W. Matolak, W. Qiong, J. J. Sanchez-Sanchez, D. Morales-Jimenez, and M. C. Aguayo-Torres, "Performance of LTE in vehicle-to-vehicle channels," in *Proc. IEEE Vehicular Technology Conference, VTC2011-Fall, San Francisco, CA*, Sept. 2011, pp. 1–4.

[14] X. Cheng, Q. Yao, M. Wen, C.-X. Wang, L.-Y. Song, and B.-L. Jiao, "Wideband channel modeling and intercarrier interference cancellation for vehicle-to-vehicle communication systems," *IEEE J. Select. Areas Commun.*, vol. 31, no. 9, pp. 434–448, Sept. 2013.

[15] A. Böhm, K. Lidström, M. Jonsson, and T. Larsson, "Evaluating CALM M5-based vehicle-to-vehicle communication in various road settings through field

trials," in *Proc. 35th IEEE Conference on Local Computer Networks (LCN)*, Oct. 2010, pp. 613–620.

[16] G. Acosta-Marum and M. A. Ingram, "A BER-based partitioned model for a 2.4 GHz vehicle-to-vehicle expressway channel," *Wireless Personal Communications (WPC)*, vol. 37, pp. 421–443, 2006.

[17] S. M. Alamouti, "A simple transmit diversity technique for wireless communications," *IEEE J. Select. Areas Commun.*, vol. 16, no. 8, pp. 1451–1458, Oct. 1998.

[18] Y. Ma and M. Pätzold, "Performance analysis of Alamouti coded OFDM systems over Rayleigh fading channels correlated in space and time," in *Proc. the 71st IEEE Vehicular Technology Conference, VTC2010-Spring, Taipei*, May 2010, pp. 1–6.

[19] A. Papoulis and S. U. Pillai, *Probability, Random Variables and Stochastic Processes*, 4th ed. New York: McGraw-Hill, 2002.

[20] B. O. Hogstad, C. A. Gutiérrez, M. Pätzold, and P. M. Crespo, "Classes of sum-of-cisoids processes and their statistics for the modeling and simulation of mobile fading channels," *EURASIP J. Wireless Commun. Netw.*, vol. 2013 (1), pp. 1–15, May 2013. doi: 10.1186/1687-1499-2013-125.